9-15-2014

Comparison of the Performance of RC and CFFT Bridge Piers under Multiple Hazards

Alicia A. Echevarria
University of Connecticut - Storrs, aechevarria5@live.com

Comparison of the Performance of RC and CFFT Bridge Piers under Multiple Hazards

Alicia Echevarria, PhD

University of Connecticut, 2014

Recent mega-disasters, such as the 2011 Great East Japan Earthquake, have prompted the technical community to understand the resilience of infrastructure when subjected to extreme events and the shortcomings of conventional structural systems under multiple hazards. Columns are the most critical load carrying elements of bridge structures, and the resilience of a bridge is significantly dependent upon the structural performance of its columns. The objective of this research is to compare the resilience of reinforced concrete (RC) and concrete-filled fiber reinforced polymer (FRP) tube (CFFT) bridge columns under multiple hazards through combined experimental and analytical studies.

The experimental work includes blast and fire testing of one-fifth scale RC and CFFT bridge columns. The performance of each type of column is studied under two severities of exposure to each type of hazard. Subsequently, axial capacity tests are performed on eight damaged columns as well as two undamaged benchmark columns, one of each type. The residual axial load carrying characteristics are used to quantify and compare the resilience of RC and CFFT columns to blast and fire. The experimental results show that CFFT columns outperform RC columns during and after blast and fire events. The FRP tube provides sufficient confinement to resist shear crack initiation in the concrete core during blast loading resulting in retention of its axial load carrying capabilities. Conversely, the RC column suffered reductions in axial ductility due to a shear-type failure under axial load. The Tyfo-CFP system allowed the concrete temperatures of the CFFT columns to remain low during fire exposure, resulting in retention of

axial capacity and stiffness. The concrete temperatures of the RC columns exceeded degradation thresholds for both strength and stiffness resulting in reduced axial capacity after fire exposure.

Analytical work consists of using an OpenSees model allows further study of the effects of blast loading on RC and CFFT columns. The model is advanced to study the seismic resilience of RC and CFFT columns, expanding the multihazard aspect of this research. The residual axial capacities of RC and CFFT columns are analytically compared after two levels of biaxial seismic ground motions. Finally, a design methodology for CFFT bridge columns with minimal amounts of longitudinal steel reinforcement is developed to facilitate the adoption of CFFT bridge columns in multihazard resilient bridge designs.

Comparison of the Performance of RC and CFFT Bridge Piers under Multiple Hazards

Alicia Echevarria

B.S., University of Nevada, Reno, 2011

A Dissertation Proposal

Submitted in Partial Fulfillment of the

Requirements for the Degree of Doctor of Philosophy

at the

University of Connecticut

2014

APPROVAL PAGE

Doctor of Philosophy Dissertation

Comparison of the Performance of RC and CFFT Bridge Piers under Multiple Hazards

Presented by

Alicia Echevarria, B.S.

Major Advisor 
Arash E. Zaghi

Associate Advisor 
Richard Christenson

Associate Advisor 
Michael Accorsi

University of Connecticut

2014

Dedication

This dissertation is dedicated to Christian. Your spirit will forever remind me to live life in the way that I choose, without reservations. Rest in Paradise, and fly with Louie.

Acknowledgment

This material is based upon work supported by the U.S. Department of Homeland Security under the DHS HS–STEM Career Development Grant Award Number 2008-ST-061-TS002. Funding for the experimental work was also supplied by The National Transportation Security Center of Excellence (NTSCOE) funded by the Department of Homeland Security Centers of Excellence (COE) grant program, administered through the DHS Science and Technology Directorate (S&T) Office of University Programs (OUP).

My deepest gratitude is expressed toward the principal investigator and chair of my advisory committee, Dr. Arash E. Zaghi. At times, he has believed in my abilities more than I do myself. His support and guidance is the fundamental reason for my academic success. I would also like to extend my thanks to my associate advisors, Dr. Richard Christenson and Dr. Michael Accorsi, and all other School of Engineering faculty members that have assisted me along the way.

Vince Chiarito, Stanley Woodson, Jared Minor, Larry Garrett, Clifford Grey, Arnette Nash, and many others from USACE-ERDC are thanked for the assistance they provided during the blast experiments. Special thanks to Matt Smith of National Oilwell Varco for donating the FRP tubes, Berlin Steel for the beams used to construct the blast test frame, and Peter Glaude and Serge Doyan for their machining and fabrication work. Also, the assistance provided by Masoud Mehrraoufi and Kevin Zmetra during construction and axial capacity testing is very much appreciated. Fyfe, Co. is acknowledged for the donation of the fire protection system for the fire experiments and Brian Flaherty for the donation of the flame retardant coating used during blast testing.

Last, but certainly not least, I would like to thank my unconditionally loving parents and fiancé. My parents have provided me with every opportunity to be great in all aspects of life, and for that, I am forever in their debt. Andy is my rock. He provided more love, support, and motivation from 3,000 miles away than I could have ever imagined.

Table of Contents

List of Tables

List of Figures

1 Introduction

1.1 Introduction

Bridges are critical elements of surface transportation networks and play a significant role in disaster response. After an extreme event, such as a terrorist attack, tanker truck fire, or earthquake, communities may suffer for an extended period of time if a bridge is impassable by first responders, emergency vehicles, or daily traffic. For instance, the tsunami following the 2011 Tohoku earthquake in Japan washed away the sole bridge to Miyatojima, Miyagi, which isolated the island and 900 residents, and inhibited the crucial supply of food, water, and medical aids (Kyodo News, 2011). The sequential devastating events following the Tohoku earthquake including the three major aftershocks of magnitude 7.0 or greater, the tsunami, and the Fukushima nuclear disaster resulted in $300 billion in damages (Spacey, 2011). The recent increase in number and severity of both natural and manmade hazards combined with the age and condition of the nation's bridges have prompted the technical community to improve its understanding of infrastructure resilience to multiple extreme events.

For a bridge structure, columns play an indispensable role in the overall resiliency of the bridge itself. While multiple components play a role in the global resiliency of bridge structures, the failure of a single column can result in total collapse of the entire bridge. Conversely, other components, such as bearings, abutment backwalls, and shear keys are designed as sacrificial elements that can be repaired or replaced easily. A bridge's columns must retain their axial capacity after an extreme event or series of events to keep the bridge in service and provide first responders and emergency vehicles access to exclusive regions affected by the event(s). The highest form of resiliency for a bridge column occurs if its response to an extreme event results in no loss of its structural capacity, eliminating the component's need for recovery completely.

The vast majority of columns currently used for bridge and elevated highway construction are conventional reinforced concrete (RC) columns. Although the RC columns used today are not exactly the same as the first RC members introduced in the United States in the 1870s (McCormac, 1978), there has been little advancement in RC systems. Technological change in the bridge construction industry has generally been comprised of incremental improvements to project design, construction methods, and materials, rather than single dramatic developments (Soshkin, 2014). Now, as the nation's bridge infrastructure ages, traffic demands increase, and both natural and manmade hazards become more prevalent, significant deterioration of bridge components is exhibited around the nation. In 2013, the American Society of Civil Engineers (ASCE) assigned bridge infrastructure with a grade of "C+" in their Report Card for America's Infrastructure (ASCE, 2013), and the Federal Highway Administration (FHWA) estimates that nearly 25% of the nation's bridges are deficient and require replacement or rehabilitation (FHWA, 2013). The poor condition of the nation's bridges combined with limited funding and increased construction costs calls for more resilient, longer lasting, and cost effective systems leading to more sustainable bridges.

To this end, this research consists of a comprehensive experimental and analytical research program comparing the performance and resilience of conventional RC columns under multiple hazards with the innovative concrete-filled fiber reinforced polymer (FRP) tube (CFFT) column system. Blast and fire experiments followed by axial capacity tests compare the performance of RC and CFFT columns during and after blast and fire hazards. An analytical study combined with observations from shake table experiments at the University of Nevada, Reno (UNR) (Zaghi et al. 2012) expand the multihazard study to include earthquake hazards as well. Finally, additional analytical work is performed to develop axial and flexural resistance

equations and curvature ductility curves intended to supplement AASHTO Specifications (2011, 2012a) for the design of lightly reinforced CFFTs.

1.2 The CFFT System

Concrete-filled fiber reinforced polymer (FRP) tube (CFFT) columns were first introduced as a highly durable alternative to conventional reinforced concrete (RC) bridge piers by Mirmiran and Shahaway (1995, 1996). It was discovered that an off-the-shelf FRP petrochemical pipe system manufactured by National Oilwell Varco (NOV) Fiberglass Systems (FGS) with fibers wound at ±55° (NOV, 2009) provides comparable capacity and superior ductility to conventional RC columns when filled with lightly reinforced regular concrete. Experiments proved that the ±55° fiber orientation is optimal for the flexural capacity and ductility of CFFT columns (Shao and Mirmiran, 2005). The durability of these composite pipes has been proven through several instances where they have stayed in-service in highly corrosive environments for nearly forty years (FGS, 2005). In addition, this CFFT system offers several advantages over RC columns in terms of structural performance and construction including: 1) the fiber alignment of the FRP tube provides both longitudinal strength and confinement to the core concrete, which allows for elimination of the entire lateral steel reinforcement and a significant reduction of longitudinal bars, 2) the tube furnishes a self-curing environment for the concrete core, 3) it omits the scaffolding, frame work, and frame removal stages of column construction, and 4) it protects the inner core in highly corrosive environments (Zaghi et al., 2012).

1.3 Review of Related Research

This section contains a review of previously conducted related research that serves as the foundation for this study. First, the studies of the structural and seismic performance of CFFT columns are presented. These studies provoked the hypothesis that CFFTs would outperform RC

columns during and after blast and fire hazards. The next two subsections contain overviews of past blast and fire studies of various types of bridge columns. These studies helped the direct development of successful experimental programs to compare the performance of RC and CFFT columns both during and after exposure to these types of hazards. Finally, a review of studies that examine bridge columns from a multihazard perspective are presented. Researchers are becoming increasingly aware of the fact that bridge columns can be subjected to multiple hazards throughout their lifespan (Liang and Lee, 2013). Thus, studies, like the one presented herein, examining the performance and resilience of bridge columns to various types of hazards can potentially impact on the future design of resilient bridge infrastructure.

1.3.1 Structural and Seismic Performance of CFFT Bridge Columns

The structural characteristics of CFFT columns were first studied at Florida International University. A series of uniaxial compression and beam-column experiments on various shapes and sizes of CFFT members studied the effect of using FRP tubes to reinforce structural columns (Mirmiran and Shahawy, 1997; Mirmiran et al., 1999, 2000; Fam, 2000). FRP tubes were found to provide an effective means of confinement for concrete resulting in increased strength and ductility over conventional RC columns. Further experimental and analytical studies compared the structural performance of CFFTs consisting of various materials and differing laminate structures (Fam et al., 2003c; Fam and Rizkalla, 2002).

The structural performance studies were followed on by studies of the CFFT system under seismic loads. The seismic performance of CFFT columns was first studied through pseudo-dynamic testing (Shao, 2003; Shao and Mirmiran, 2005; Sheikh and Yau, 2002; Shi et al., 2011, 2013; Zhu et al., 2006b). These studies were then expanded to analytical models (Zhu

et. al, 2006a; Shao et al., 2005) and CFFTs containing ultra-high performance concrete (Zohrevand and Mirmiran, 2013).

Several experimental shaking table studies have since been conducted on large scale CFFT bridge columns at the University of Nevada, Reno (UNR) (Zaghi and Saiidi, 2010a,b; Zaghit et al., 2012); Cruz Nogues and Saiidi, 2012; Saiidi et al., 2011; Motaref et al., 2011). These shake table experiments on CFFT columns demonstrated that FRP tubes have the ability to provide a ductile alternative to conventional reinforcement in areas of high seismicity. These studies not only tested and compared the seismic performance of CFFTs with conventional RC columns, but they also included several advanced materials and construction details including engineered cementitious composites, pipe pin hinges, and shape memory alloys.

1.3.2 Blast Studies of Bridge Columns

The attacks on September 11, 2001 (9/11) prompted engineers to not only develop protection measures for building structures, but also protection methods for the nation's bridge infrastructure. Since 9/11 several experimental studies have been conducted on the blast performance of conventional RC columns resulting in new analysis, design, and retrofit methods for increased blast resistance (Winget et al., 2005a,b; Williamson and Winget 2005; Williamson and Marchand, 2006; Williams and Williamson 2012; Williamson et al., 2010, 2011a,b; Davis et al., 2009; Williams, 2009; Gram et al. 2006).

The blast performance of alternative novel systems such as steel reinforced polymer (SRP), carbon and glass fiber reinforced polymer (CFRP/GFRP) wrapped concrete columns, (Crawford, 2013; Berger et al., 2008; Gram et al., 2006; Muszynski and Purcell, 2003), concrete-filled steel tube (CFST) columns (Fujikura et al. 2007, 2008; Keller et al. 2009; Fukikura and Bruneau 2008, 2011; Huo, 2013), and CFFT columns (Qasrawi, 2014) has also been studied.

Additionally, Fujikura and Bruneau (2012), Yi et al. (2014a,b), Agrawal and Yi (2009), Islam and Yazdani (2008), Elsanadedy et al. (2011), and Jayasooriya et al. (2014) have analytically studied the blast performance of CFST, RC, CFRP wrapped, and steel-concrete composite columns. However, the residual axial performance, or blast resilience, of CFFT columns has not been quantified, experimentally or analytically, prior to this research.

1.3.3 Fire Studies of Columns

In general, building columns are at higher risk of fire exposure than bridge columns, and fire studies of bridge structures are typically dedicated to the performance of steel superstructures. Thus, literature dedicated solely to the resistance of bridge columns to fire is limited. However, studies of building column performance can be easily translated to bridge columns, and there is literature dedicated to the performance of concrete, both confined and unconfined, subjected to extreme temperature exposure (Chang et al., 2006; Knaack et al., 2009; Zaidi et al., 2012). The fire resistance of conventional RC columns has also been studied extensively by the National Research Council Canada (Lie and Wollerton, 1988; Lie, 1989; Lie and Lin, 1986).

More recently, studies have been conducted on advanced materials and systems such as high strength concrete and concrete-filled steel columns (Kodur and Phan, 2007; Hernandez-Olivares and Barluenga, 2004; Kodur, 1999; Han, 2001). Previous studies have also been conducted on both CFFT and FRP wrapped columns (Bisby et al., 2005; Kodur et al., 2007; Gefu et al., 2008). Chowdhury et al. (2007) investigated insulated FRP-wrapped columns under concentric axial load during fire testing. However, studies comparing the residual axial capacity characteristics of RC and CFFT columns after fire exposure had not been conducted prior to this research.

1.3.4 Multihazard Studies of Bridge Columns

A combination of multiple hazards acting concurrently or spaced over time may drastically increase the vulnerability of a bridge structure designed for a single extreme event. One such damaging scenario that has been studied extensively in recent years is corrosion and earthquake (Alipour, et al., 2011; Choe et al., 2008, 2009; Li, et al., 2009; Ghosh and Padgett, 2010; Simon, et al., 2010; Aquino and Hawkins, 2007; Rokneddin, et al., 2013). In areas where deicing salts or marine and industrial environments expose a bridge structure to chlorides, corrosion of rebar can lead to structural degradation and reduced seismic performance.

More often than not a large earthquake does not consist of just one ground motion but a main shock plus one or more aftershocks. This main shock-aftershock is another form of multihazard exposure. Franchin and Pinto (2007, 2009), Kumar and Gardoni (2012), and Ghosh et al. (2013) have studied this phenomenon.

The combined effect of scour and seismic has also been previously studied (Alipour, et al., 2010, 2013; Prasad and Banerjee, 2013; Liang and Lee, 2013b,c). There are still many other possible scenarios affecting bridge column performance that should be comprehended through extensive research programs. Examples of which are the interaction of independent events such as fire and earthquake and blast and earthquake. A series of studies at the University at Buffalo have studied concrete filled steel tubes under independent blast and seismic events (Fujikura and Bruneau, 2008, 2011, 2012; Fujikura et al., 2007, 2008; Bruneau et al., 2011).

The research presented herein studies the effects of three different hazards, blast, fire, and earthquake, and sets up the framework for future studies aimed at studies of the combination and interactions of multiple hazards for CFFT bridge columns.

1.4 Objectives and Scope of Work

The goals of this research are to comparatively study the resilience of RC and CFFT columns to blast, fire and seismic hazards through a comprehensive four phase research program. Because bridge columns are primarily axial load carrying members, the residual axial load carrying characteristics of the two types of columns are used as the measures of resilience in this study. The first phase consists of experimental blast testing of one-fifth scale RC and CFFT columns at the United States Army Corps of Engineers (USACE) Engineering Research and Development Center (ERDC) in Vicksburg, MS. The second phase consists of experimental fire testing at the Guardian Fire Testing Laboratory in Buffalo, NY. During the third phase, all of the blast and fire damaged bridge column specimens are loaded axially to failure to obtain residual axial capacity characteristics in the Structural and Material Research Laboratory at the University of Connecticut (UConn).

In the final phase, the experimental data from the first three phases is processed, and an analytical model is calibrated to further study the dynamic effects of blast on RC and CFFT columns. The analytical model is subsequently advanced to further study the axial performance of RC and CFFT columns after seismic events. Additionally, a series of analytical cross sectional analyses are conducted and validated using experimental results to develop a design methodology for lightly reinforced CFFT columns for use in multihazard scenarios.

1.4.1 Experimental Studies

To study the resilience of RC and CFFT bridge columns to blast and fire events, an experimental program including blast, fire, and residual axial capacity testing was developed and performed by UConn. The blast experiments were conducted in collaboration with the Army Corps of Engineers at the Big Black test site in Vicksburg, MS; the fire testing was conducted at Guardian

Fire Testing Facility in Buffalo, NY; and the residual axial capacity tests were performed at the Structures Laboratory at UConn.

The objective of the experimental program was to compare the performance and resilience of RC and CFFT columns subjected to blast and fire hazards. The experiments included five blast tests conducted on two RC and two CFFT column specimens to study the blast performance of the two column types, two fire tests conducted on two RC and two CFFT columns to test the performance of the column types when exposed to extreme temperatures, and ten axial capacity tests on the eight blast and fire damaged columns and an undamaged benchmark column of each type to quantify the resilience of RC and CFFT columns after blast and fire events.

1.4.2 Analytical Studies

In addition to the experimental investigations, several analytical studies were conducted during this research utilizing OpenSees (PEER, 2012) and XTract (Imbsen, 2007) software packages.

First an OpenSees model was developed to further study the dynamic effects of blast loading on RC and CFFT columns. This model was calibrated using the longitudinal strain histories recorded at midspan of each column during the experimental blast tests. The OpenSees model was advanced to study the resilience of RC and CFFT columns to seismic events. Although many experimental studies at the University of Nevada, Reno (UNR) have studied the performance of both types of columns under seismic ground motions (Zhu, et al., 2006; Zaghi et al., 2012; Kavianipour and Saiidi, 2012), the residual capacities of the columns were not determined experimentally. This model was validated using the axial capacity results obtained from the tests of the undamaged RC and CFFT columns at UConn as well as the results of the experimental shake table results obtained by Zaghi et al. (2012).

Finally, OpenSees and XTract were used together to conduct extensive cross sectional analyses on a generalized CFFT column to develop axial and flexural resistance equations and curvature ductility curves for load- and displacement-based design of lightly reinforced CFFTs. The resulting axial resistance equation was validated using the results of the undamaged CFFT axial test at UConn, and the flexural resistance equation was validated using the moment capacity of the CFFT column obtained from the experimental shake table test performed at UNR (Zaghi et al., 2012).

1.5 Document Layout

This introductory chapter is followed by a chapter detailing the experimental blast and fire studies. Specimen designs, drawings, test set up details, material properties, instrumentation, and loading protocols are all included in Chapter 2.

Chapter 3 is comprised of the results and observations collected from the blast and fire experiments. The chapter includes general observations, strain and load history data, and data collected from free field pressure gauges for the blast tests. Additionally, the furnace and concrete temperature data recorded during the fire exposure experiments is presented.

The axial capacity experiment details, results, and observations are presented in Chapter 4. The loading protocol, instrumentation, and axial load-deformation results are reported. Two types of axial capacity comparisons are made. First the blast and fire damaged RC and CFFT specimens are compared to their respective undamaged benchmark columns. Then the residual load carrying capacities of the RC and CFFT columns are compared to each other.

Chapter 5 presents the analytical work of this study. All components of the OpenSees blast and seismic models are explained. The cross sectional analyses performed using both

OpenSees and XTract are described. The analytical data and experimental results are also compared and discussed in this chapter.

This research studies RC and CFFT columns under multiple separate hazard events. However, some multihazard design implications can be inferred from the results of this work. These multihazard implications are presented in Chapter 6.

In Chapter 7, the cross sectional analyses of a generic full-scale CFFT column and the resulting axial and flexural resistance equations and ductility curves for CFFTs containing a small amount of steel reinforcement are presented.

The completed research program is summarized in Chapter 8. This chapter also includes significant observations and conclusions from each phase of the study.

2 Experimental Blast and Fire Studies

2.1 Introduction

The project consists of three experimental phases: I) Experimental Blast Loading – Army Corps of Engineers Research and Development Center (ERDC), Vicksburg, MS; II) Experimental Fire Exposure – Guardian Fire Testing Laboratory, Buffalo, NY; and III) Residual Axial Capacity Testing – UConn Structures Laboratory, Storrs, CT. This chapter contains detailed information on the first two phases. The details of the third phase are presented in Chapter 4. The details of the RC and CFFT column specimens including the design and material properties are consistent for all three phases. Thus, they are only described once. The concept and purpose, instrumentation, test set-up, and loading protocol of the blast and fire experiments are unique from each other and as such are presented in separate sections.

2.2 RC Specimens

2.2.1 Introduction

Conventionally reinforced concrete (RC) bridge columns are designed in accordance with Section 5 of the AASHTO LRFD Bridge Design Specifications (2012b) for non-seismic applications. A separate AASHTO specification (AASHTO, 2011) is utilized for the seismic design of bridge columns. Conventional column reinforcement consists of rebar running longitudinally within the concrete to provide flexural resistance, and either spiral or tie reinforcement encompassing the longitudinal rebar for concrete confinement and shear resistance. Spiral reinforcement consists of a continuous steel spiral with a specified pitch that runs the length of the longitudinal reinforcement and is tied to the longitudinal bars using steel tie wire. The alternative to spiral reinforcement is using tied transverse reinforcement. Ties are similar to spirals except each hoop is a singular piece as opposed to running continuously. The

spacing of each tied hoop is specified in much the same manner as the pitch of the spiral reinforcement. Each hoop is tied in place using steel tie wire; also very similarly to spiral reinforcement. Figure 2-1 displays a general schematic for a circular column with spiral and tied reinforcement.

In the past RC bridge columns have shown vulnerabilities to many types of hazards including earthquakes, blast, and fire. To study the performance of RC columns subjected to blast and fire hazards, five one-fifth scale RC columns were constructed. Two were instrumented specifically for blast testing, two specifically for fire testing, and the fifth column was instrumented as a benchmark column. All five columns were subjected to axial capacity testing after the blast and fire experiments to measure the post-extreme-event functionality of the columns. The results of the blast and fire experiments are presented in Chapter 3, and the details and results of the axial capacity tests can be found in Chapter 4.

2.2.2 RC Specimen Design

It was critical that the axial capacity of the RC specimens did not exceed the capacity of the 400k load frame in the UConn Structures Lab that was used for the axial capacity testing of the column models.

A two-span highway bridge design example developed by Modjeski and Masters, Inc. (2003) was used as a basis for the design of the RC specimens. The diameter and height of the full-scale prototype column were geometrically scaled by one-fifth, and comparable longitudinal and lateral reinforcement ratios were incorporated. The final design of the RC specimens was in compliance with the American Association of State Highway Transportation Officials (AASHTO) (2012b) Seismic Zone 1 Specifications. The RC specimens had a diameter of 8in. (203mm) and a height of 48in. (1.22m). The longitudinal reinforcement consisted of eight Gr.

60 #3 (0.375in. (9.525mm) -diameter) bars resulting in a steel reinforcement ratio of 1.75%. The transverse reinforcement was provided by 6.35mm (0.25in.) -diameter smooth wire spirals with a pitch of 63.5mm (2.5in.). The rebar cages are shown in Figure 2-2.

XTract (Imbsen, 2007) section analysis software was used to determine the axial and flexural strength of the RC columns based on specified 4ksi (27.6MPa) concrete and 60ksi (414MPa) reinforcing steel. The Mander et al. (1988) model for confined concrete was used to model the core of the column. The design axial load-strain and moment-curvature relationships are shown in Figures 2-3 and 2-4. The ultimate axial and flexural capacities of the design are 267.9kip (1192kN) and 182.4k-in (20.6kN-m), respectively. The shear capacity of the column was determined following the procedure of Kowalsky and Priestley (2000). The shear capacity was calculated as 27.9kip (124.2kN). Assuming the blast pressure would be applied as a uniform distributed load along the column length, the plastic shear demand was calculated from the ultimate moment capacity of the column as shown in Eq. 1

$$V_p = \frac{4M_u}{L} \quad (1)$$

where V_p is the plastic shear demand, M_u is the ultimate moment capacity, and L is the length of the column. The plastic shear demand was calculated as 67.7kN (15.2kip).

2.3 CFFT Specimens

2.3.1 Introduction

CFFTs consist of FRP tubes filled with regular lightly or unreinforced concrete. CFFTs were first used in the field as marine piles (Fam et al., 2003a) and later as precast piles for a Route 40 highway bridge in Virginia (Fam et al., 2003b). Although there are a few cases where CFFTs have been used in the field, the system is relatively new to the bridge design community. The first edition AASHTO Guide Specifications for Design of Concrete-Filled FRP Tubes for

Flexural and Axial Members (2012a), referred to as "Guide Spec" hereafter, was released in January 2013. Prior to the release of the Guide Spec, CFFTs were typically used as columns only in research environments with the design of the system under the discretion of the researchers.

Five one-fifth scale CFFT bridge columns were designed and constructed for comparison with the RC columns under blast and fire hazards. Similar to the RC specimens, two were instrumented specifically for blast testing, two specifically for fire testing, and the fifth column was instrumented as a benchmark column. Again, all five of the CFFT columns were subjected to axial capacity testing after the blast and fire experiments to measure the post-extreme-event functionality of the columns. The results of the blast and fire experiments are presented in Chapter 3, and the axial capacity test details and results can be found in Chapter 4.

2.3.2 CFFT Specimen Design

As it was with the RC column design, it was critical that the axial capacity of the CFFT specimens did not exceed the capacity of the 400k load frame in the UConn Structures Lab that was used for the axial capacity testing of the column models.

The aforementioned first edition Guide Spec (AASHTO, 2012a) had not been released when the CFFT specimens were designed for this study. Previously conducted shaking table experiments showed that a minimal number of longitudinal bars are necessary to compensate for the lack of inelastic energy dissipation of unreinforced CFFT columns (Zaghi et al., 2012). Therefore, XTract (Imbsen, 2007) was used to determine a CFFT design with similar axial capacity and flexural yield strength to the RC specimens while complying with the AASHTO C5.7.4.2 requirement for a minimum steel ratio of 1% (AASHTO, 2012b).

A Red Thread® II fiber glass composite pipe manufactured by NOV FGS (NOV, 2009) was used for the CFFT design. The pipe had an outer diameter of 219mm (8.64in) and a wall thickness of 3.56mm (0.14in). The fiber orientation of this particular off-the-shelf pipe is aligned at $\pm 55°$ with respect to the longitudinal axis of the pipe providing both longitudinal and hoop strength to the column. Therefore no transverse steel reinforcement was included in the CFFT specimens, and the longitudinal steel reinforcement was reduced to six #3 Gr. 60 (9.525mm (0.375in.) -diameter) bars, resulting in a steel ratio of 1.12%. Figure 2-5 shows the rebar cages used in the CFFT columns. The design axial load-strain and moment-curvature relationships obtained from XTract for the CFFT design are shown in Figures 2-6 and 2-7. The design axial and flexural capacities are based on specified 4ksi (27.6MPa) concrete, 60ksi (414MPa) reinforcing steel, and the tri-liner FRP material model presented by Zaghi et al. (2012). The FRP-confined concrete model described by Saiidi, et al. (2005) was utilized to model the concrete core. It should be noted that the approximately linear stress-strain relationship of the FRP tube material results in a large post-yield stiffness of the CFFT columns.

The ultimate axial and felxural capacities of the CFFT specimens assuming design concrete and steel strengths are 395.1kip (1758kN) and 348.6k-in (39.4kN-m), respectively. The plastic shear demand was calculated as 29.1kip (129.2kN) using Eq. 1. The shear capacity of the concrete core was determined from Kowalsky and Priestley (2000), and the capacity contribution of the FRP tube, V_{FRP}, was determined following the method used by Zaghi and Saiidi (2010) shown in Eq. 2

$$V_{FRP} = \frac{\pi \cdot t_{FRP} f_{FRP,h} D_{FRP}}{2} \tag{2}$$

where t_{FRP} is the thickness of the tube, $f_{FRP,h}$ is the tensile strength of the tube in the hoop direction, and D_{FRP} is the outside diameter of the tube minus t_{FRP}. From Zaghi and Saiidi (2010),

the value of f_{FRP} is one half of the ultimate hoop stress of 34.0ksi (234.4MPa). The resultant shear capacity of the CFFT column was calculated as 38.8kip (172.7kN). This value was confirmed through comparison with the results of Fam et al. (2007) where a similar CFFT member with comparable FRP confining stress was found to have a normalized shear capacity $V/(D^2 f'_c)=0.154$. Substituting $D=8.64in$ *(219mm)* and $f'_c=4.0ksi$ *(27.6MPa)* results in an approximate shear capacity of 46.0kip (204.5kN) for the specimens in this study.

2.4 Instrumentation and Construction

2.4.1 Rebar Cage Construction

The reinforcement for all ten specimens was fabricated in the UConn Machine Shop. The longitudinal rebar was delivered cut-to-length, and the wire for the spiral reinforcement of the RC columns was delivered pre-wound. The reinforcement cage material is shown in Figure 2-8. Two wooden discs were used to hold the longitudinal bars in place while the spiral was slid over the bars. The ends of the spiral were spot welded to prevent torsion loads from being applied to the cages. The spiral was then tied to the longitudinal bars at the specified pitch. Small pieces of the spiral reinforcement were used to hold the longitudinal bars of the CFFT columns in place. The small pieces did not provide any transverse reinforcement as shown in Figure 2-4.

2.4.2 Blast Specimen Instrumentation

The two RC columns constructed for the experimental blast tests and the benchmark RC column were instrumented with six 350 Ohm linear strain gauges. All strain gauges were adhered to the steel reinforcement cages within the columns. Two gauges were placed at midspan of the column on longitudinal reinforcing bars, one at the front of the column and one at the back. The other four strain gauges were placed on the spiral reinforcement. One was placed at the top, midspan, and bottom of the column at a 90 degree offset from the front longitudinal bar, and the

final gauge was placed on the spiral reinforcement at midspan near the front of the column. An example of an installed strain gauge is shown in Figure 2-9, and a schematic showing the location of the strain gauges for the RC columns is show in Figure 2-10.

The two CFFT columns constructed for the experimental blast tests were instrumented with two 350 Ohm strain gauges. The two gauges were placed on longitudinal bars at the front and back of the column and at midspan. No spiral reinforcement was present in the CFFT columns. Therefore, there was no transverse reinforcement to instrument. A schematic showing the location of the strain gauges for the CFFT columns is show in Figure 2-11.

The benchmark RC and CFFT columns to remain undamaged were instrumented in the same manner as the blast specimens.

2.4.3 Fire Specimen Instrumentation

Each of the four fire test specimens was instrumented with two type K Omega® high temperature ceramic insulation thermocouples with Inconel® overbraid (Omega, 2013). The thermocouples were rated for temperatures as high as 1090°C. Both thermocouples were placed at midspan along the length of each column. One thermocouple was fastened to one of the longitudinal bars to record temperatures at the level of the steel reinforcement, and the other was suspended at the center of each column to record core temperatures as shown in Figure 2-12.

2.4.4 Specimen Construction and Preparation

A custom-made wood frame was constructed by the personnel at the UConn machine shop to hold the sonotube forms for the RC columns and FRP tubes for the CFFT columns during construction. Figure 2-13 shows the framework used to keep the columns plumb while casting concrete. Each of the reinforcement cages was placed within its respective sonotube or FRP tube as shown in Figures 2-14 and 2-15. Spacers were used to maintain the 0.5in. (12.7mm) clear

cover, and a hole was cut in each tube to accommodate the instrumentation wires. The RC and CFFT columns were filled from the top down with specified 27.6Mpa (4ksi) regular concrete with maximum aggregate size of 9.53mm (0.375in.). The concrete was delivered by truck, and all specimens were cast from a single batch. Figure 2-16 displays all of the tubes filled with fresh concrete. Eighteen 3in.x6in. (76.2mmx152.4mm) test cylinders were cast at the time of column construction to determine the concrete material properties at 28 days, at the time of blast testing, and at the time of residual axial capacity testing. The test cylinders can be seen in Figure 2-17.

Because FRP materials are vulnerable to extreme temperatures (Gefu et al., 2008; Bisby et al., 2005; Kodur et al., 2007, possibly more), precautions were taken to protect the FRP tubes from the fireball during blast testing. A thin layer of a flame retardant paint manufactured by Thermal Product Research (TPR^2, 2013) was applied to the CFFT specimens prior to blast testing.

For the more extreme fire tests, the Tyfo® CFP System (Fyfe, 2013) was applied to the surface of the two CFFT columns. The Tyfo® CFP System is a three part, low profile system able to provide up to a 4-hour fire protection rating for square and circular columns per ASTM E119 and a Class 1 flame and smoke rating per ASTM E84. The application process was completed by Fibrwrap® technicians. First, the Tyfo® VG Primer was generously applied to the surface area of the columns as shown in Figure 2-18. Following the primer, the second component of the CFP System, the Tyfo® VG Dash Coat, was spray-applied in a non-continuous spatter pattern and was allowed to dry for approximately 30 minutes. As the final component of the system, the Tyfo® WR-AFP was applied in multiple layers to achieve a thickness of 0.625in (15.9 mm). A photo of the spray application process is displayed in Figure 2-19 . To ensure the

thickness of the fire protection reached 0.625in (15.9 mm), the prescribed thickness was marked on a piece of wire which was inserted into the wet material as shown in Figure 2-20. The two CFFT specimens with the complete fire protection system applied are displayed in Figure 2-21.

2.5 Material Properties

Testing of the materials for the column specimens was done for two purposes. The first was to ensure that the concrete and reinforcement had properties that were consistent with the design and reflected the properties of typical highway bridge column materials. The second was to obtain the constitutive relationships of the materials for the analytical modeling phases of this research. Compression testing was conducted on the concrete cylinders cast during construction, and tensile tests were conducted on the steel longitudinal and spiral reinforcement.

2.5.1 Concrete Properties

The compressive properties of the concrete was determined at 28 days, 100 days, and 1 year after casting to coincide with the dates of blast testing (approximately 100 days) and fire and axial capacity testing (approximately 1 year). The compressive strengths obtained from the concrete test cylinders on these dates were 3.33ksi, 3.39ksi, and 4.67ksi, respectively. The stress strain curves for the concrete at 100 days is provided in Figure 2-22, and the compressive strengths are tabularized in Table 2-1.

2.5.2 Steel Reinforcement Properties

Tension tests were conducted on the #3 Gr. 60 longitudinal rebar and 0.25in. (6.35mm) diameter wire spiral used to reinforce the specimens. The yield and ultimate strengths of the rebar and spiral materials are tabularized in Table 2-1. Figures 2-23 and 2-24 display the stress-strain curves of the rebar and spiral reinforcement. Details of the 2% offset method used to determine the yield strength of the wire spirals is also included in the figure. The average yield strengths of

the rebar and wire spiral were 58.7ksi (405MPa) and 78.6ksi (542MPa), respectively. The average ultimate stresses for the same materials were 93.7ksi (646MPa) and 90.4ksi (623MPa), respectively.

2.5.3 FRP Tube Properties

The material properties for the FRP tube were obtained from the manufacturer's technical information. Table 2-2 summarizes the properties provided by the technical brochure at 75°F (24°C) and 210°F (99°C). For most civil engineering applications, only the properties at 75°F (24°C) are of concern, but because this study also includes blast and fire testing, the properties at the higher temperature are also included for reference.

2.6 Blast Test Support Frame

2.6.1 Introduction

To support each column specimen during testing, a steel frame was designed and fabricated at UConn and shipped in pieces to the Big Black test site in Vicksburg, MS. The frame incorporated three wide-flange members: one acting as the vertical member; the other two as cantilever beams with moment connections to the vertical element. The frame was designed in such a way that the loaded column was held in isolation with pin-pin support conditions.

2.6.2 Design

The steel support frame consists primarily of three W12x58 beam sections fabricated in the shape of a large C-Clamp. The geometry of the frame was designed such that each specimen was subjected to an ideal spherical pressure wave. Shock wave velocities were extracted from Figure 2-7 of UFC-3-340-02 (UFC, 2008) to ensure that reflected pressure waves from the ground and the reaction structure would not have a significant effect on the response of the column. The length of time between when the shock wave first reaches the specimen and when

the wave reflected from the reaction structure returns to the column is approximately 4.5 times the natural period of the specimens, ensuring that a significant portion of each specimen's response would occur prior the return of the reflected wave.

The frame was designed with sufficient capacity to support the maximum reaction forces that were expected to be exerted by each column. Because the CFFT column has a higher flexural capacity than the conventional RC column, the plastic shear force of the CFFT column was used to determine the required capacities of the plates, bolts, and threaded rods used for fabrication. Figures and 2-25 and 2-26 display the side and top view of the support frame, respectively.

In addition to the main W12x58 sections used to construct the support frame, several smaller steel components were used for lateral bracing and clamping of the concrete column. Four 1in. (25.4mm) threaded rod, turnbuckle, and clevis systems along with small angle sections with slotted holes restricted the frame from moving laterally during blast loading. Two 1in. (25.4mm) threaded rods were used to keep the beams from *opening* due to the pressure of the shock wave. Side, top, and front view drawings of the steel frame are shown in Figures 2-27, 2-28, and 2-29, respectively.

For each pair of columns, a set of 0.75in. (19.1mm) -thick and 1.5in. (38.1mm) -high steel collars welded to 1in. (25.4mm) -thick steel plates was used to hold the end of the columns in the frame. These end caps bolted to the free ends of the cantilever arms to facilitate installation and removal of each column before and after each test. A 0.0625in. (1.6mm) gap was provided to allow for end rotations and provide pin-pin support conditions. For the same reason, a cork pad was placed between the column ends and steel caps.

2.6.3 Material and Fabrication

The experimental blast frame was fabricated in-house at the UConn Machine Shop. The W12x58 steel beams were donated by The Berlin Steel Construction Co. After the initial fabrication, the steel frame was dismantled and shipped with the test specimens to ERDC in Vicksburg, MS as shown in Figure 2-30. The frame was reassembled by the ERDC fabrication team and connected to the existing concrete filled steel wall at the Big Black test site as shown in Figure 2-31.

2.7 Blast Loading Protocol and Test Set-up

2.7.1 Parameter Selection

Charge weight and standoff distance are the two main parameters that determine the intensity of a specific blast threat. The main objectives in choosing the parameters for the blast tests in this study were to: 1) simulate realistic threats for typical bridge columns, 2) apply two distinct intensities for each type of column, called "Moderate" and "Severe" hereafter, and 3) apply equivalent load intensities to each type of column. These objectives had to be met without causing complete failure of any of the columns.

The methodology used to size the charge and standoff is as follows. First, the average distance from the center of the left traffic lane to a typical overpass bridge column was chosen as a constant standoff distance, R. Next, a charge weight, W, resulting in a scaled standoff value, $Z=R/W^{1/3}$, of ~1.0 was selected as the CFFT-Severe threat. The values of R and W were scaled using the cubed-root method for the 1/5-scale specimens.

Because the RC and CFFT columns have different ultimate moment capacities, a load intensity ratio (LIR) based on moment-curvature analysis was used to determine an equivalent charge weight for the RC-Severe test. The LIR is defined as the ratio of the theoretical maximum

moment demand due to the reflected blast pressure applied as a uniform distributed load ($M_{P,RC}$ and $M_{P,CFFT}$), to the moment capacity of the column at a curvature ductility of 4 ($M_{\mu=4,RC}$ and $M_{\mu=4,CFFT}$) as shown in Eq. 3

$$LIR = {M_{P,CFFT}}/{M_{\mu=4,CFFT}} = {M_{P,RC}}/{M_{\mu=4,RC}} \quad (3)$$

The steps used to determine the LIR and equivalent load for the CFFT-Severe and RC-Severe columns are outlined:

- Determine the yield curvature for each column, $K_{y,RC}$ and $K_{y,CFFT}$ using a cross-sectional analysis program such as XTract. The yield curvature is defined as the curvature corresponding to steel strain equal to 0.002.
- Determine the moment capacity of each column at a ductility level of 4, $M_{\mu=4,RC}$ and $M_{\mu=4,CFFT}$. The moment at a ductility level of 4 is defined as the moment corresponding to 4 times the yield curvature.
- Select initial charge weight for CFFT column, W, for a scaled standoff value, $Z=R/W^{1/3}$, approximately equal to 1.0.
- Use BlastX (USACE, 2007) to determine the maximum reflected pressure, $P_{r,CFFT}$, for CFFT column.
- Calculate maximum theoretical moment due to $P_{r,CFFT}$ applied as a uniform distributed load using Eq. 4:

  $$M_{P,CFFT} = {P_{r,CFFT} S_c D L^2}/{8} \quad (4)$$

  Where P_r is the peak reflected pressure, S_c is a shape factor to account for the reduction in reflected pressure for a circular cross-section vs. a rectangular cross-section (Williams, 2009), and D is the diameter of the column.

- Calculate *LIR* using Eq. 3.
- With known *LIR* and $M_{\mu=4,RC}$, calculate equivalent $M_{P,RC}$ and $P_{r,RC}$ using Eqs. 5 and 6:

$$M_{P,RC} = LIR * M_{\mu=4,RC} \quad (5)$$

$$P_{r,RC} = {}^{8M_{P,RC}}\Big/_{S_C DL} \quad (6)$$

- Determine charge weight with resultant $P_{r,RC}$ using BlastX (USACE, 2007).

The CFFT-Moderate charge weight was chosen as the threat size resulting in a peak reflected pressure equal to 80% of the peak reflected pressure of the CFFT-Severe test. The same process was used to determine the equivalent charge weight for the RC-Moderate test. The final blast test parameters are shown Table 2-3. After the RC-Moderate and -Severe tests, there was no observable damage to either column. Thus, an additional test was conducted on the RC-Severe specimen (Test No. 3 in the table) to push the limits of the blast experiments.

Three different software packages, Bridge Explosive Loading (BEL) (USACE 2004), ATP-Bridge (Williamson, et al. 2011), and OpenSees (PEER, 2012), were used to verify that the chosen threats would not impose large permanent deformations that would prevent residual axial capacity testing.

BEL is used to estimate spall and breach thresholds (the minimum thickness of a RC element to resist spalling or breaching of the member) of bridge components for specified blast threats. Spall thresholds of 5.85in (149mm), 7.45in (189mm), and 10.1in (257mm) were predicted for the RC-Moderate, -Severe, and -Severe-2 tests, respectively. Thus, the RC specimen with a column diameter of 8.0in (203mm) is near the spall threshold for the RC-Severe test and is less than the threshold of the RC-Severe-2 test; thus, no spalling was expected for the first two tests, but light spalling was expected for the second RC-Severe test.

ATP-Bridge is used to predict displacements and permanent deformation of concrete columns and steel plates under blast loading. The software is not able to model small scale columns; thus the full-scale prototype was necessarily modeled. The resulting peak and residual displacements of the full-scale column were scaled down by the one-fifth geometric scale to predict the displacements and spall lengths at midspan of the test columns. The software program predicted peak midspan displacements, δ_{PK}, as large as 3.43in. (87.3mm) and residual midspan displacements, δ_{RES}, as large as 3.15in. (80.1mm) for the RC-Severe-2 test. The δ_{PK} and δ_{RES} predictions for all of the RC tests are summarized in Table 2-4. ATP-Bridge did not predict any spalling for the RC-Moderate or -Severe tests. For the RC-Severe-2 test, the software predicted a spall length of 5.16in. (131mm) at midspan.

Because ATP-Bridge is a blast mitigation design tool, and neither ATP-Bridge nor BEL could be used to predict the performance of the CFFT columns, the RC and CFFT columns were modeled in OpenSees where material models and element formulations can be further refined for more accurate displacement predictions. The blast pressure time history of each test was applied along the length of the column using the pressure distribution obtained from BlastX. Table 2-4 also lists the δ_{PK} and δ_{RES} predictions obtained from the OpenSees models for each of the RC and CFFT tests. Although the δ_{PK} and δ_{RES} predictions from the OpenSees model are smaller than the ATP-Bridge predictions for the RC columns, residual displacements of 0.111in. (2.82mm) and 0.323in. (8.20mm) were expected at midspan for the RC-Severe and -Severe-2 tests, respectively. The δ_{PK} predictions for the CFFT-Moderate and -Severe tests of 0.250in. (6.35mm) and 0.36in. (9.38mm), respectively, were larger than the equivalent RC tests. However, the predicted residual displacements for the CFFT columns were negligible.

Although all three of the software packages predicted some permanent deformation after the more severe tests, the residual displacement predictions were small enough to ensure that residual axial capacity testing could be accomplished for all of the columns after the blast experiments.

2.7.2 Instrumentation and Test Set-Up

After the steel test frame was reassembled at the test site, four Interface 1200 Precision Universal Low Profile™ 50kip (222kN) load cells were mounted using two 2in. (50.8mm) -thick steel spreader plates welded to the frame and then brought into contact with the reaction structure using the turnbuckle and clevis assemblies to capture the reaction histories, as shown in Figure 2-32. The load cells were zeroed after each turnbuckle was post-tensioned to 10kip (44.5kN) to isolate the blast load on the column from turnbuckle forces.

Next, the steel caps designed for each column type were placed on each end of the specimens, and the column was slid into place. The caps were then bolted to the steel beams using high-strength bolts, and the threaded rods were snug-tightened. A rack and pinion displacement gauge was mounted to the bottom beam of the test frame and epoxied to the surface of each column in an attempt to measure midspan deflections during the tests. The displacement gauge set-up is displayed in Figure 2-33.

Two free field piezoelectric pressure gauges were used to measure the incident pressure of the blast wave at two different standoff distances. The gauges were placed at XX-m (xx-in.) and YY-m (yy-in.) from the center of the charge (due to security reasons, the distance from the charge may not be reported). Although not placed at the exact standoff distance as the columns, the data obtained from these gauges was used to estimate the reflected pressure at the surface of

the columns using BlastX software (USACE, 2007). A photo of the complete test setup is shown in Figure 2-34.

2.8 Fire Test Protocol and Set-up

The objective of the fire exposure experiments was to subject each type of column to durations of extreme heat resulting in two levels of damage but allowing the columns to sustain future axial capacity tests. It was decided to conduct the two tests following the ASTM E119 testing procedure and temperature curve shown in Figure 2-35. In the first and more severe test, one RC column and one CFFT column were subjected to two hours of extreme temperature following the ASTM E119 curve; this test will be referred to as "2-Hr" test hereafter. The second set of columns was subjected to one hour of extreme temperature following the ASTM E119 temperature curve, and is referred to as the "1-Hr" test, hereafter.

The fire exposure tests were conducted at Guardian Fire Testing Facility in Buffalo, NY. The laboratory's furnace had a square footprint with inside dimensions of approximately 4ft (1.25m) and an adjustable height. The furnace was equipped with two natural gas burners located at the center of two adjacent walls. Five type K thermocouples owned by the fire testing facility were used to record the furnace temperature as well as the ambient temperature of the laboratory. After the columns were placed in the furnace, cinder blocks and insulation were used to adjust the height prior to placing the concrete slab cap. A schematic of the fire testing set up is shown in Figure 2-36, and a photo of the RC- and CFFT-1Hr test specimens just after being placed in the furnace is shown in Figure 2-37.

3 Experimental Results and Observations

3.1 Introduction

The results and observations of the blast and fire experiments described in the previous chapter are presented herein. The contents of this chapter include general observations for all tests, measured experimental data, and analyses of the raw experimental data.

3.2 Blast Tests

The results and observations of the five experimental blast tests on two RC and two CFFT columns conducted at the USACE-ERDC Big Black Test Site in Vicksburg, MS are presented in this section. First, general observations immediately following each test are provided in section 3.2.1 as a preliminary performance evaluation. Then, the data recorded from the instruments described in Chapter 2 are analyzed in Sections 3.2.2 through 3.2.4 for a more in depth study of the columns' performance under blast loading.

3.2.1 General Observations

The RC-Moderate column was subjected to blast on July 30, 2012. The expectation for this test was to see cracking near midspan of the column with no residual displacement. Post-blast examination of the column showed minimal hairline cracking, no residual displacement, and some charring on the front face of the column. Figures 3-1 and 3-2 display before and after pictures of the RC-Moderate test specimen.

The RC-Severe specimen was tested on July 31, 2012. The post-test damage was very similar to that of the RC-Moderate specimen. There was visible charring on the face of the column caused by the fireball of the explosion, but only very minor cracking was evident. There was also no visible permanent deformation. Photos of the RC-Severe threat specimen before and after blast testing can be seen in Figures 3-3 and 3-4.

Because neither the RC-Moderate nor the RC-Severe specimens showed any significant signs of damage after testing, it was decided to subject the RC-Severe specimen to an additional test with a larger charge weight, called "RC-Severe-2" hereafter. Even after this additional test, observable damage was limited to fine flexural and shear cracks at the center and the bottom of the column, respectively. Figure 3-5 displays the condition of the RC specimen after the RC-Severe-2 test.

Similar to the RC columns, neither of the CFFT columns showed any signs of damage after the Moderate and Severe tests. After the CFFT-Moderate test on July 31, 2012 and the CFFT-Severe test on August 1, 2012, the flame retardant coating that had been applied to the specimens had been charred, but no other signs of damage could be detected. Figures 3-6, 3-7, 3-8, and 3-9 show the pre- and post-test photos of the CFFT-Moderate and -Severe specimens, respectively.

3.2.2 Load and Displacement Response

The first 50ms of the load time history recorded from each of the four load cells is presented for all five of the blast tests. In each case, the loads from each load cell are summed together to show the total load time history.

The load history response for the RC-Moderate test is presented in Figure 3-10. The total load time history presents two major peaks. The first peak is 26.5kip (117.9kN) and occurs at 3.70ms. The second peak and maximum load recorded for the entire system is 40.3kip (179.3kN) occurring at 8.40ms.

The load cell time history response for the RC-Severe and -Severe-2 tests are presented in Figures 3-11 and 3-12. Just as in the RC-Moderate test, two major peaks are present in the load history data for the two more severe tests. The two peaks occur at 3.39ms and 8.42ms and

3.18ms and 8.14ms for the RC-Severe and -Severe-2 tests, respectively. For the RC-Severe test, the maximum load recorded at the first peak is 33.6kip (149.5kN), and the maximum load recorded for the entire test at the second peak is 43.1kip (191.7kN). For the RC-Severe-2 test, the first peak load is 38.1kip (169.7kN), and the second peak load is 56.0kip (249.0kN).

The load time histories from the CFFT tests follow the same pattern that was observed in the RC tests. In the CFFT-Moderate test, the first peak load is 35.0kip (155.5kN) at 2.95ms, and the second peak is 50.4kip (224.3kN) at 8.09ms. The load time history for the CFFT-Moderate test is shown in Figure 3-13. In the CFFT-Severe test, the first peak load of 39.6kip (175.9kN) occurs at 3.30ms. The second peak load of 64.0kip (284.7kN) occurs at 7.94ms. The load time history response of the CFFT-Severe test is displayed in Figure 3-14. Figures 3-15 and 3-16 show the relationship between the scaled standoff distance, *Z*, of each test and the first and second peaks of the load strain histories, respectively.

The midspan displacement histories for all five of the blast tests are shown in Figures 3-17, 3-18, 3-19, 3-20, and 3-21. The RC-Moderate test was the only test for which the displacement gauge stayed intact with the column for the duration of the test. However, it appears that peak midspan displacement readings can be extracted from all of the time histories except for that of the RC-Severe-2 test. Table 3-1 lists the peak midpsan displacement readings and the time of occurrence for each test. It should be noted that the accuracy of these readings may be low do to the debonding of the rack and pinion device from the column surfaces.

3.2.3 Pressure Measurements

The incident pressure time histories recorded during each of the blast tests by the two free field pressure gauges is presented. The standoff distances for the pressure gauges were chosen so as not to exceed the pressure range of each of the probes. The exact standoff distances of the two

gauges cannot be disclosed for security purposes. For the purpose of this publication, the gauge nearer to the charge will be called the "X" gauge and the gauge further from the charge will be referred to as the "Y" gauge. All of the experimental pressure time histories presented in this section are compared with BlastX pressure time history predictions. Validating the accuracy of the BlastX predictions allows for predicting the peak reflected pressure at the surface of each column during testing.

Unfortunately, a data acquisition error occurred for the RC-Moderate test. Thus, the pressure data for that test is not reliable. However, the BlastX predictions of the pressure time histories for the RC-Moderate test are shown in Figures 3-22 and 3-23.

The data acquisition error was resolved, and reliable incident pressure data was captured for the subsequent tests. The X and Y gauge recorded pressure time histories and their corresponding BlastX predictions are shown in Figures 3-24 and 3-25, respectively. The same plots for the RC-Severe-2 test are shown in Figures 3-26 and 3-27, respectively. The incident pressure recordings and BlastX predictions for the CFFT-Moderate and -Severe tests are shown in Figures 3-28, 3-29, 3-30, and 3-31 for the X and Y gauges, respectively.

Table 3-2 compares the experimental pressure wave arrival times, t_a, and peak incident pressures, P_{PK}, with the BlastX predictions for each gauge and each test. The "X" or "Y" in the subscript of each variable designates to which gauge the values correspond. Because the BlastX predictions correspond well with the experimental pressures, the program was used to estimate the peak reflected pressure at the surface of the columns for each test. From BlastX, the peak reflected pressures at midspan for the RC-Moderate, -Severe, and -Severe-2 tests are 4569psi (31.5MPa), 5605psi (38.6MPa), and 7163psi (49.4MPa), respectively. The peak reflected pressures at midpsan for the CFFT-Moderate and -Severe tests are 6229psi (42.9MPa) and

7862psi (54.2MPa), respectively. Figure 3-32 displays the relationship between the scaled standoff distance, *Z*, and peak reflected pressures of the five tests.

3.2.4 Measured Strains

This section presents the strain time histories measured by the gauges installed on the steel reinforcement for each column. Both longitudinal and spiral strain histories are presented for the RC columns. The CFFT columns only contain longitudinal reinforcement, thus only those strain histories can be provided. For further details on the locations of these gauges, refer to Chapter 2.

Longitudinal Strains

Two strain gauges were placed at midspan on the longitudinal steel reinforcement within each column such that one was on the bar nearest the charge (extreme compression) and the other was on the bar furthest form the charge (extreme tension). These two gauges will be referred to as the "Compression" and "Tension" gauges, and the strain histories recorded from these gauges are presented in this section.

Figure 3-33 shows the longitudinal strains recorded at midspan during the RC-Moderate test. The peak tensile strain of 3824με was recorded 2.47ms after detonation. The compression gauge malfunctioned during this test, and the presented strain history is not reliable for determining the peak compressive strain. The midspan longitudinal compression and tension strain histories for the RC-Severe test are presented in Figure 3-34. The peak tensile strain equal to 8508με was recorded 2.86ms after detonation, and the peak compressive strain of 2324με was recorded at 1.99ms. The RC-Severe-2 longitudinal strain histories are shown in Figure 3-35. The peak tensile strain for this test was 16,038με and the peak compression strain was 6690με. These peak values occurred at 3.11ms and 3.43ms, respectively.

The longitudinal strain histories for the CFFT-Moderate and -Severe tests are shown in Figures 3-36 and 3-37, respectively. The peak tensile strains for the Moderate and Severe tests were 12,199με and 18,054με, respectively. The peak compressive strains for the same tests were 16,974με and 3868με, respectively. It should be noted that the compression strain history for the CFFT-Moderate test does not fit the general trend of the other tests, and the results from this gauge may not be reliable. The extreme spike in strain at approximately 0.3ms is likely caused by the arrival of the shock wave, and the use of the data from this test should be done with caution, if at all.

In general, the compression strain histories contain an excessive amount of noise when the shock wave first comes into contact with the column specimens. The initial shock applied to the compression gauges may have caused some erratic readings, especially in the case of the RC- and CFFT-Moderate cases. The use of the compression strain data should be done with caution. However, the tension gauges performed well in all tests, and these results can be used with a higher level of confidence. Figure 3-38 shows the relationship between the scaled standoff, *Z*, and peak tensile strain for all five tests.

Although none of the specimens showed any signs of plastic deformation, the peak tension and compression strains recorded during the tests were well beyond the yield strains of both steel and concrete material. Further studies of this phenomenon are presented in Chapter 5.

Spiral Strains

Four strain gauges were installed on the spiral reinforcement of the RC specimens. One gauge was placed along the side of the specimen at the top, bottom, and midpspan of the column, and the fourth was placed at the front of the column at midspan. Figures 3-39 and 3-40 display the spiral strain time histories for the RC-Moderate test. The first figure consists of the strains

measured near the supports of the column. The second figure consists of the strains recorded by the strain gauges placed on the spirals at midspan. It is difficult to extract distinct peaks for the spiral strain data. However the magnitude of the strains near the supports is larger than at midspan indicating that shear strains were higher near the top and bottom of the columns.

The spiral strain histories for the RC-Severe test are presented in Figures 3-41 and 3-42, and those for the RC-Severe-2 tests are shown in Figures 3-43 and 3-44. In each case, the strain histories for the spirals near the supports are presented first followed by the midspan time histories. One interesting characteristic of the spiral strain histories for the two more severe tests, is the extreme peaks that occur at approximately 10-12ms. Strain gauges are accurate instruments, but cracks and the interaction of aggregates and ribs on the bars with the cement paste can cause highly localized strains. Therefore, erratic measurements may be recorded during some tests. With the limited number of tests, it is difficult to confirm whether the peak at 10-12ms is coincidence or meaningful to the tests.

3.3 Fire Tests

The results and observations of the fire exposure tests conducted on two RC and two CFFT columns at the Guardian Fire Testing Facility in Buffalo, NY are presented in this section. First, general observations immediately following each test are provided as a preliminary performance evaluation of the specimens. Then, the temperature data recorded from the thermocouples described in Chapter 2 is analyzed for a more in depth study of the columns' performance under fire exposure.

3.3.1 General Observations

Upon removal from the furnace, none of the columns showed any significant outward signs of material degradation as shown by the pre- and post-test photos in Figures 3-45 and 3-46. The

most noticeable signs of damage included discoloration of the FRP tube of the CFFT column after the 2-Hr test. Figure 3-47 shows the CFFT-1Hr and -2Hr specimens after the fire protection layer was removed. The acoustic properties of the RC columns were altered after both the 1- and 2-Hr tests. After the RC columns were removed from the furnace, a sound similar to that of a ceramic material was emitted when the surfaces of the columns were tapped, instead of the concrete sound that was heard prior to testing.

3.3.2 Furnace Temperature Data

Furnace temperatures were recorded every five minutes throughout the duration of both tests, and the recorded temperature time histories for the 1-Hr and 2-Hr tests are shown in Figures 3-48 and 3-49, respectively. Although the furnace burners were able to closely match the steep initial temperature rate of the ASTM E119 curve, the average furnace temperatures were about 400°F (204°C) below the ASTM curve for the majority of each test. The peak average furnace temperatures recorded were 1285°F (696°C) and 1446°F (786°C) for the 1-Hr and 2-Hr tests, respectively.

Because the furnace temperatures did not meet the ASTM standard, the 2-Hr test was extended by an additional 20 minutes. By prolonging the 2-Hr test, the total amount of temperature exposure, defined herein as the area beneath the temperature curve, was 177,244°F-min (96,000°C-min). This value falls within 10% of the total amount of temperature exposure for two hours following the ASTM E119 curve, or 193,726°F-min (105,000°C-min). To maintain the differentiable levels of damage between the two tests, the furnace burners were extinguished at exactly 60 minutes for the 1-Hr test.

3.3.3 Concrete Temperature Data

The temperatures of the interior concrete for the 1-Hr and 2-Hr tests are shown in Figures 3-50 and 3-51, respectively. Although the columns showed no evidence of structural damage, the temperatures of the internal concrete indicated that there would be reductions in both the compressive strength and elastic modulus of the RC columns. Chang et al. (2006) established a database of concrete mechanical properties after being heated to temperatures as high as 1472°F (800°C). The study showed that the compressive strength of concrete is reduced by 10% at a temperature of 392°F (200°C) and by 35% at 752°F (400°C). Similarly, the elastic modulus of concrete is reduced by 20% at 392°F (200°C) and by 60% at 752°F (400°C).

During the 1-Hr test the concrete temperature at the level of the rebar reinforcement of the RC column reached 541°F (283°C) exceeding the 392°F (200°C) threshold. During the 2-Hr test, the concrete of the RC column reached 807°F (431°C) at the core and 915°F (491°C) at the level of the rebar. Both temperatures exceed the 752°F (400°C) threshold, indicating significant losses in strength and stiffness of the entire cross section.

In comparison, the maximum concrete temperature recorded at the level of the rebar of the CFFT column during the 1-Hr test was 195°F (91°C). For the longer duration tests, the peak concrete temperature of the CFFT column was 320°F (160°C) at the level of the rebar. Because the fire protection system was able to keep concrete temperatures of the CFFT columns below 392°F (200°C) during both test durations, no significant losses in strength or stiffness were expected in the following residual axial capacity tests.

4 Residual Axial Capacity Testing

4.1 Introduction

All eight of the blast and fire damaged columns were returned to the UConn Structures Lab for residual axial capacity testing. In addition to the eight damaged columns, one undamaged benchmark column of each type, referred to as RC-Benchmark and CFFT-Benchmark hereafter, were also loaded axially to failure to obtain the undamaged characteristics of each column design. In this study, the residual axial load carrying characteristics of the two column types were used as measures of resilience to blast and fire hazards. The classical definition of resilience provided by Merriam-Webster (2014) is "an ability to recover from or adjust easily to misfortune or change". In the case of this research, the misfortune or change is caused by blast loading or fire exposure. As primarily axial load carrying members, a bridge column that is able to adjust easily to these extreme load cases and maintain its ability to carry axial load exhibits the highest form of resilience.

The test setup, loading protocol, and results of the ten axial capacity tests are presented in this chapter. Two types of comparisons are made. First, the blast and fire damaged columns of each type are compared to their respective benchmark columns. Next, the resiliencies of RC and CFFT columns to blast and fire hazards are compared directly to each other.

4.2 Test Setup and Loading Protocol

The ten column specimens were tested using a Satec 1,779kN (400k) load frame controlled by an MTS FlexTest 40 controller. A photo of the empty load frame is shown in Figure 4-1. The same steel end caps used in the blast experiments were installed on the columns before testing using high strength epoxy grout. Two rigid spherical bearings were used at the ends of specimens to eliminate end fixity moments. Four 50mm (1.97in.) Novotek displacement potentiometers

measured relative longitudinal movements and relative rotations of the end caps. In addition to axial deformations, the load was captured by the MTS controller, and strain readings on longitudinal bars (both types of columns) and spiral reinforcement at midspan (RC columns only) were recorded using an NI CompactDAQ Chassis. Figure 4-2 displays the complete test setup.

A quasi-static multi-step axial loading scenario described in Table 4-1 was used to evaluate the capacity of each column under incremental axial loads. The first five steps of the loading protocol were incremented by 50 kip (222kN) until the load reached 250kip (1,112kN) at Step 5. The displacement was recorded at this step, and the remaining steps were incremented using displacement control to capture softening behavior until the load carrying capacity of the columns dropped significantly. The columns were unloaded to 22.2kN (5.0kip) after each step to capture unloading and reloading characteristics.

4.3 Blast Specimens

4.3.1 RC Specimens

Failure Progression

Figures 4-3, 4-4, and 4-5 show the axial failure progression of the RC-Benchmark, -Moderate, and -Severe columns, respectively. The most significant observation from the progression of damage of the RC columns was the failure mode for the blast damaged columns. The RC-Benchmark column failed due to concrete crushing at midspan of the column which is an expected failure mode for an RC column under pure axial loading. However, the two blast damaged columns failed near the base of the column in a shear-type manner as highlighted in Figure 4-6. This failure mode is not expected and is generally undesirable for RC columns and is most probably due to shear crack initiation caused by blast loading.

Strains and Cap Rotations

RC-Benchmark: Figures 4-7 and 4-8 show the relationship between axial load and the strain recorded at midspan of the front and back longitudinal bars, respectively. The relationship between the axial load and the midpsan spiral strains of the RC-Benchmark column are shown in Figures 4-9 and 4-10. The strain plots confirm concrete crushing at midspan as the failure mode. Both longitudinal gauges show large jumps in strain at step 5 (250kip) where the column first exhibited signs of crushing.

After the cover concrete began to spall on the left side, the longitudinal bars began to buckle, and the column began to deform in bending resulting in rotation at the column supports. To determine whether this rotation was due to global buckling or due to a small eccentricity in the axial load, the Euler buckling load was calculated using Eq. 8

$$P_{CR} = {\pi^2 EI}/{L^2} \tag{7}$$

where E is the modulus of elasticity, and I is the moment of inertia of the column section. As a conservative approximation, the modulus of elasticity of concrete was used, and the resulting Euler buckling load was 2833kip (12,602kN). This value of P_{CR} confirms that the flexural deformation of the columns was due to a slight eccentricity in the applied axial load. Figure 4-11 depicts the cap rotation at each step as a 3-D plot. The maximum cap rotation recorded during the test was 7.634° (0.133rad).

RC-Moderate: The same strain vs. axial load relationships that are provided for the RC-Benchmark column are also provided for the RC-Moderate column in Figures 4-12, 4-13, 4-14, and 4-15. Again, the strain values recorded at midspan confirm the failure mode for the RC-Moderate column. Because the blast damaged column failed due to shear cracking near the

bottom of the column, the spiral strains recorded at midspan are significantly smaller than those that were measured during the RC-Benchmark test.

The maximum cap rotation of the RC-Moderate specimen was also much less than that of the RC-Benchmark specimen. The maximum rotation recorded was 1.191° (0.021rad) The 3-D plot showing the cap rotation at each step is shown in Figure 4-16.

RC-Severe: Similar to the first two specimens, the longitudinal and spiral strain vs. axial load relationships of the RC-Severe column are presented in Figures 4-17, 4-18, 4-19, and 4-20. Similar to the RC-Moderate specimen, the failure occurred near the base of the RC-Severe specimen. Unfortunately the spiral strain gauges near the supports were not utilized during axial testing. The spiral strains recorded at midspan are insignificant, because the failure was localized near the base of the column.

The cap rotation of the RC-Severe specimen is shown in Figure 4-21. There was minimal cap rotation for the first 6 steps of axial testing. However the cap rotation became more significant for the last two steps of the axial test. The maximum rotation at step 8 is 3.160° (0.055rad) which is more than the RC-Moderate but less than the RC-Benchmark specimens.

Axial Capacity and Ductility

The axial load-displacement curves of the RC-Benchmark, -Moderate, and -Severe columns are displayed in Figures 4-22, 4-23, and 4-24, respectively. Figure 4-25 shows the backbone curves of the three tests in a single plot for comparison. Table 4-2 summarizes the results of the RC-Blast axial capacity tests. The ultimate axial capacity and displacement ductility as well as the axial capacity at two separate ductility levels, $\mu_{D,P}$, are reported for each specimen.

Ductility is traditionally defined as the ratio of ultimate displacement over yield displacement. However, the definitions of ultimate displacement and yield displacement are not always easily defined for reinforced concrete structures. In this study, the axial yield displacement is defined as the displacement corresponding to an average axial strain of 0.002, marked by the yield line in Figure 4-25, and the ultimate displacement is defined as the displacement at which the axial load drops to 85% of maximum. When compared to the RC-Benchmark column, the ultimate axial displacement ductilities of the RC-Moderate and -Severe specimens were compromised by 50.0% and 36.3%, respectively.

Despite the large loads and strains generated by the blast tests, the ultimate capacities of the RC columns were not compromised. However, the blast damaged columns exhibited sharp drops in strength at lower ductility levels than the undamaged benchmark column. At $\mu_{D,P}$=3, the RC-benchmark column was still able to maintain its ultimate strength. At the same ductility level, the RC-Moderate and -Severe specimens had lost 33.0% and 10.7% of their ultimate capacities, respectively. Further, at $\mu_{D,P}$=4, the RC-Moderate and RC-Severe specimens had lost 65.7%, and 71.3% of their ultimate capacities, while the RC-Benchmark specimen was just beginning to exhibit axial strength degradation.

4.3.2 CFFT Specimens

Failure Progression

Figures 4-26, 4-27, and 4-28 show the axial load failure progressions of the CFFT-Benchmark, -Moderate, and -Severe columns, respectively. While the blast damaged RC columns showed a change in failure mode from the undamaged benchmark column, all three CFFT columns exhibited the same mode of failure when the FRP shells ruptured at midspan. The FRP tube prevented shear crack initiation in the concrete core under blast loading and provided significant

confinement to the concrete core allowing it to uphold under large longitudinal strains during axial testing.

Strains and Cap Rotations

CFFT-Benchmark: Figures 4-29 and 4-30 show the relationship between axial load and the longitudinal strains recorded at midspan of the front and back longitudinal bars, respectively. After making two large jumps in strain, the gauge on the front bar was lost at step 6. The gauge on the back bar remained in working condition throughout the duration of the test. After step 7 the increase in local strain was minimal for the remainder of the test.

Prior to rupture of the FRP tubes, the CFFT-Benchmark column exhibited significant flexural deformation while maintaining axial load. This large flexural deformation is likely due to the differences in the mechanical properties of the FRP material in tension and compression. To depict the flexural deformation, the cap rotations of the columns are shown in the form of 3-D plots. The 3-D plot of the CFFT-Benchmark cap rotation is displayed in Figure 4-31. The maximum cap rotation recorded during the final step was 7.850° (0.137rad).

CFFT-Moderate: The relationship of the longitudinal strain recorded on the back bar of the CFFT-Moderate specimen is shown in Figure 4-32. Both longitudinal gauges were connected at the start of testing, but the gauge on the front bar was no longer in working condition after the blast tests. The gauge on the back bar had a significant residual strain after blast testing and was also lost early in the axial test.

The CFFT-Moderate specimen exhibited the same flexural deformations seen in the CFFT-Benchmark test. The 3-D plot of cap rotation for the CFFT-Moderate specimen is shown in Figure 4-33. The maximum cap rotation was 7.131° (0.124rad) which is very similar to the maximum cap rotation of the benchmark column.

CFFT-Severe: The longitudinal bar strains for the CFFT-Severe specimen are shown in Figures 4-34, and 4-35. The gauge on the front bar remained intact for the entirety of the test and showed consistent increases in longitudinal strain up to about 2%. The gauge on the back bar was lost during a big jump in strain at step 4.

Again, the CFFT-Severe specimen sustained large flexural deformations prior to rupture of the tube at midspan. The flexural deformation is captured by the 3-D plot of cap rotation shown in Figure 4-36. This specimen had a maximum cap rotation of 10.1° (0.176rad) which is the largest maximum cap rotation at failure for the CFFT blast specimens.

Axial Capacity and Ductility

The axial load-deformation curves of the CFFT-Benchmark, -Moderate, and -Severe columns are displayed in Figures 4-37, 4-38, and 4-39, respectively. Figure 4-40 shows the backbone curves of the three tests in a single plot for comparison, and Table 4-3 summarizes the results of the CFFT-Blast axial capacity tests. The same definitions of yield and ultimate displacement provided for the RC columns were utilized to determine the ductility of the CFFT columns. The ultimate ductility of the CFFT-Benchmark column was 3.24 times that of the RC-Benchmark specimen. Additionally, the blast damaged CFFT columns maintained their residual axial ductility much better than the RC columns. The ultimate axial displacement ductilities of the CFFT-Moderate and -Severe specimens were compromised by just 10.1% and 28.3%, respectively, when compared with the CFFT-Benchmark specimen. Additionally, the average ultimate ductilities of the CFFT columns were 4.25 times the ultimate ductilities of the RC columns, for each damage state.

The ultimate axial capacities of the blast damaged CFFT columns were unaffected as the FRP tube provided sufficient reinforcement to resist blast effects. The damaged CFFT columns

were able to maintain larger percentages of strength at equivalent ductility levels to those presented for RC columns. To determine equivalent levels of ductility for the CFFT columns, the values of $\mu_{D,P}$=3 and $\mu_{D,P}$=4 used for the RC columns were scaled by the ratio of the ultimate ductility of the CFFT-Benchmark column over the ultimate ductility of RC-Benchamrk column, resulting in equivalent ductility levels of $\mu_{D,P}$=9.75 and $\mu_{D,P}$=13 for the CFFT columns, respectively. Due to the post-yield stiffness characteristics of the CFFT columns, the load-displacement curves of all three CFFT columns are still increasing at $\mu_{D,P}$=9.75. Thus, no significant capacity losses are reported. At $\mu_{D,P}$=13, neither the CFFT-Benchmark nor the CFFT-Moderate columns exhibited any loss in strength. However, the capacity of the CFFT-Severe capacity had been compromised by 50.8%.

Figure 4-41 directly compares the load-deformation curves of the RC and CFFT specimens to show the superiority of the CFFT columns under axial load in both the undamaged and blast damaged states.

4.4 Fire Specimens

4.4.1 RC Specimens

Failure Progression

Figures 4-42, 4-43 show the axial failure progression of the RC-1Hr and -2Hr columns, respectively. The cover concrete of the fire damaged columns began to spall much earlier and more severely than the RC-Benchmark column. This can be attributed to the reduced compressive strength of the concrete material caused by the extreme temperature exposure. In the case of the 2-Hr specimen, nearly all of the cover concrete had spalled off at the time of failure.

Cap Rotations

The fire specimens were not instrumented with strain gauges. Thus only the recorded cap rotations are presented. Figures 4-44 and 4-45 display the 3-D plots depicting the cap rotations for the RC-1Hr and -2Hr specimens, respectively. As the cover concrete began to spall, and the reinforcing bars began to buckle under compression, the end caps exhibited large rotations. The maximum rotations recorded for the RC-1Hr and -2Hr specimens were 5.77° (0.101rad) and 8.96° (0.156rad), respectively.

Axial Capacity and Stiffness

The axial load-displacement curves of the RC-1Hr and -2Hr columns are displayed in Figures 4-46 and 4-47, respectively. Figure 4-48 shows the backbone curves of the two fire damaged specimens as well as the RC-Benchmark specimen in a single plot for comparison. The results of the RC-Fire tests are summarized in Table 4-4. The same axial load carrying characteristics that were provided for the blast specimens, ultimate axial capacity and displacement ductility and the axial capacity at two separate ductility levels, are reported for each specimen. In addition, the initial axial stiffness of each specimen is also provided.

The fire damaged RC columns not only lost axial strength at the larger ductility levels, but also lost a significant amount of their ultimate axial capacity as well. The losses in ultimate strength for the RC-1Hr and -2Hr columns were 15.4%and 26.6%, respectively. Even more significantly, the fire damaged columns lost an excessive amount of their initial axial stiffness due to the degradation of the concrete material. The RC-1Hr column lost 41.7% of its axial stiffness while the RC-2Hr column lost 66.5%. Due to the dramatic decrease in initial axial stiffness, the ultimate ductility of the fire damaged columns was not compromised.

4.4.2 CFFT Specimens

Failure Progression

Figures 4-49, 4-50 show the axial load failure progression of the CFFT-1Hr and -2Hr columns, respectively. The fire exposed CFFT columns exhibited the same failure mode, rupture of the FRP tube at midspan, as the CFFT-Benchmark and -Blast specimens. Additionally, both columns showed the same ability to withstand large axial deformations prior to failure.

Cap Rotations

The CFFT-Fire specimens were not instrumented with strain gauges. Thus only the recorded cap rotations are presented. The 3-D plots depicting the cap rotations of the CFFT-1Hr and -2Hr specimens are displayed in Figures 4-51 and 4-52, respectively. Similar to the blast specimens, the fire exposed columns began to deform flexurally at large axial strains due to the differing tensile and compressive properties of the FRP tube. The maximum cap rotations recorded were 12.0° (0.209rad) for the CFFT-1Hr specimen and 5.77° (0.101rad) and 8.03° (0.140rad) for the CFFT-2Hr specimen.

Axial Capacity and Stiffness

The axial load-displacement curves of the CFFT-1Hr and -2Hr columns are displayed in Figures 4-53 and 4-54, respectively. Figure 4-55 shows the backbone curves of the two fire damaged specimens as well as the CFFT-Benchmark specimen in a single plot for comparison. The results of the CFFT-Fire tests are summarized in Table 4-5. The same axial load carrying characteristics that were provided for the CFFT-blast specimens plus the added characteristic of initial axial stiffness are provided in the table.

While the fire damaged RC columns exhibited significant losses in axial capacity exposure to fire, the CFFT-1Hr column retained all of its axial strength, and the CFFT-2Hr column showed an increase in axial strength of 5.83%. The fire protection system succeeded in keeping the temperature of the FRP tube and concrete below detrimental levels. In addition, the

FRP tube prevented moisture evaporation in the concrete core creating a steam curing effect that actually increased the concrete strength.

The fire exposed CFFT columns did see slight decreases in ductility and stiffness. The CFFT-1Hr and -2Hr specimens lost 25.2% and 15.1% of axial ductility, respectively, when compared to the CFFT-Benchmark column. However, on average, the fire exposed CFFT columns still had axial ductility nearly 2.5 times the fire damaged RC columns. While the CFFT-1Hr did not lose any initial axial stiffness, the -2Hr specimen saw a 25.4% loss in the same parameter.

The axial load-deformation responses of the RC- and CFFT-fire specimens are directly compared in Figure 4-56. Very little variation in the CFFT curves is seen when compared to large losses in axial capacity and stiffness of the fire damaged RC columns.

5 Analytical Studies

5.1 Blast Studies

5.1.1 RC Columns

After conducting the blast experiments and processing the load and strain data, a few unexpected observations were made. First, the peak tensile and compressive strains recorded during the RC tests were significantly larger than the typical yield strains of steel and concrete material, yet no visible damage to the column was observed. Secondly, the shear demands placed on the RC columns, obtained by halving the peak load recorded for each of the tests, is greater than the theoretical plastic shear demand obtained from moment-curvature analysis, reported in Sections 2.2.2 and 2.3.2. Finally, the pre-test analyses performed using three different software programs, ATP-Bridge, BEL, and OpenSees, predicted that there would be significant midspan displacements and permanent deformations for each test (Section 2.7.1).

5.1.1.1 Model Details

To further study these phenomena, the OpenSees model used for the pre-test analyses was advanced to account for dynamic effects on steel and concrete materials. The "Pinching4" uniaxial material model was used to model the cover and core concrete materials for each RC test. This material was selected because it offers fine control of the backbone curve parameters. Details regarding the "Pinching4" parameters can be found on the OpenSees wiki (PEER, 2012). "ReinforcingSteel" material was used for the longitudinal steel, and the gap between the column and the steel cap was modeled using a "zeroLengthElement" combined with "ElasticPPGap" material and a parallel elastic spring to account for the gap stiffness. Shear stiffness of the column is accounted for using the bilinear "Steel01" material and "Section Aggregator". The

uncracked shear stiffness of the section is applied until the concrete rupture modulus is reached; the post linear shear stiffness is defined as 0.2 times the uncracked shear stiffness.

5.1.1.2 Dynamic Increase Factors

One possible explanation for the lack of permanent deformation observed during the blast tests is the effect of strain rate on the strength of steel and concrete materials. There is a general consensus in the blast research and design communities that high strain rates have significant effects on the mechanical properties of steel and concrete (Malvar and Crawford, 1998a,b; Grote et al., 2001; Al-Azawi et al., 2006). However, there is a wide variety in the extent and magnitude of these effects reported in past studies. Because the variability of steel DIFs from past experiments is much less than that of the DIFs for concrete (Malvar and Crawford, 1998a,b), it was decided to set the steel strength DIF to a constant value of 1.22, which is the default value used by the US Army Corps of Engineers in SBEDs (USACE, 2012), and vary the concrete strength DIFs. The CEB formulation reported by Malvar and Crawford (1998b), shown herein as Eq. 7, was used as a starting point to estimate the concrete material DIFs for each test.

$$DIF = \left(\frac{\dot{\varepsilon}}{\dot{\varepsilon}_s}\right)^{1.026\alpha_s} \tag{7}$$

Where $\dot{\varepsilon}$ and $\dot{\varepsilon}_s$ are the experimental and quasi-static strain rates respectively, and $\alpha_s = 1/(5+9f'_c/1450)$, with f'_c in psi. The DIF and softening characteristics of the core and cover concrete material models were then finely adjusted until the strain histories for each test were closely matched, as shown in Figures 5-1, 5-2, and 5-3 for the RC-Moderate, -Severe, and -Severe-2 tests, respectively. The strain histories were used to validate the model due to lack of reliable midspan displacement data. The analytical cover and core concrete material models resulting in the best strain history matches are shown in Figures 5-4 and 5-5, respectively, and a

comparison of all experimental and analytical peak compressive and tensile strains is presented in Table 5-1.

The tensile strain rates recorded at the level of the reinforcement for each test, the DIFs calculated from Eq. 9, and the DIFs obtained from the analytical material models are shown in Table 5-2. To obtain the DIFs for the cover material, the peak compressive strength form the analytical material was divided by f'_c = 3.33ksi (22.96MPa) which is the concrete compressive strength for the column specimens obtained through material testing. For the core material, the peak confined compressive strength, f'_{cc}, from the each model was divided by the value of f'_{cc} that is obtained from Mander's model for confined concrete (1988) with f'_c = 3.33ksi (22.96MPa) to obtain the DIF.

5.1.1.3 Overpressure Confinement Effect: A Hypothesis

One significant observation that can be made from the cover concrete material models is that the shape follows the Mander formulation for confined concrete (1988) when f'_{cc} is equal to f'_c multiplied by the corresponding DIF. One hypothesis for the increased ductility and reduced softening of the cover concrete could be attributed to what the author terms a blast overpressure confinement (OPC) effect. As the incident blast pressure wave engulfs the column, it provides confining pressure to the concrete, instantaneously improving the strength and ductility of the concrete material.

This hypothesis was investigated by applying the incident blast pressure occurring at the column surface during each test as a confining pressure to cover concrete with f'_c = 3.33ksi (22.96MPa). The resulting OPC concrete models are very similar to those displayed in Figure 5-4. A similar investigation was carried out on the core material models. When a confining pressure accounting for both the incident blast pressure and the spiral reinforcement is applied to

the core material using Mander's formulation and f'_c = 3.33ksi (22.96MPa), the resulting material model very closely resembles the core material models shown in Figure 5-5.

5.1.1.4 Midspan Displacement and Shear Demand

After the model was validated by the strain history comparisons (Figs. 5-1, 5-2, and 5-3 and Table 5-1), the midspan displacement of each column was extracted from the analyses. The peak midspan displacements for the RC-Moderate, -Severe, and -Severe-2 tests are 0.199in. (5.06mm), 0.243in. (6.19mm), and 0.271in. (6.89mm), respectively, and the residual midspan displacement obtained for the RC-Severe-2 test was limited to less than 0.032in. (0.81mm). The plastic shear demand of the RC columns was re-evaluated taking the increased material strengths into account and using the pressure distribution obtained from BlastX. With these modifications, the maximum shear demands of the RC-Moderate, -Severe, and -Severe-2 tests were calculated as 25.9kip (115.2kN), 26.6kip (118.3kN), and 27.6kip (122.8kN), respectively.

5.1.2 CFFT Columns

5.1.2.1 Model Details

A "Pinching4" material backbone curve based on the FRP confined concrete model proposed by Saiidi, et al. (2005) and the longitudinal FRP material model presented by Zaghi, et al. (2012) are used to model the CFFT column. Again, "ReinforcingSteel" and the "zeroLengthElement" with "ElasticPPGap" material and parallel elastic spring are used for the reinforcement and gap, respectively. Because of the contribution of the FRP tube in the shear capacity of CFFT columns, the post yield shear stiffness of the CFFT column was set to 0.9 times the uncracked stiffness using "Section Aggregator".

5.1.2.2 Dynamic Increase Factors and Reduced OPC Effect

Although the concrete material of the RC columns was significantly affected by the dynamic effects of blast loading, the effects were less significant for the CFFT columns. The same steel DIF of 1.22 that was used for the RC column model was also used for the CFFT column. Unlike the RC column model, using the default concrete DIF from SBEDS (USACE, 2012) of 1.19 resulted in nearly matching experimental and analytical strain histories as evidenced by Figures 5-6 and 5-7 and the peak strain values reported in Table 5-1.

The smaller increase factor needed for the CFFT columns compared to the RC column may be justified by the fact that the major portion of the blast over pressure is resisted by hoop stresses in the FRP tube. Therefore, the incident blast pressure and OPC effect is insignificant for CFFT columns. Midspan displacements of the CFFT columns were extracted from the validated model showing no residual displacements and peak midspan displacements of 7.45mm (0.3in.) and 9.88mm (0.39in.) for the CFFT-Moderate and -Severe tests, respectively.

5.2 Residual Axial Capacity of Earthquake Damaged Columns

A previously conducted experimental research project at the University of Nevada, Reno (UNR) (Zaghi, et. al. 2012) studied the performance of a scaled two-column bridge bent integrating one RC column and one CFFT column under simulated ground motions using a shaking table. However, the columns were seismically loaded in increments to failure, so the residual axial capacities of the two column types were never determined. To further expand the multihazard resilience application of this dissertation research, an OpenSees model of a CFFT and RC column was developed to determine the post-earthquake axial load carry capabilities of the two column types after two magnitudes of biaxial ground motion. A brief overview of the UNR experiment is provided in Section 5.2.1. For in depth details of the study, refer to Zaghi et al.

(2012). Sections 5.2.2 through 5.2.4 describe the model, ground motions, and residual axial capacity characteristics used to study how RC and CFFT columns perform after experiencing seismic loads.

5.2.1 UNR Experiments

The RC and CFFT columns were designed to have comparable lateral load capacity at a 5% drift ratio. The largest diameter column that could be pushed to failure without exceeding the shaking table capacity was selected. The CFFT column incorporated a 14.5-in. (370-mm) outside diameter Red Thread® II (NOV, 2009) FRP pipe with a wall thickness of 0.27in. (7mm). The CFFT column contained eight, #4- (0.5in.- (12.7mm-) diameter) longitudinal reinforcing bars (ρ_s=1.04%). The conventional RC column was 14in. (356mm) in diameter and consisted of twenty #4- (0.5in.- (12.7mm-) diameter) longitudinal bars (ρ_s=2.6%). A two-way hinge connection was utilized at the tops of the columns. The embedment length of the CFFT column into the footing was 1.5 times the column diameter. Figure 5-8 shows the bent before the footing was cast.

The two-column pier model was subjected to seven uniaxial shaking table runs of 0.1, 0.4, 0.7, 1.0, 1.3, 1.6, and 1.9 times the ground acceleration recorded at the Sylmar Converter Station during the 1994 Northridge Earthquake. While the CFFT column exhibited no signs of damage until the seventh shake table run (PGA = 1.73g), spalling of the cover of the RC column started during Run 4 (PGA = 0.91g). During the last run, the maximum lateral displacement ductility of the CFFT and RC columns were measured as 12.2 and 10.5, respectively. The CFFT column exhibited a plastic hinge length double that of the RC column which contributed to 60% more energy dissipation with respect to the steel ratio of each column. The ductility and hysteresis energy dissipation capacity of the CFFT system including a small percentage of

reinforcement led to the conclusion that the CFFT system is a valid alternative for the seismic design of RC bridge columns.

5.2.2 Analytical Modeling Method

Unlike the blast and fire damaged columns of this study, the residual axial capacities of seismic damaged columns were evaluated utilizing analytical models of CFFT and RC columns rather than experimentally. OpenSees software (PEER, 2012) was used to simulate the shaking table response of the UNR two-column bent based on the nonlinear fiber section modeling technique used by Zaghi et al. (2012). After validating the model with the shake table response, the model was further refined by comparing the axial capacity of the columns with the data obtained from the axial load experiments on the RC- and CFFT-Benchmark columns reported in Chapter 4 of this study. Two columns with designs similar to those of the one-fifth scale blast and fire test columns were modeled and pushed axially to failure. Figure 5-9 shows the comparison of analytical model results with those obtained from axial experiments for both the RC and CFFT specimens.

The validated modeling method was then used to investigate the effects of seismic ground motions on the axial load capacity of RC and CFFT columns. The models were subjected to two intensities of biaxial ground motion, and subsequently pushed axially to failure to obtain the residual axial capacities of the damaged columns. Each column was modeled as a cantilever with an axial dead load equivalent to 10% of the column's full axial capacity to represent the superstructure weight. This dead load assumption is typical of the axial load carried by bridge columns. A lateral mass corresponding to the same dead load was assigned to the end of the columns.

"Concrete04" material was used to model the cover and confined core concrete of the RC column. "Concrete01" material was used to model the FRP tube confined concrete material of the CFFT column, and the tube was modeled using a trilinear "Hysteretic" material model using the backbone curve provided by Zaghi et al. (2012). The reinforcement for both column types was modeled using "reinforcingSteel" material. The section aggregator was used to account for shear cracking by assigning a cracked shear stiffness equal to 0.3 times the uncracked shear stiffness of the RC column and 0.9 times the uncracked shear stiffness for the CFFT column. The "MinMax" material of OpenSees was used to eliminate the contribution of FRP fibers that exceed 3% strain in axial tension and compression, respectively. The contribution of the FRP tube confined concrete was also eliminated at these rupture strains. Fiber sections were used to model the cross section of each column type. Four "dispBeamColumn" elements with four integration points each were used to model the one-fifth scale columns.

5.2.3 Ground Motions

The horizontal ground accelerations recorded from the Sylmar Olive View Medical Center during the 1994 Northridge Earthquake, shown in Figures 5-10 and 5-11 were scaled separately for each column type to impose "Moderate" and "Severe" levels of seismic damage to the each type of column. Lateral drifts of 4% and 7% were used as the Moderate and Severe drift levels, respectively.

5.2.4 Residual Axial Capacity

After each nonlinear time-history analysis, the residual axial capacities of the columns were determined through a displacement controlled axial pushover analysis. After experiencing 4% and 7% peak lateral drifts, the axial load-displacement relationships for the seismically damaged RC and CFFT columns were compared with the axial capacities of the columns prior to any

imposed ground motion as shown in Figures 5-12 and 5-13, respectively. The axial load-deformation relationships of all six analyses were then compared in a single plot in Figure 5-14.

A summary of the axial capacity results of the RC and CFFT models after experiencing 4% and 7% drift levels are shown in Tables 5-3 and 5-4, respectively. The same axial load carrying capacity parameters that were used as measures of resilience in the experimental blast and fire tests (capacity, ductility, and initial stiffness) are included in the tables.

Minimal loss in the maximum axial capacities of the columns was observed for all analysis cases. Although the CFFT column lost a comparable amount of ductility to the RC column after a 7% drift level, the CFFT column showed virtually no change in axial load carrying characteristics after experiencing 4% drift. After experiencing 4% and 7% drift levels, the RC column showed losses of 27.9% and 46.3% in ultimate ductility, respectively, when compared to the no motion case. The CFFT columns exhibited losses of 0.7% and 45.9% in ultimate ductility for the same drift levels, respectively. Additionally, on average, the ultimate ductility of the CFFT column was 3.2 times that of the RC column for each analysis case.

6 Multihazard Implications

There are many different ways that the term "multihazard" can be interpreted. It could be argued that multihazard implies multiple hazards acting simultaneously or sequentially, but it could also be argued that multihazard implies that a structural component has the inherent ability to resist multiple hazards without specific hardening for each separate hazard. Keller et al. (2009) describe a multihazard bridge pier as one that has desirable characteristics to protect and satisfy the demands of multiple hazards. The CFFT column has shown that it has desireable characteristics for seismic, blast, and fire hazards when designed properly. Additionally, the experimental and analytical work performed in this study, has implications for multiple hazards that may occur sequentially.

The first multihazard inference that can be made is that an RC column may exhibit an unexpected shear failure during an earthquake if it has been previously exposed to a blast hazard. RC columns in seismic regions are designed such that their rebar reinforcement will yield, resulting in plastic hinging and energy dissipation. Although a RC bridge column may need repair after an earthquake, yielding in the plastic hinge region is a ductile means of damage formation. The axial capacity tests performed after the blast experiments showed that blast loading can initiate shear cracking in RC columns without any outward signs of damage. This shear cracking changes the expected failure mode and can be detrimental to the performance of the column in a future earthquake.

Another multihazard inference that can be made from the work performed as part of this research is that the concrete material degradation that occurs when a RC column is exposed to extreme temperature can reduce its resistance to hazards that may occur subsequent to a fire event. The axial capacity tests following the fire experiments, revealed losses in both

compressive strength and elastic modulus of the concrete material. Although the residual strength tests were done under pure axial compression, the observed losses can be translated into flexural capacity losses as well. The lower elastic modulus results in reduced flexural stiffness observed through basic mechanics of materials equations, i.e. $k=3EI/L^3$ for a cantilever beam. The lower compressive strength of the concrete leads to a reduced moment capacity by reducing the contribution of the concrete material in the effective compression block of the column/beam section. From a global perspective, a member with reduced capacity and stiffness could result in unexpected load concentrations in other members during an earthquake, flood, or other hazardous event, leading to unexpected global failure modes.

In contrast to the RC columns tested, the CFFT columns were able to maintain capacity, ductility, and stiffness characteristics after extreme event exposure. The FRP tube was able to provide sufficient confinement to the concrete core to prevent shear cracking during blast loading. Because the blast exposed CFFT columns failed in exactly the same manner as the CFFT-Benchmark column under axial loading, it can be hypothesized that their seismic performance would remain relatively unchanged. However, more experimental work is needed to confirm this hypothesis. Similarly, the experiments performed in this study indicate that CFFTs would maintain their performance level as elements of a global system, leading to more predictable global behavior under future hazards.

7 Design Method for Lightly Reinforced CFFTs

7.1 Introduction

The experiments and analytical studies described in the previous chapters provide grounds to introduce the CFFT system as a viable alternative to conventional RC bridge columns vulnerable to multiple hazards. However, a lack in the awareness of the system and limiting design standards have prevented the system from being implemented as a column alternative in the bridge design community. This chapter aims to discuss the limiting components of AASHTO's 1st edition of LRFD Guide Specifications for Design of CFFTs as Flexural and Axial Members (AASHTO, 2012a) and to introduce new axial and flexural resistance equations as well as curvature ductility curves for strength-based and displacement-based design of lightly reinforced CFFT bridge columns.

Rigorous cross-sectional analyses of a generic CFFT cross section were performed and cross-checked simultaneously using XTract (Imbsen, 2007) and OpenSees (PEER, 2012) software to develop a new set of axial and flexural resistance equations consistent with the Guide Specification and Seismic Specifications (AASHTO, 2011) format. The new equations include the added resistance of minimal amounts of longitudinal steel reinforcement for the design of CFFTs resilient to multiple hazards. The new resistance equations along with a combined axial-flexural (P-M) interaction equation are presented for load-based CFFT design. Additionally, a set of curvature ductility curves with respect to the axial load of a column are presented for the displacement-based design method used for the seismic design of bridge components (AASHTO 2011; Caltrans, 2006).

7.2 AASHTO LRFD First Edition

AASHTO has recently released the 1st edition of LRFD Guide Specifications for Design of CFFTs as Flexural and Axial Members (AASHTO, 2012a), referred to as "Guide Specification" hereafter. The Guide Specification serves as a supplement to the AASHTO LRFD Bridge Design Specifications (AASHTO, 2012b) for the analysis and design of CFFTs as structural components in bridges. The Guide Specification includes equations to compute the capacity of CFFT members subjected to flexure, axial compression, and combined flexure and axial compression. Although the Guide Specification enables the use of CFFT components in bridge design, it lacks pivotal aspects that would allow CFFTs to be utilized as bridge columns resilient to multiple hazards.

The Guide Specification limits the design of the CFFT system in two ways. First, the Guide Specification limits the applicability of the CFFT system for extreme events. Section 1.3 explicitly states that CFFTs shall not be used as ductile earthquake resisting elements (AASHTO, 2012a). Section 2.7.4 of the Guide Specification states that a structure consisting of CFFT members shall be proportioned to resist collapse due to extreme events, specified in Table 3.4.1-1 of AASHTO-LRFD (AASHTO, 2012b). While earthquake loads and blast loads are included in the table, no guidance is provided for the design of CFFT members that may be subjected to such loading, nor are there any provisions for fire protection of the system.

The second limitation of the Guide Specification is that its axial compression and flexural resistance equations do not account for longitudinal steel reinforcement within CFFT members. The blast and seismic studies previously summarized have indicated that modest amounts of longitudinal steel reinforcement can positively impact the axial strength, ductility, and energy dissipation performance of CFFTs during and after extreme events. In fact, with a steel

reinforcement ratio of around 1.0% and fire protection, CFFT columns outperform and exhibit superior resilience to blasts, fires, and earthquakes compared to conventional RC columns (Zaghi et al., 2012; Echevarria et al., 2014a,b,c,d,e). Including a small amount of longitudinal steel can provide the CFFT system with the strength and ductility needed to prevent a total collapse, and even maintain the serviceability of a bridge structure after extreme events.

7.3 Axial and Flexural Resistance of Lightly Reinforced CFFTs

Rigorous axial capacity and moment-curvature analyses of the generic CFFT cross section shown in Figure 7-1 were performed using XTract and OpenSees software. The modeling method was kept very general as if being used in the bridge design industry. The steel reinforcement ratio for the section, ρ_s, was varied between 0.002 and 0.016 to develop a set of capacity equations. In this generalized section the concrete core diameter to shell thickness, *D/t*, was assumed to have a constant value of 60 based on an average *D/t* ratio of Red Thread II® FRP tubes (NOV, 2009).

The FRP tube used for the development of the capacity equations is assumed to have a fiber orientation of ±55º with respect to the longitudinal axis of the column to be consistent with the previously conducted experiments. The FRP tube was modeled using the hysteretic FRP material model presented by Zaghi et al. (2012). The experimental results of the axial compression tests in Chapter 4 and shaking table tests by Zaghi et al. (2012) described in Section 5.2.1 were used to determine the compression and tension rupture strains of the FRP material. A rupture strain of 30,000με was measured on the FRP tube during the axial testing of the undamaged column. In the experiments performed by Zaghi et al. (2012), tension rupture of the FRP tube was observed at a strain of 70,000με, while no compression failure was reported during the shaking table experiments. Thus, 30,000με and 70,000με are the assumed

compression and tension strain limits of the FRP tube, respectively. The steel reinforcement is assumed to be ASTM A615 Grade 60 with an expected yield strain of 2300με and ultimate tensile strain of 90,000με (AASHTO, 2011). The FRP tube confined concrete core was modeled following the backbone curve presented in Figure 7-2. On this curve, ε_{co} and f'_{co} correspond to the break point suggested by Lam & Teng (2003) where f_{co} is the unconfined compressive strength of the concrete and ε_{co} is calculated using Eq. 8.

$$\varepsilon_{co} = \frac{2 f_{co}}{E_c - E_2} \tag{8}$$

where E_c is the elastic modulus of unconfined concrete and E_2 is the slope of the linear second branch calculated as:

$$E_2 = \frac{f_{cu} - f_{co}}{\varepsilon_{cu}}$$

The values of ε_{cu} and f_{cu} are determined following AASHTO specifications for FRP confined concrete compressive strain and strength, respectively (AASHTO, 2012a). After the concrete strain surpasses ε_{cu}, its stress remains constant at f_{cu} until reaching the rupture strain, ε_{rup}. The axial capacity experiments performed in this study showed no loss in strength until the rupture of the FRP tubes. Thus, the value of ε_{rup} is assumed equal to the compressive rupture strain of the FRP tube.

The results of the axial capacity and moment-curvature analyses were compiled to develop equations for the nominal axial and flexural capacities, as well as a combined P-M interaction equation for CFFT columns with longitudinal steel reinforcement. The axial load index (ALI) of a column is defined as the compressive load divided by the product of the gross cross sectional area and the unconfined concrete compressive strength. The typical range of ALI for bridge columns is 5%-25% with the recommended value being 10% for seismic regions

(Correal et al., 2004). For this reason, the proposed equations have been optimized only for ALI's less than or equal to 25%. The results of the axial capacity analyses were normalized by the axial load index (ALI) and correlated with ρ_s. Similarly, the results of the moment-curvature analyses were normalized by the product of the ALI and the diameter of the concrete core and correlated with ρ_s. Regression analysis was then used to develop the following axial and flexural resistance equations based on the 110 axial capacity and moment-curvature analyses.

- Nominal axial capacity under pure compression:

$$P_n = (1.5 + 18\rho_s) f'_c A_g \tag{9}$$

- Nominal moment capacity under pure flexure:

$$M_n = (0.135 + 7\rho_s) f^* A_g D \tag{10}$$

- For CFFTs under combined loading, the applied axial and flexural loads P and M, respectively, must satisfy:

$$\frac{M}{M_n} = 1 + \alpha\left(\frac{P}{P_n}\right) + \beta\left(\frac{P}{P_n}\right)^2 \tag{11}$$

$$\alpha = 3.75 - 140\rho_s \tag{12}$$

$$\beta = -8.25 + 200\rho_s \tag{13}$$

Where P_n is the nominal axial compressive resistance with no flexural load, M_n is the nominal flexural resistance with no axial load, A_g is the gross area of the CFFT cross section, f'_c is the specified unconfined concrete compressive strength, f^* is 4.0ksi, D is the diameter of the concrete core, and ρ_s is the longitudinal steel reinforcement ratio (the ratio of the area of steel reinforcement to the gross cross section area).

In Eq. 10, f^* is used to normalize the flexural capacity. In the moment-curvature analyses, it is assumed to have the same value as f'_c. However, for cases where f'_c is larger or smaller than

4.0ksi, the value of f^* shall remain set to 4.0ksi. The flexural capacity of CFFTs is not significantly affected by the compressive strength of the concrete and scaling the flexural capacity directly by f'_c results in unrealistic values. Conversely, the axial capacity of CFFTs is heavily dependent on the compressive strength concrete. Thus, f'_c is directly used in Eq. 9 to normalize the axial load capacity.

Table 7-1 compares a sample set of the axial and flexural capacities of the generic CFFT column (Figure 6-1) with varying ρ_s and ALI values obtained from refined moment-curvature analyses with the axial and flexural capacities found through utilization of the presented resistance equations. In addition, Figure 7-3 displays the P-M interaction for the generic section with increasing ρ_s obtained from moment-curvature analysis and computed using Eq. 11. The largest margin of error is 1.71% for all values of axial and moment capacity when compared to moment-curvature analyses, which demonstrates that the proposed equations are accurate for ALI's less than 25%.

To further validate these equations, the experimental axial capacity of the undamaged CFFT-Benchmark column from Chapter 4 was compared to the axial resistance predicted by Eq. 9. The input variables for the CFFT-Benchmark column are $\rho_s=0.0112$, $f'_c=3.33ksi$ $(23.0MPa)$, and $A_g=58.63in^2$ $(37{,}826mm^2)$. The experimental capacity of the column was obtained as 334.4kip (1487.5kN), and the nominal axial capacity from Eq. 9 is 332.4kip (1478.7kN). This confirms that the proposed equation is reliable for determining the axial capacity of a CFFT column.

Next, the moment capacity of the CFFT column tested in the UNR shaking table experiments as described in Section 5.2.1 was used to verify the interaction equation (Eq. 11). The maximum base shear force and lateral displacement of the CFFT column recorded during

the last run of the shaking table tests were 44.5kip (197.9kN) and 5.4in. (137.2mm), respectively (Zaghi et al., 2012). The axial load on the CFFT column at its maximum lateral displacement was 70kip (311.4kN), resulting in ALI = 6.11%. By multiplying the maximum base shear by the length of the column, and assuming that the axial load acts at the center of the bearing area at top of the column, the ultimate moment capacity, including P-Delta effects, was 2874kip-in (324.6kN-m).

The UNR CFFT column had ρ_s*=0.0104.* Because the CFFT column tested at UNR contained rebar with higher yield strength and smaller *D/t* ratio than the generic cross section, the moment capacity determined by Eq. 11 is modified to account for the actual yield strength of steel reinforcement and the actual *D/t* ratio of the CFFT column in the shaking table tests. To do so, the predicted moment is scaled by the ratio of actual steel strength (75ksi) to the generic steel strength of 60ksi, and by the ratio of the generic *D/t* ratio of 60 to the actual *D/t* ratio of 52.15. The scaled moment capacity is computed as 2892kip-in (326.8kN-m), confirming the accuracy of Eq. 11.

7.4 Displacement-Based Design of Lightly Reinforced CFFTs

To enable displacement based seismic design of CFFT columns (AASHTO, 2011), the moment-curvature relationships were used to develop curvature ductility-axial load relationships. A sample set of these curves for common design values of ρ_s are presented in Figure 7-4. The curvature ductility, μ_φ, of a column can be used to determine the displacement ductility of the column using Equation C4.9-6 of the AASHTO Seismic Specifications (2011), shown in Eq 14.

$$\mu_D = 1 + 3(\varphi_u/\varphi_y - 1)\, L_p/L\,(1 - 0.5\, L_P/L) \tag{14}$$

Where φ_u is ultimate curvature, φ_y is the idealized yield curvature from bilinearization, L_p is the plastic hinge length, and L is the length of the column from the point of maximum moment to the point of contraflexure.

Although the displacement based design methodology described by AASHTO assumes an elastic-perfectly plastic moment curvature relationship for reinforced concrete members, an elastic-plastic bilinearization with post-yield hardening is more appropriate for CFFT columns due to the large post-yielding slope of the moment-curvature relationships as shown in Figure 7-5. A plastic hinge length of 1.45D for CFFT columns is proposed by Zaghi et al. (2012) and is used herein.

The presented ductility curves were validated using the experimental results of the UNR shake table studies discussed in Section 5.2.1 (Zaghi et al., 2012). From the presented curves (Figure 6-4), a CFFT column with ρ_s=0.010 and ALI=6.11% has a curvature ductility, $\mu_{\varphi,}$ of 14.27. This value results in displacement ductility, $\mu_{D,}$ equal to 12.22 using Eq. C4.9-6 (AASHTO, 2011). The displacement ductility reported by Zaghi et al. (2012) during the shaking table experiments was 12.2, providing a validation for the proposed curvature ductility curves.

8 Summary and Conclusions

8.1 Summary

Recent increases in the severity and occurrence of both manmade and natural hazards coupled with the current age and deteriorated state of the nation's bridges have prompted researchers to study the performance and resilience of bridge structures from a multihazard perspective. Because the failure of a single column can prove detrimental to the structural integrity of the global bridge system, significant research has been dedicated to improving the performance of columns when subjected to various types of hazards such as: earthquakes, blasts, fire, corrosion, and scour.

One column type that has presented itself as a viable alternative to conventional RC column systems is the CFFT column. The primary objectives of this study were to comparatively study the resilience of RC and CFFT columns to blast, fire and seismic hazards through a comprehensive four phase research program. The four phases of the study were: (I) experimental blast testing of one-fifth scale RC and CFFT columns at the United States Army Corps of Engineers (USACE) Engineering Research and Development Center (ERDC) in Vicksburg, MS, (II) experimental fire testing at the Guardian Fire Testing Laboratory in Buffalo, NY, (III) axial capacity testing of benchmark and blast and fire damaged RC and CFFT columns to determine the blast and fire resilience of each column type, and (IV) data processing and analytical studies including an axial performance study of RC and CFFT columns after seismic events and the development of a design methodology for lightly reinforced CFFT columns for use in multihazard scenarios.

Ten one-fifth scale column models, five RC and five CFFT, were constructed for the experimental blast, fire, and axial capacity testing. This experimental work serves to fill the

literature gap present for tests on CFFTs subjected to blast and fire hazards. The axial capacity experiments were used to compare the post-extreme event performance of RC and CFFT columns. The residual axial capacity characteristics served as measures of resilience of each type of column to blast and fire exposure.

The analytical work was completed to supplement the experimental findings. An analytical model was developed to further study the effects of blast loading on both types of columns, but primarily focused on RC columns. The same model was advanced to study the residual axial capacity characteristics of RC and CFFT columns after seismic loading. Finally, a series of moment-curvature analyses were used to develop axial and flexural resistance equations and curvature ductility curves to facilitate the design of lightly reinforced CFFTs to be used in multihazard applications.

8.2 Observations and Conclusions

The following observations and conclusions present the highlights from all phases of this research:

- The dynamic effects produced by a blast shock wave have a significant effect on the response of conventional RC columns subjected to blast. The effect of increased material strengths due to strain rate and the hypothesized OPC effect temporarily improve the strength and ductility of the concrete resulting in a greater flexural capacity of the column. In turn, the higher flexural capacity results in shear demands that are nearly double that of the design shear demand for RC columns.
- The increased shear demand placed on RC columns due to dynamic effects and OPC can affect the axial load carrying capacity without any outward signs of damage post-blast.

- Blast loading caused shear crack initiation in the RC columns resulting in a shear-type failure mode under axial loading. This failure mode was unexpected and differed from the concrete crushing failure mode exhibited by the undamaged benchmark RC column.
- The ultimate axial displacement ductility of RC columns subjected to blast threats with scaled standoff values ranging from 1.23 to 1.02 can be compromised by as much as 50%. The ultimate axial ductility loss exhibited by CFFT columns under equivalent threats (scaled standoff values ranging from 0.958 to 1.06) was 28.3% or less.
- Blast damaged RC columns exhibited significant axial strength losses at $\mu_{D,P}=3$ and had lost an average of 68.5% of axial strength at $\mu_{D,P}=4$. At equivalent ductility levels of $\mu_{D,P}=9.75$ and $\mu_{D,P}=13$, blast damaged CFFT columns exhibited no loss, and an average of 25.4% in axial strength, respectively.
- The FRP tube of the CFFT columns provided sufficient confinement to the concrete core to resist shear crack initiation during blast loading resulting in consistent failure modes for undamaged and blast loaded CFFTs.
- The Tyfo-CFP protection system provides sufficient protection to CFFTs from exposure to fires with temperatures exceeding 1400°F (760°C) and lasting longer than two hours.
- RC columns exhibited losses of 15.4% and 26.6% in axial capacity and 41.8% and 66.4% in initial axial stiffness under 1-Hr and 2-Hr exposure to extreme temperature, respectively. The significant loss of axial strength and stiffness observed in the fire damaged RC columns resulted in larger values of axial ductility when compared to the undamaged column.
- Protected CFFTs exhibited a slight increase in axial capacity after the same durations of fire exposure because the FRP tube provided a pseudo steam-curing environment for the core

concrete. The protected CFFTs exhibited a 25.5% loss in initial axial stiffness after 2-Hr exposure.

- The RC column model used in the analytical seismic studies exhibited losses of 52.0%, 10.1%, and 27.9% in axial strength, stiffness, and ductility, respectively, after experiencing 4% lateral drift. The CFFT system, under the same drift level, had losses of 0.35%, 29.0%, and 0.33% for the same resilience measures.
- After 7% drift, the RC column model lost 66.2%, 21.3%, and 46.3% of its axial strength, stiffness, and ductility, respectively, while the CFFT column lost 3.69%, 34.7%, and 45.7% for the same resilience measures.
- The proposed formulation for lightly reinforced CFFTs was able to accurately predict the axial and flexural capacity of CFFT columns with less than 2% error when compared to experimental values.
- The presented P-μ_φ curves utilized in conjunction with Eq. C4.9-6 (AASHTO, 2011) were able to accurately predict the lateral displacement ductility of a CFFT column experimentally tested on a shaking table at UNR.
- The results of this research validate the CFFT system as a viable alternative to RC columns at risk for exposure to multiple hazards. The construction benefits of the system add to the attractiveness of CFFT columns.

REFERENCES

Agrawal, A.K. and Yi, Z. (2009). Blast Load Effects on Highway Bridges, University Transportaion Research Center, New York, NY.

Alipour, A., Shafei, B., Shinozuka, M. (2010). "Failure estimation of highway bridges undercombined effects of scouring and earthquake." *Proc. 5th International Conference on Bridge Maintenance, Safety, and Management*. IABMAS, Philadelphia, PA.

Alipour, A., Shafei, B., Shinozuka, M. (2011). "Performance Evaluation of Deteriorating Highway Bridges Located in High Seismic Areas." *J. of Bridge Engineering*, 16(5), 597-611.

Alipour, A., Shafei, B., Shinozuka, M. (2013). "Reliability-Based Calibration of Load and Resistance Factors for Design of RC Bridges under Multiple Extreme Events: Scour and Earthquake." *J. of Bridge Engineering*, 18(5), 362-371.

American Association of Highway Transportation Officials (AASHTO). (2011). *Guide Specifications for LRFD Sesimic Bridge Design, 2nd Edition*. AASHTO, Washington, DC.

AASHTO (2012a). *LRFD Guide Specifications for Design of Concrete-Filled FRP Tubes for Flexural and Axial Members*. AASHTO, Washington DC.

AASHTO (2012b). *LRFD Bridge Design Specifications, 6th Edition*. AASHTO, Washington DC.

Al-Azawi, T.K, Al-Azawi, R.K, and Ibrahim, T.H. (2006). " Curvature Ductility of Reinforced Concrete Column Sections under Different Strain Rates." *Tikrit Journal of Engineering Schiences.* 13(2): 67-92.

American Society of Civil Engineers. (2013). Report Card for America's Infrastructure. ASCE, Reston, VA.

Aquino, W. and Hawkins, N.M. (2007). "Seismic Retrofitting of Corroded Reinforced Concrete Columns Using Carbon Composites." *ACI Structural J.,* American Concrete Institute (ACI), 104(3), 348-356.

Berger, J.O., Heffernan, P. J., and Wight, R.G. (2008). "Blast testing of CFRP and SRP strengthened RC columns." *Structures Under Shock and Impact* 98(X), 95-104.

Bisby, L.A., Kodur, V.K.R., and Green, M.F. (2005). "Fire Endurance of Fiber-Reinforced Polymer-Confined Concrete Columns. *ACI Structural J.,* ACI, 102(6), 883-891.

Bruneau, M., El-Bahey, S., Fujikura, S., and Keller, D. (2011). "Structural Fuses and Concrete-Filled Steel Shapes for Seismic- and Multi-Hazard Resistant Design," *Bulletin of the New Zealand Society for Earthquake Engineering*, 44(1), 44-52.

California Department of Transportation (Caltrans). (2006). *Seismic Design Criteria Version 1.4*. Caltrans, Sacramento, CA.

Chang, Y.F., Chen, Y.H., Sheu, M.S., and Yao, G.C. (2006). "Residual stress-strain relationship for concrete after exposure to high temperatures." *Cement and Concrete Research*, Elsevier, 36, 1999-2005.

Choe, D.E., Gardoni, Paolo, Rosowsky, D. Haukaas, T. (2008) "Probailistic capacity models and sesimic fragility estimates for RC columns subjected to corrosion." *Reliability Engineering and System Safety*, Elsevier, 93(3), 383-393.

Choe, D.E., Gardoni, Paolo, Rosowsky, D. Haukaas, T. (2009) "Seismic fragility estimates for reinforced concrete bridges subject to corrosion." *Structural Safety*, Elsevier, 31(4), 275-283.

Correal, J.F, Saiidi, M., and Sanders, D.H. (2004). *Seismic Performance of RC Bridge Columns Reinforced with Two Interlocking Spirals.* Report No. CCEER-04-06, University of Nevada, Reno.

Cruz Noguez, C.A. and Saiidi, M. (2012). "Shake-Table Studies of a Four-Span Bridge Model with Advanced Materials." *J. of Structural Engineering,* ASCE, 138(2), 183-192.

Davis, C., Williams, G., Williamson, E., Marchand, K., McKay, A., and Bayrak, O. (2009) "Design and Detailing Guidelines for Bridge Columns Subjected to Blast and Other Extreme Loads". Structures Congress 2009: pp. 1-10.

Echevarria, A., Zaghi, A.E., Chiarito, V., Christenson, R., (2014a). "Blast Resilience of Concrete-Filled FRP Tube (CFFT) Bridge Columns." *Proc. IABMAS 2014*. IABMAS, Shanghai, China.

Echevarria, A., Zaghi, A.E., Christenson, R., Chiarito, V. (2014b). "The seismic, blast and fire resilience of concrete-filled FRP tube (CFFT) bridge columns." *Proc. IABMAS 2014*. IABMAS, Shanghai, China.

Echevarria, A, Zaghi, A.E., Chiarito, V., Christenson, R., Woodson, S. (2014c). "Experimental Comparison of the Performance and Residual Capacity of CFFT and RC Bridge Columns Subjected to Blasts". Submitted *J. of Bridge Engineering*, ASCE.

Echevarria, A, Zaghi, A.E., Chiarito, V., Christenson, R., Woodson, S. (2014d). "Design of CFFT Bridge Columns for Multihazard Resilience". Submitted *J. of Structural Engineering*, ASCE.

Echevarria, A, Zaghi, A.E., Chiarito, V., Christenson, R., Woodson, S. (2014e). "Experimental Comparison of the Performance and Residual Capacity of CFFT and RC Bridge Columns Subjected to Fire". To be Submitted *Composites for Construction*, Elsevier.

Elsanadedy, H.M., Almusallam, T.H., Abbas, H., Al-Salloum, Y.A., and Alsayed, S.H. (2011). "Effect of blast loading on CFRP-Retrofitted RC columns – a numerical study." *Latin American Journal of Solids and Structures*, 8(2011), 55-81.

Fam, A. (2000). "Concrete-Filled Fiber-Reinforced Polymer Tubes for Axial and Flexural Structural Members." Doctoral Dissertation, University of Manitoba, Winnipeg, Mannitoba, Canada.

Fam, A., Cole, B, and Mandal, S. (2007). "Composite Tubes as an Alternative to Steel Spirals for Concrete Members in Bending and Shear." *Construction and Building Materials*, Elsevier, 21(2007), 347-355.

Fam, A., Greene, R., and Rizkalla, S. (2003a). *Field Applications of Concrete-Filled FRP Tubes for Marine Piles.* ACI Report SP-215-9. ACI, Farmington Hills, MI.

Fam, A., Pando, M., Filz, G., and Rizkalla, S. (2003b). "Precast Piles for Route 40 Bridge in Virginia Using Concrete Filled FRP Tubes". PCI Journal, 48(3), 32-45.

Fam, A., Flisak, B., and Rizkalla, S. (2003c). "Experimental and Analytical Investigations of Concrete-Filled Fiber-Reinforced Polymer Tubes Subjected to Combined Bending and Axial Loads." *ACI Structural J.*, ACI, 100(4), 499-509.

Fam, A. and Rizakalla, S. (2002). "Flexural Behavior of Concrete-Filled Fiber-Reinforced Polymer Circular Tubes." *J. of Composites for Construction,* ASCE, 6(2), 123-132.

FHWA. (2013). National Bridge Inventory, <http://www.fhwa.dot.gov/bridge/nbi.cfm>. FHWA, Washington, DC.

Fiberglass Systems (FGS). (2005). "Time-Tested Fiberglass Piping Systems for Water Applications Smith Fibercast". Bulletin No. C3320. FGS, Little Rock, AR.

Franchin, P. and Pinto, P.E. (2007). “Transitability of mainshock-damaged bridges.” *Proc. 1st US-Italy Seismic Bridge Workshop,* Pavia, Italy.

Franchin, P. and Pinto, P.E. (2009). “Allowing Traffic over Mainshock-Damaged Bridges.” *J. of Earthquake Engineering,* Taylor and Francis, 13(5), 585-599.

Fujikura, S., and Bruneau, M. (2008). "Blast Resistance of Seimically Designed Bridge Piers." *Proc. 14th World Conference on Earthquake Engineering*, Beijing, China.

Fujikura, S., and Bruneau, M. (2011). "Experimental Investigation of Seismically Resistant Bridge Piers under Blast Loading." *J. of Bridge Engineering*, 16(1), 63-71.

Fujikura, S., and Bruneau, M. (2012). "Dynamic Analysis of Multihazard Resistant Bridge Piers Having Concrete-Filled Steel Tube under Blast Loading." *J. of Bridge Engineering,* 17(2), 249-258.

Fujikura, S., Bruneau, M., and Lopez-Garcia, D. (2007). "Experimental Investigation of Blast Performance of Seismically Resistant Concrete-Filled Steel Tube Bridge Piers." *Rep. No. MCEER-07-005,* University at Buffalo, NY.

Fujikura, S., Bruneau, M., and Lopez-Garcia, D. (2008). "Experimental Investigation of Multihazard Resistant Bridge Piers Having Concrete-Filled Steel Tube under Blast Loading." *J. of Bridge Engineering,* ASCE, 13(6), 586-594.

Fyfe. (2013). Tyfo® CFP System. Fyfe, Co., LLC, San Diego, CA.

Gefu, J., Li, G., Li,X., Pang, S. and Jones, R. (2008). “Experimental study of FRP tube encased concrete cylinders exposed to fire.” *Composite Structures*, Elsevier, 85(2), 149-154.

Ghosh, J. and Padgett, J.E. (2010). “Aging Considerations in the Development of Time-Dependent Seismic Fragility Curves.” *J. of Structural Engineering,* ASCE, 136(12), 1497-1511.

Ghosh, J., Padgett, J.E., Sanchez-Silva, M. (2013). “Seismic Damage Accumulation of Highway Bridges in Earthquake Prone Regions”. *Earthquake Spectra,* EERI, in press.

Gram, M.M., Clark, A.J., Hegemier, G.A. and Seible, F. (2006). “Laboratory simulation of blast loading on building and bridge structures.” *Structures Under Shock and Impact* IX, (2006): 33-44.

Grote, D.L., Park, S.W., and Zhou, M. (2001). “Dynamic behavior of concrete at high strain rates and pressures: I. experimental characterization”. *International Journal of Impact Engineering*, 25(9): 869-886.

Han, L. (2001). “Fire performance of concrete filled steel tubular beam-columns.” *Journal of Constructional Steel Research,* 57(6), 697-711

Hernández-Olivares, H., Barluenga, G. (2004). “Fire performance of recycled rubber-filled high-strength concrete”, *Cement and Concrete Research,* 34(1), 109-117.

Imbsen Software Systems. (2007). *XTract*. TRC, Sacramento, CA.

Islam, A.K.M.A. and Yazdani, N. (2008) "Performance of AASHTO girder bridges under blast loading." Engineering Structures, 30, 1922-1937.

Jayasooriya, R., Thambiratnam, D.P., Perera, N.J. (2014). “Blast response and safety evaluation of a composite column for use as key element in structural systems”, *Engineering Structures,* 61(1), 31-43.

Kavianipour, F. and Saiidi, M. (2012). “Shake table testing of a quarter-scale 4-span bridge with composite piers,” *Proc. 6th IABMAS,* Stresa, Italy, 1966-1973.

Keller, D., Fujikura, S., Fouche, P., Bruneau, M. (2009). "Multi-Hazard (Blast, Seismic, Tsunamis, Collision) Resitant Bridge Piers." *80th Shock & Vibration Symposium (SAVIAC),* San Diego, CA.

Kodur, V.K.R. (1999). “Performance-based fire resistance design of concrete-filled steel columns.” *Journal of Constructional Steel Research,* 51(1), 21-36

Kodur, V.K.R., Bisby, L.A., and Green, M.F. (2007). “Preliminary Guidance for the Design of FRP-strengthened Concrete Members Exposed to Fire.” *J. of Fire Protection Engineering*, SFPE, 17(1), 5-26.

Kodur, V.K.R., Phan, L. (2007). “Critical factors governing the fire performance of high strength concrete systems”, *Fire Safety Journal*, 42(6-7), 482-488.

Kowalsky, M.J. and Priestley, M.J.N. (2000). “Improved Analytical Model for Shear Strength of Circular Reinforced Concrete Columns in Seismic Regions.” *ACI Structural J.*, 97(3), 388-396.

Knaack, A.M., Kurama, Y.C., Kirkner, D.J. (2009). *Stress-Strain Properties of Concrete at Elevated Temperatures*. Report No. NDSE-09-01. University of Notree Dame, Notre Dame, Indiana.

Kumar, R. and Gardoni, P. (2012). “Modeling Structural Degradation of RC Bridge Columns Subjected to Earthquakes and Their Fragility Estimates.” *J. of Structural Engineering,* ASCE, 138(1), 42-51.

Kyodo News. (2011). "Survivors on cut-off isle were ready for disaster." *Japan Times.* http://www.japantimes.co.jp/news/2011/03/19/news/survivors-on-cut-off-isle-were-ready-for-disaster/#.UkXsZdJLkRF.

Lam, L. and Teng, J.G., (2003). “Design-oreiented stress-strain model for FRP-confined concrete.” *Construction and Building Materials.* Elsevier, 17(6-7), 471-489.

Li, J., Gong, J., Wang, L. (2009). "Seismic behavior of corrosion-damaged reinforced concrete columns strengthened using combined carbon fiber-reinforced polymer and steel jacket." *Construction and Buildign Materials,* Elsevier, 23(7), 2653-2663.

Liang, Z and Lee, G.C. (2013a). "Towards establishing practical multi-hazard bridge design limit states," *Earthquake Engineering and Engineering Vibration*. 2013(12), 333-340.

Liang Z and Lee GC (2013b), "Bridge Failure Probabilities under Combined Hazard Effects of Scour, Truck and Earthquake, Part I, Occurrence Probabilities," *Earthquake Engineering and Engineering Vibration*, 12(2): 229–240(3).

Liang Z and Lee GC (2013c), "Bridge Failure Probabilities under Combined Hazard Effects of Scour, Truck and Earthquake, Part II, Failure Probabilities*," Earthquake Engineering and Engineering Vibration*, 12(2): 241–250.

Lie, T.T. (1989). "Fire Resistance of Reinforced Concrete Columns: A Parametric Study". *Journal of Fire Protection Engineering*. 1(4), 121-129.

Lie,T.T., and Lin, T.D. (1986). "Influence of Restraint on Fire Performance of Reinforced Concrete Columns." Fire Safety Science - Proceedings of the First International Symposium, 291-300.

Lie, T. T., and Woollerton, J. L. (1988). *Fire Resistance of Reinforced Concrete Columns: Test Results*. Report No. 569, National Research Council of Canada, Ottawa, Canada.

Mander, J.B., Priestley, M.J.N., and Park, R. (1988). "Theoretical stress-strian model for confined concrete." *J. of Structural Engineering*, 114: 1804-1826.

Malvar, L.J. and Crawford, J.E. (1998a). "Dynamic Increase Facots for Steel Reinforcing Bars". *Twenty-Eighth DDESB Seminar.* Naval Facilities Engineering Service Center.

Malvar, L.J. and Crawford, J.E. (1998b). “Dynamic Increase Facots for Steel Reinforcing Bars”. *Twenty-Eighth DDESB Seminar.* Naval Facilities Engineering Service Center.

Mander, J.B., Priestley, M.J.N., and Park, R. (1988). "Theoretical Stress-Strain Model for Confined Concrete." *ASCE J. of Structural Engineering*, 114(8), 1804-1826.

McCormac, Jack C. (1978). *Design of Reinforced Concrete*. Harper and Row, New York, NY.

Merriam-Webster. (2014). "Resilience." Merriam-Webster, n.d. <http://www.merriam-webster.com/dictionary/resilience>.

Mirmiran, A. and Shahawy, M. (1995). "A novel FRP-concrete composite construction for the infrastructure." *Proc. of the ASCE Structures Congress XIII*. Boston, MA, 1663-1666.

Mirmiran, A. and Shahawy, M. (1996). "A new concrete-filled hollow FRP composite column." *Composites Part B: Engineering*, 27B(3-4), 263-268.

Mirmiran, A. and Shahawy, M. (1997). “Behavior of Concrete Columns Confined by Fiber Composites.” *J. of Structural Engineering*, ASCE, 123(5), 583-590.

Mirmiran, A., Shahawy, M., Khoury, C.E., and Naguib, W. (2000). "Large Beam-Column Tests on Concrete-Filled Composite Tubes." *ACI Structural J.*, 97(2), 268-276.

Mirmiran, A., Shahawy, M., and Samaan, M. (1999) "Strength and Ductility of Hybrid FRP-Concrete Beam-Columns." *J. of Structural Engineering*, ASCE, 125(10), 1085-1093.

Modjeski and Masters, Inc. (2003). *Comprehensive Design Example for Prestressed Concrete (PSC) Girder Superstructure Bridge with Commentary*. Federal Highway Administration, Arlington, VA.

Motaref, S., M. Saiidi, and D. Sanders. (2011). *Seismic Response of Precast Bridge Columns with Energy Dissipating Joints.* Report No. CCEER-11-1, University of Nevada, Reno.

Muszynski, L.C. and Purcell, M.R. (2003). "Composite Reinforcement to Strengthen Existing Concrete Structures against Air Blast." *J. of Composites for Construction,* 7(2), 93-97.

NOV Fiberglass Systems. (2009). "Red Thread II Piping Systems." National Oilwell Varco. <http://www.corrosionfluid.com/assets/pdf/smith-fibercast-red-thread-2-ii-fiberglass-pipe-piping-brochure.pdf>.

Omega. (2013). "High Temperature Inconel Overbraided Ceramic Fiber Insulated Thermocouples." Omega Engineering, Inc, Stamford, CT.

Pacific Earthquake Engineering Research Center (PEER). (2012). *OpenSees v2.4.2.* University of Califdornia, Berkeley. <http://opensees.berkeley.edu>.

Prasad, G.G. and Banerjee, S. (2013). "The Impact of Flood-induced Scour on Seismic Fragility Characteristics of Bridges." *J. of Earthquake Engineering,* Taylor and Francis, 17(6) 803-828.

Popovics, S. (1973). "A numerical approach to the complete stress-strain curve of concrete." *Cement and Concrete Research,* 3(5), 583-599.

Rokneddin, K., Ghosh, J., Duenas-Osorio, L., and Padgett, J.E. (2013). "Bridge retrofit prioritisation for ageing transportation newtworks subjected to seismic hazards." *Structure and Infrastructure Engineering: Maintenance, Management, Life-Cycle Design and Performance,*Taylor and Francis, 9(10), 1050-1066.

Saiidi, M., Sureshkumar, K., Pulido, C. (2005). "A simple model for confined concrete." *J. Structural Engineering,* 9(1):101-4.

Saiidi, M., A. Vosooghi, C. Cruz, S. Motaref, C. Ayoub, F. Kavianipour, and M. O'Brien. (2011). "Earthquake-Resistant Bridges of the Future with Advanced Materials," *Performance-Based Seismic Engineering- Vision for an Earthquake Resilient Society*.

Shao, Y. (2003). “Behavior of FRP- Concrete Beam-Columns under Cyclic Loading.” Ph.D Thesis, North Carolina State University, Raleigh, NC.

Shao, Y., Aval, A., and Mirmiran, A. (2005). “Fiber Element Model for Cyclic Analysis of Concrete-Filled FRP Tubes.” *J. of Structural Engineering*, ASCE, 131(2), 292-303.

Shao, Y. and Mirmiran, A. (2004). "Nonlinear Cyclic Response of Laminated Glass FRP Tubes Filled with Concrete." *J. of Composite Construction,* 65(1), 263-273.

Shao, Y. and Mirmiran, A. (2005). "Experimental Investigation of Cyclic Behavior of Concrete-Filled Fiber Reinforced Polymer Tubes." *J. of Composites for Construction*, 9(3), 263-273.

Sheikh, A.A. and Yau, G. (2002). “Seismic Behavior of Concrete Columns Confined with Steel and Fiber-Reinforced Polymers.” *ACI Structural J.,* ACI, 99(1), 72-80.

Shi, Y., Li, B., and Mirmiran, A. (2011). “Combined Shear and Flexural Behavior of Hybrid FRP-Concrete Beams Previously Subjected to Cyclic Loading,” *J. of Composites for Construction*, ASCE, 15(5), 841-849.

Shi, Y., Zohrevand, P., and Mirmiran, A. (2013). “Assessment of Cyclic Behavior of Hybrid FRP-Concrete Columns,” *J. of Bridge Engineering*, ASCE, 18(6), 553-563.

Simon, J., Bracci, J.M., and Gardoni, P. (2010). “Seismic Response and Fragility of Deteriorated Reinforced Concrete Bridges.” *J. of Structural Engineering,* ASCE, 136(10), 1273-1281.

Soshkin, Maksim. (2014). *Bridge & Tunnel Construction in the US*, IBISWorld Industry Report 234122014. IBISWorld, Santa Monica, CA.

Spacey, John. (2011). *Japan Talk.* <http://www.japan-talk.com/jt/new/21-scary-statistics-about-the-2011-japan-earthquake>.

Thermal Product Research (TPR^2). (2013). "Fireshell NFPA 286 Thermal Barrier Intumescent Coating." TPR^2. < http://www.tpr2.com/f10e.html>.

Timoshenko, S., Goodier, J.N. (1951). *Theory of Elasticity*. McGraw-Hill, Palo Alto, CA.

United Facilities Criteria (UFC). (2008). Structures to Resist the Effects of Accidental Explosions. Department of Defense, Washington, DC.

United States Army Corp of Engineers (USACE). (2007). *BlastX*. USACE, Vicksburg, MS.

USACE. (2012). *Methodology Manual for the Single-Degree-of-Freedom Blast Effects Design Spreadsheets (SBEDS).* Report No. PDC-TR-06-01 Rev 2. Vicksburg, MS.

USACE. (2004). *Bridge Explosive Loading (BEL)*. USACE, Vicksburg, MS.

Williams, II, G.D. (2009). *Analysis and Response Mechanisms of Blast-Loaded Reinforced Concrete Columns*. Thesis. University of Texas, Austin, TX.

Williams, G. and Williamson, E. (2011). "Response of Reinforced Concrete Bridge Columns Subjected to Blast Loads." *J. Struct. Eng. 137, SPECIAL ISSUE: Commemorating 10 Years of Research since 9/11,* 903–913.

Williams, G. and Williamson, E. (2012). "Procedure for Predicting Blast Loads Acting on Bridge Columns." *J. Bridge Eng*., 17(3), 490–499.

Williamson, E. and Marchand, K. (2006) "Recommendations for Blast-Resistant Design and Retrofit of Typical Highway Bridges". Structures Congress 2006: pp. 1-6.

Williamson, E.B., and Winget, D.G. (2005). "Risk Management and Design of Critical Bridges for Terrorist Attacks." *J. of Bridge Engineering,* ASCE, 10(1), 96-106

Williamson, E., Bayrak, O., Davis, C., and Williams, G. (2011a). "Performance of Bridge Columns Subjected to Blast Loads. I: Experimental Program." *J. Bridge Eng. 16,*

SPECIAL ISSUE: AASHTO-LRFD Bridge Design and Guide Specifications: Recent, Ongoing, and Future Refinements, 693–702.

Williamson, E., Bayrak, O., Davis, C., and Williams, G. D. (2011b). "Performance of Bridge Columns Subjected to Blast Loads. II: Results and Recommendations." *J. Bridge Eng. 16, SPECIAL ISSUE: AASHTO-LRFD Bridge Design and Guide Specifications: Recent, Ongoing, and Future Refinements,* 703–710.

Williamson, E.B., Bayrakk, O., Williams, G.D., Davis,C.E., Marchand, K.A., McKay, A.E., Kulicki, J., and Wassef, W. (2010). *NCHRP Report 465: Blast-Resistant Highway Bridges: Design and Detailing Guidelines*. Transportation Research Board (TRB), Washington D.C.

Williamson, E.B, Summarco, E.L., Hendryx, R., and Bui, J.Q. (2011). *Anti-Terrorist Planner for Bridges*. US Army Corp of Engineers, Vicksburg, MS.

Winget, D., Marchand, K., and Williamson, E. (2005a). "Analysis and Design of Critical Bridges Subjected to Blast Loads." J. Struct. Eng., 131(8), 1243–1255.

Winget, D.G., Williamson, E.B., Marchand, K.A., Gannon, J.C. (2005b). "Recommendations for Blast Design and Retrofit of Typical Highway Bridges." *J. of the Transportation Research Board,* TRB, CD 11-S, 1-8.

Zaghi, A., and M. Saiidi. (2010a) "Seismic Performance of Pipe-Pin Two-Way Hinges in Concrete Bridge Columns," *J. of Earthquake Engineering*, 14(8): 1253-1302.

Zaghi, A.E., Saiidi, M. (2010b). Report No. CCEER-10-1: Seismic Design of Pip-Pin Connections in Concrete Bridges. Univeristy of Nevada, Reno, NV.

Zaghi, A.E., Saiidi, M, and Mirmiran, A. (2012). "Shake table response and analysis of a concrete-filled FRP tube bridge column." *Composite Structures,* Elsevier, 94(5), 1564-1574.

Zaidi, K.A., Sharma, U.K., Bhandari, N.M. (2012). "Effect of temperature on uni-axial compressive behavior of confined concrete." *Fire Safety Journal*, 48, 58-68.

Zhu, Z., Ahmad, I., and Mirmiran, A. (2006a). "Fiber Element Modeling for Seismic Performance of Bridge Columns Made of Concrete-Filled FRP Tubes," *Engineering Structures*, Elsevier, 28(14), 2023-2035.

Zhu, Z., Ahmad, I., and Mirmiran, A. (2006b). "Seismic Performance of Concrete-Filled FRP Tube Columns for Bridge Substructure." *J. of Bridge Engineering*, ASCE, 11(3), 359-370

Zohrevand, P. and Mirmiran, A. (2013). "Seismic Response of Ultra-High Performance Concrete-Filled FRP Tube Columns." J. of Earthquake Engineering, Taylor and Francis, 17(1), 155-170.

TABLES

Table 2-1. Mechanical Properties of Concrete and Steel Materials

Material	**ksi (MPa)**
28 Day Concrete Compressive Strength	3.33 (23.0)
100 Day Concrete Compressive Strength	3.39 (23.4)
1 Year Concrete Compressive Strength	4.67 (32.3)
Steel Rebar Yield Stress	58.7 (405)
Steel Rebar Ultimate Stress	93.7 (646)
Steel Spiral Yield Stress	78.6 (542)
Steel Spiral Ultimate Stress	90.4 (623)

Table 2-2. Mechanical Properties of FRP Tube

Mechanical Property	**75°F (24°C) ksi (MPa)**	**210°F (99°C) ksi (MPa)**
Ultimate Tensile Stress	10.3 (71.0)	7.7 (53.0)
Tensile Modulus of Elasticity	1820 (12,550)	1210 (8343)
Ultimate Compressive Stress	33.0 (228)	19.4 (134)
Compressive Modulus of Elasticity	1260 (8687)	600 (4137)
Ultimate Bending Stress	23.0 (159)	16.0 (110)
Bending Modulus of Elasticity	1460 (10,066)	960 (6630)
Ultimate Hoop Stress	34.0 (234)	43.5 (300)

Table 2-3. Final Parameters for Blast Tests

Test No.	**Column Type**	**Load Intensity Ratio, LIR**	**Charge Wt, W [lbs TNT]**	**Standoff, R [ft]**	**Scaled Standoff, Z [ft/lb$^{1/3}$]**
1	RC	41.1	0.467W	R	1.23
2	RC	32.9	0.6W	R	1.14
3	RC	55.6	0.833W	R	1.02
4	CFFT	41.1	0.733W	R	1.06
5	CFFT	32.9	W	R	0.958

Table 2-4. Analytical Displacement Predictions for Blast Tests

	RC Tests						CFFT Tests	
	Moderate		Severe		Severe-2		Mod.	Severe
	ATP-Bridge	Open-Sees	ATP-Bridge	Open-Sees	ATP-Bridge	Open-Sees	Open-Sees	Open-Sees
$\delta_{PK,}$ in. (mm)	1.52 (38.7)	0.200 (5.08)	2.36 (59.8)	0.291 (7.39)	3.43 (87.3)	0.556 (14.1)	0.250 (6.35)	0.369 (9.38)
δ_{RES}, in. (mm)	1.24 (31.5)	0.017 (0.442)	2.07 (52.7)	0.111 (2.82)	3.15 (80.1)	0.323 (8.20)	0.013 (0.330)	0.035 (0.889)

Table 3-1. Experimental Peak Midspan Displacements

	RC Tests			CFFT Tests	
	Moderate	**Severe**	**Severe-2**	**Moderate**	**Severe**
$\delta_{PK,}$ in.	0.538	1.58	--	0.753	2.85
(mm)	(13.7)	(40.1)	(--)	(19.1)	(72.4)

Table 3-2. Experimental and BlastX Pressure Comparison

	RC Tests						CFFT Tests	
	Moderate		**Severe**		**Severe-2**		**Mod.**	**Severe**
	Exp.	**BlastX**	**Exp.**	**BlastX**	**Exp.**	**BlastX**	**Exp.**	**BlastX**
$t_{a,X}$, ms	--	0.908	0.636	0.846	0.646	0.766	0.558	0.795
$P_{PK,X}$, psi	--	136.5	135.3	164.52	193.4	213.4	225.6	193.5
(MPa)	(--)	(0.941)	(0.932)	(1.13)	(1.33)	(1.47)	(1.56)	(1.33)
$t_{a,Y}$, ms	--	1.72	1.01	1.59	1.32	1.43	1.38	1.35
$P_{PK,Y}$, psi	--	60.3	71.6	72.8	98.0	97.3	108.9	113.9
(MPa)	(--)	(0.416)	(1.18)	(1.18)	(0.675)	(0.671)	(0.751)	(0.785)

Table 4-1. Axial Capacity Testing Load Protocol

Step	Control Type	Increment
1	Load	+50kip (+222kN)
2	Load	+50kip (+222kN)
3	Load	+50kip (+222kN)
4	Load	+50kip (+222kN)
5	Load	+50kip (+222kN)
6	Displacement	+0.1in. (+2.54mm)
7	Displacement	+0.2in. (+5.08mm)
8	Displacement	+0.2in. (+5.08mm)
9	Displacement	+0.25in. (+6.35mm)
10	Displacement	To Failure

Table 4-2. Summary of Axial Capacity Tests of Blast Damaged RC Columns

	RC Specimens		
	Benchmark	**Moderate**	**Severe**
Yield Displacement, in. (mm)	0.096 (2.44)	0.096 (2.44)	0.096 (2.44)
Ultimate Displacement, in. (mm)	0.471 (12.0)	0.235 (5.98)	0.299 (7.59)
Ultimate Ductility	4.90	2.45	3.12
Ultimate Axial Capacity, kip (kN)	247.0 (1099)	235.8 (1049)	259.6 (1155)
Axial Capacity at μ_D=3, kip (kN)	238.5 (1061)	157.9 (702.6)	231.8 (1031)
Axial Capacity at μ_D=4, kip (kN)	240.8 (1071)	80.9 (360)	74.4 (331)

Table 4-3. Summary of Axial Capacity Tests of Blast Damaged CFFT Columns

	CFFT Specimens		
	Benchmark	**Moderate**	**Severe**
Yield Displacement, in. (mm)	0.096 (2.44)	0.096 (2.44)	0.096 (2.44)
Ultimate Displacement, in. (mm)	1.53 (38.9)	1.37 (34.9)	1.09 (27.7)
Ultimate Ductility	15.9	14.3	11.4
Ultimate Axial Capacity, kip (kN)	334.4 (1488)	321.9 (1432)	319.9 (1423)
Axial Capacity at μ_D=9.75, kip (kN)	317.4 (1412)	309.1 (1375)	304.6 (1355)
Axial Capacity at μ_D=13, kip (kN)	329.1 (1464)	313.6 (1395)	157.4 (700)

Table 4-4. Summary of Axial Capacity Results of Fire Damaged RC Specimens

	RC Specimens		
	Benchmark	**1-Hr**	**2-Hr**
Yield Displacement, in. (mm)	0.096 (2.44)	0.096 (2.44)	0.096 (2.44)
Ultimate Displacement, in. (mm)	0.471 (12.0)	5.98 (0.235)	7.59 (0.299)
Ultimate Ductility	4.90	4.27	6.44
Ultimate Axial Capacity, kip (kN)	247.0 (1099)	238 (1058)	187 (834)
Axial Capacity at μ_D=3, kip (kN)	238.5 (1061)	218.9 (937.9)	161.5 (718.4)
Axial Capacity at μ_D=4, kip (kN)	240.8 (1071)	206.8 (919.9)	175.8 (781.8)
Initial Axial Stiffness, k/in (kN/mm)	2413 (423)	1406 (246)	808 (142)

Table 4-5. Summary of Axial Capacity Results of Fire Damaged CFFT Specimens

	CFFT Columns		
	Benchmark	**1-Hr**	**2-Hr**
Yield Displacement, in. (mm)	0.096 (2.44)	0.096 (2.44)	0.096 (2.44)
Ultimate Displacement, in. (mm)	1.53 (38.9)	5.98 (0.235)	7.59 (0.299)
Ultimate Ductility	15.9	11.9	13.5
Ultimate Axial Capacity, kip (kN)	334.4 (1488)	321.3 (1429)	353.9 (1574)
Axial Capacity at μ_D=9.75, kip (kN)	317.4 (1412)	317.2 (1411)	317.9 (1414)
Axial Capacity at μ_D=13, kip (kN)	329.1 (1464)	256.1 (1139)	353.8 (1574)
Initial Axial Stiffness, k/in (kN/mm)	2377 (416)	2529 (443)	1772 (310)

Table 5-1. Experimental and Analytical Peak Strain Comparisons

	Experimental Strains (με)		Analytical Strains (με)	
	$\varepsilon_{t,\,Peak}$	$\varepsilon_{c,\,Peak}$	$\varepsilon_{t,\,Peak}$	$\varepsilon_{c,\,Peak}$
RC-Moderate	3824	N/A	4630	-2196
RC-Severe	8508	-2324	7126	-3122
RC-Severe-2	16,038	-6690	14,365	-5580
CFFT-Moderate	12,199	N/A	10,146	-4257
CFFT-Severe	18,054	-3868	16,114	-6938

Table 5-2. Dynamic Increase Factors for the Concrete Materials for RC Tests

	Strain Rate (s^{-1})	CEB Formulation DIF (Malvar and Crawford, 1998b)	DIF for Cover from the Analytical Model	DIF for Core from the Analytical Model
RC-Moderate	5.346	1.621	2.228	1.614
RC-Severe	6.734	1.636	2.366	1.675
RC-Severe-2	21.477	1.714	2.550	1.760

Table 5-3. Summary of Axial Capacity Results of Earthquake Damaged RC Models

	RC Model		
	No Motion	4% Drift	7% Drift
Yield Displacement, in. (mm)	0.096 (2.44)	0.096 (2.44)	0.096 (2.44)
Ultimate Displacement, in. (mm)	0.506 (12.9)	0.365 (9.27)	0.272 (6.90)
Ultimate Ductility	5.27	3.80	2.83
Ultimate Axial Capacity, kip (kN)	253.7 (1129)	253.7 (1128)	243.9 (1085)
Axial Capacity at μ_D=3, kip (kN)	253.6 (1128)	253.3 (1127)	138.3 (615.2)
Axial Capacity at μ_D=4, kip (kN)	250.9 (1116)	139.7 (621.4)	87.2 (387.9)
Initial Axial Stiffness, k/in (kN/mm)	3566 (625)	3207 (562)	2812 (492)

Table 5-4. Summary of Axial Capacity Results of Earthquake Damaged CFFT Models

	CFFT Columns		
	No Motion	**4% Drift**	**7% Drift**
Yield Displacement, in. (mm)	0.096 (2.44)	0.096 (2.44)	0.096 (2.44)
Ultimate Displacement, in. (mm)	1.44 (36.5)	1.43 (36.3)	0.780 (19.8)
Ultimate Ductility	15.0	14.9	8.12
Ultimate Axial Capacity, kip (kN)	363.7 (1618)	363.5 (1617)	331.3 (1474)
Axial Capacity at μ_D=9.75, kip (kN)	317.4 (1412)	317.2 (1411)	--
Axial Capacity at μ_D=13, kip (kN)	329.1 (1464)	256.1 (1139)	--
Initial Axial Stiffness, k/in (kN/mm)	3846 (674)	2729 (478)	2512 (440)

Table 5-5. Comparison of Axial and Flexural Capacities Obtained from Cross Section Analysis and Proposed Design Equations

	Steel Ratio, ρ_s									
	0.002		**0.006**		**0.008**		**0.01**		**0.016**	
	Sect. Anal.	**Design Eq.**	**Sect. Anal.**	**Design Eq.**	**Sect. Anal.**	**Design Eq.**	**Sect. Anal.**	**Design Eq.**	**Sect. Anal.**	**Design Eq.**
$\bar{\mathbf{P}}$	1.521	1.536	1.589	1.608	1.629	1.644	1.663	1.680	1.771	1.788
$\bar{\mathbf{M}}_{\mathbf{ALI=0\%}}$	0.150	0.149	0.176	0.177	0.191	0.191	0.205	0.205	0.245	0.247
$\bar{\mathbf{M}}_{\mathbf{ALI=5\%}}$	0.164	0.165	0.189	0.192	0.205	0.205	0.218	0.218	0.257	0.256
$\bar{\mathbf{M}}_{\mathbf{ALI=10\%}}$	0.178	0.178	0.202	0.204	0.217	0.217	0.229	0.229	0.263	0.264
$\bar{\mathbf{M}}_{\mathbf{ALI=15\%}}$	0.190	0.188	0.212	0.214	0.224	0.226	0.236	0.238	0.269	0.270
$\bar{\mathbf{M}}_{\mathbf{ALI=20\%}}$	0.197	0.196	0.218	0.222	0.230	0.233	0.241	0.244	0.273	0.273

Note: $\bar{\mathbf{P}} = P_n/(f'_c A_g)$

$\bar{\mathbf{M}} = M_n/(f'_c A_g D)$

FIGURES

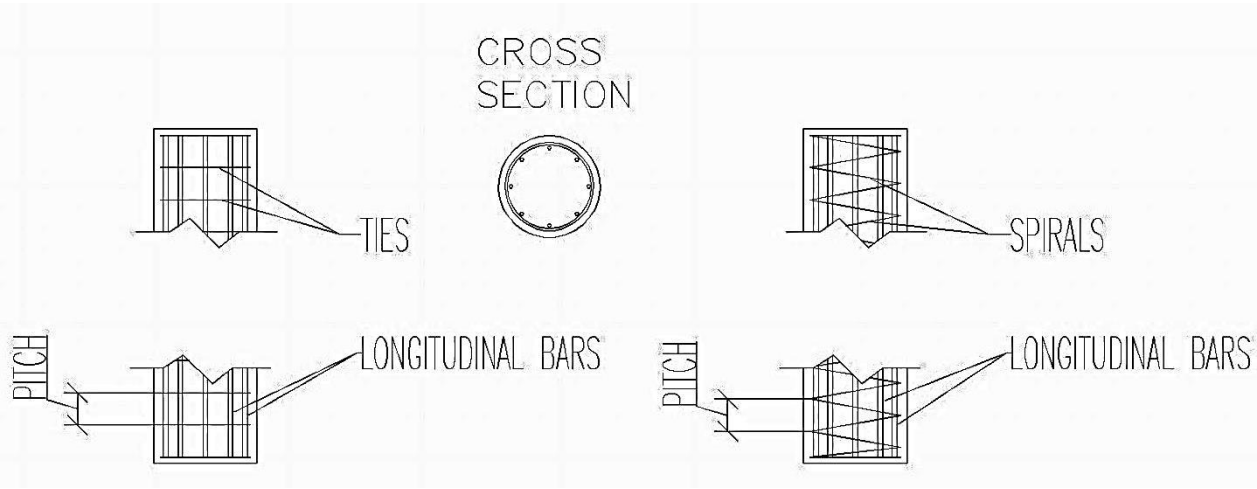

Figure 2-1 Conventional Circular Column Reinforcement: Ties (left) or Spiral (right)

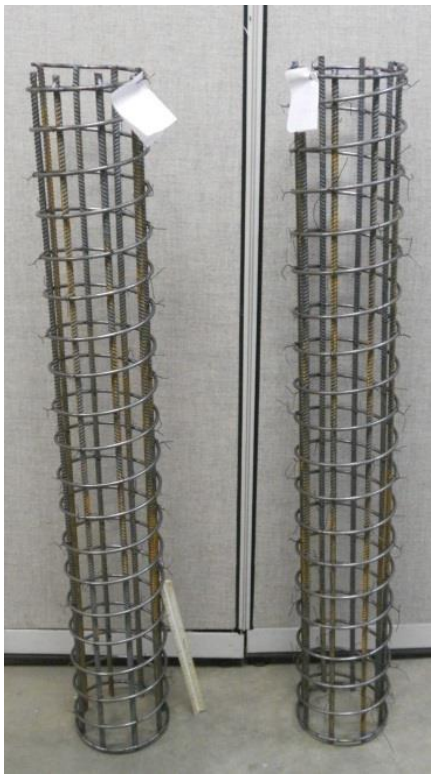

Figure 2-2 RC Column Reinforcement Cages

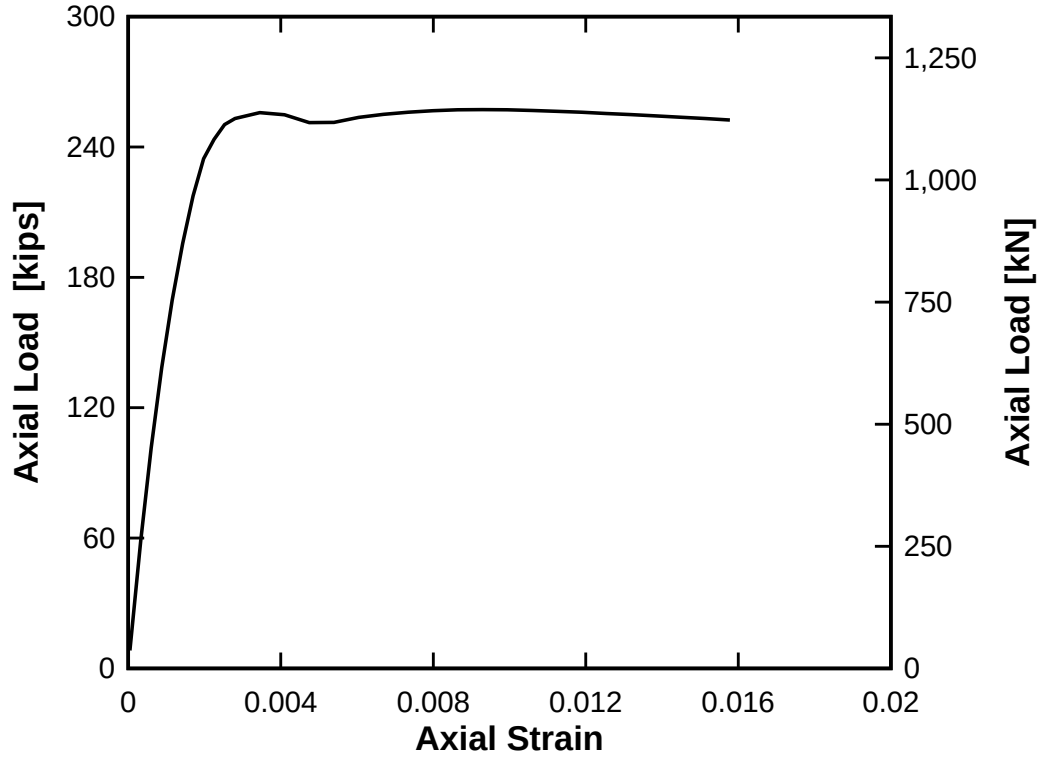

Figure 2-3 XTract Axial Load-Strain Relationship for RC Design

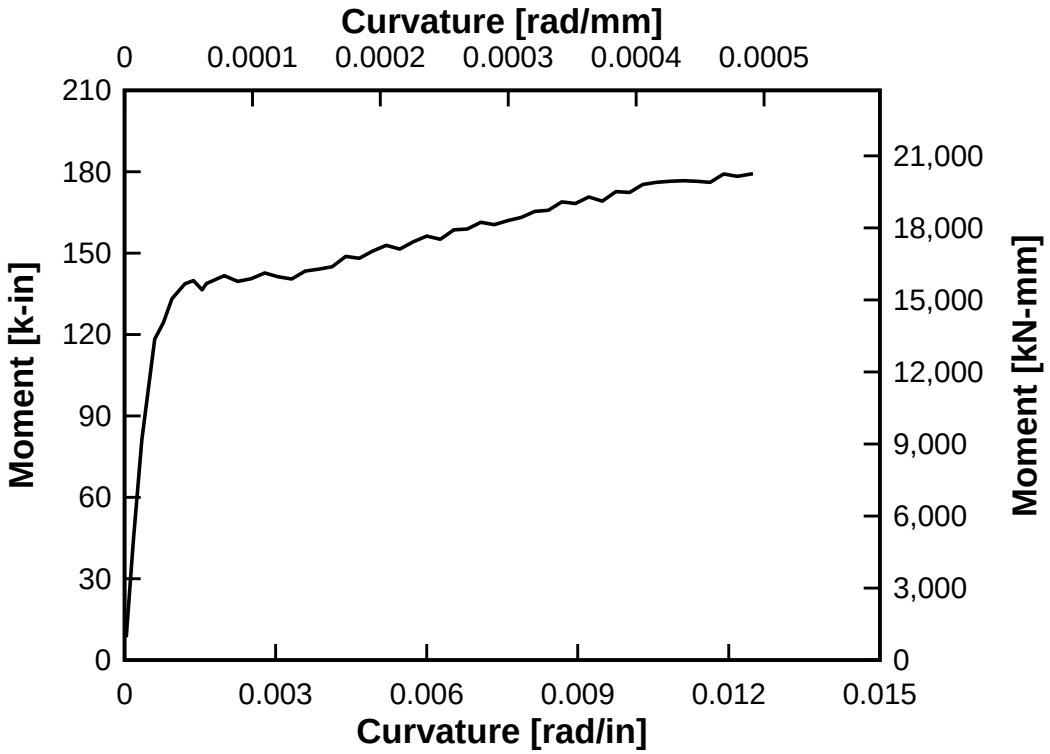

Figure 2-4 XTract Moment-Curvature for RC Design

Figure 2-5 CFFT Rebar Cages

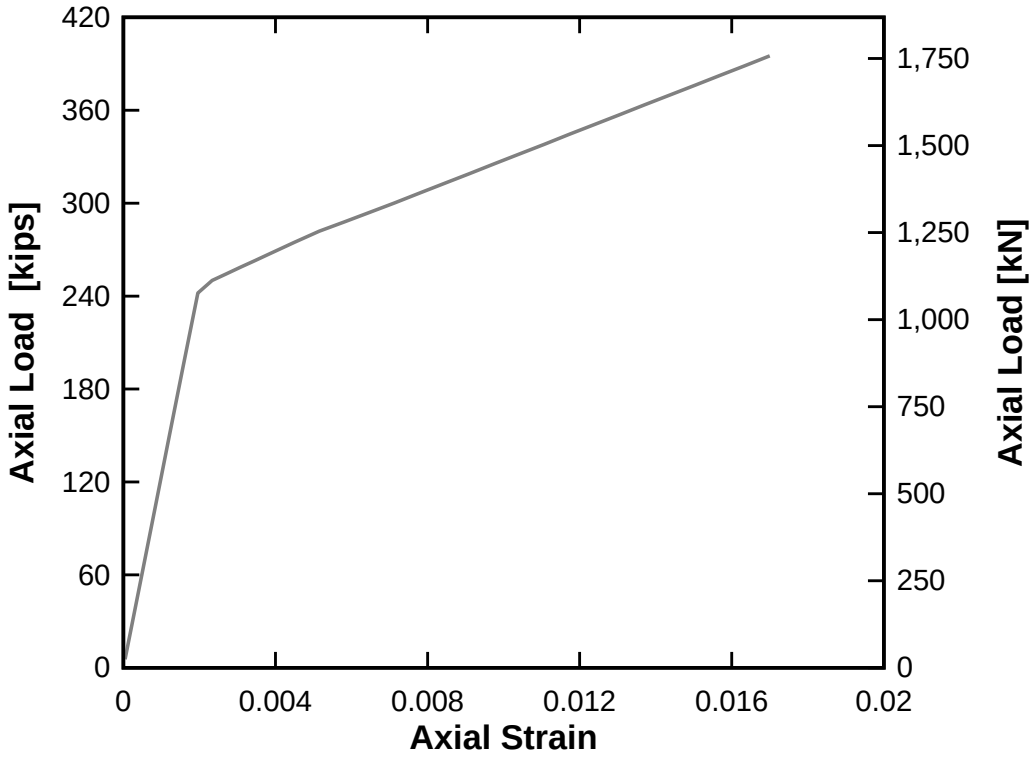

Figure 2-6 XTract Axial Load-Strain Relationship for CFFT Design

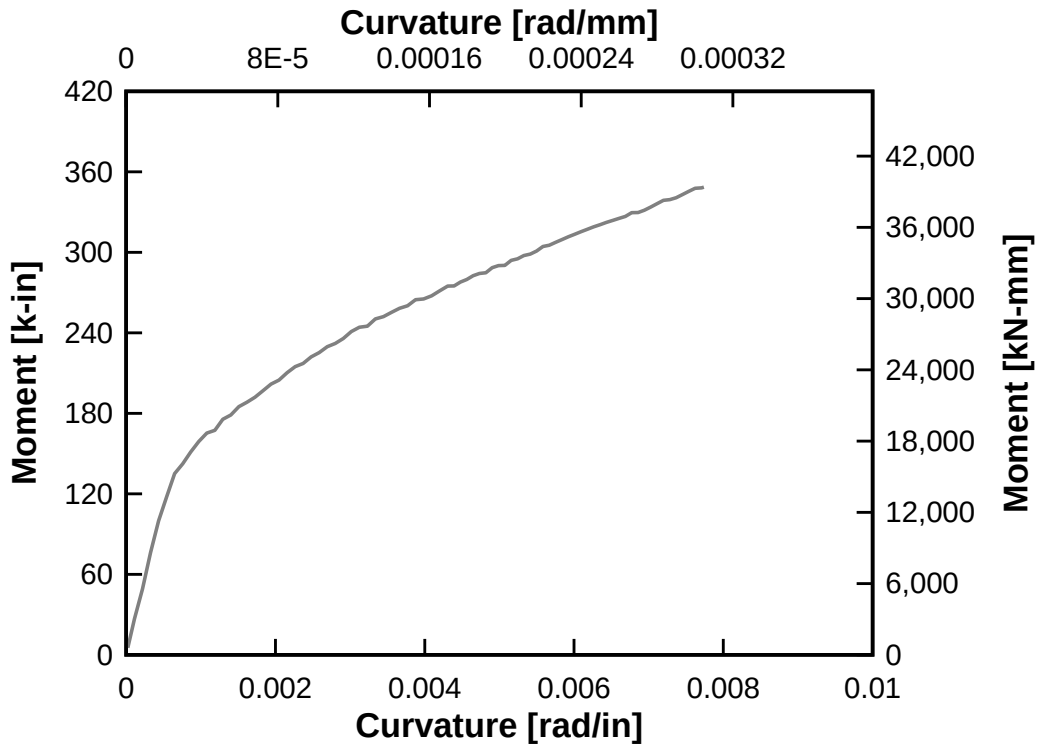

Figure 2-7 XTract Axial Moment-Curvature Relationship for CFFT Design

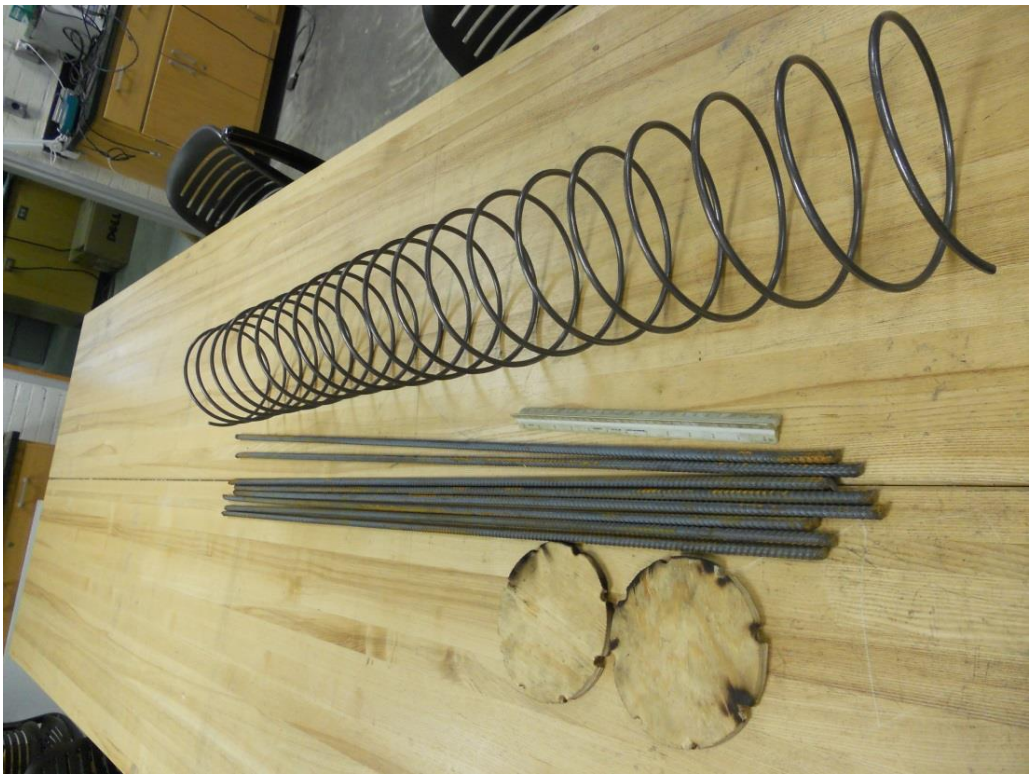

Figure 2-8 Reinforcement Cage Materials Prior to Fabrication

Figure 2-9 Installed Strain Gauge

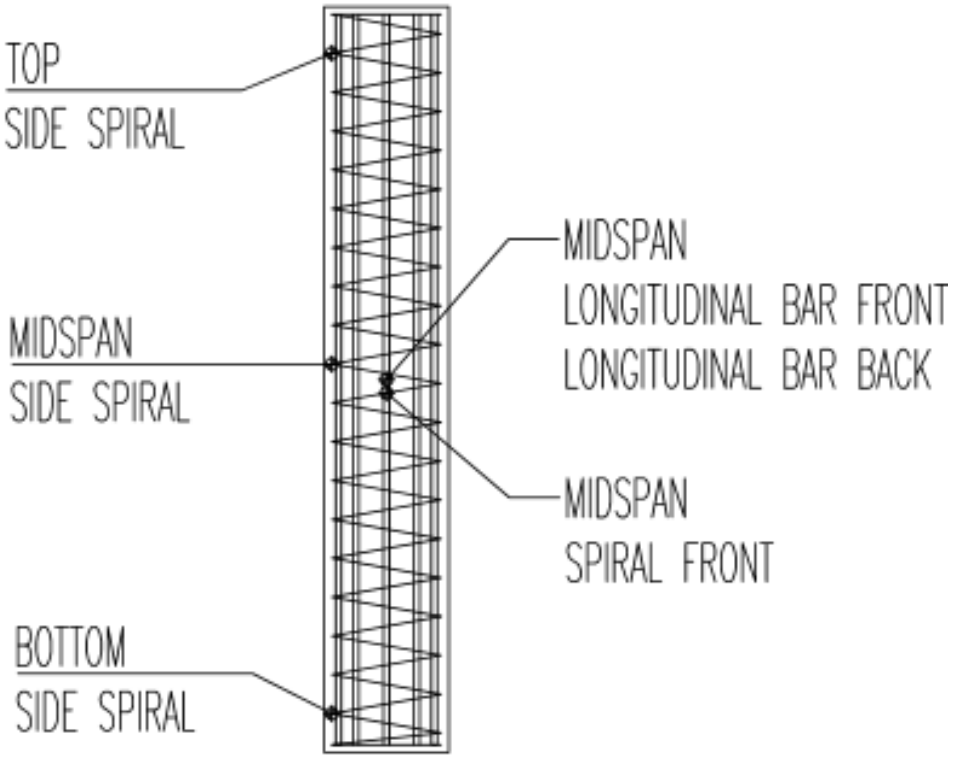

Figure 2-10 Strain Gauge Locations for RC Blast Specimens

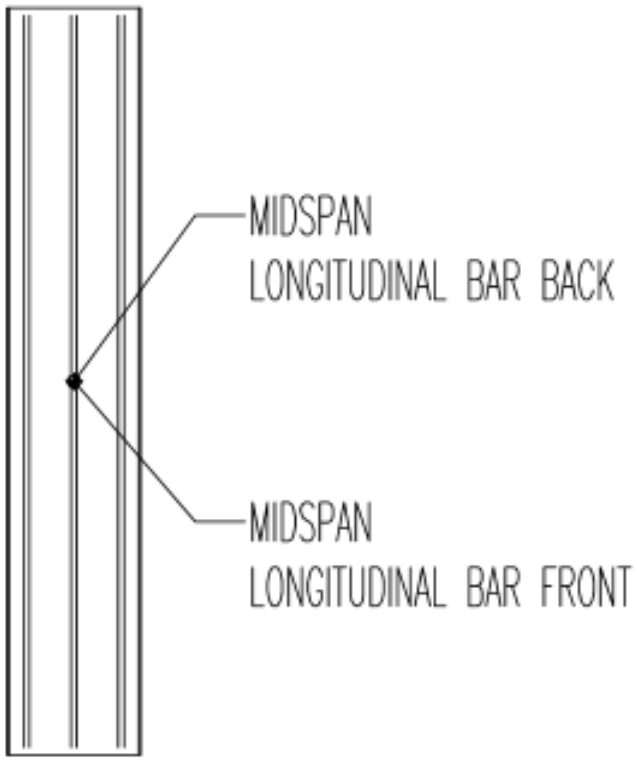

Figure 2-11 Strain Gauge Locations for CFFT Blast Specimens

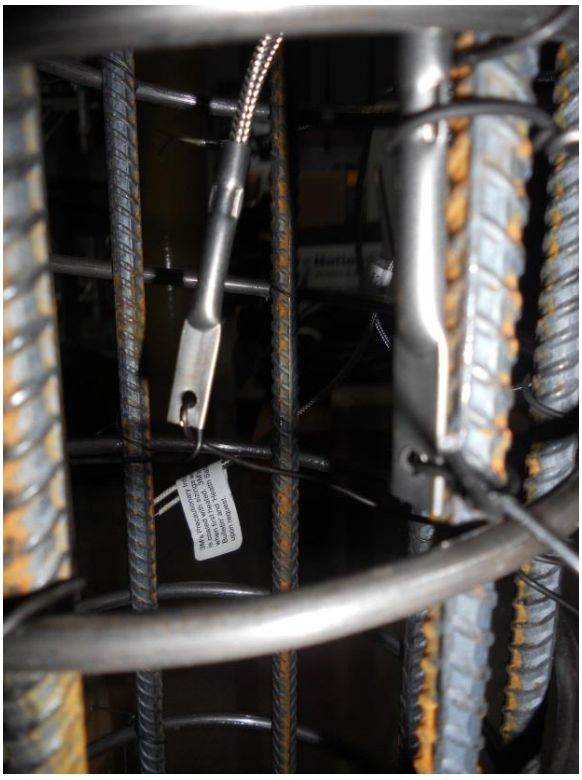

Figure 2-12 Installed Thermocouples

Figure 2-13 Wooden Frame Work, Sonotubes, and FRP Tubes

Figure 2-14 RC Rebar Cage inside Sonotube

Figure 2-15 CFFT Rebar Cage inside FRP Tube

Figure 2-16 Complete Column Construction

Figure 2-17 Test Cylinders

Figure 2-18 Fire Protection Primer Application

Figure 2-19 Spray Appplication of Fire Protection System

Figure 2-20 Wire to Check Fire Protection Material Thickness

Figure 2-21 CFFT Columns with Appplied Fire Protection

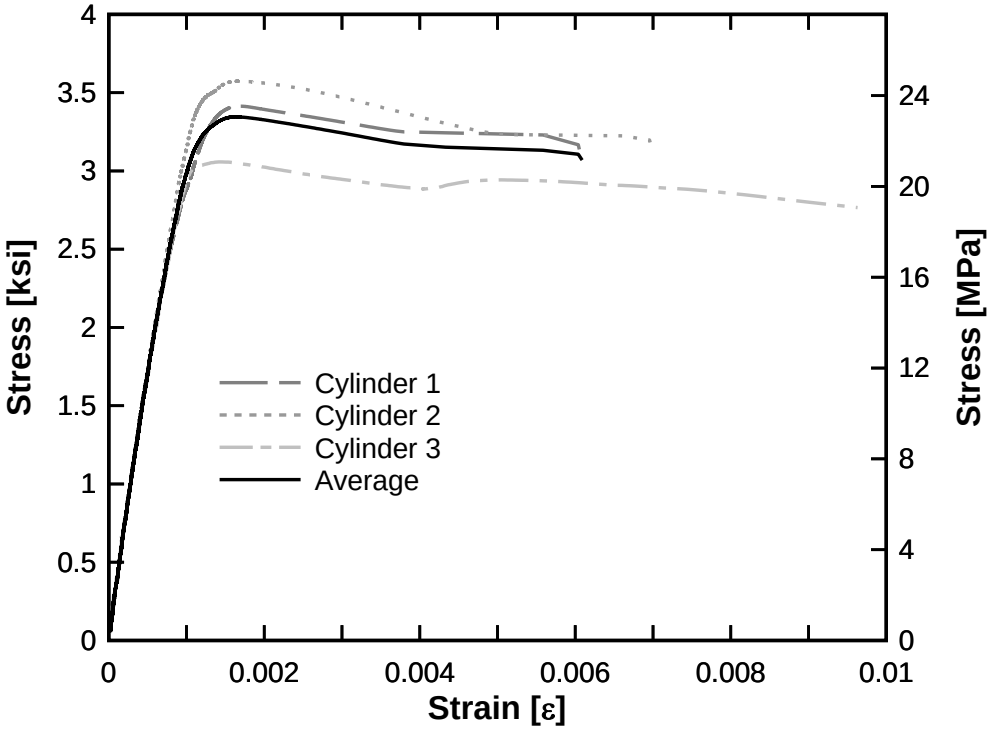

Figure 2-22. 100-Day Compressive Stress Strain Curves for Concrete

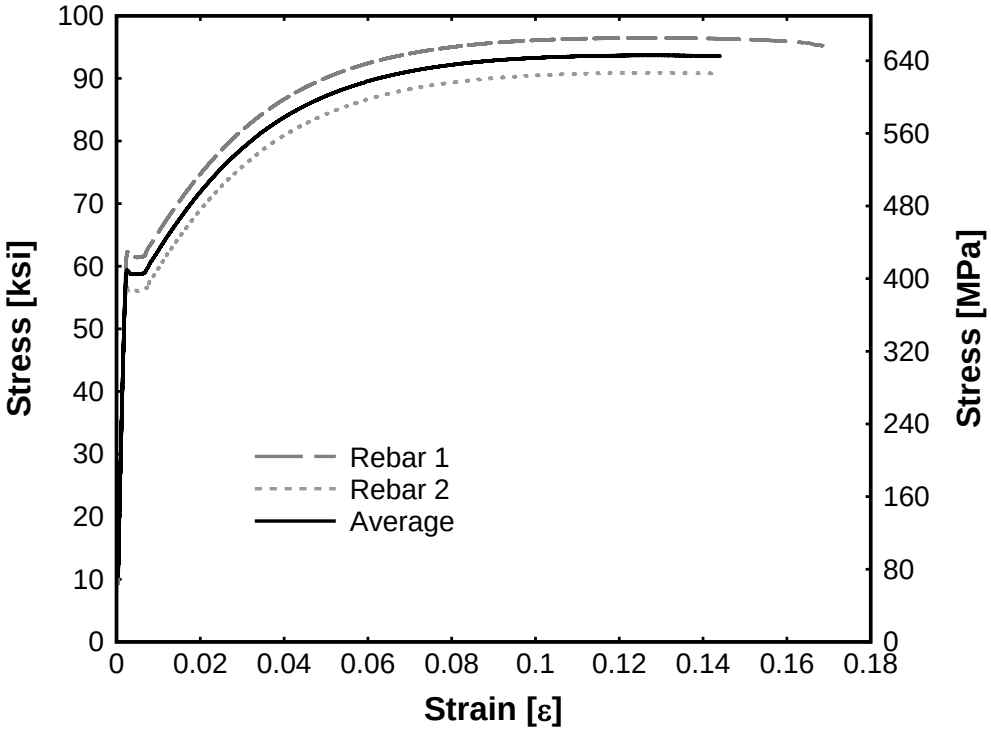

Figure 2-23. Stress Strain Curves of Rebar Reinforcement

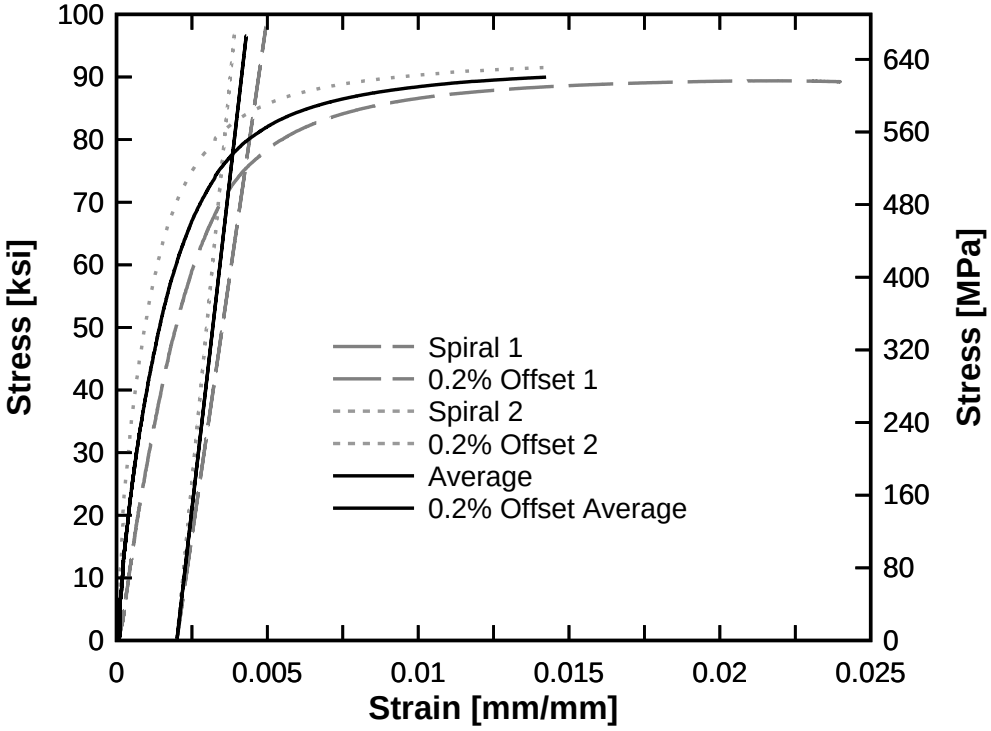

Figure 2-24. Stress Strain Curves of Spiral Reinforcement

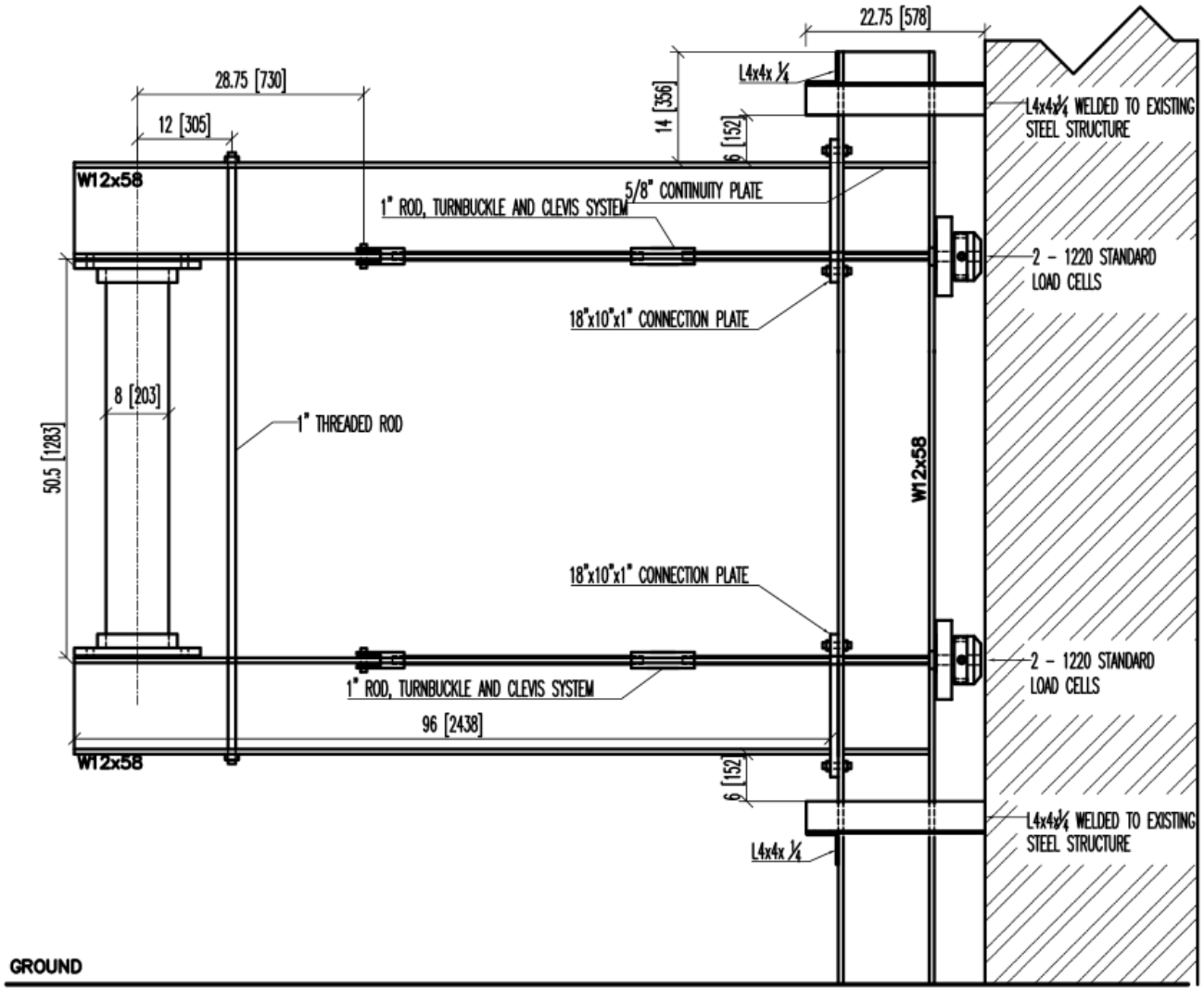

Figure 2-25. Side View of Blast Test Frame

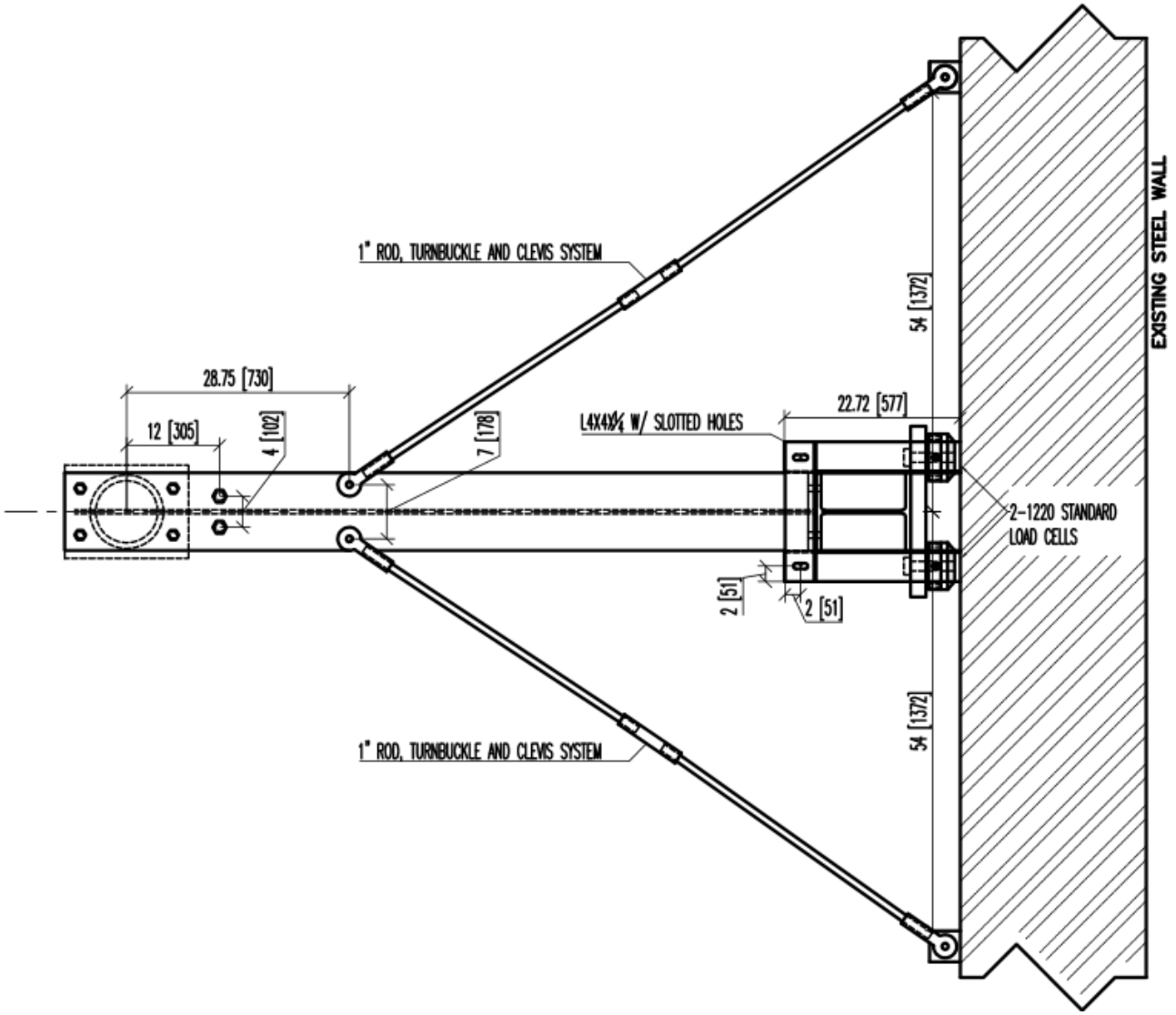

Figure 2-26. Top View of Blast Test Frame

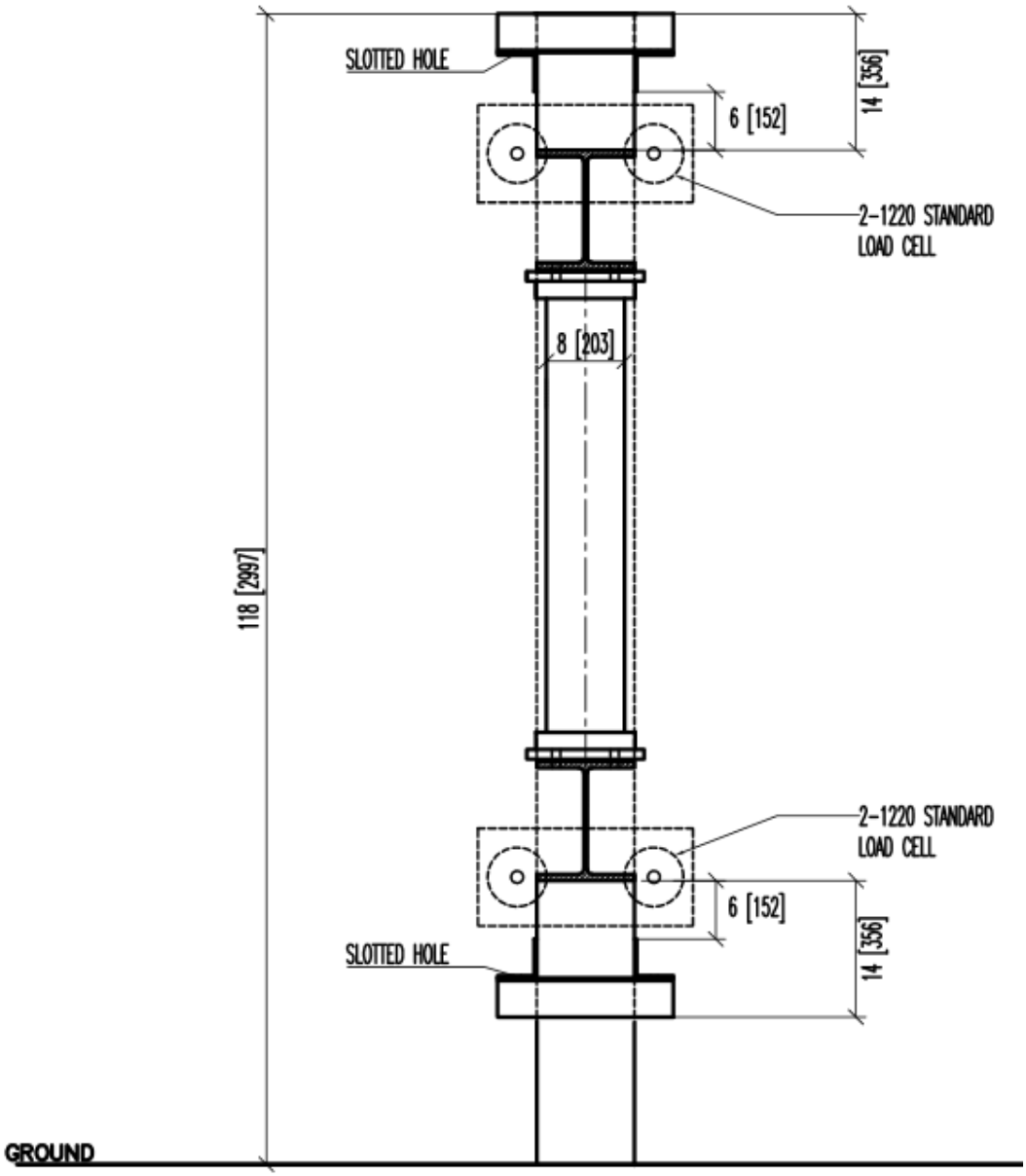

Figure 2-27. Front View of Blast Test Frame

Figure 2-28. Dismantled Test Frame as Delivered to ERDC

Figure 2-29. Reassembled Test Frame at Big Black Test Site

Figure 2-30. Two Loads Cells in Contact with Reaction Structure

Figure 2-31. Rack-and-Pinion Displacement Gauge Set-Up

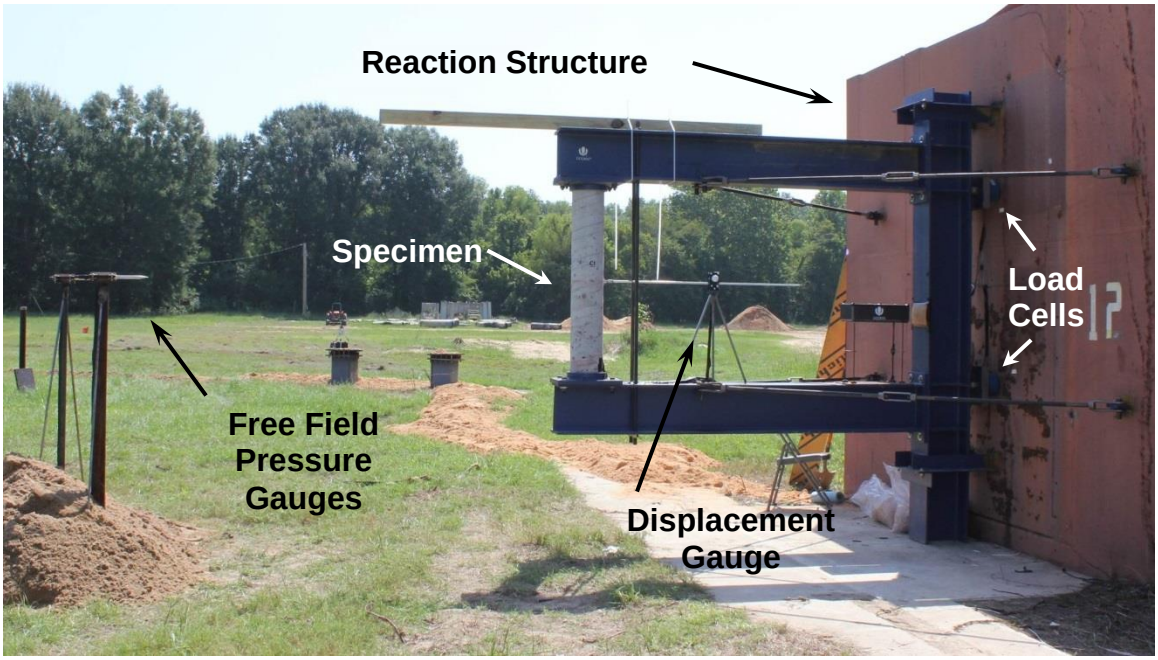

Figure 2-32. Complete Blast Test Set-Up

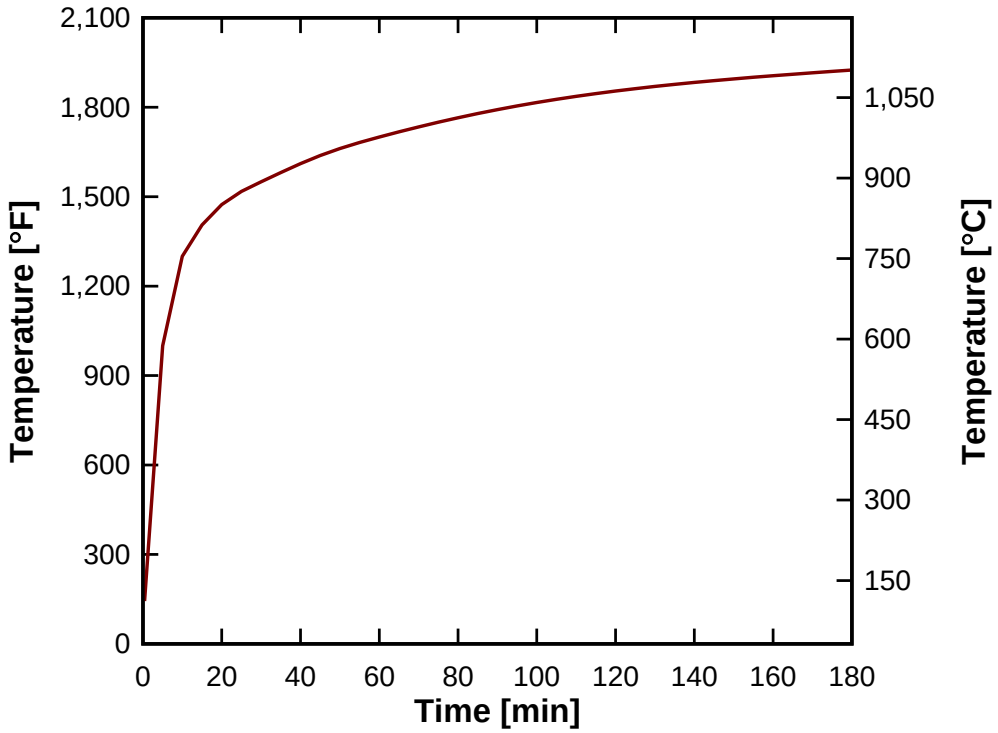

Figure 2-33. ASTM E119 Temperature Curve

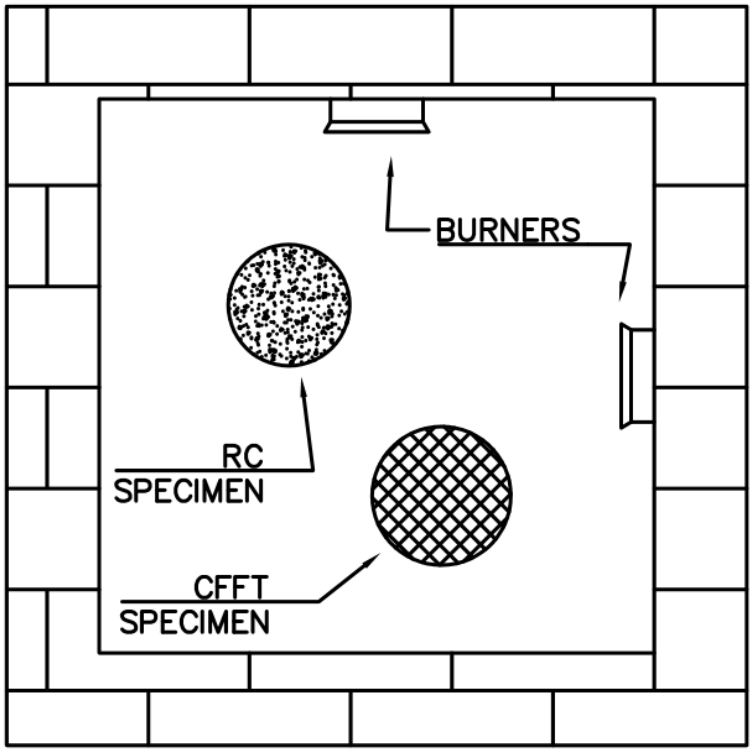

Figure 2-34. Schematic of Fire Test Set-Up


Figure 2-35. Schematic of Fire Test Set-Up

Figure 3-1 RC Moderate Pre-Test: Top front, back, right, and left (top photos). Bottom front, back, right and left (bottom photos)

Figure 3-2 RC Moderate Post-Test: Top front, back, right, and left (top photos). Bottom front, back, right and left (bottom photos).

Figure 3-3 RC Severe Pre-Test: Top front, back, right, and left (top photos). Bottom front, back, right and left (bottom photos)

Figure 3-4 RC Severe Post-Test: Top front, back, right, and left (top photos). Bottom front, back, right and left (bottom photos)

Figure 3-5 RC-Severe-2 Post-Test: Top front, back, right, and left (top photos). Bottom front, back, right and left (bottom photos)

Figure 3-6 CFFT Moderate Threat Pre-Test: Top front, back, right, and left (top photos). Bottom front, back, right and left (bottom photos)

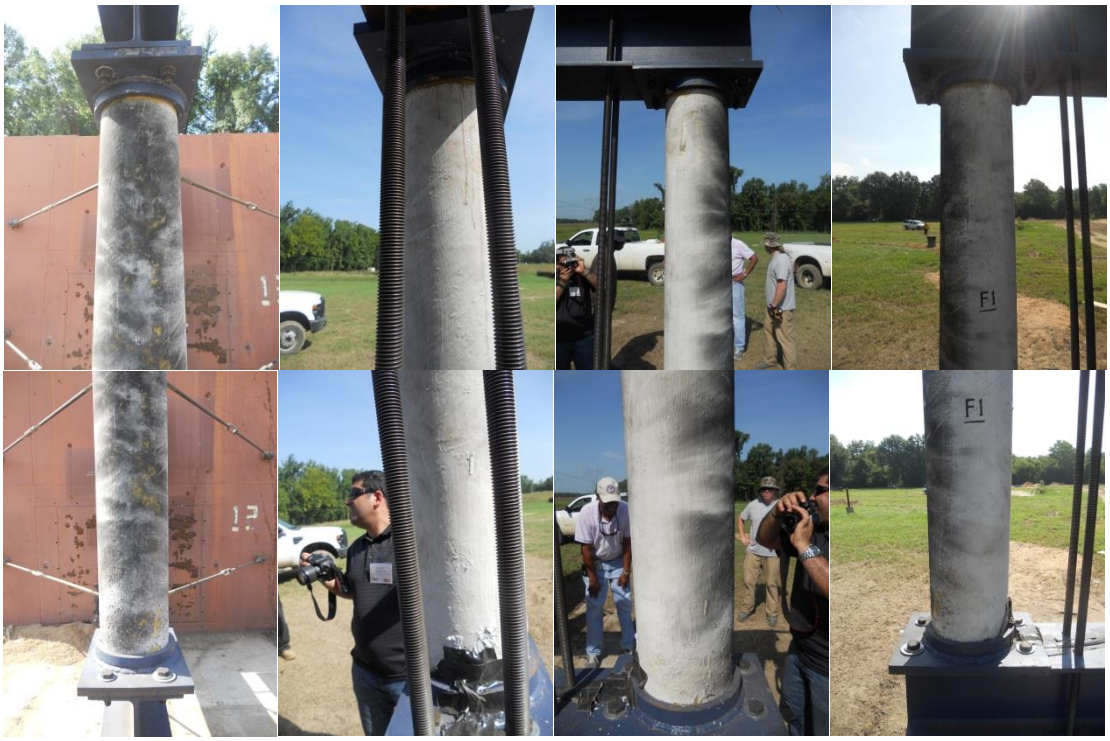

Figure 3-7 CFFT Moderate Threat Post-Test: Top front, back, right, and left (top photos). Bottom front, back, right and left (bottom photos)

Figure 3-8 CFFT Severe Threat Pre-Test: Top front, back, right, and left (top photos). Bottom front, back, right and left (bottom photos)

Figure 3-9 CFFT Severe Threat Post-Test: Top front, back, right, and left (top photos). Bottom front, back, right and left (bottom photos)

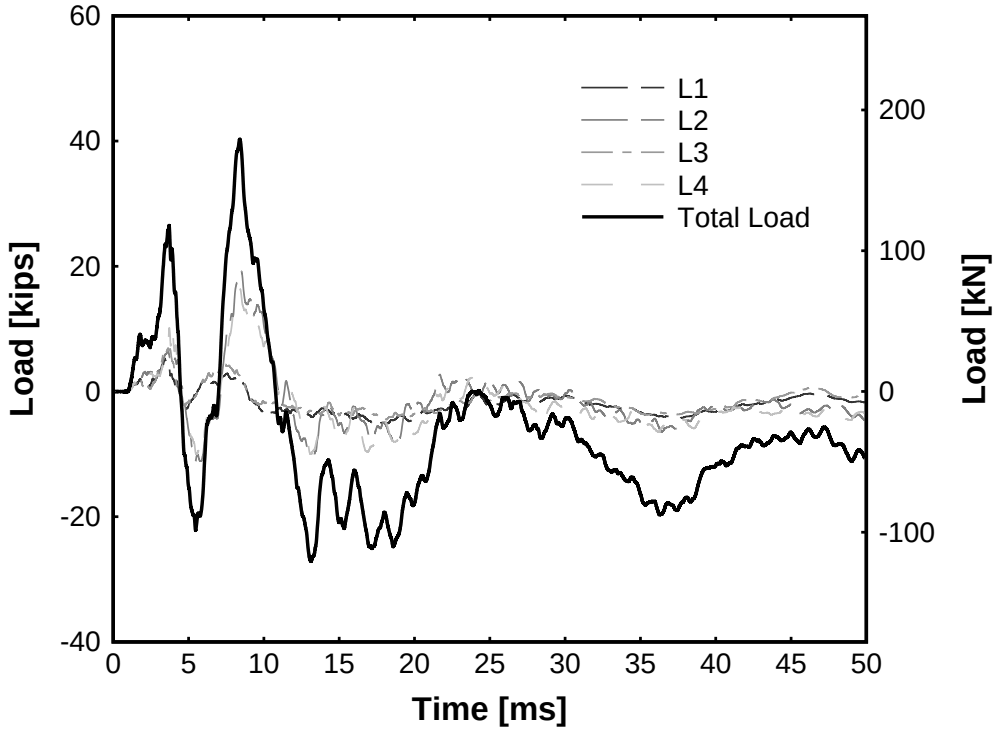

Figure 3-10. RC-Moderate Test Load Cell Data

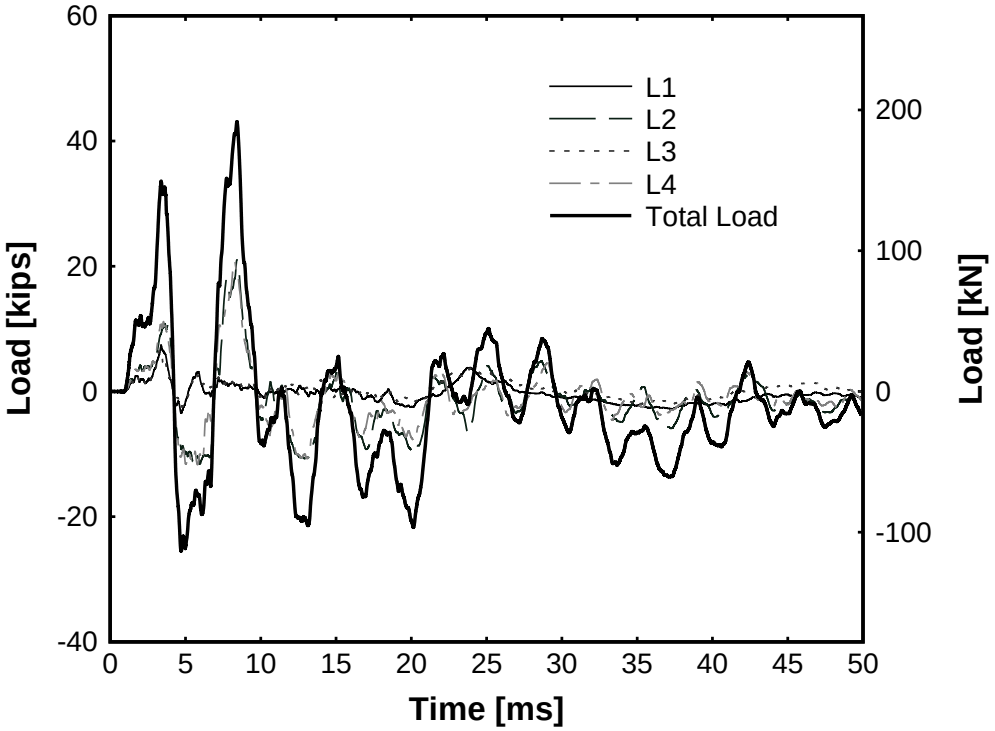

Figure 3-11. RC-Severe Test Load Cell Data

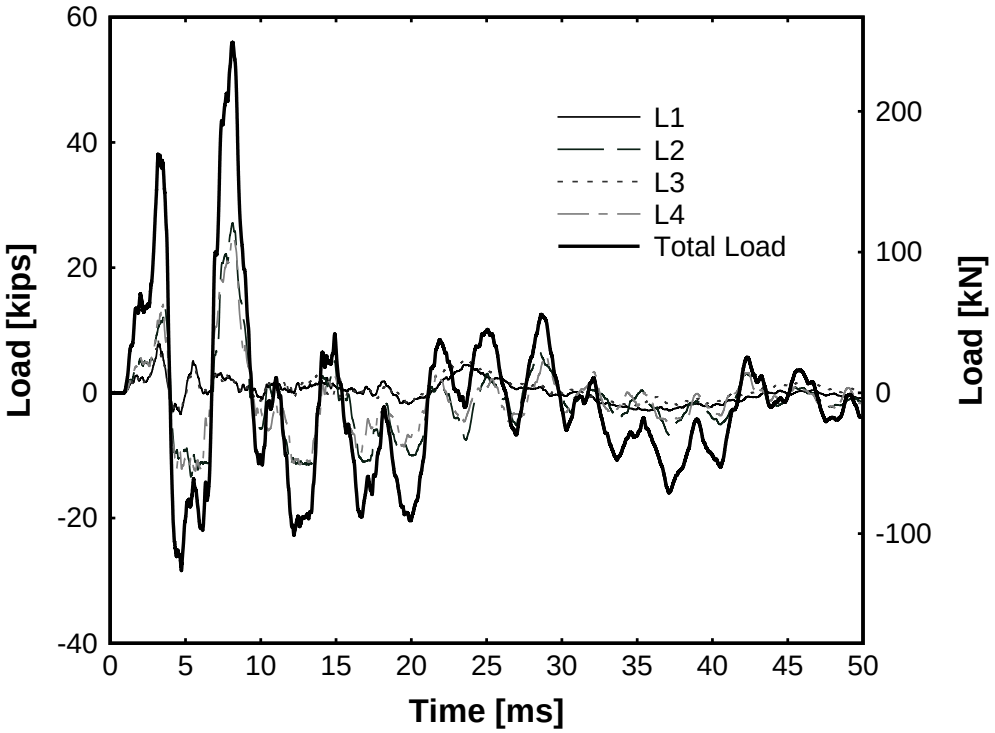

Figure 3-12. RC-Severe-2 Test Load Cell Data

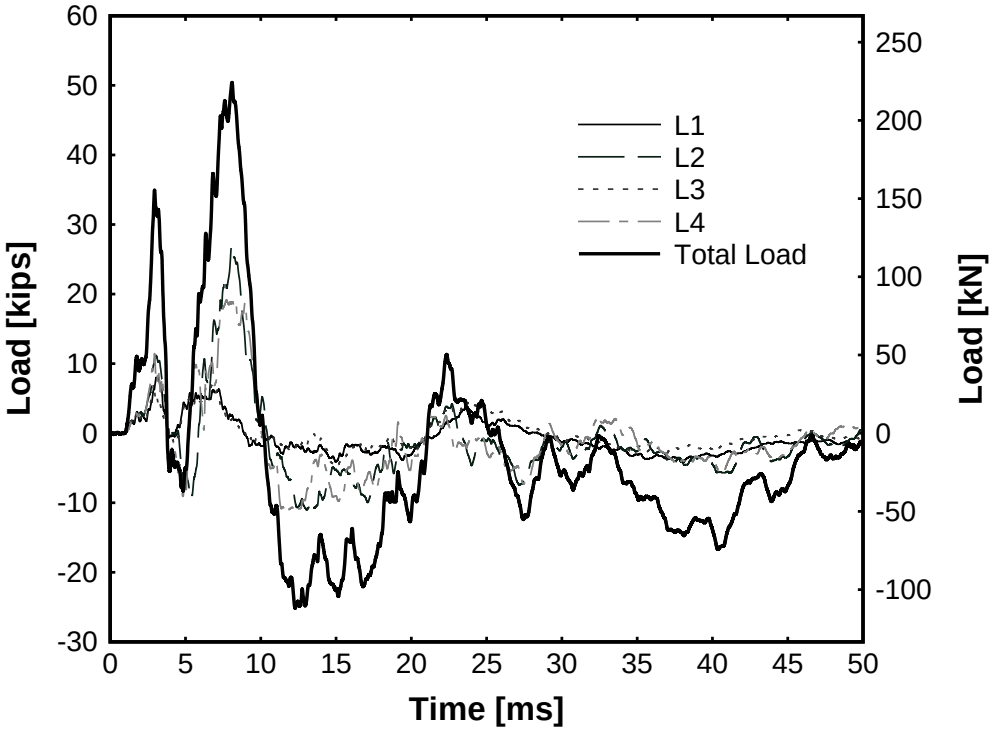

Figure 3-13. CFFT-Moderate Test Load Cell Data

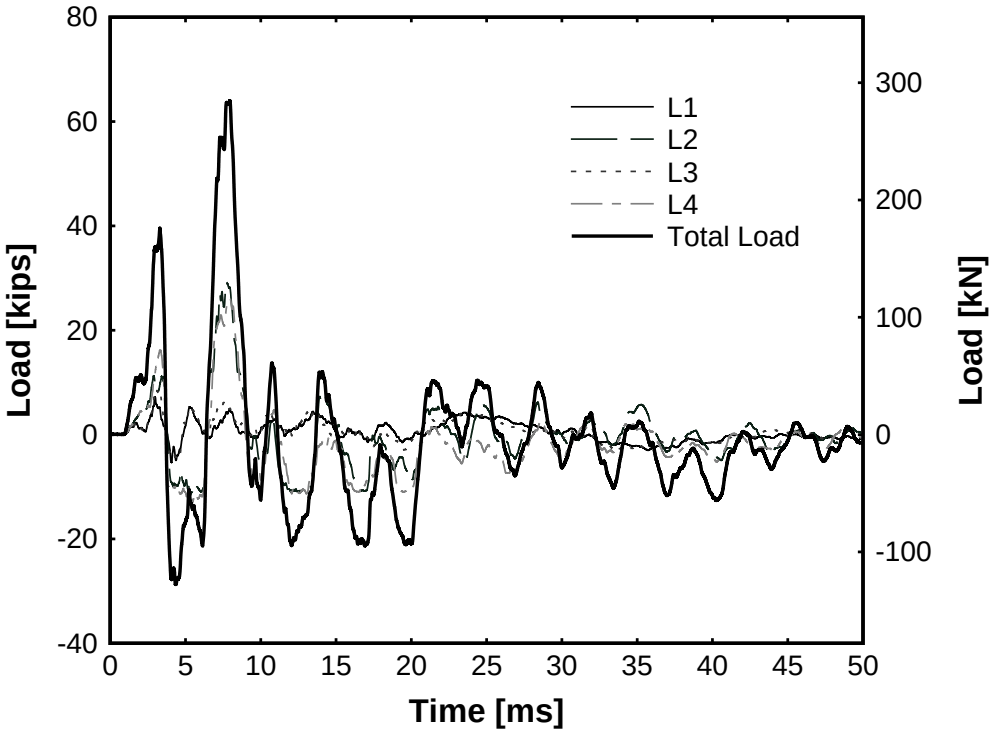

Figure 3-14. CFFT-Severe Test Load Cell Data

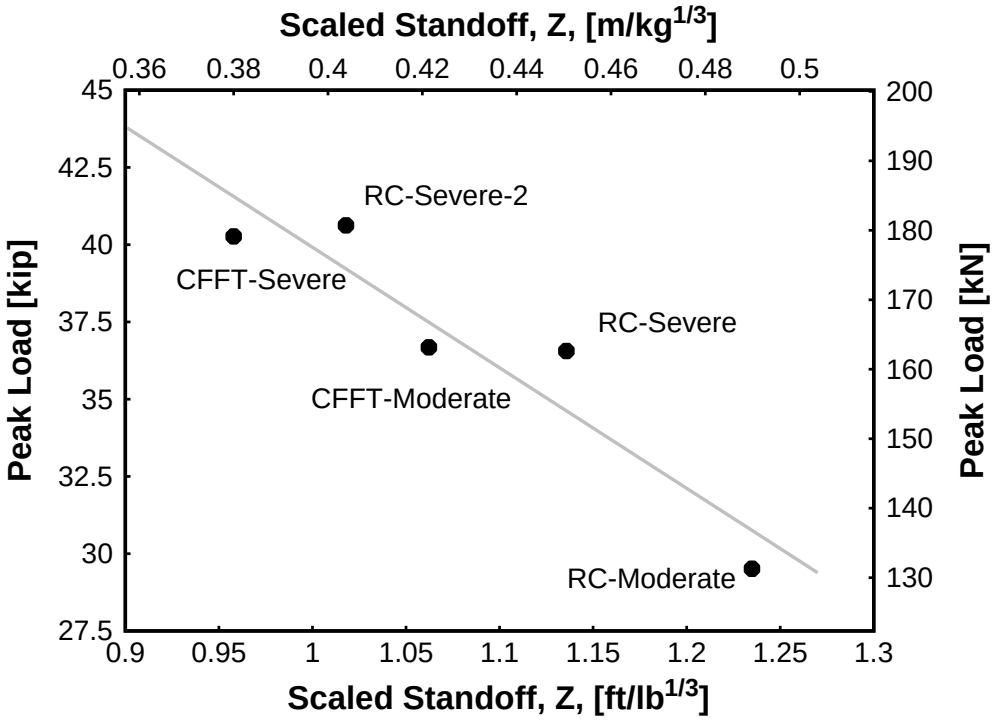

Figure 3-15. Scaled Standoff Vs. First Peak Load

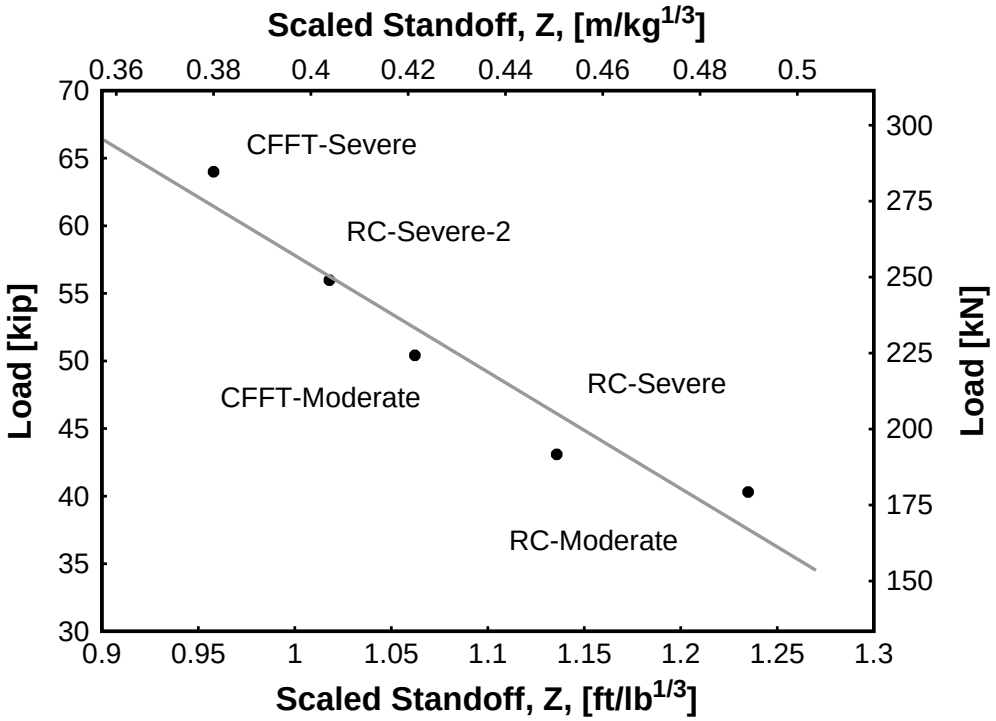

Figure 3-16. Scaled Standoff Vs. Second Peak Load

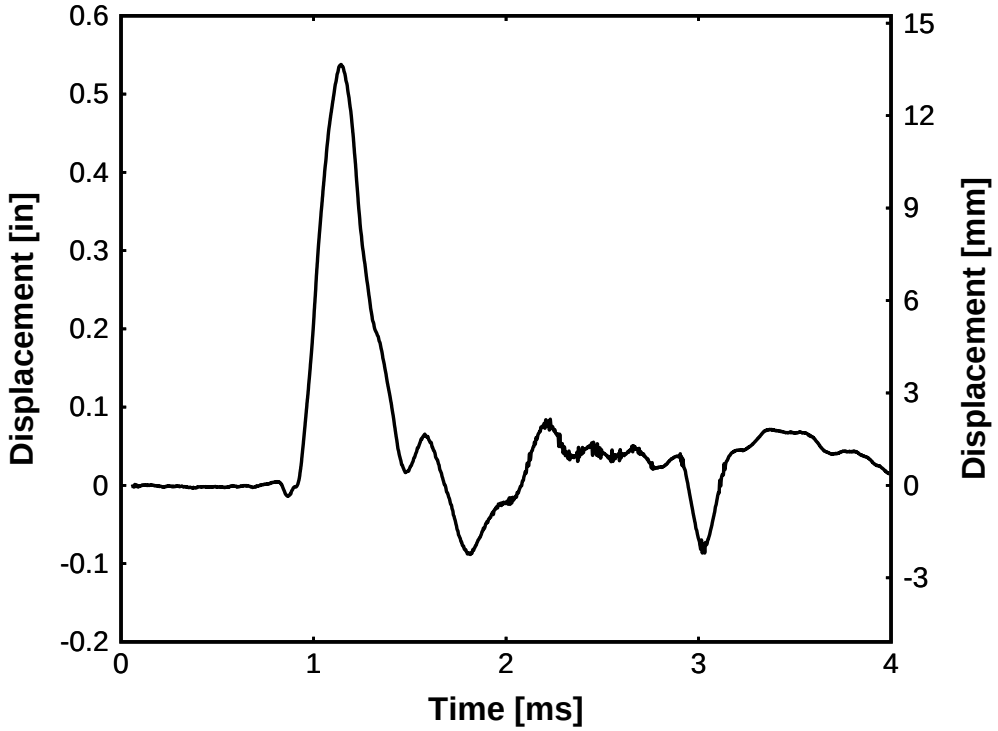

Figure 3-17. RC-Moderate Midspan Displacement

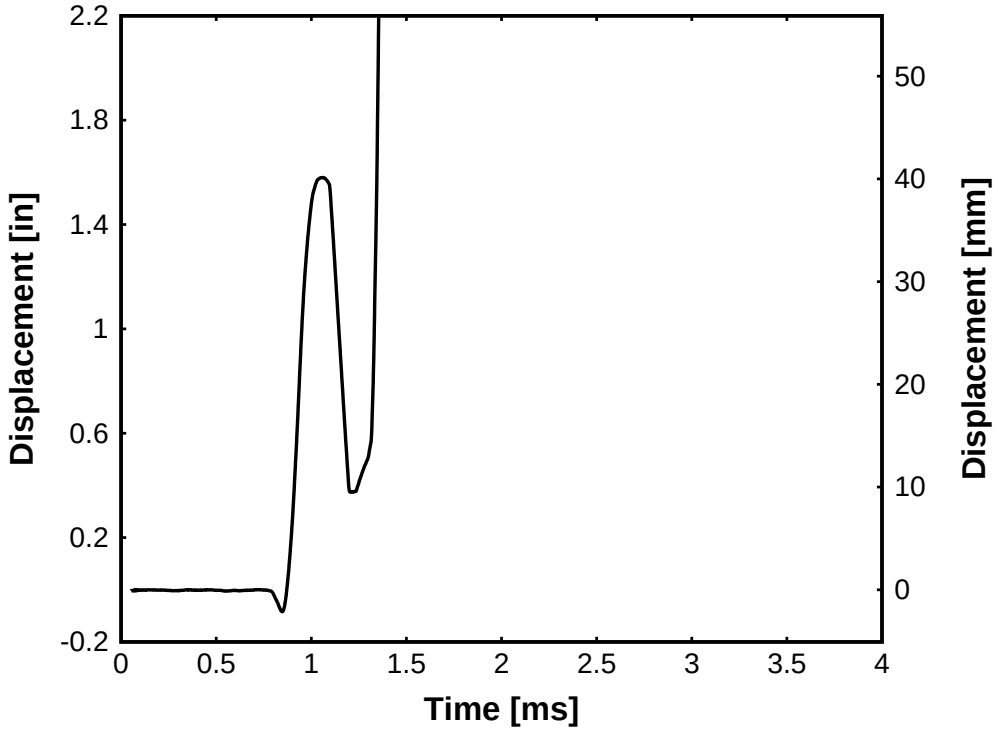

Figure 3-18. RC-Severe Midspan Displacement

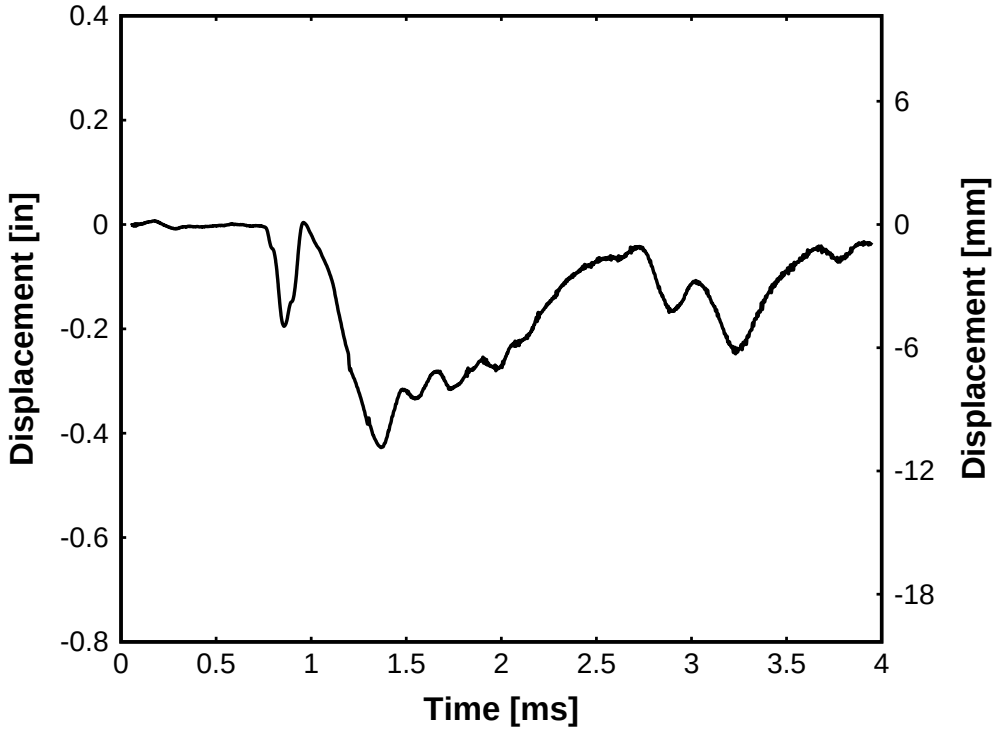

Figure 3-19. RC-Severe-2 Midspan Displacement

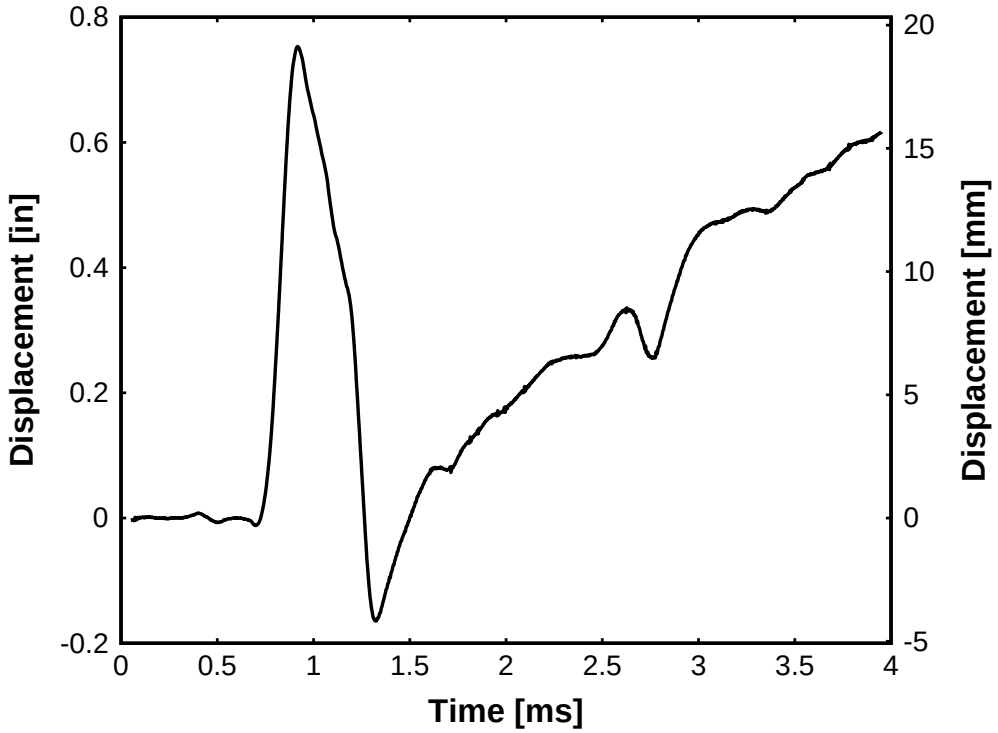

Figure 3-20. CFFT-Moderate Midspan Displacement

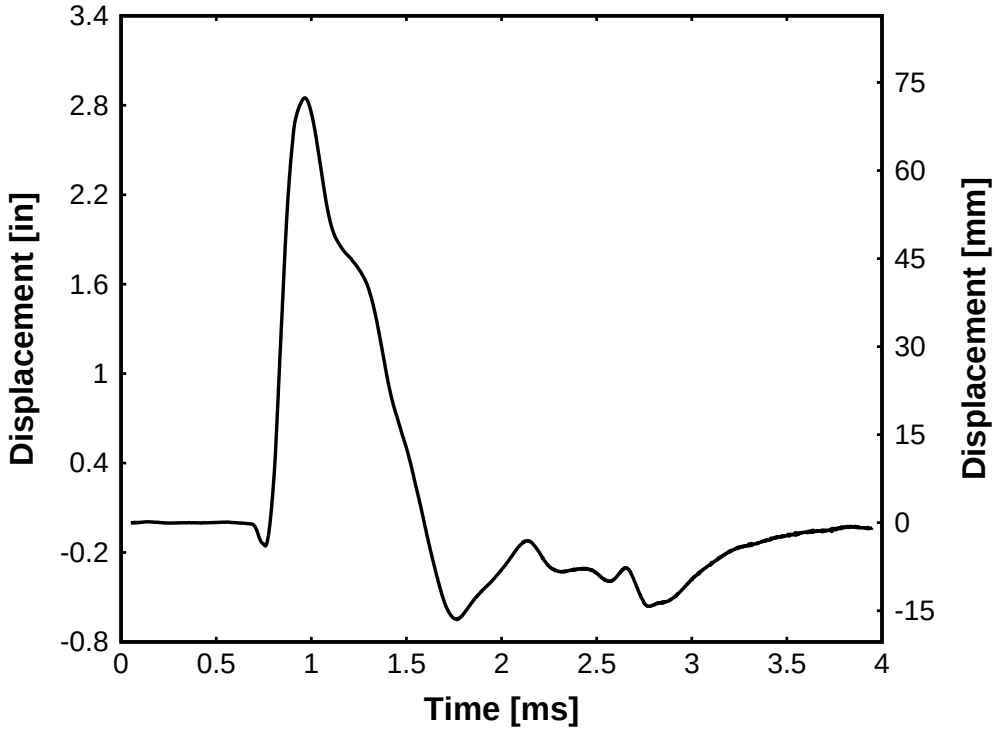

Figure 3-21. CFFT-Moderate Midspan Displacement

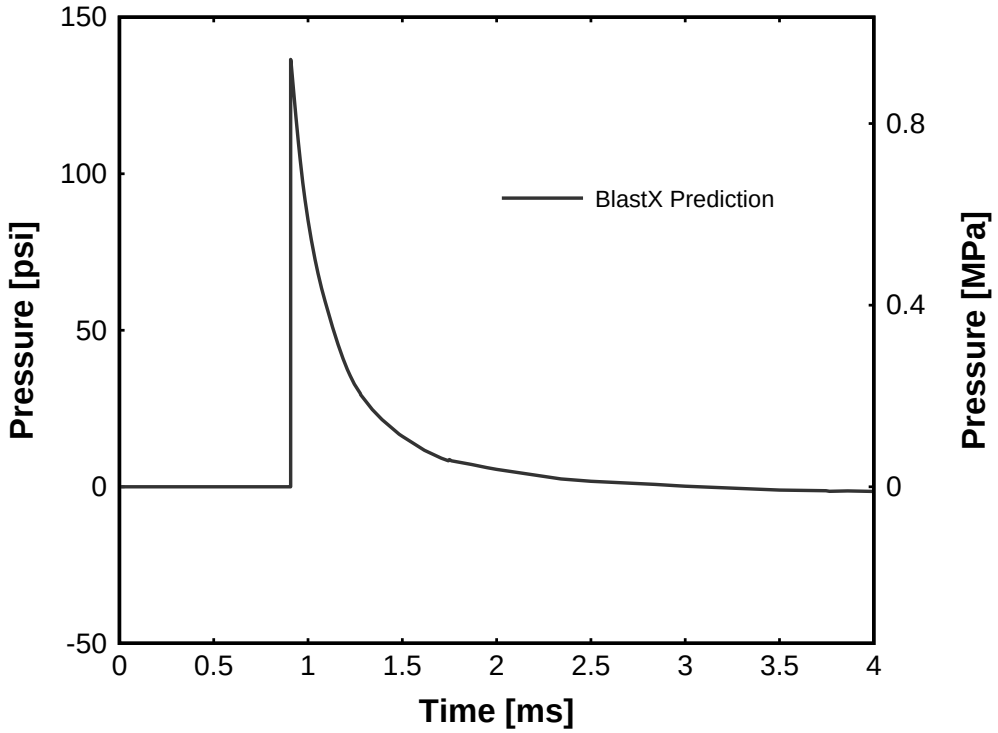

Figure 3-22. RC-Moderate BlastX Prediction for Gauge X

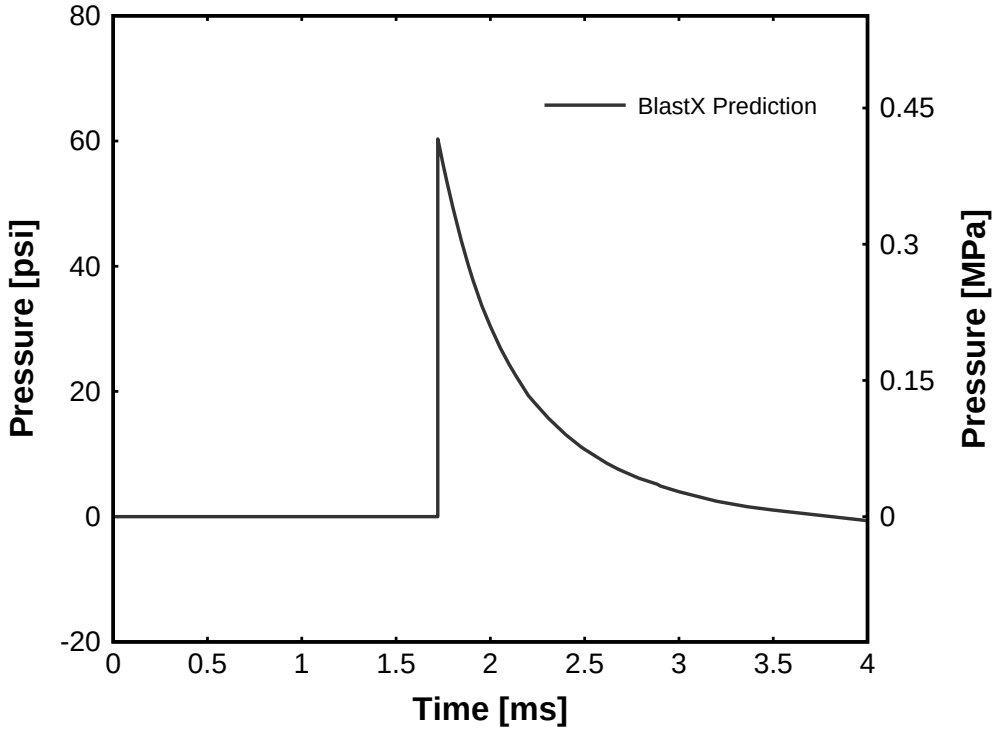

Figure 3-23. RC-Moderate BlastX Prediction for Gauge Y

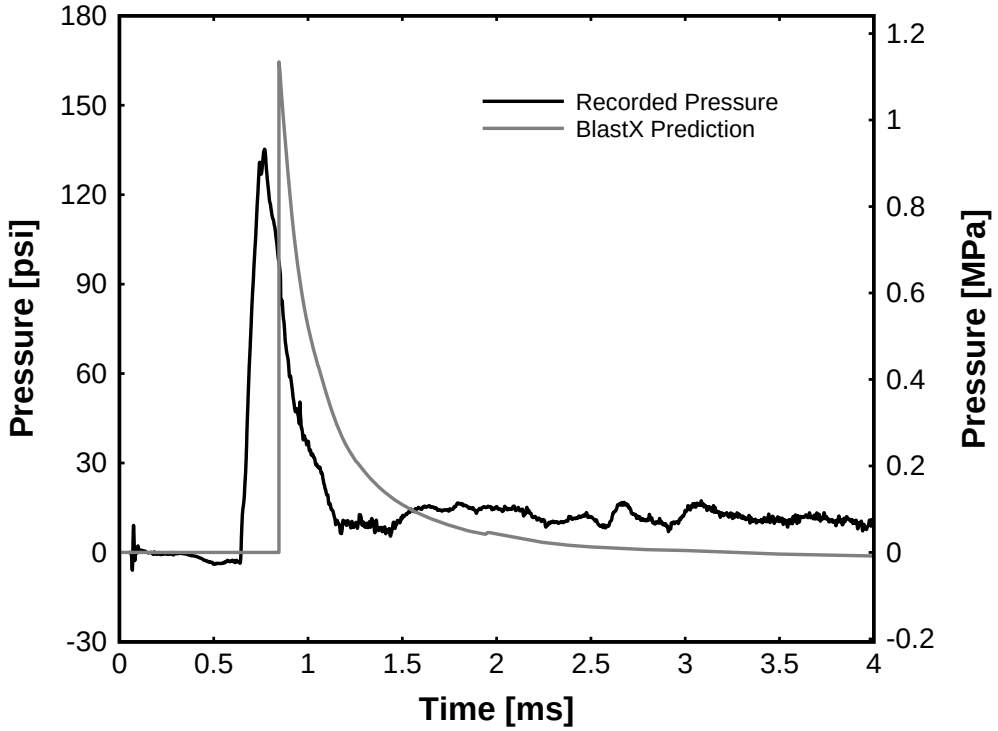

Figure 3-24. RC-Severe Recorded Pressure and BlastX Prediction at Gauge X

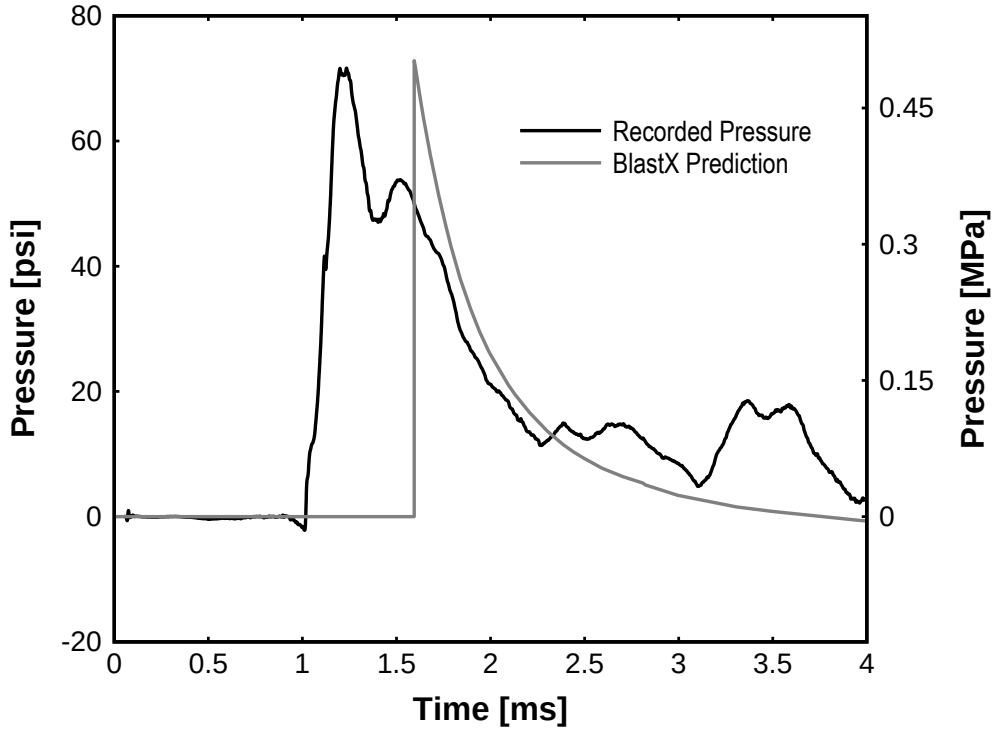

Figure 3-25. RC-Severe Recorded Pressure and BlastX Prediction at Gauge Y

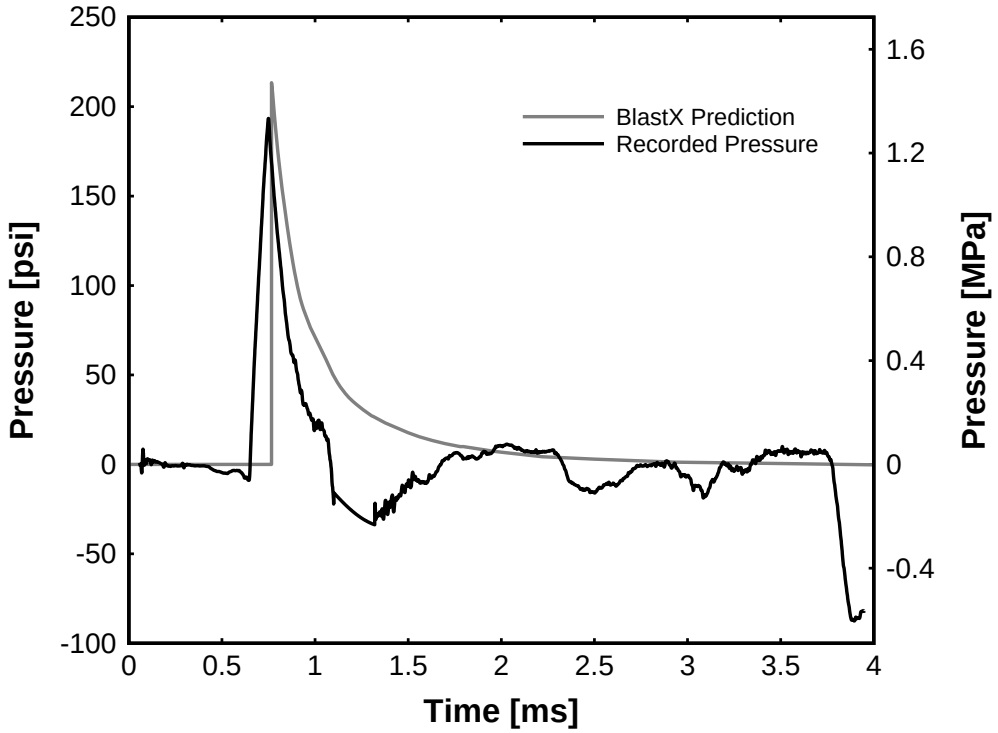

Figure 3-26. RC-Severe-2 Recorded Pressure and BlastX Prediction at Gauge X

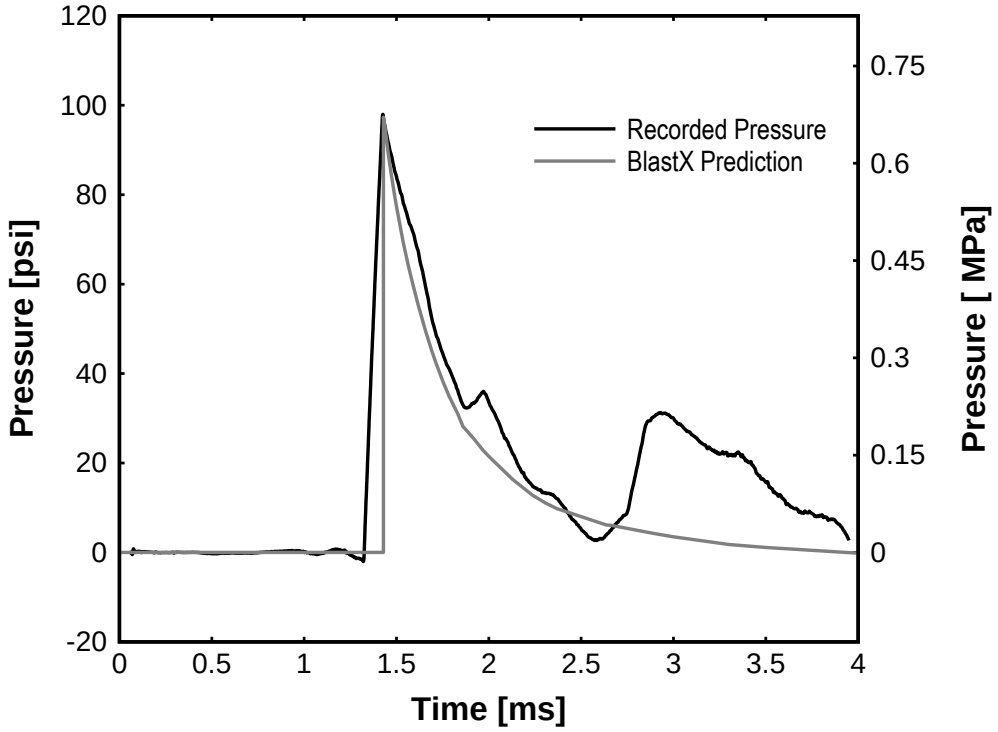

Figure 3-27. RC-Severe-2 Recorded Pressure and BlastX Prediction at Gauge Y

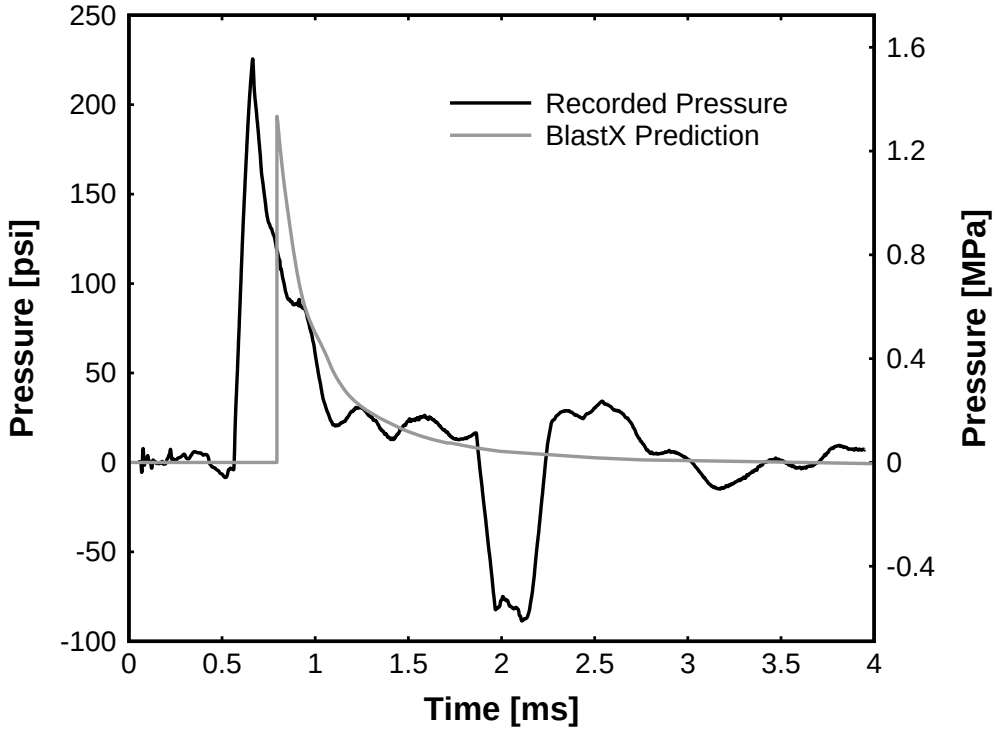

Figure 3-28. CFFT-Moderate Recorded Pressure and BlastX Prediction at Gauge X

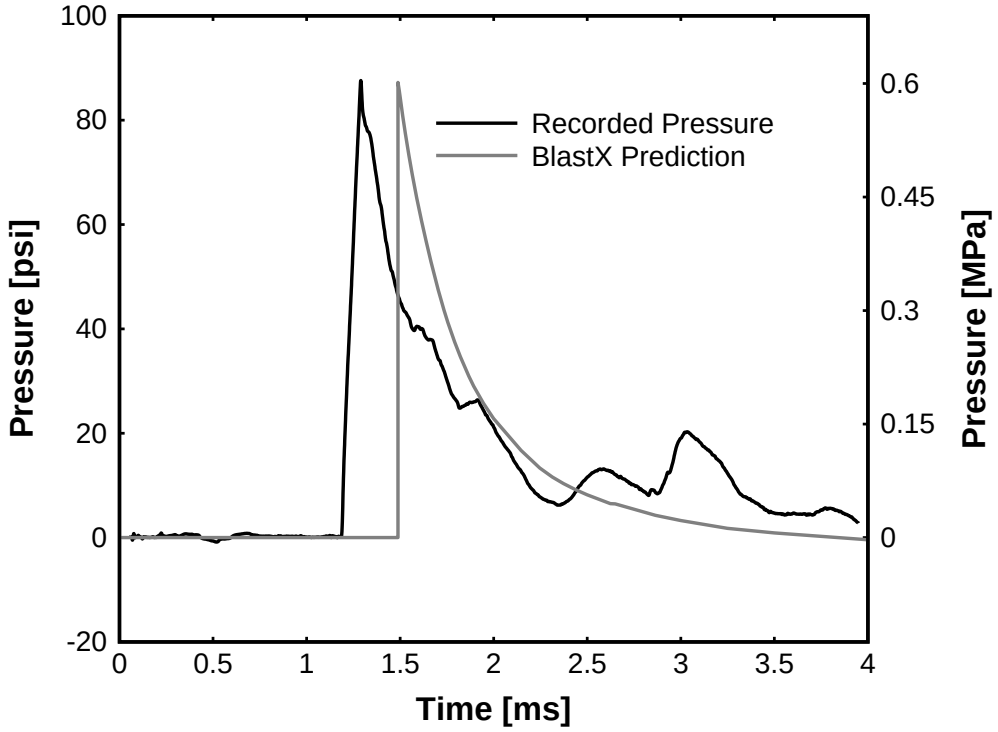

Figure 3-29. CFFT-Moderate Recorded Pressure and BlastX Prediction at Gauge Y

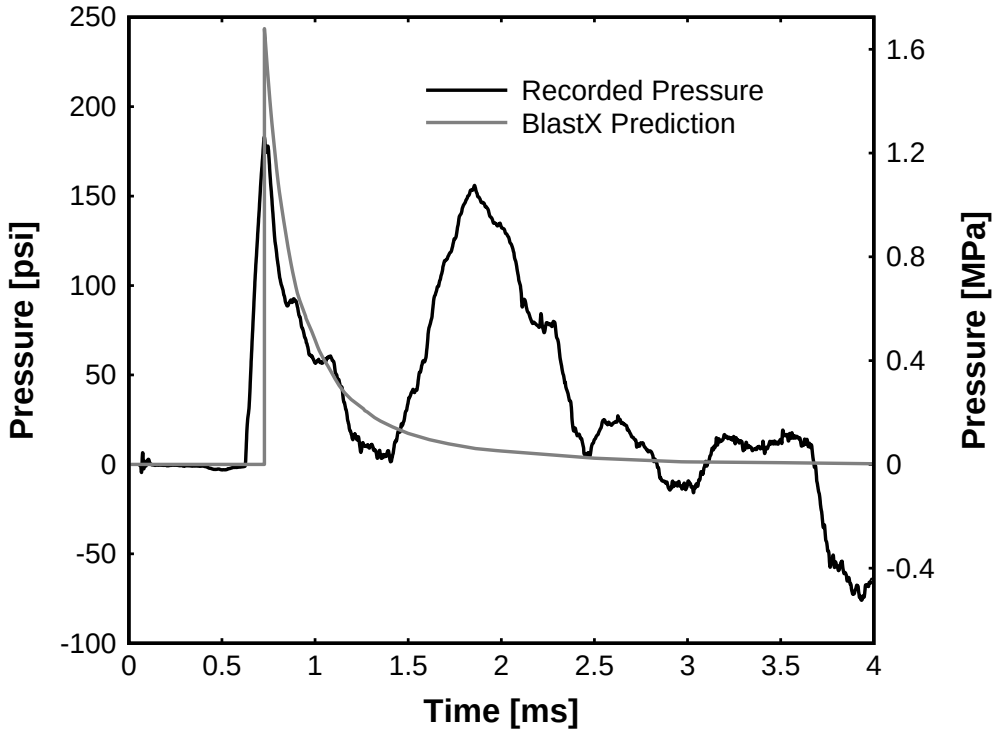

Figure 3-30. CFFT-Severe Recorded Pressure and BlastX Prediction at Gauge X

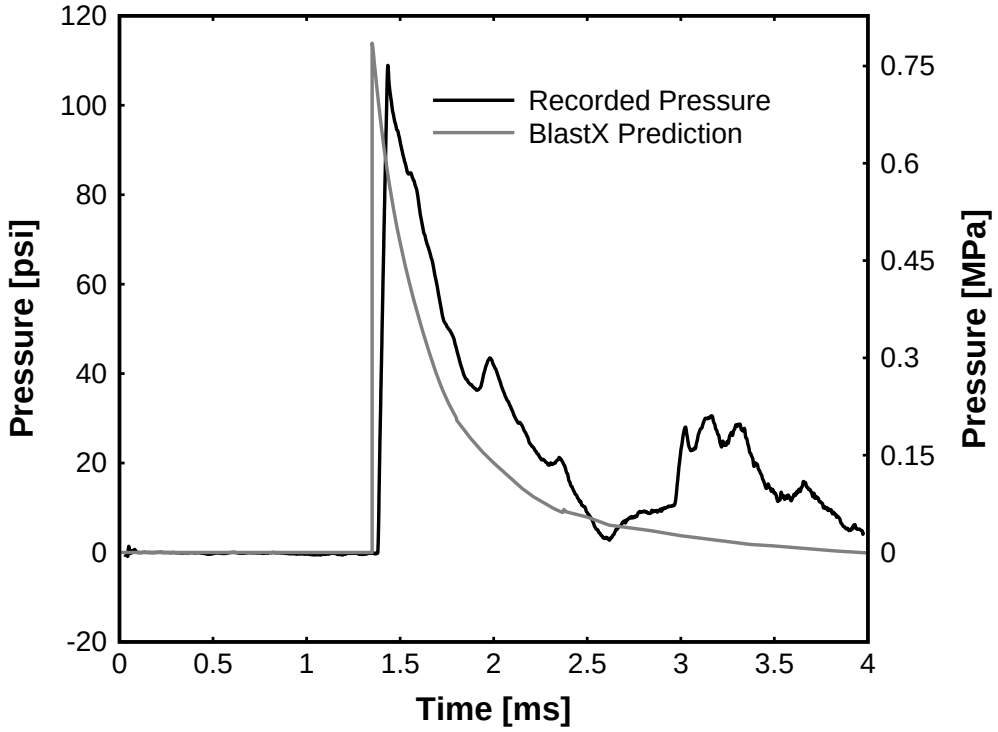

Figure 3-31. CFFT-Severe Recorded Pressure and BlastX Prediction at Gauge Y

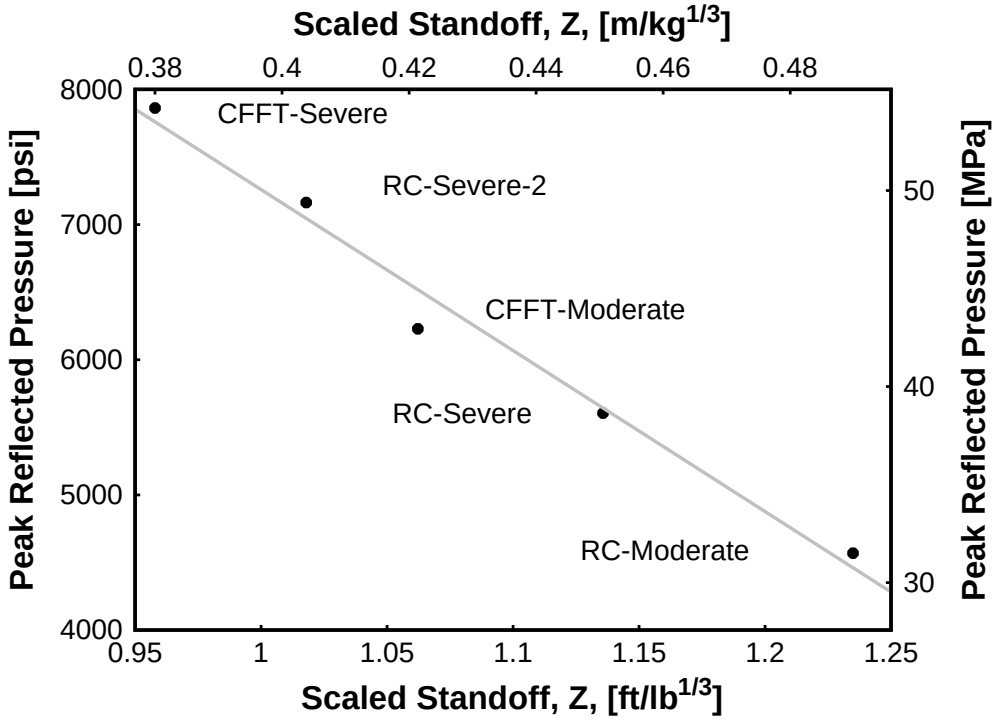

Figure 3-32. Scaled Standoff Vs. Peak Reflected Pressure at Column Surface

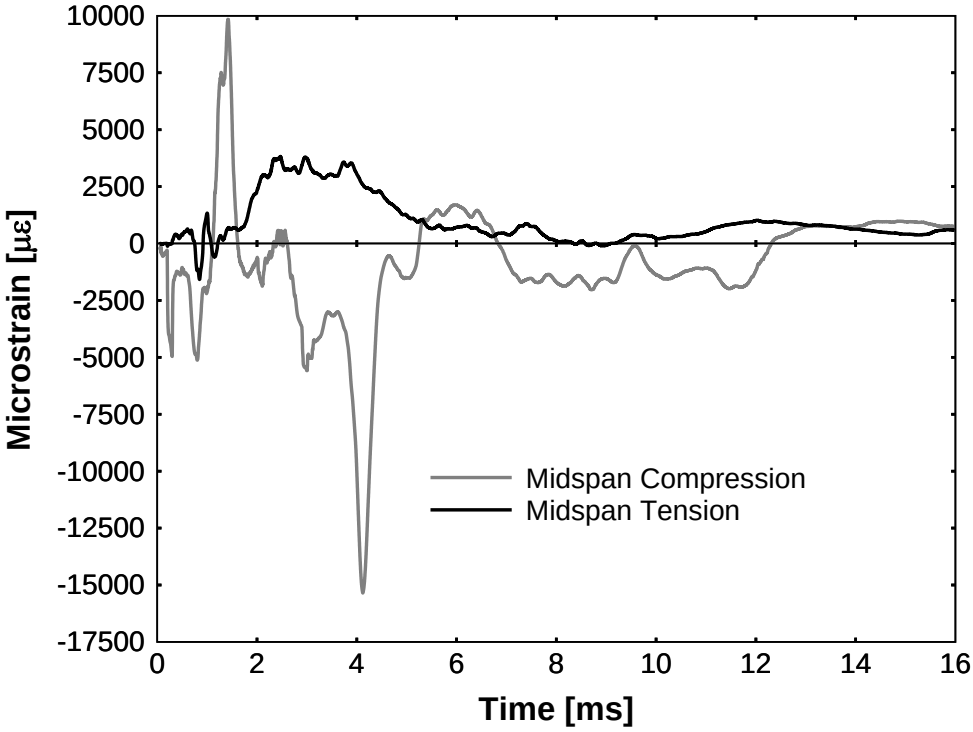

Figure 3-33. RC-Moderate Longitudinal Strains at Midspan

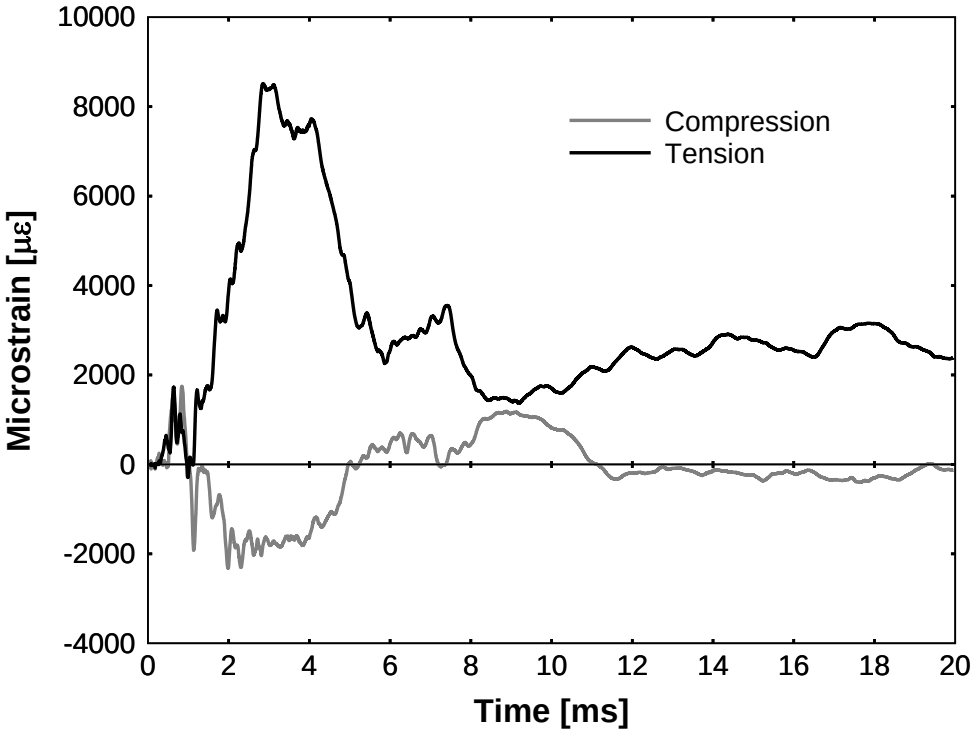

Figure 3-34. RC-Severe Longitudinal Strains at Midspan

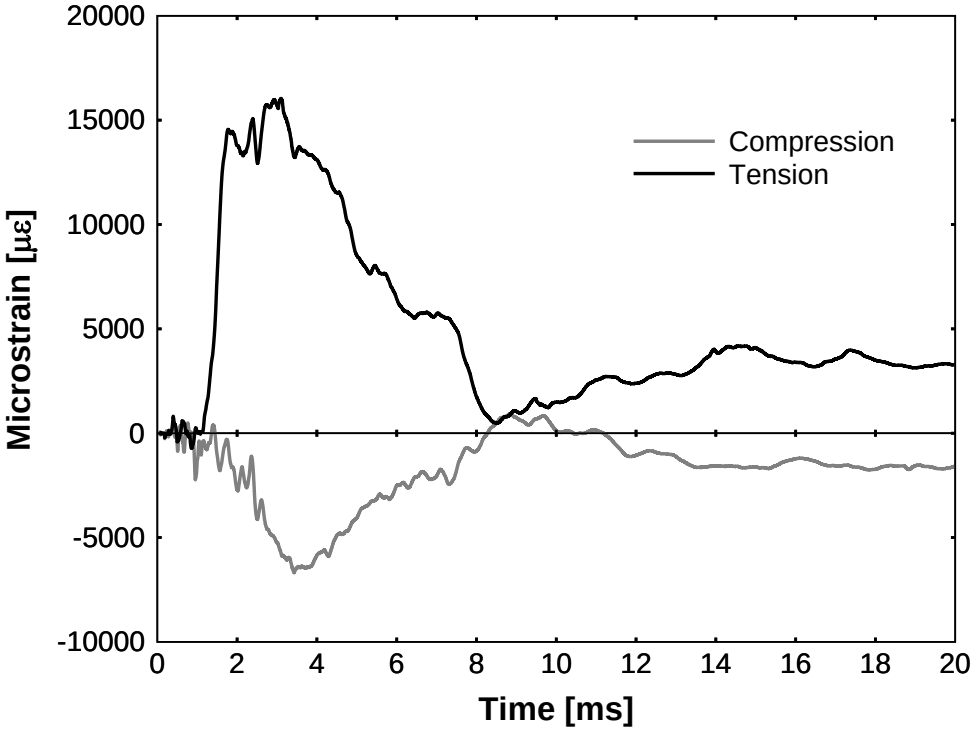

Figure 3-35. RC-Severe-2 Longitudinal Strains at Midspan

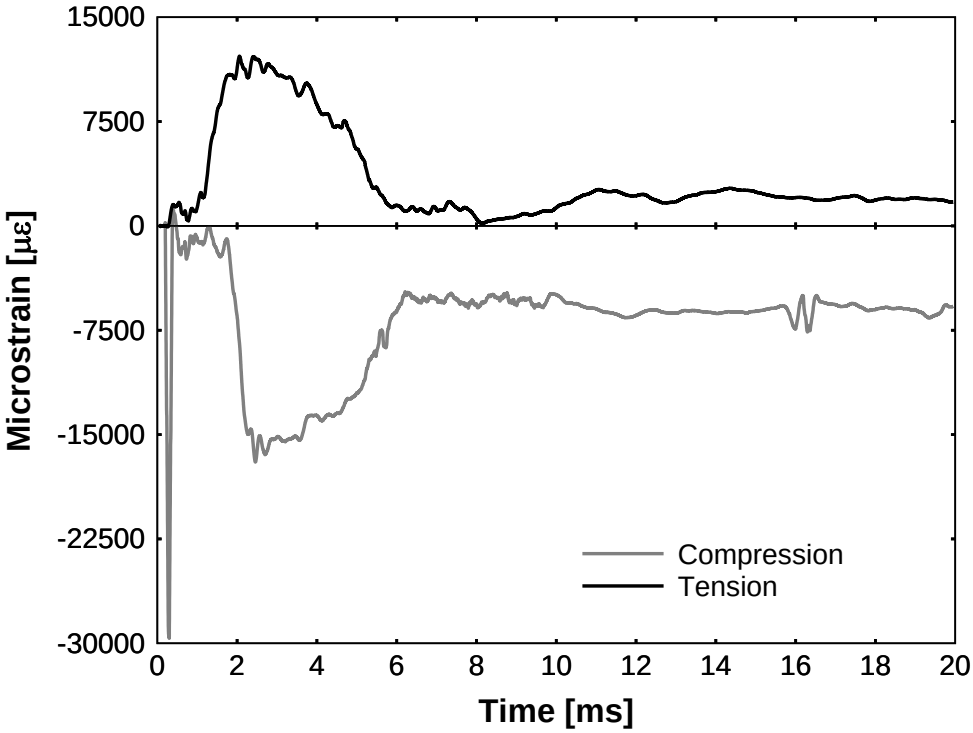

Figure 3-36. CFFT-Moderate Longitudinal Strains at Midspan

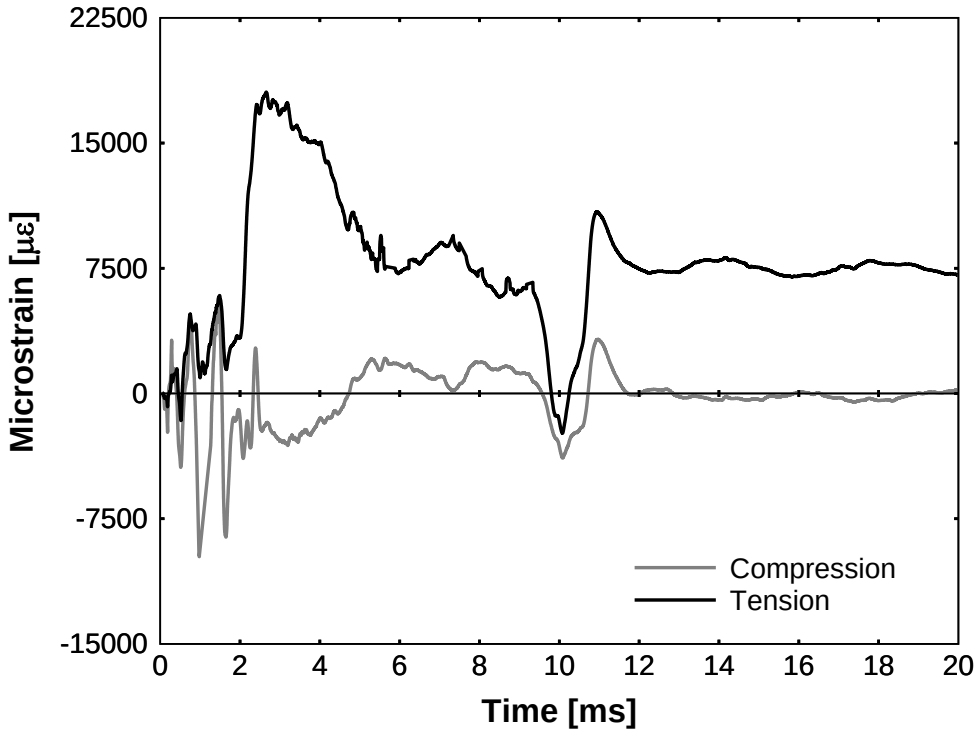

Figure 3-37. CFFT-Severe Longitudinal Strains at Midspan

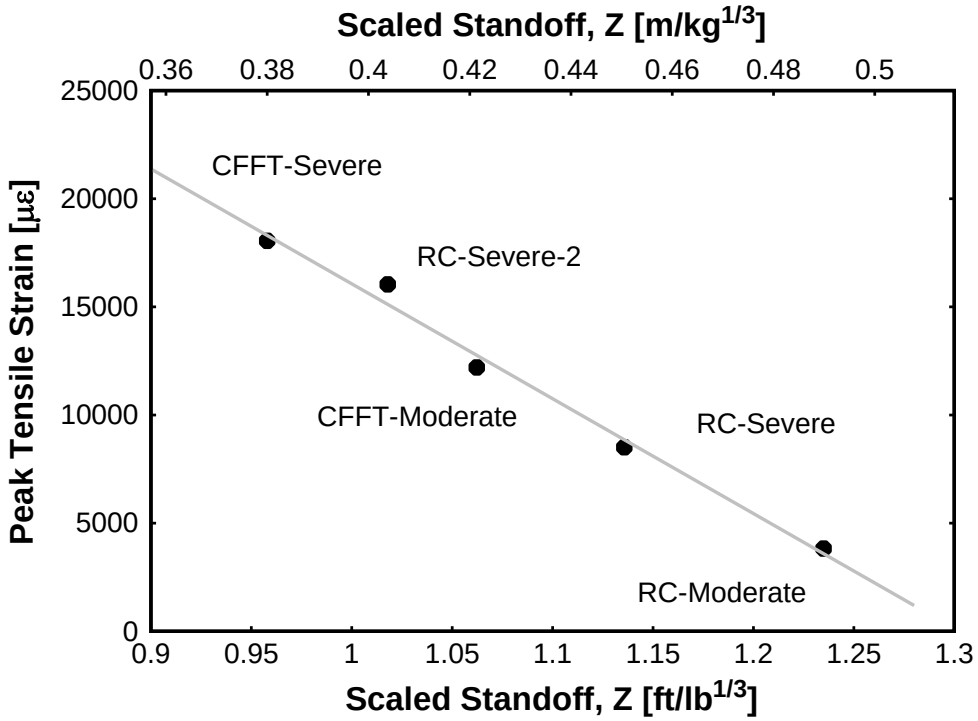

Figure 3-38. Scaled Standoff Vs. Peak Tensile Strain at Midspan

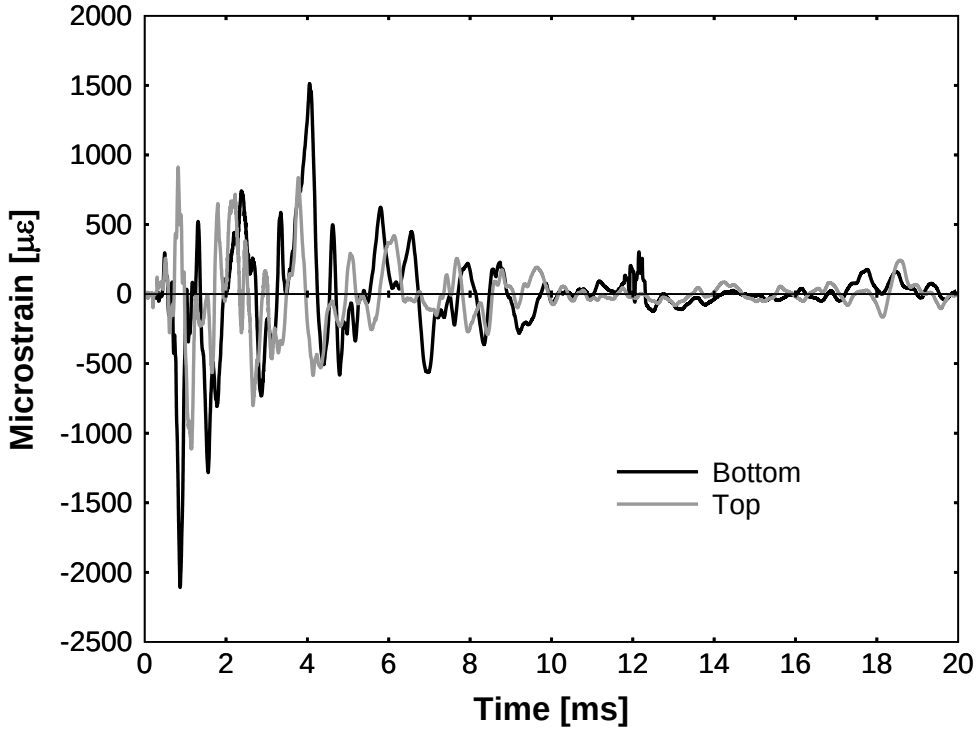

Figure 3-39. RC-Moderate Spiral Strains Near Supports

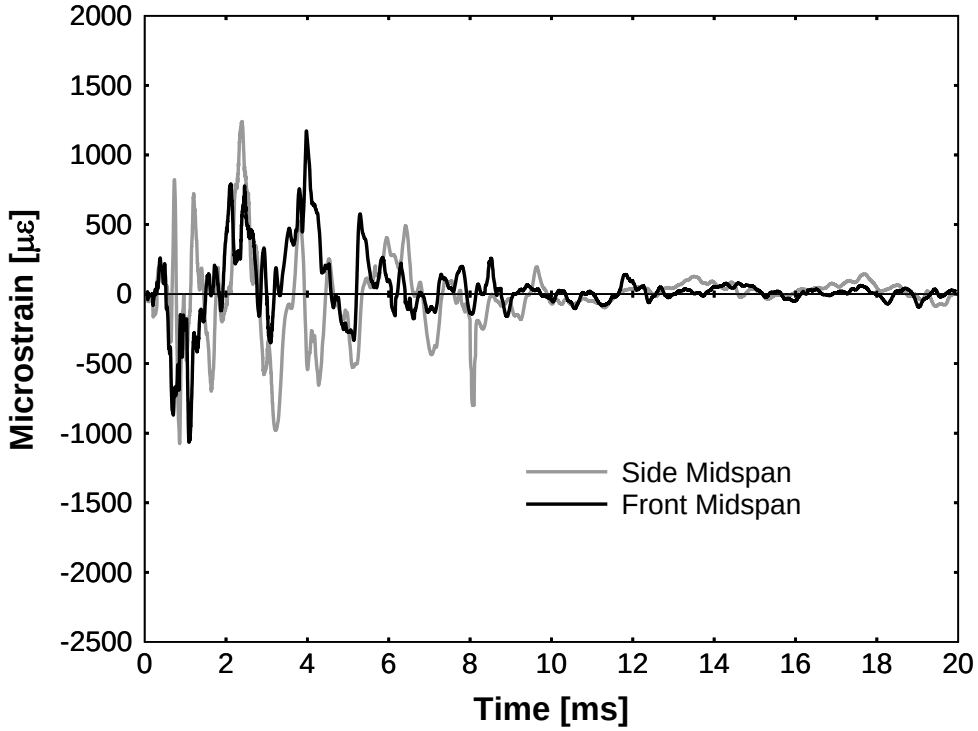

Figure 3-40. RC-Moderate Spiral Strains at Midspan

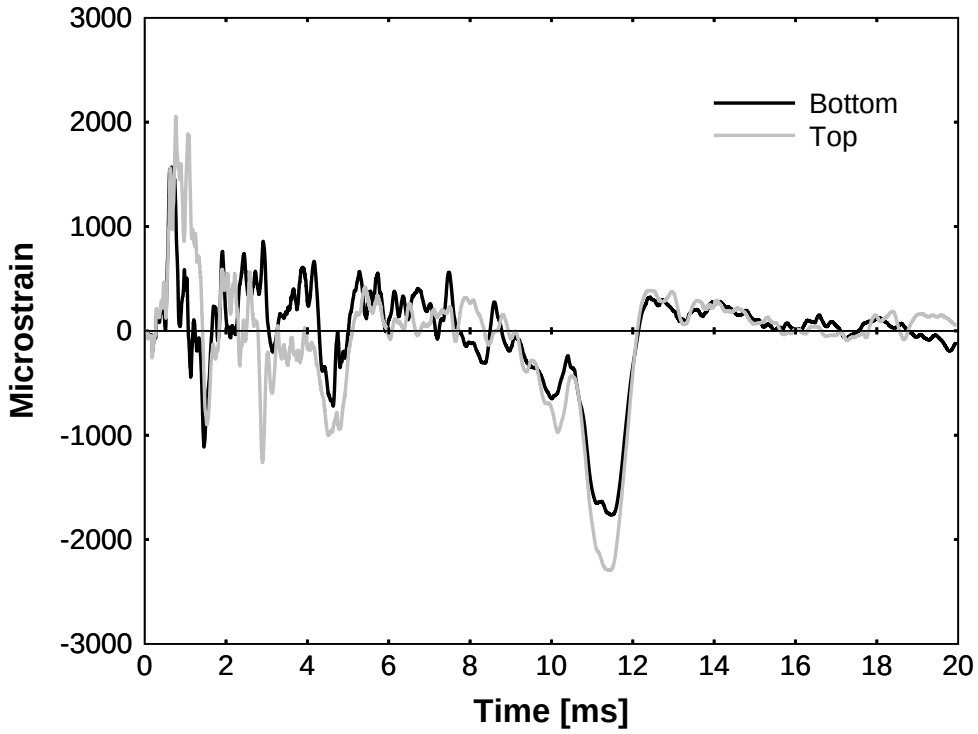

Figure 3-41. RC-Severe Spiral Strains Near Supports

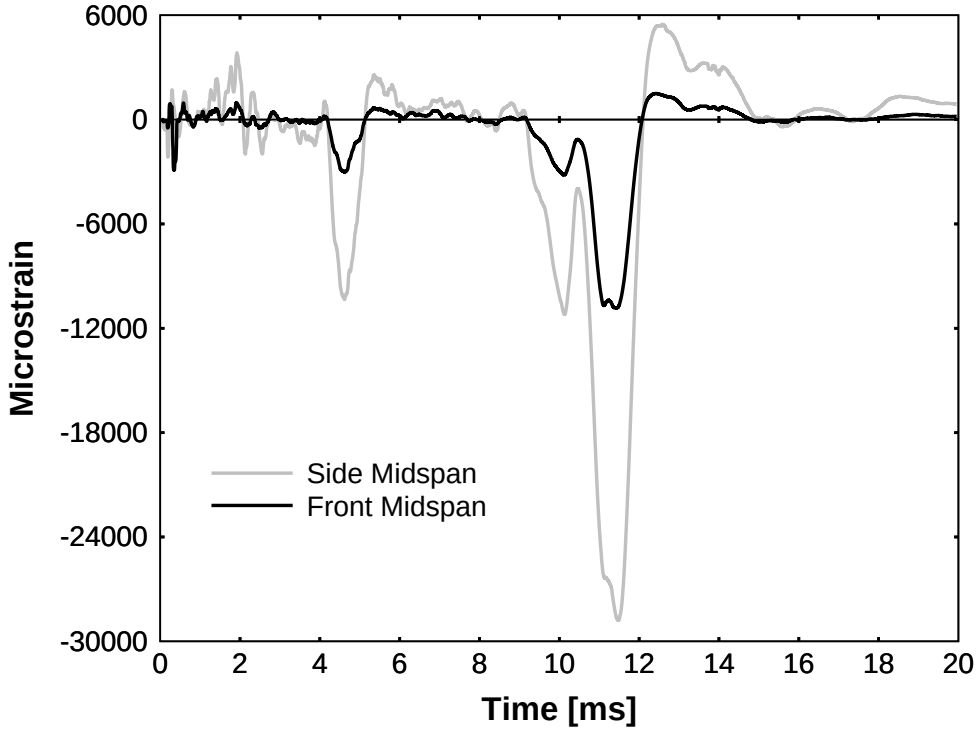

Figure 3-42. RC-Severe Spiral Strains at Midspan

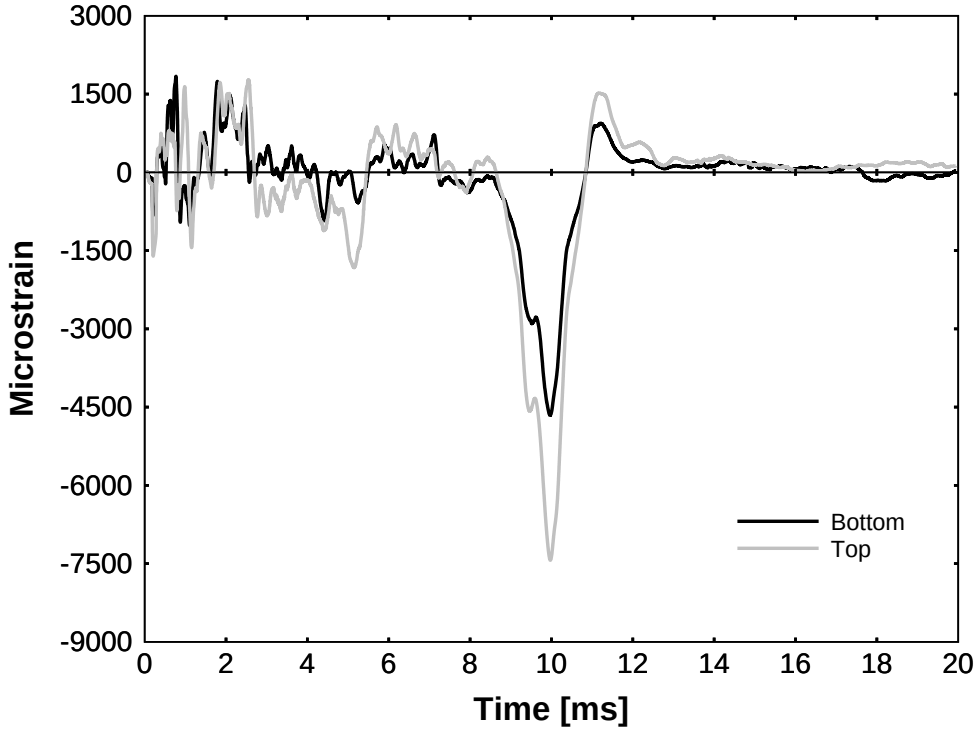

Figure 3-43. RC-Severe-2, Spiral Strains Near Supports

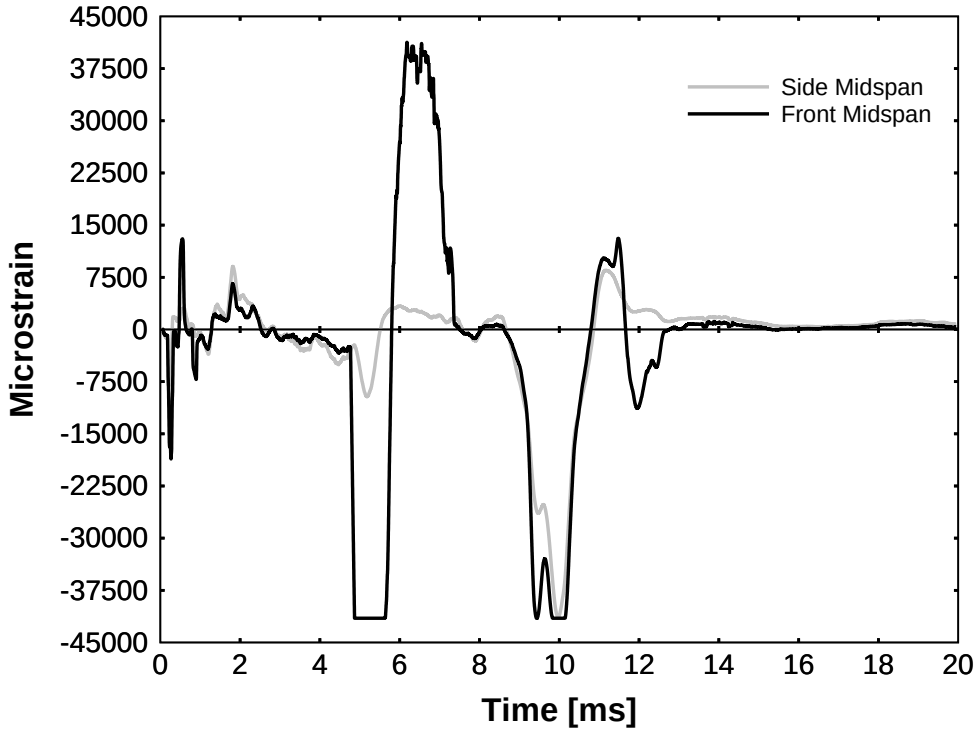

Figure 3-44. RC-Severe-2 Spiral Strains at Midspan

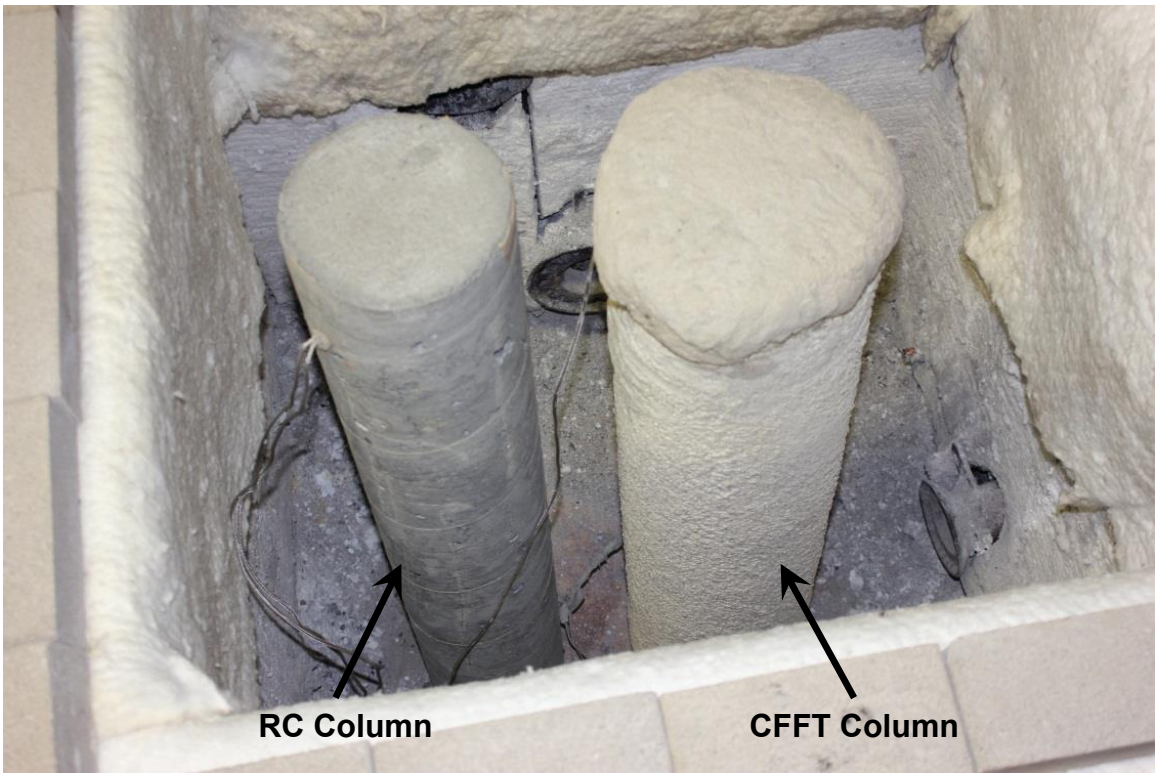

Figure 3-45. RC and CFFT Fire Columns Pre-Test

Figure 3-46. RC and CFFT Fire Columns Post-Test

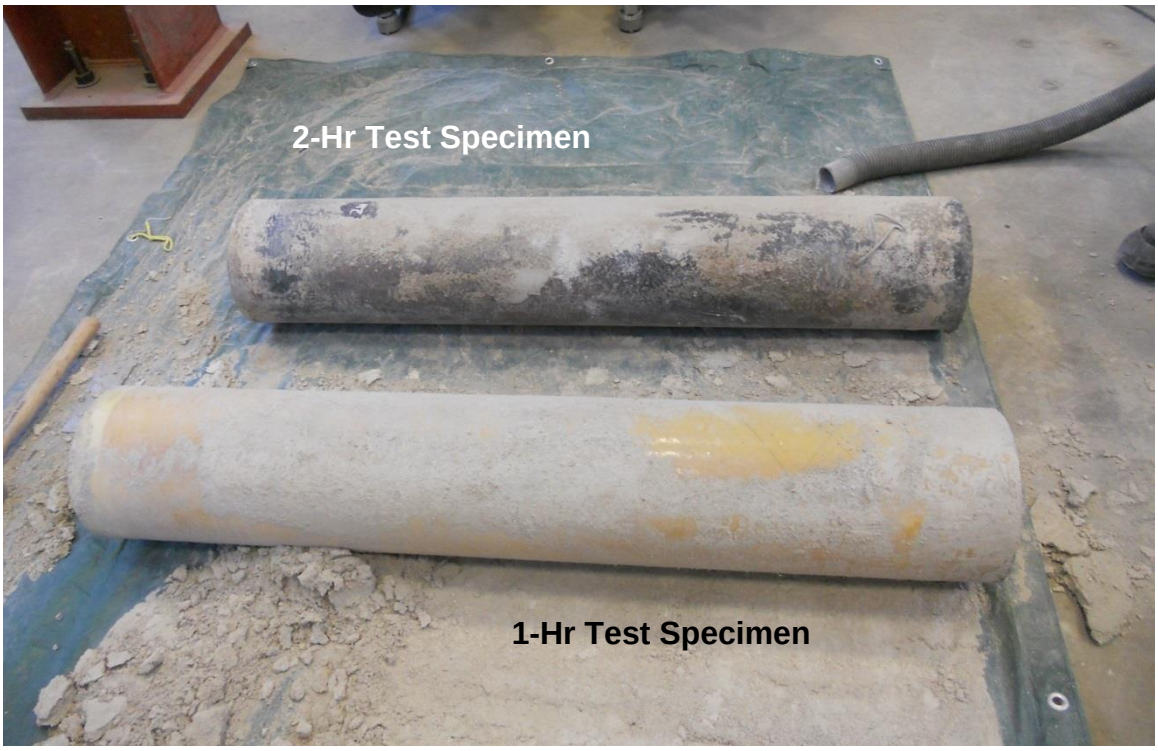

Figure 3-47. CFFT Columns after Extreme Fire Exposure

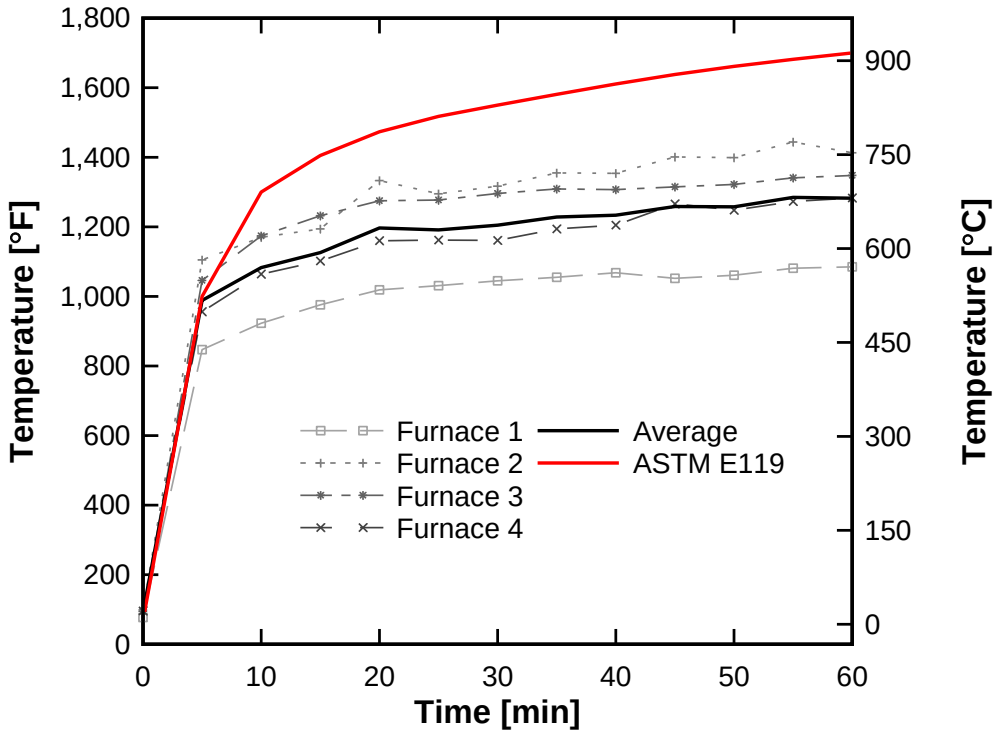

Figure 3-48. 1-Hr Test Furnace Temperature Time History

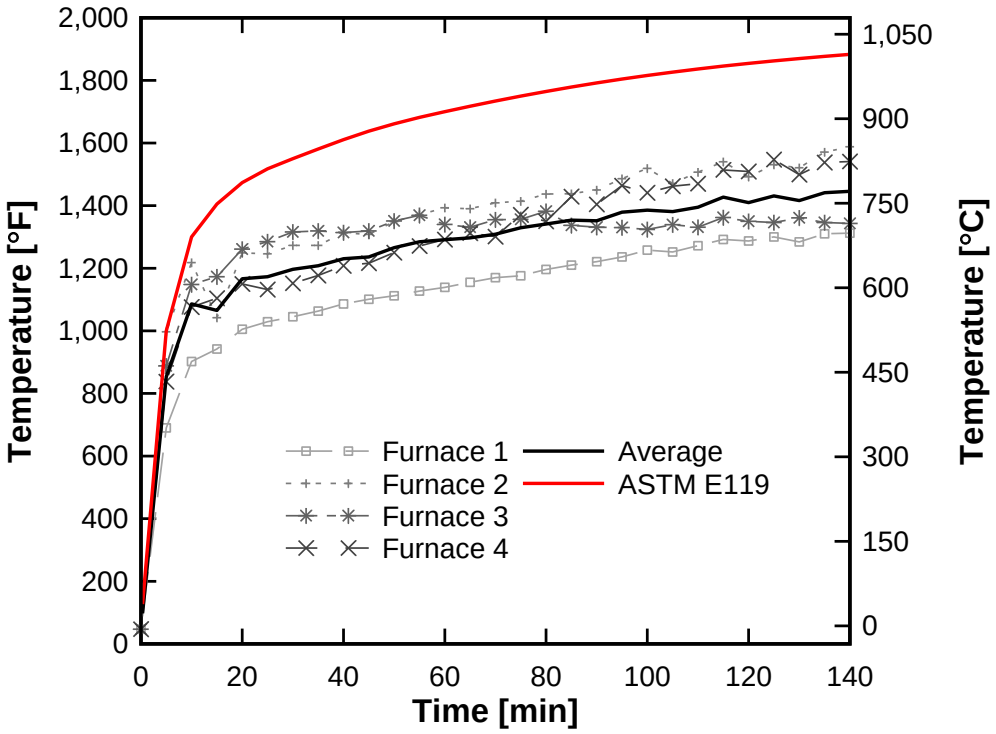

Figure 3-49. 2-Hr Test Furnace Temperature Time History

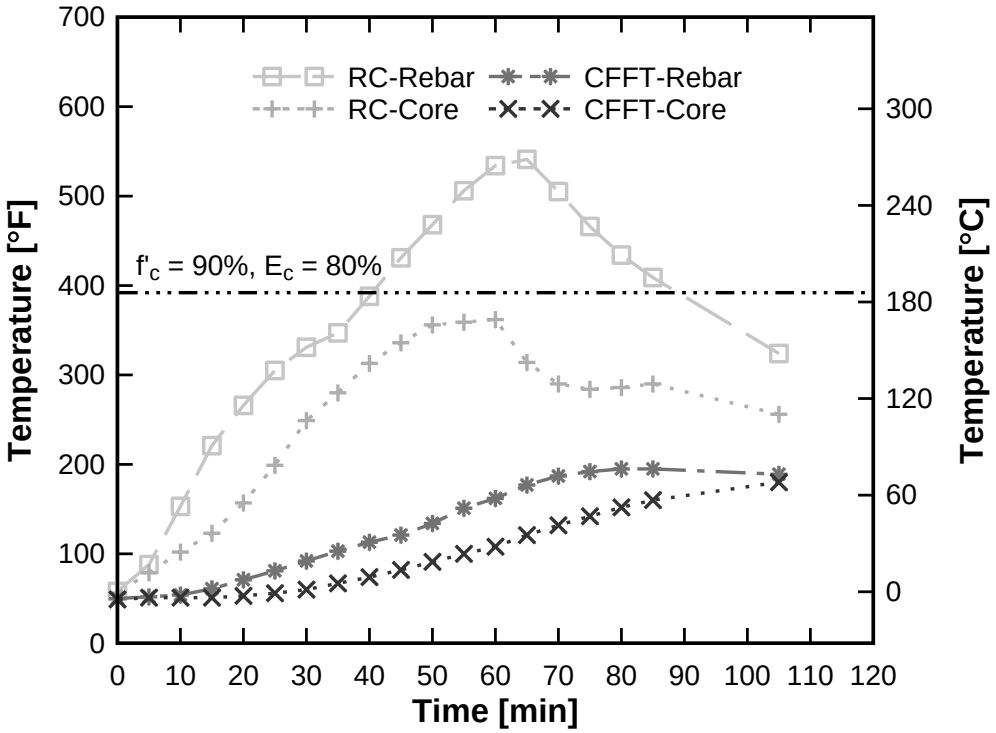

Figure 3-50. 1-Hr Test Concrete Temperature Time Histories

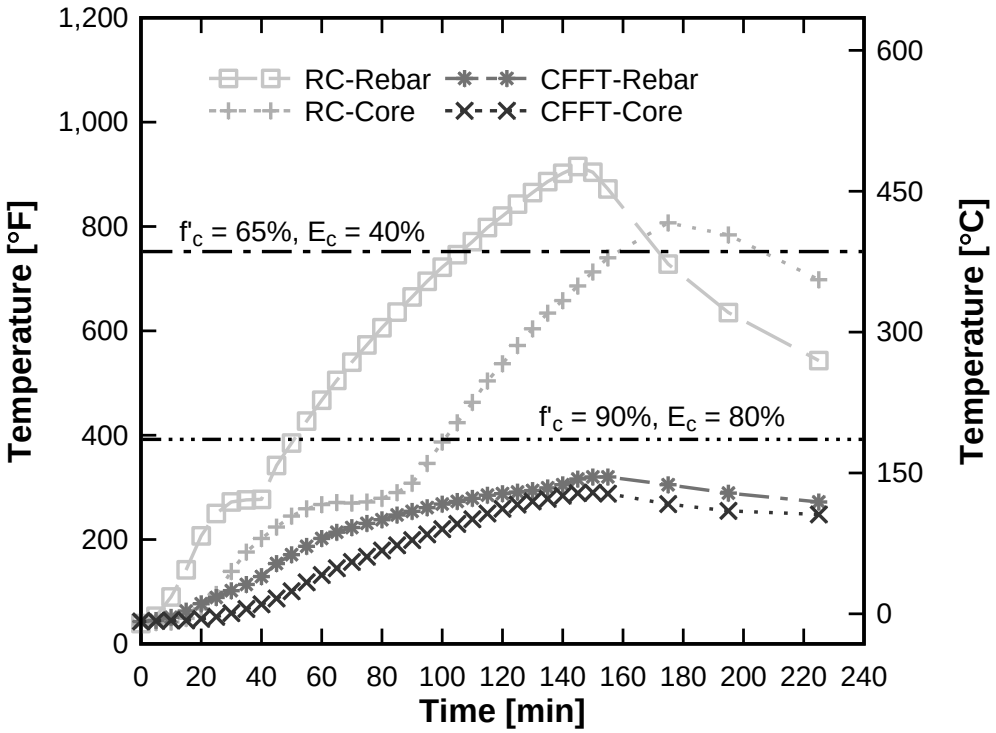

Figure 3-51. 2-Hr Test Concrete Temperature Time Histories

Figure 4-1. UConn Structures Lab 400kip Load Frame

Figure 4-2. Axial Capacity Test Setup

Figure 4-3. Failure Progression of RC-Benchmark Column

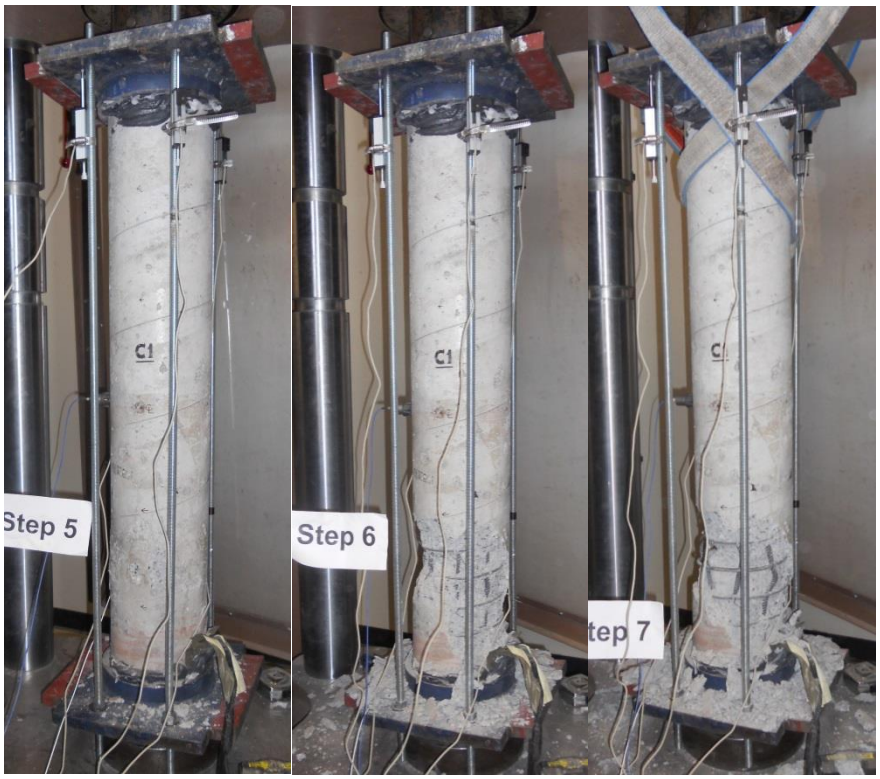

Figure 4-4. Failure Progression of RC-Moderate Column

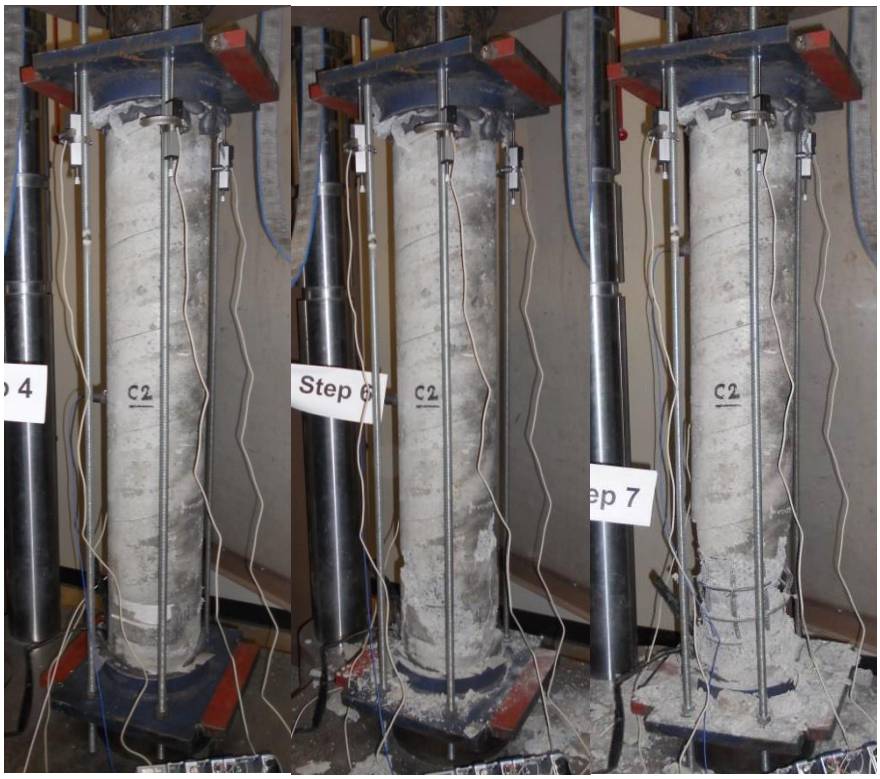

Figure 4-5. Failure Progression of RC-Severe Column

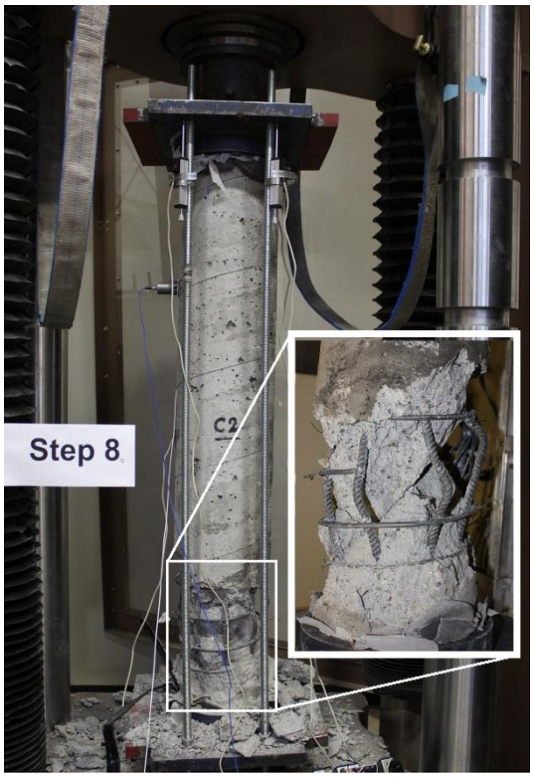

Figure 4-6. Failure Mode of RC-Severe Column

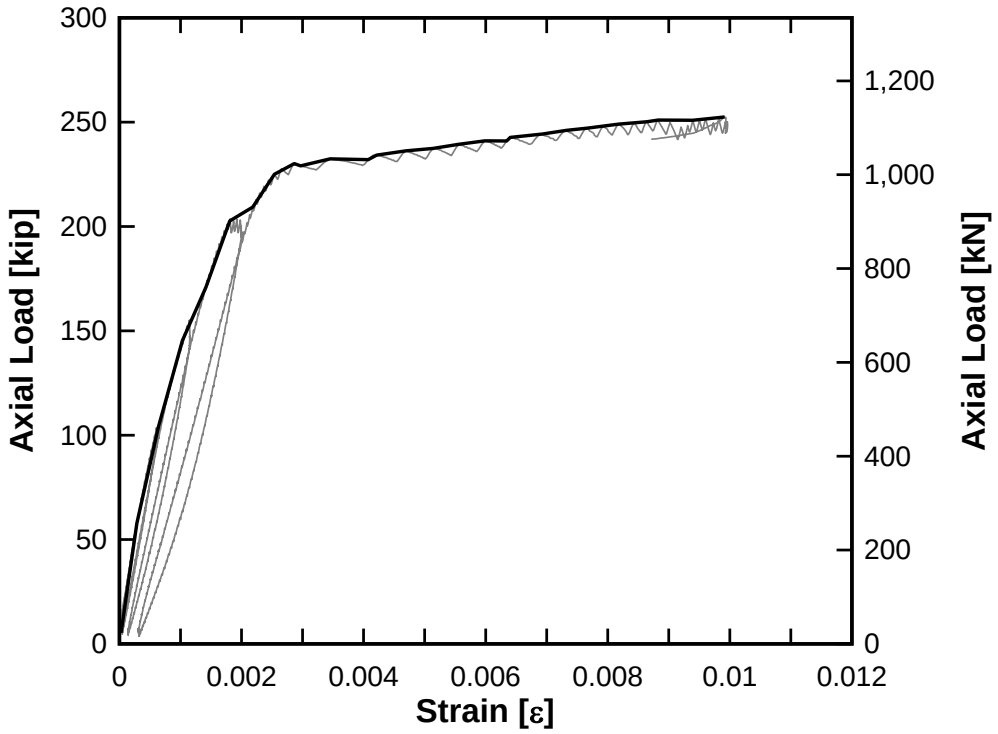

Figure 4-7. RC-Benchmark Front Bar Longitudinal Strain vs. Axial Load

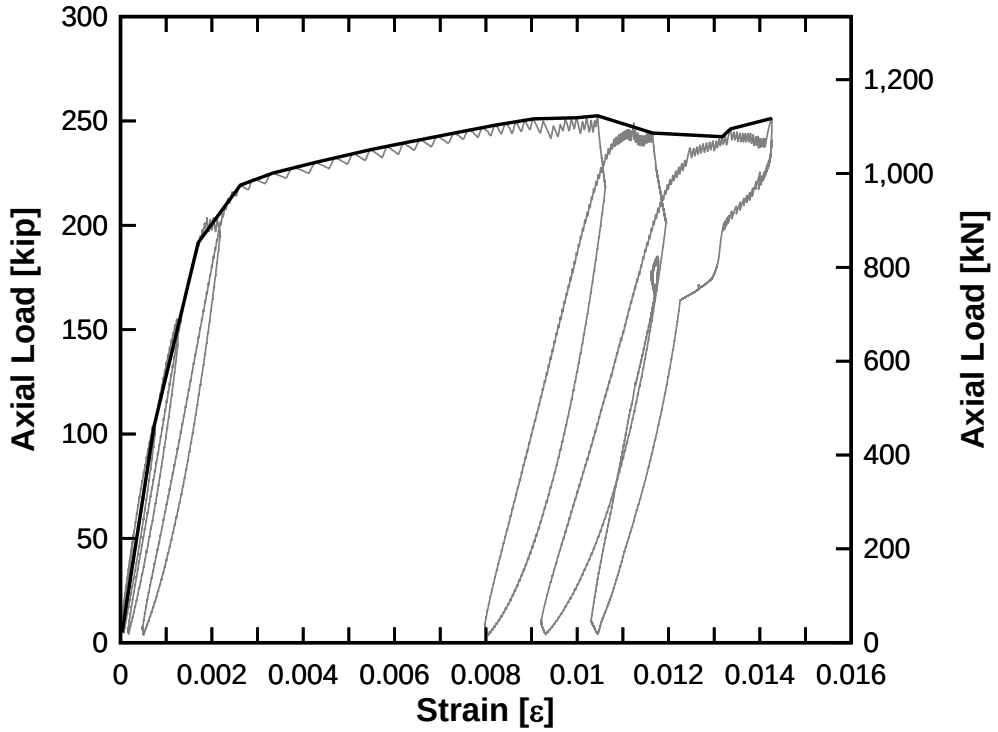

Figure 4-8. RC-Benchmark Back Bar Longitudinal Strain vs. Axial Load

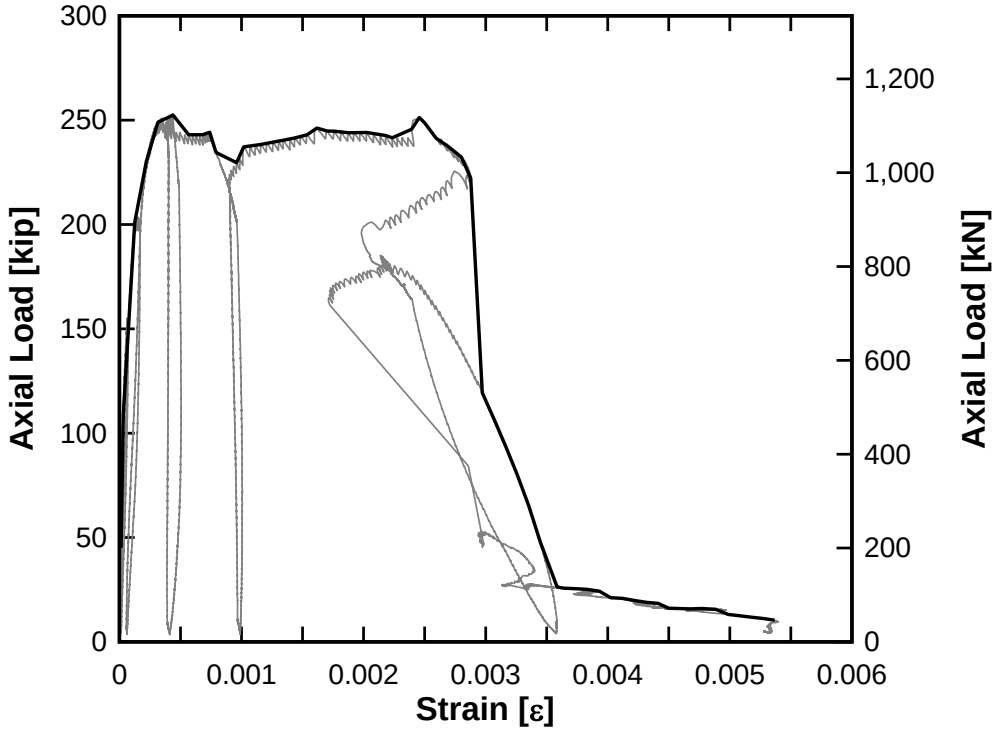

Figure 4-9. RC-Benchmark Side Spiral Strain vs. Axial Load

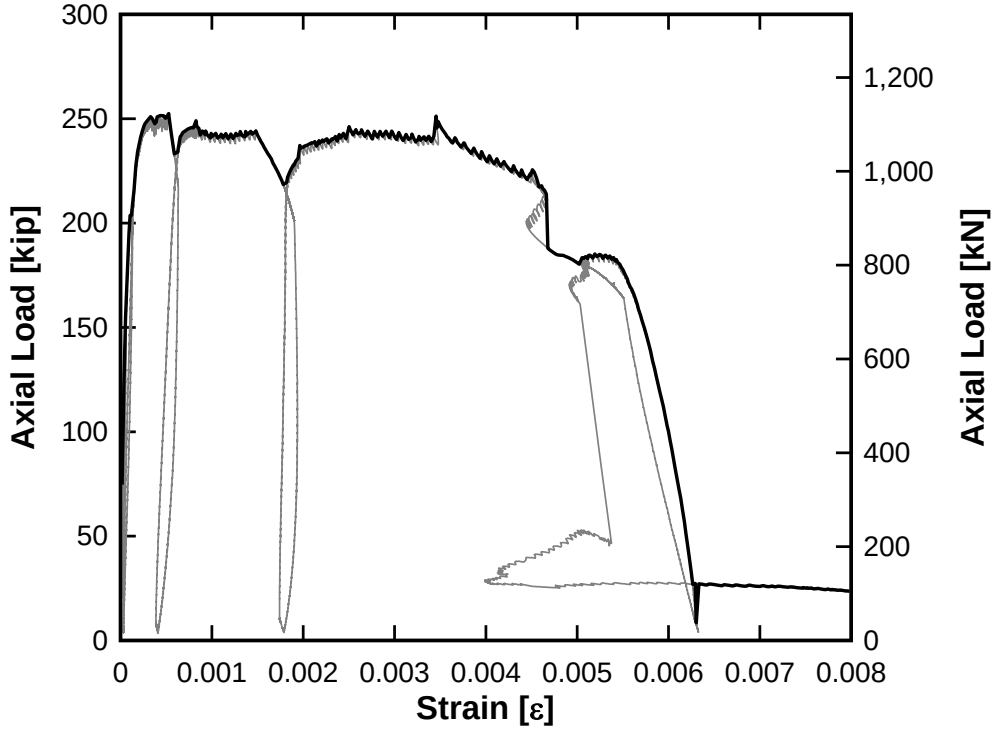

Figure 4-10. RC-Benchmark Front Spiral Strain vs. Axial Load

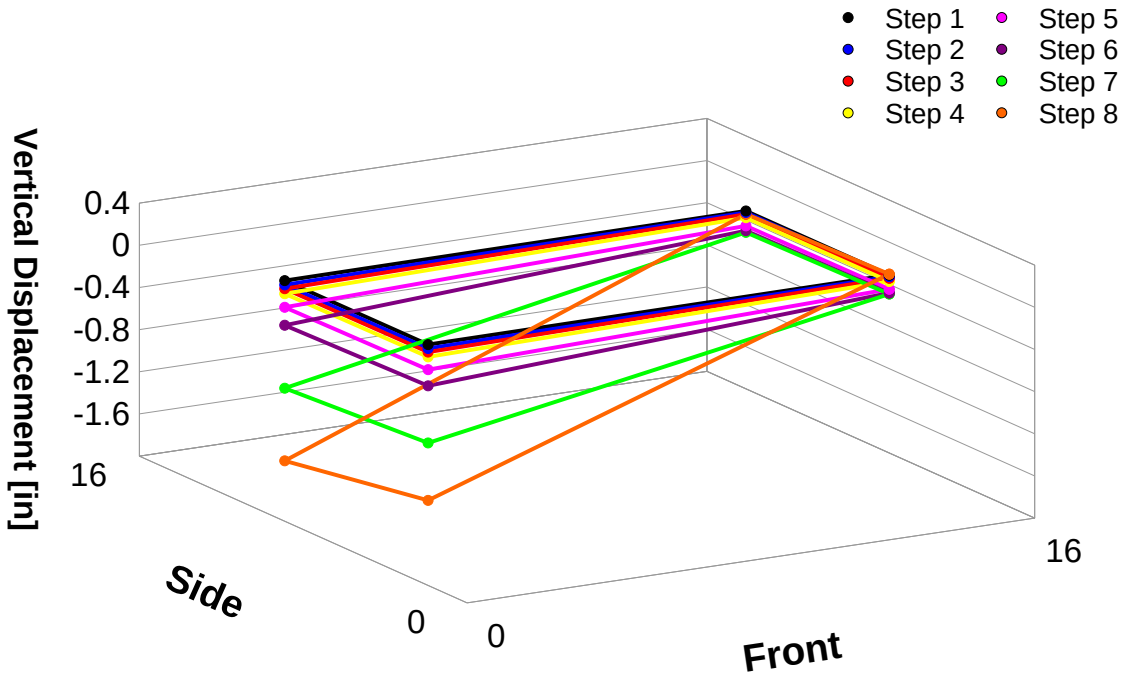

Figure 4-11. RC-Benchmark 3-D Cap Displacement

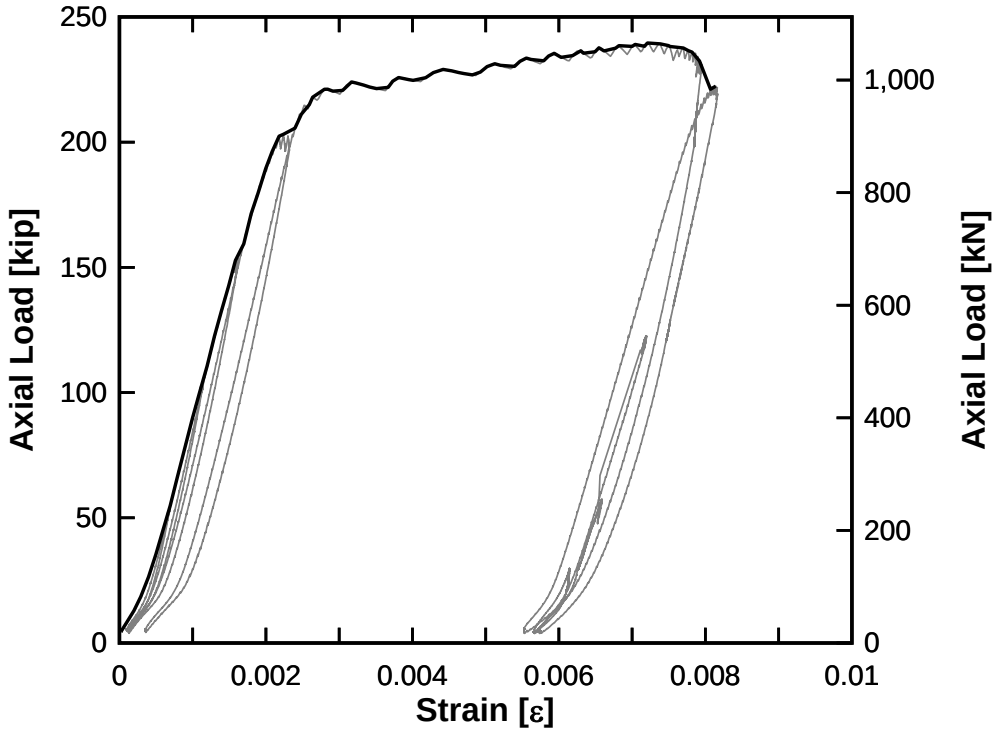

Figure 4-12. RC-Moderate Front Bar Longitudinal Strain vs. Axial Load

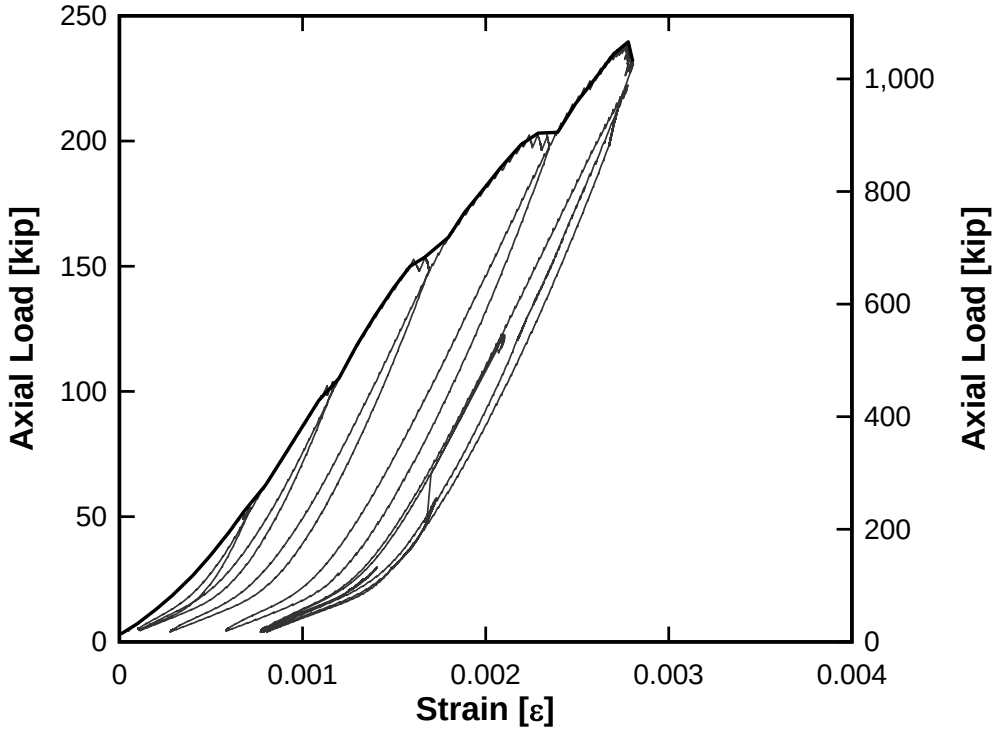

Figure 4-13. RC-Moderate Back Bar Longitudinal Strain vs. Axial Load

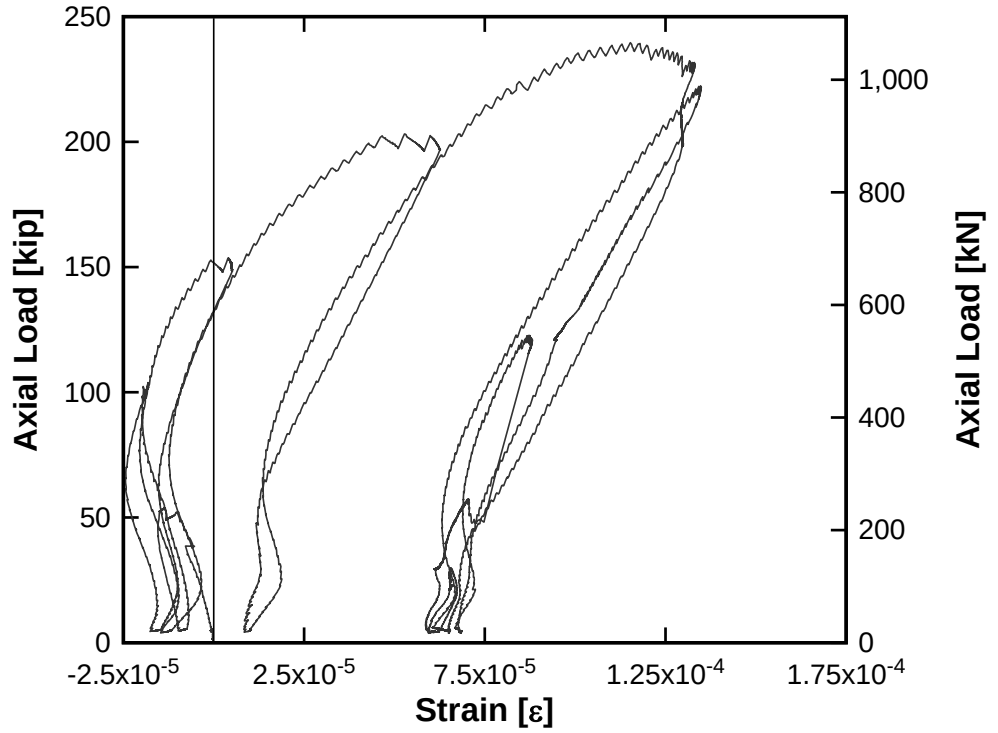

Figure 4-14. RC-Moderate Side Spiral Strain vs. Axial Load

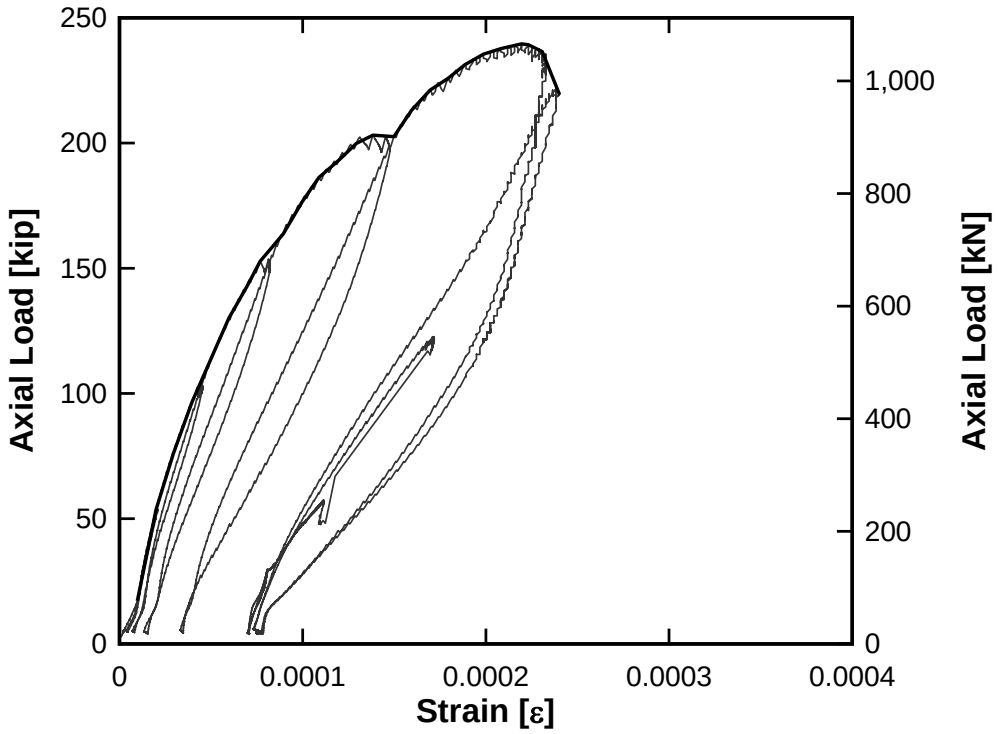

Figure 4-15. RC-Moderate Front Spiral Strain vs. Axial Load

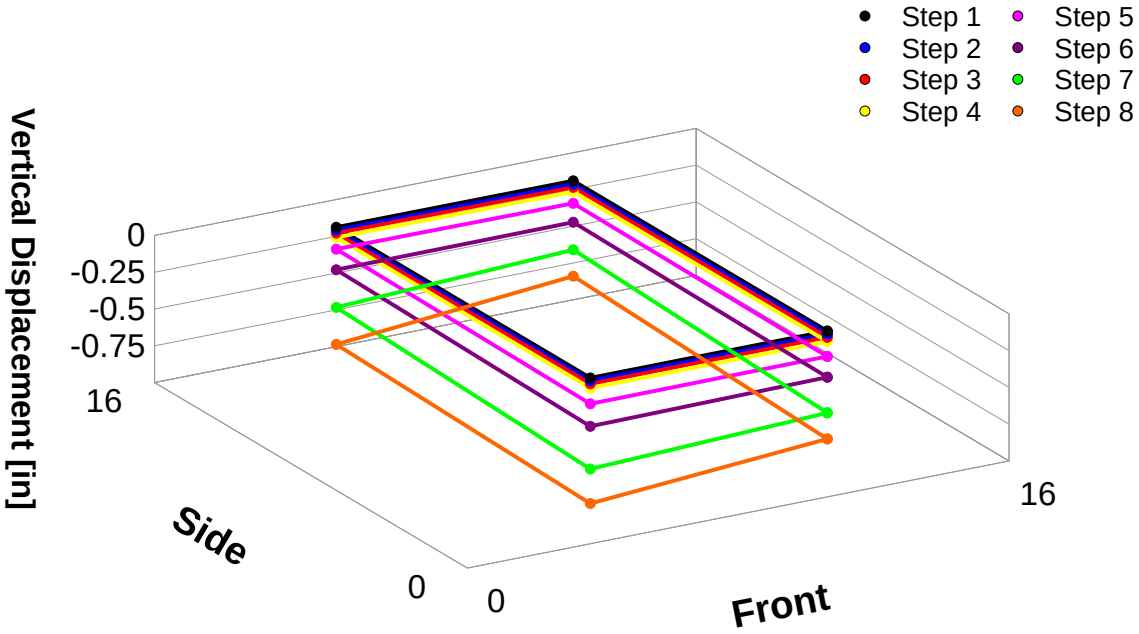

Figure 4-16. RC-Moderate Damage 3-D Cap Displacement

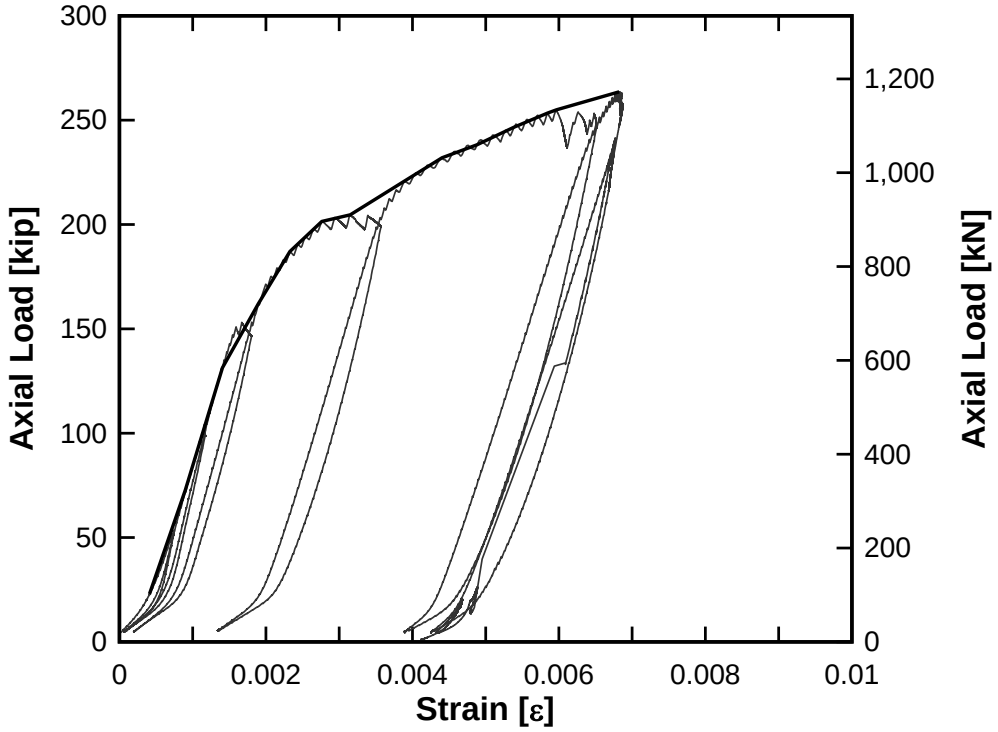

Figure 4-17. RC-Severe Front Bar Longitudinal Strain vs. Axial Load

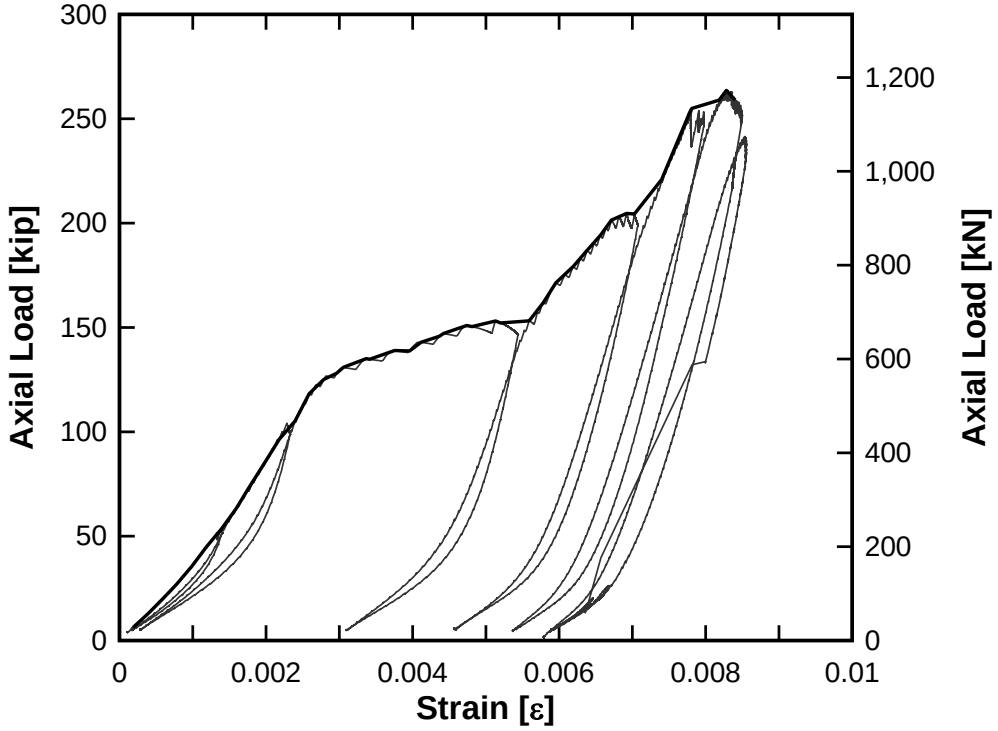

Figure 4-18. RC-Severe Back Bar Longitudinal Strain vs. Axial Load

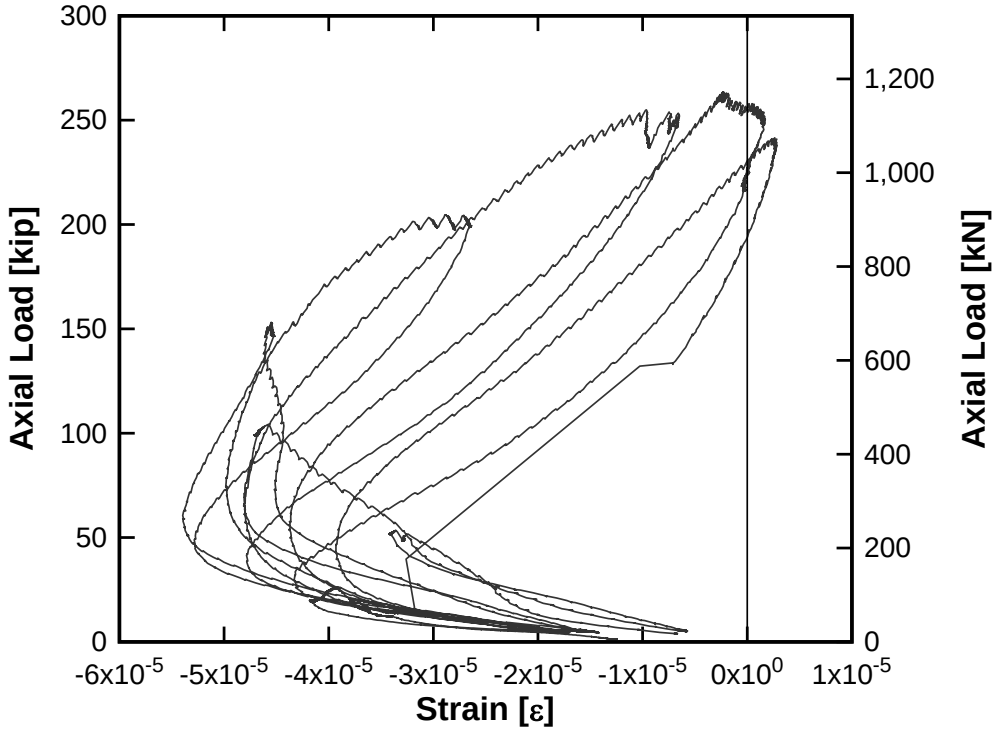

Figure 4-19. RC-Severe Front Spiral Strain vs. Axial Load

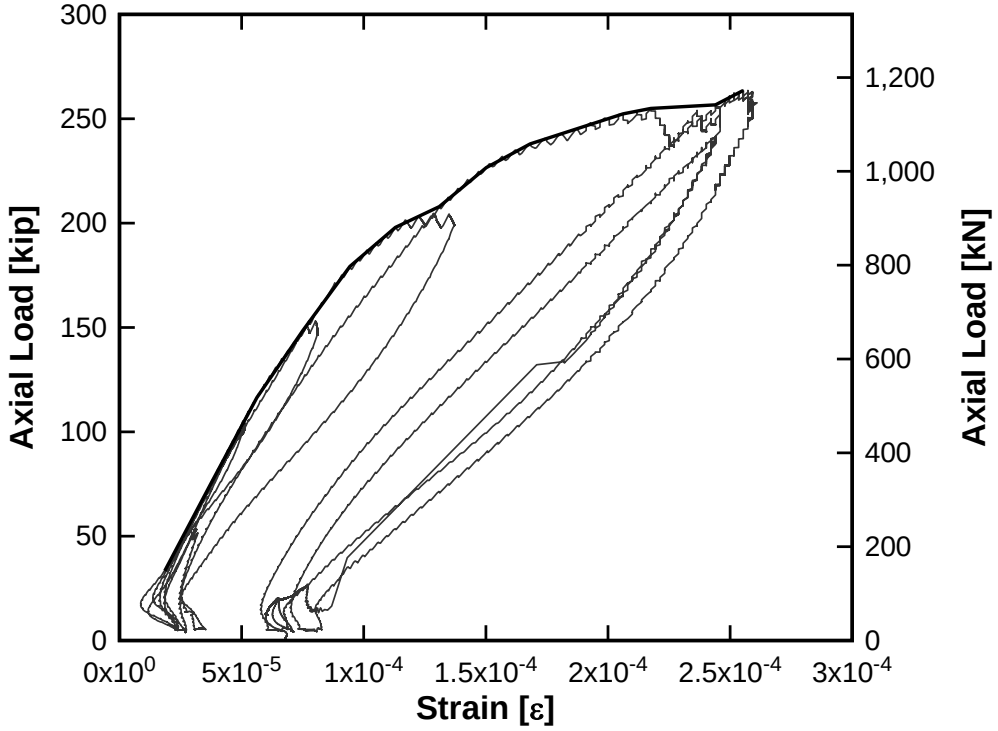

Figure 4-20. RC-Severe Side Spiral Strain vs. Axial Load

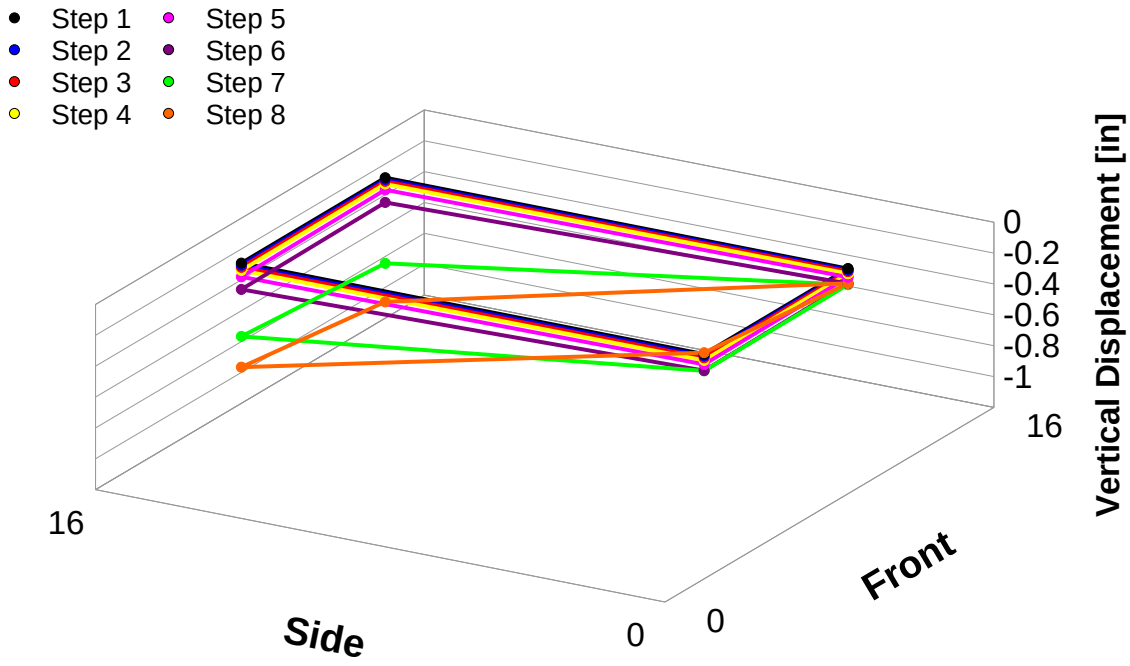

Figure 4-21. RC-Severe Damage 3-D Cap Displacement

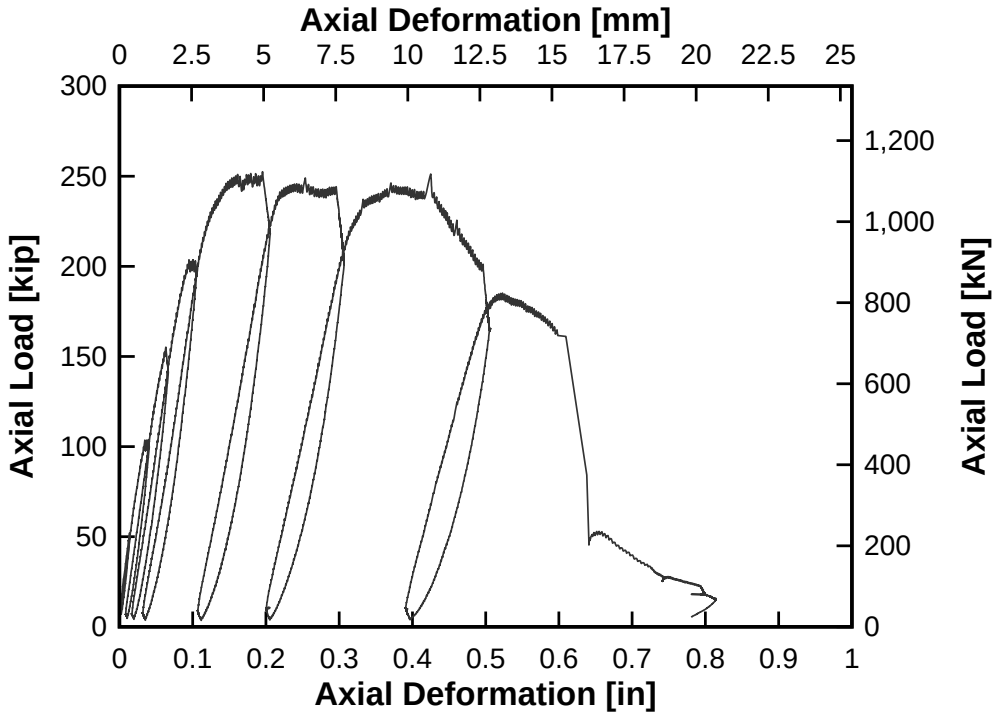

Figure 4-22. RC-Benchmark Axial Load-Deformation Response

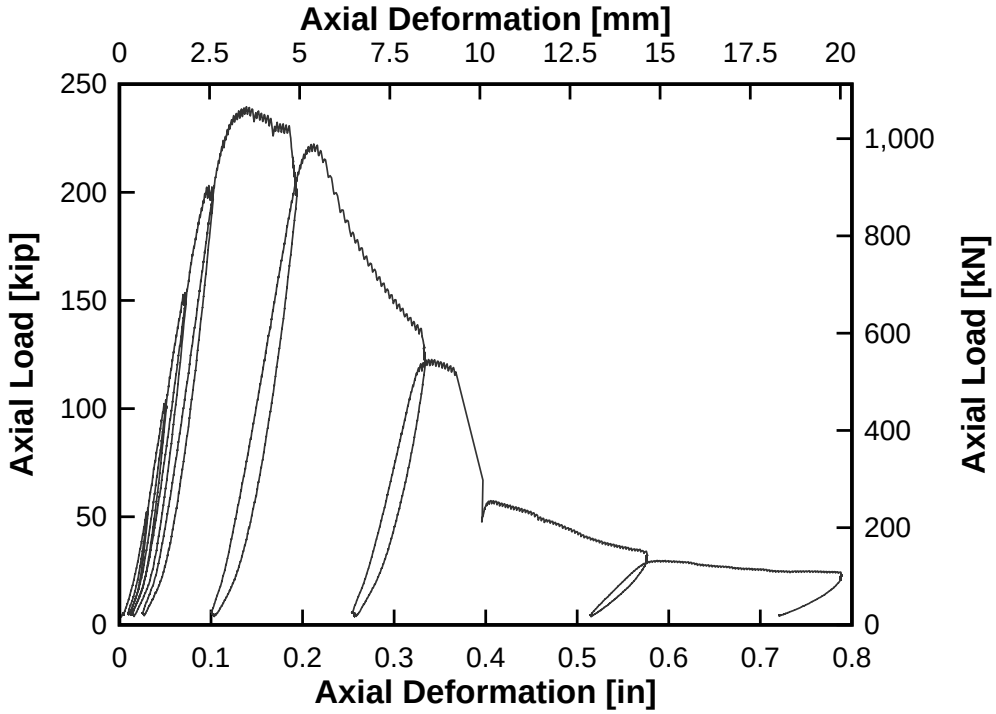

Figure 4-23. RC-Moderate Axial Load-Deformation Response

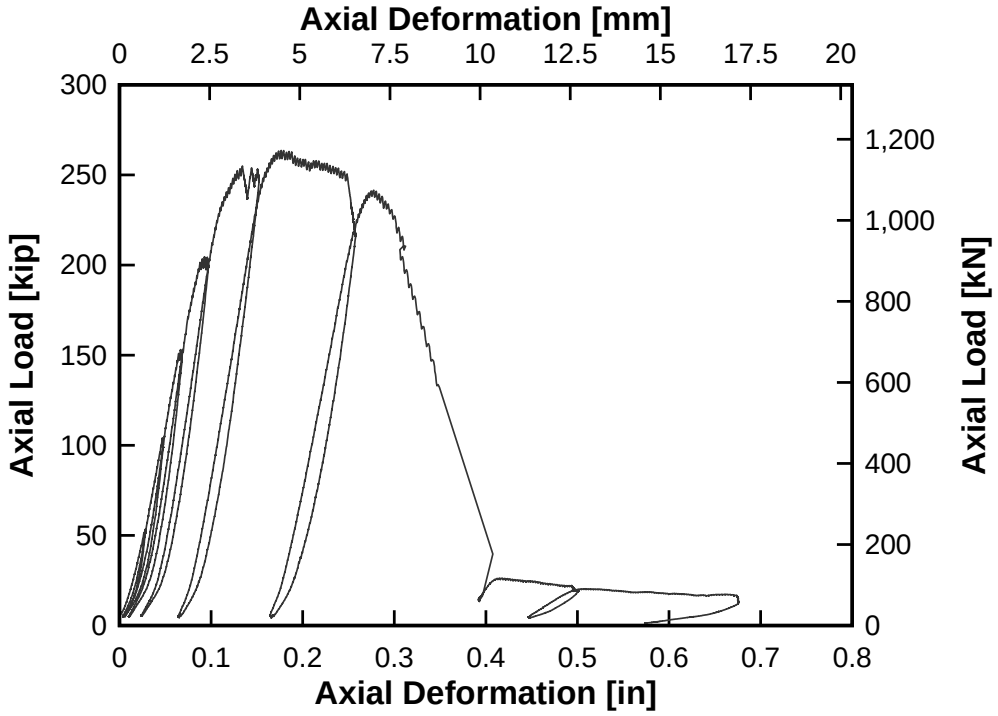

Figure 4-24. RC-Severe Axial Load-Deformation Response

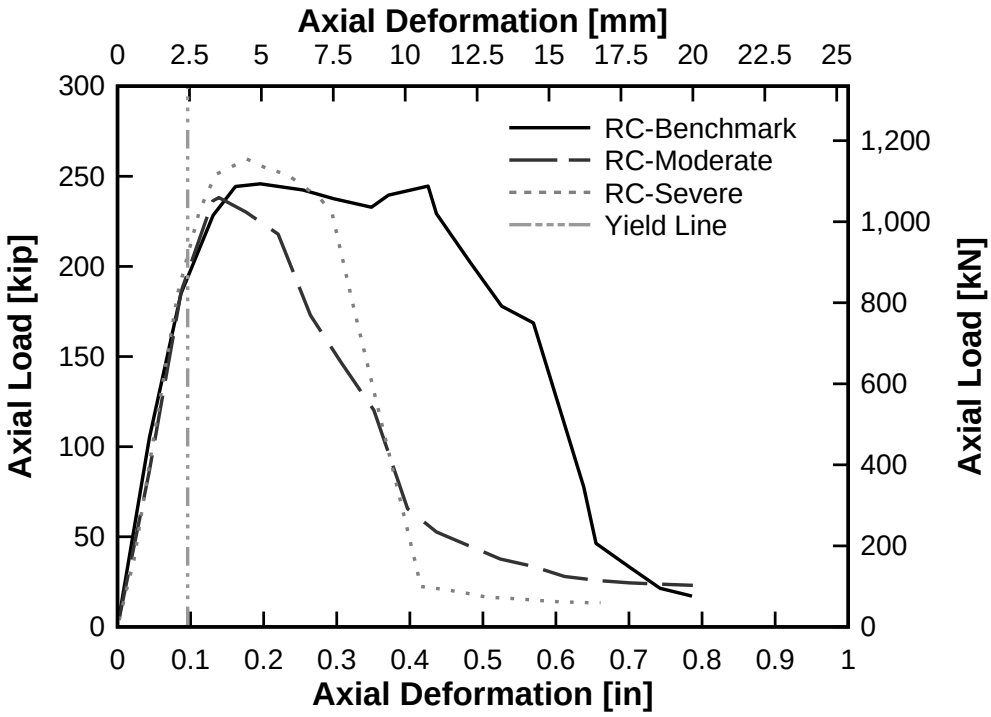

Figure 4-25. RC-Blast Axial Load-Deformation Comparison

Figure 4-26. Failure Progression of CFFT-Benchmark Column

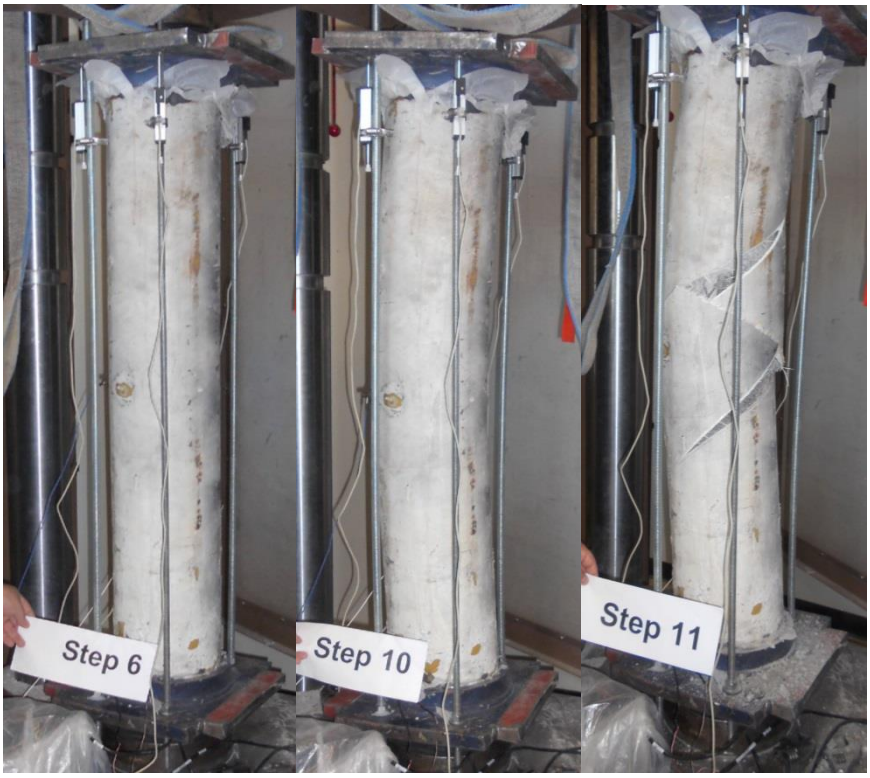

Figure 4-27. Failure Progression of CFFT-Moderate Column

Figure 4-28. Failure Progression of CFFT-Severe Column

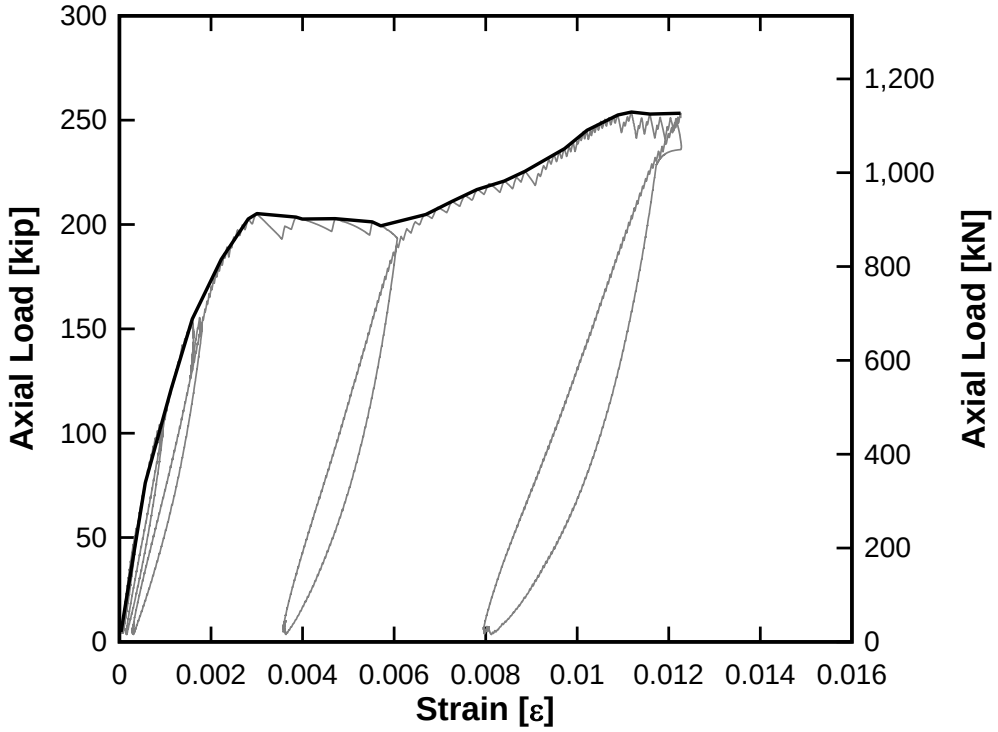

Figure 4-29. CFFT-Benchmark Front Bar Longitudinal Strain vs. Axial Load

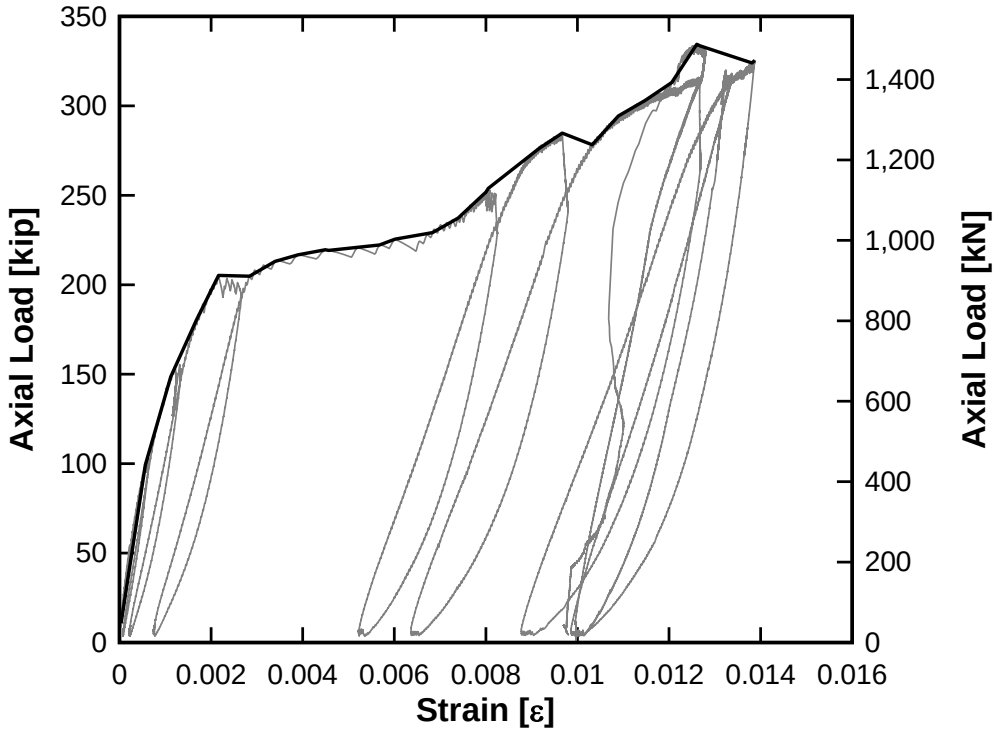

Figure 4-30. CFFT-Benchmark Back Bar Longitudinal Strain vs. Axial Load

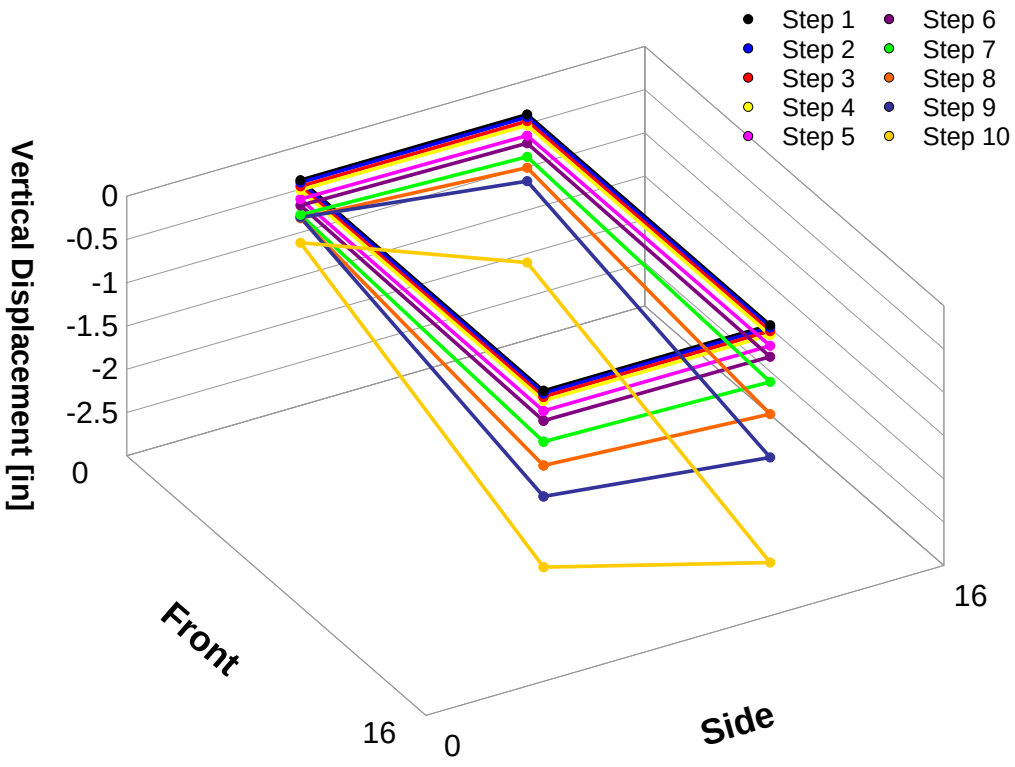

Figure 4-31. CFFT-Benchmark 3-D Cap Displacement

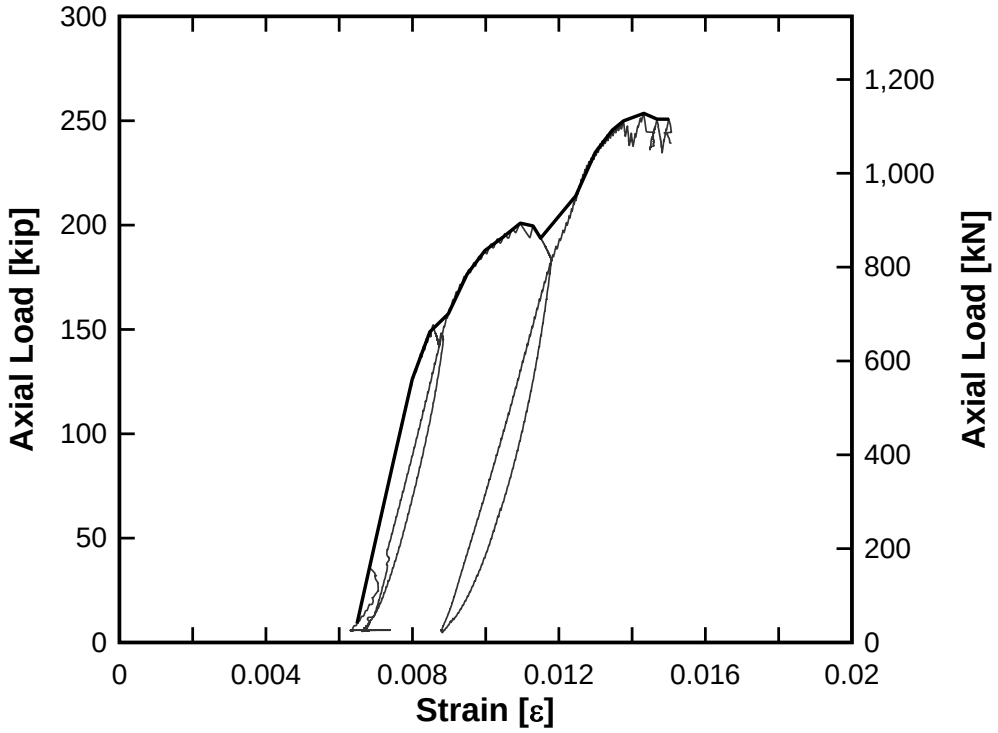

Figure 4-32. CFFT-Moderate Back Bar Longitudinal Strain vs. Axial Load

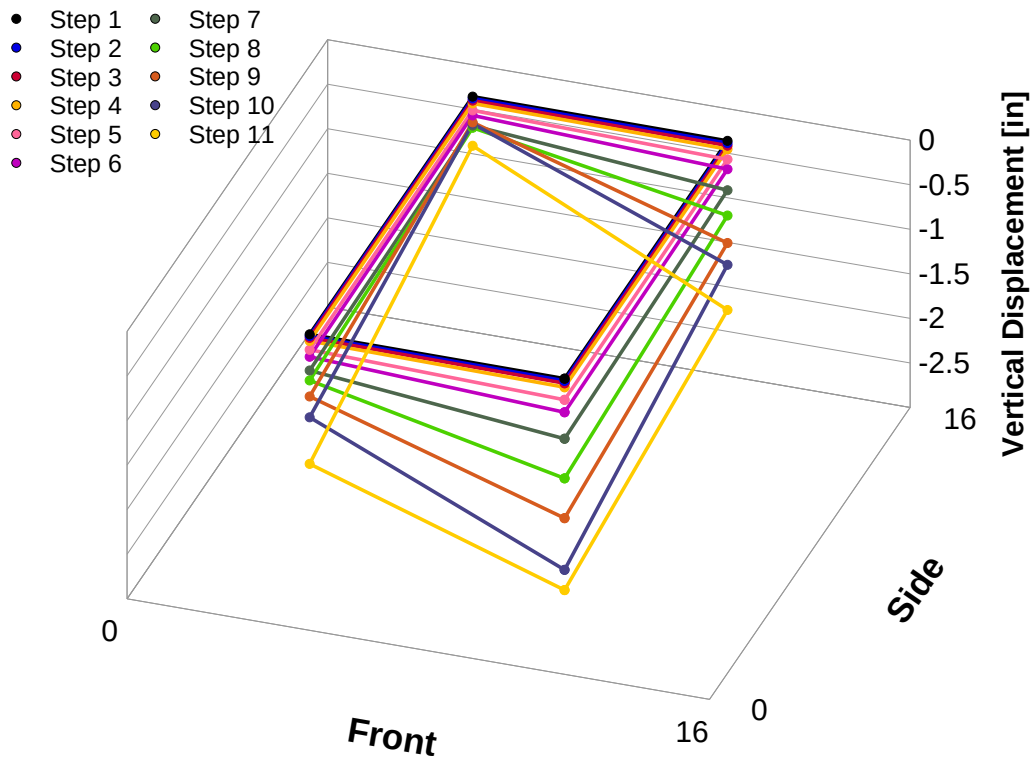

Figure 4-33. CFFT-Moderate 3-D Cap Displacement

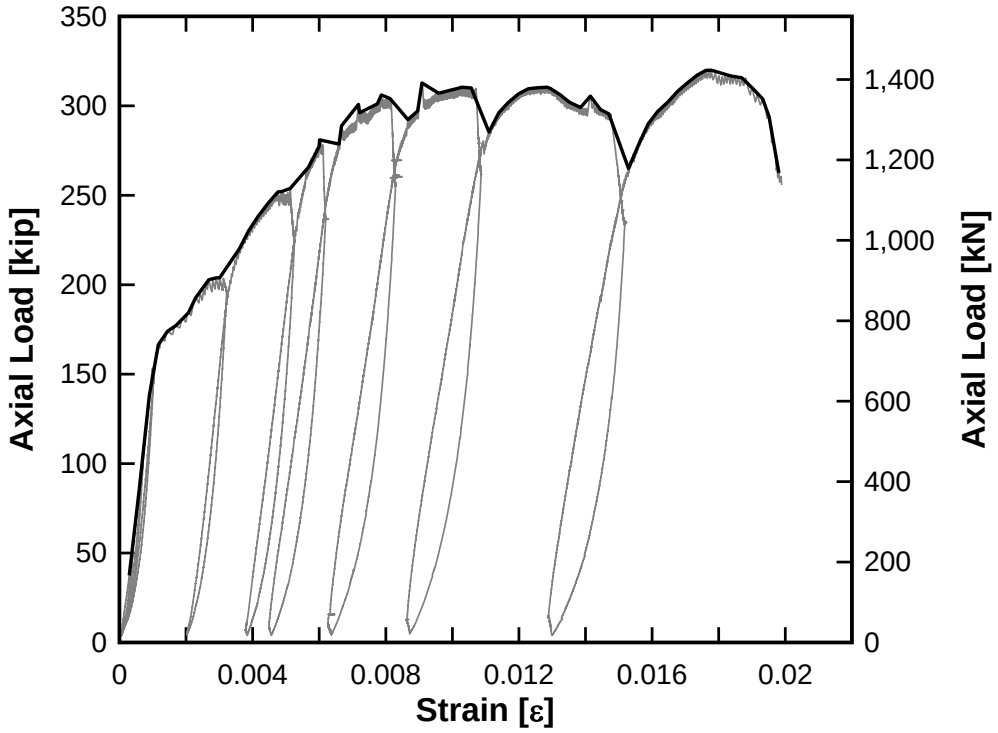

Figure 4-34. CFFT-Severe Front Bar Longitudinal Strain vs. Axial Load

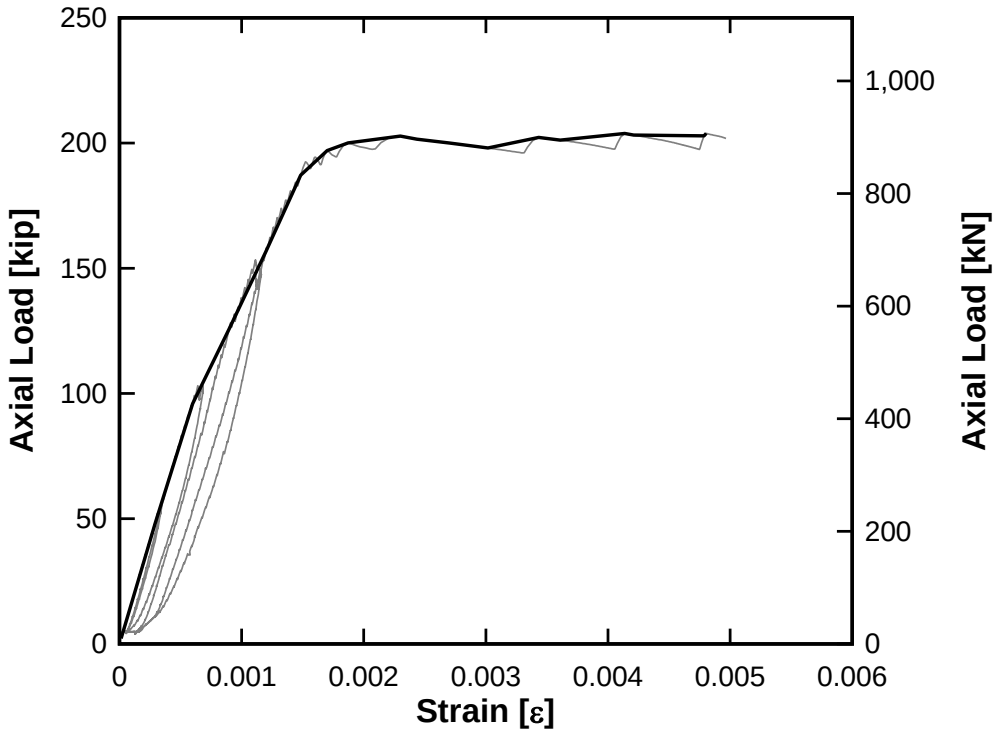

Figure 4-35. CFFT-Severe Back Bar Longitudinal Strain vs. Axial Load

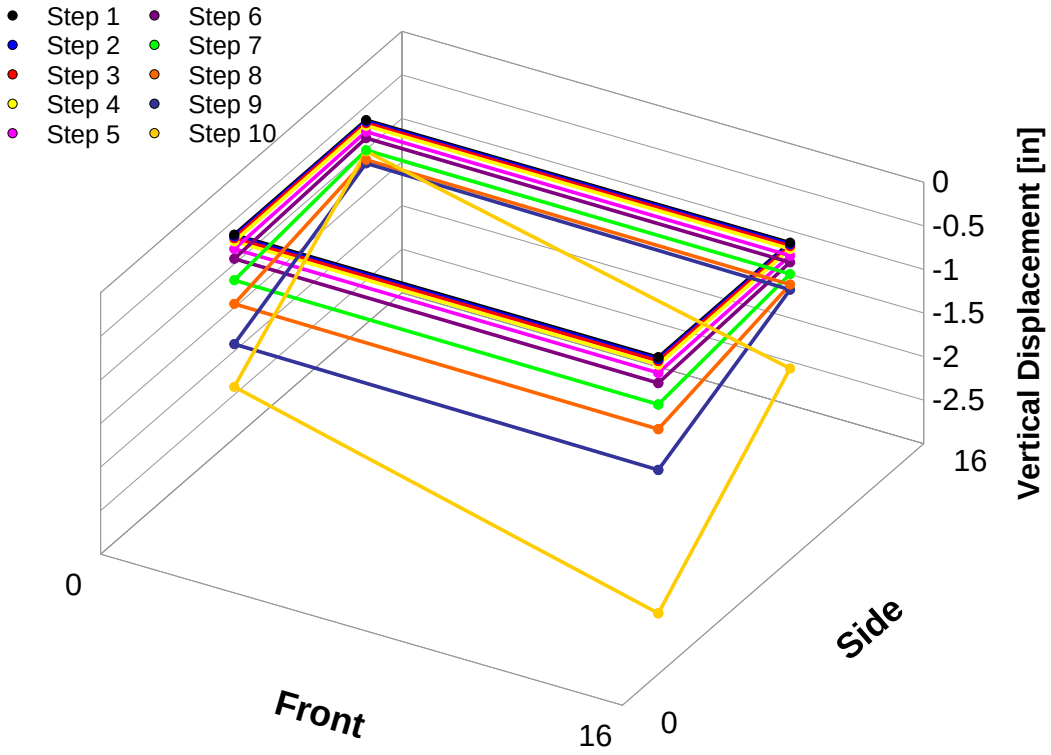

Figure 4-36. CFFT-Severe 3-D Cap Displacement

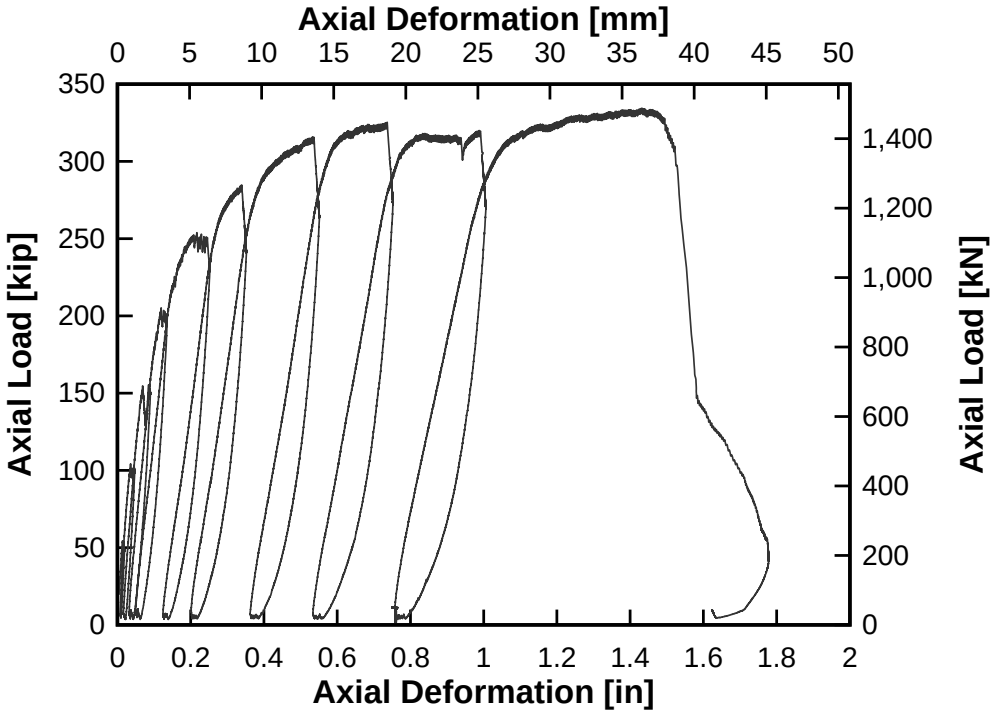

Figure 4-37. CFFT-Benchmark Axial Load-Deformation Response

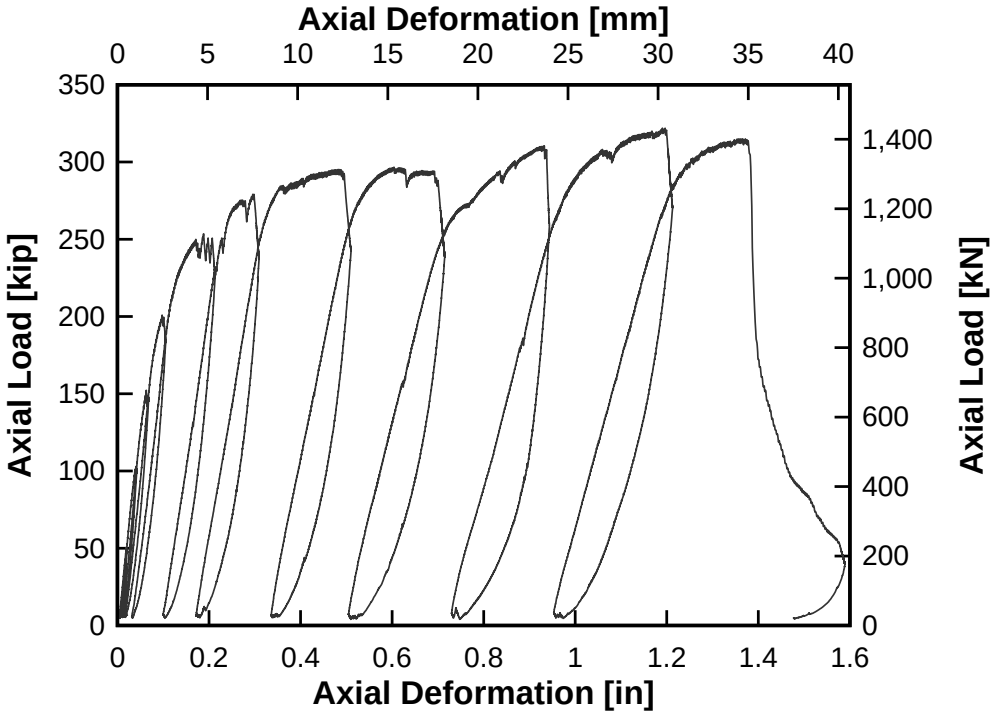

Figure 4-38. CFFT-Moderate Axial Load-Deformation Response

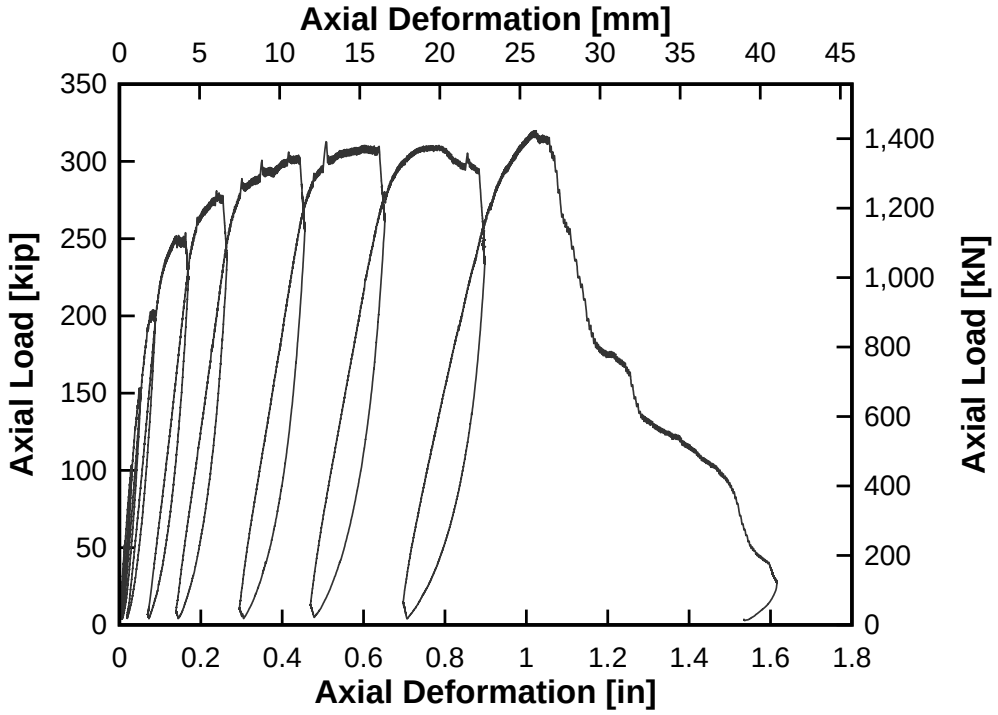

Figure 4-39. CFFT-Severe Axial Load-Deformation Response

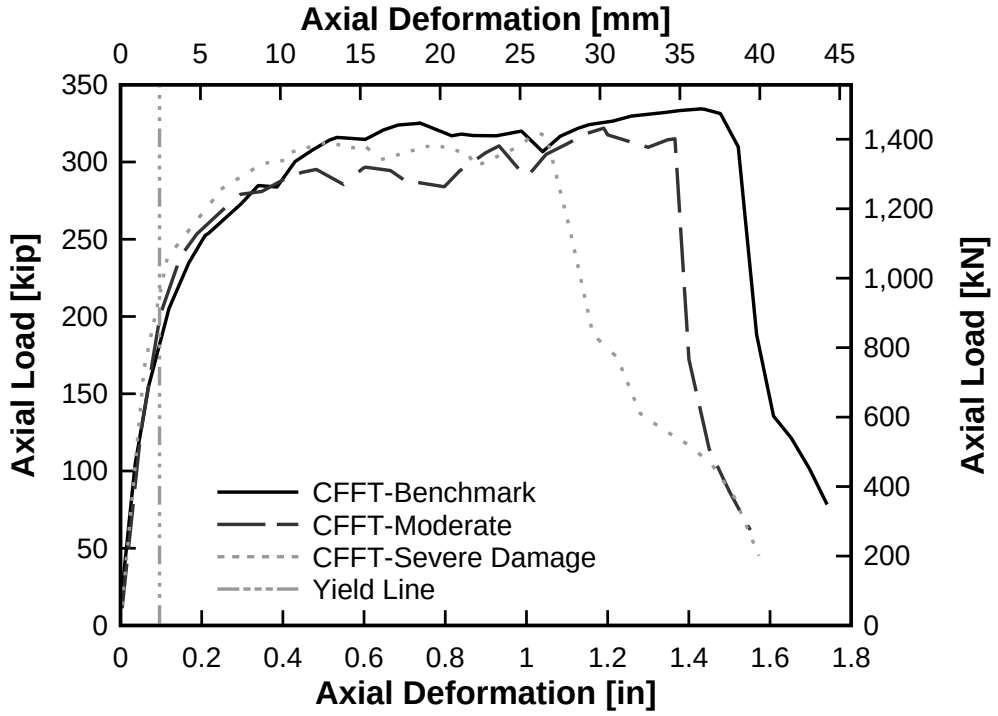

Figure 4-40. CFFT-Blast Axial Load-Deformation Comparison

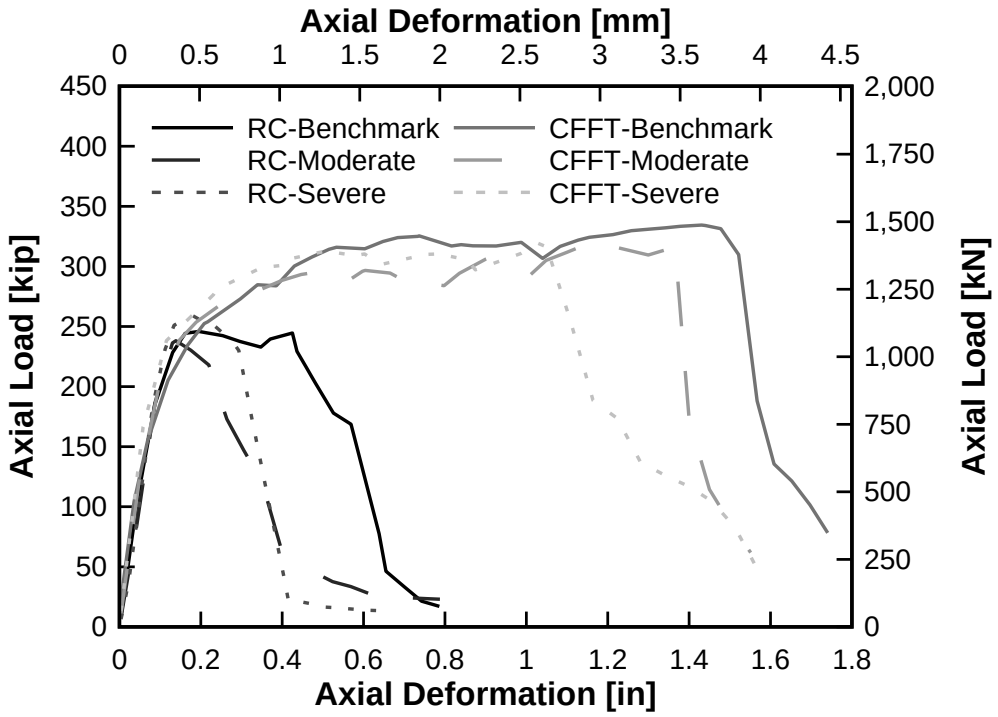

Figure 4-41. RC- and CFFT-Blast Axial Load-Deformation Comparison

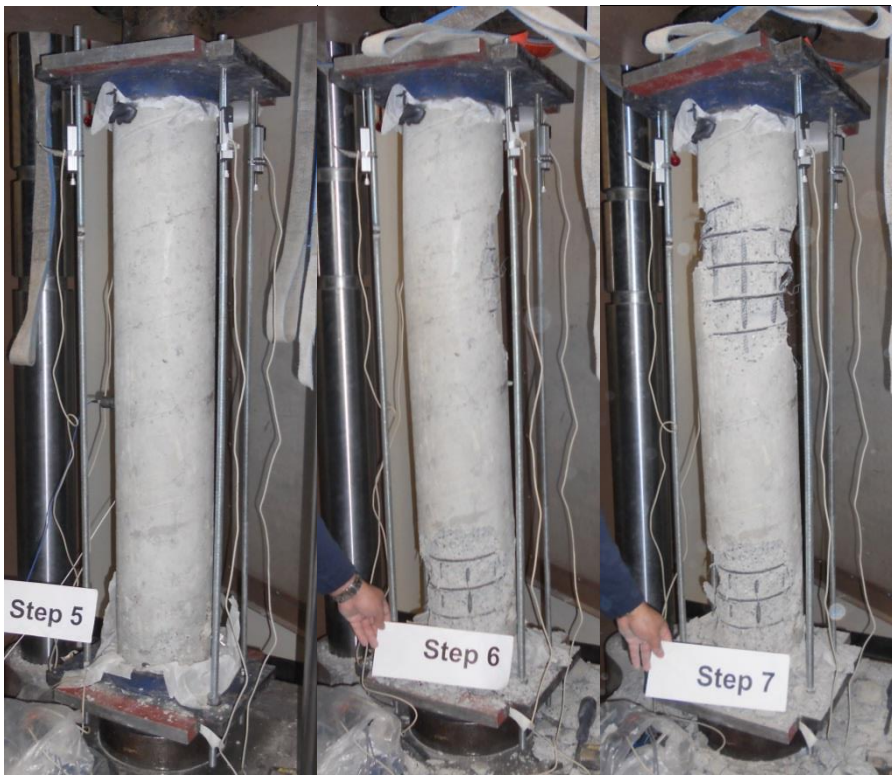

Figure 4-42. Failure Progression of RC-1Hr Column

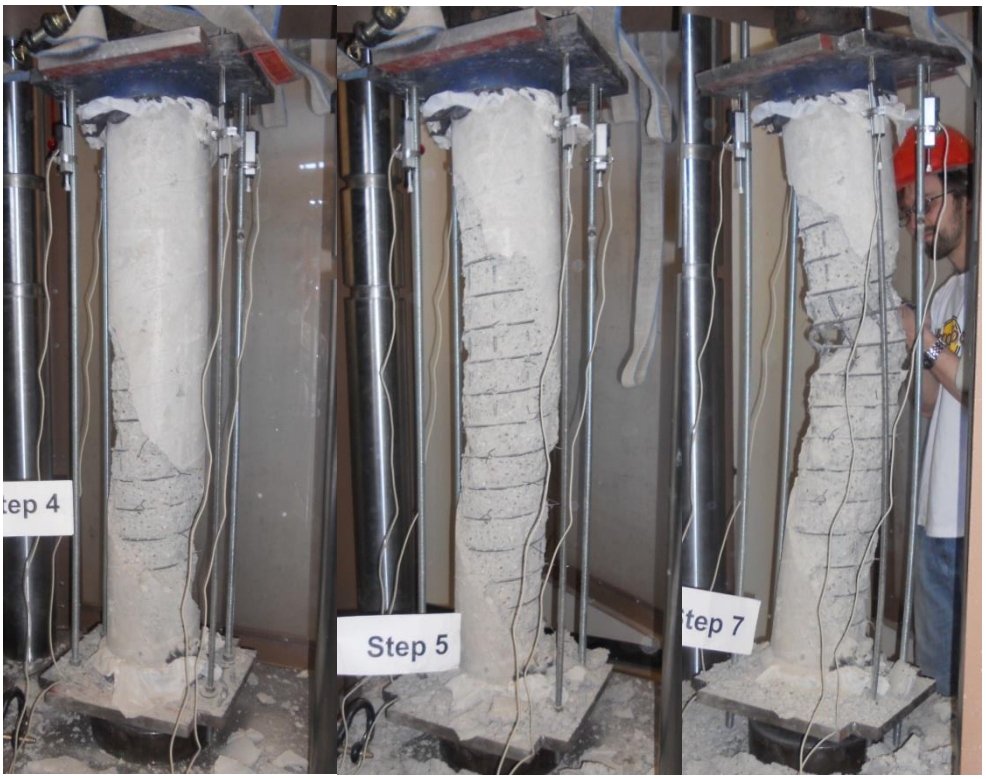

Figure 4-43. Failure Progression of RC-2Hr Column

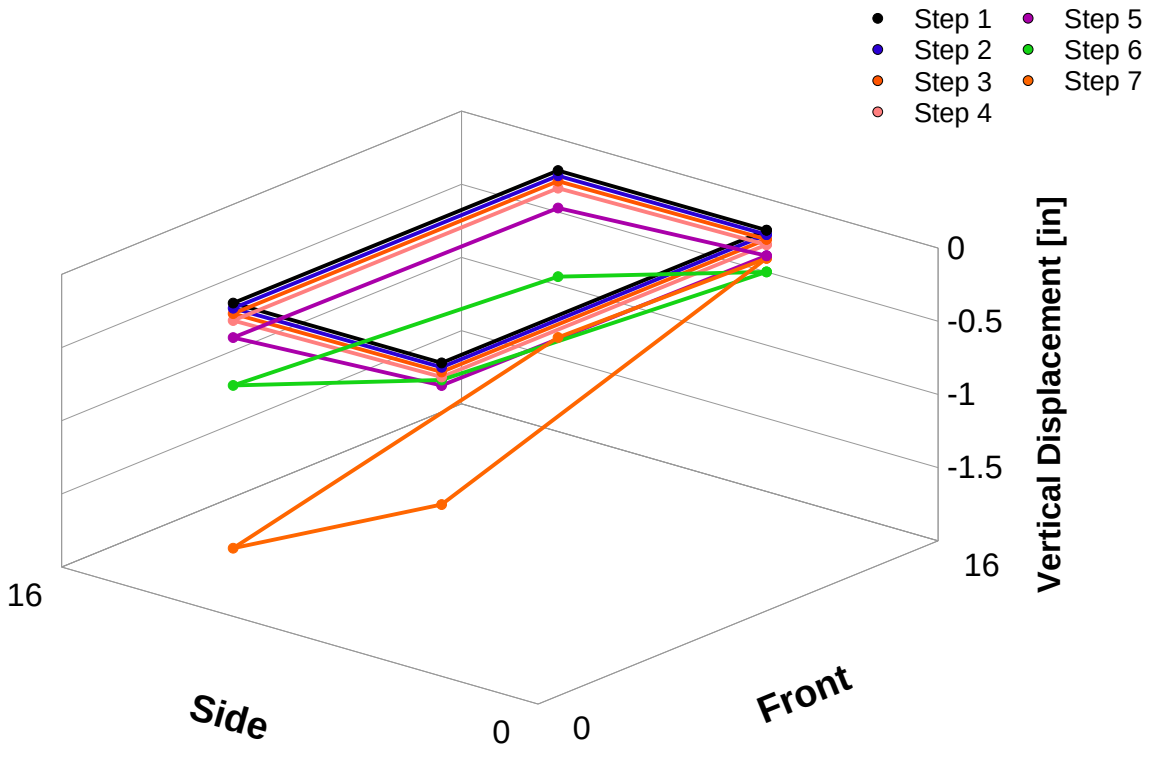

Figure 4-44. RC-1-Hr 3-D Cap Displacement

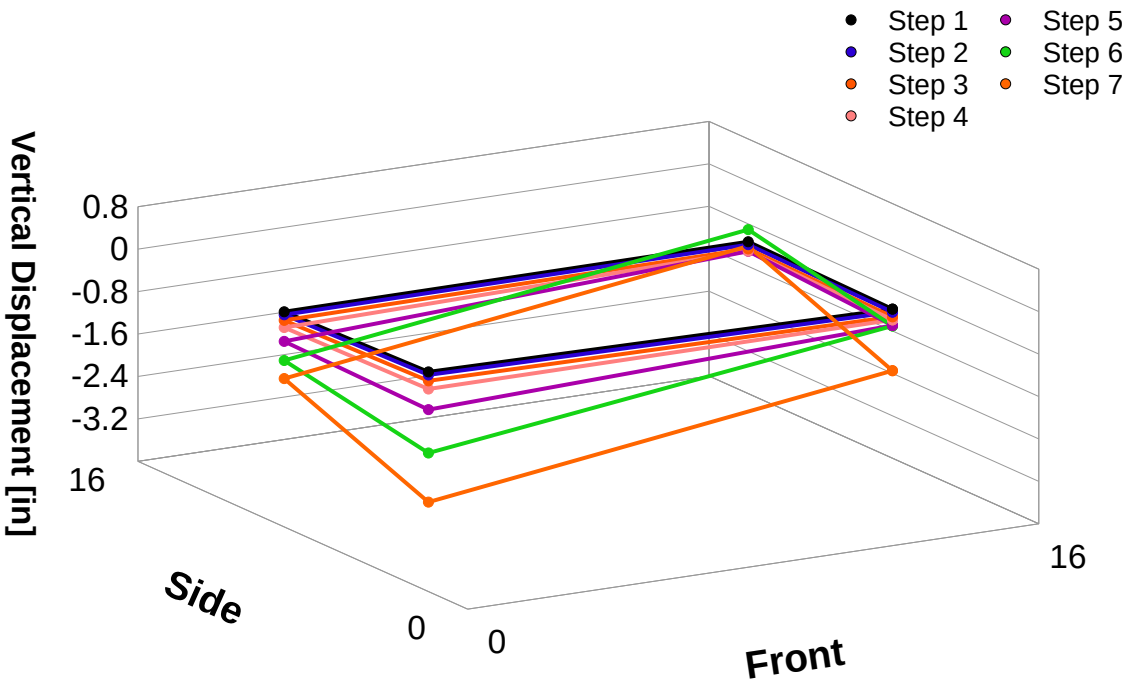

Figure 4-45. RC-2-Hr 3-D Cap Displacement

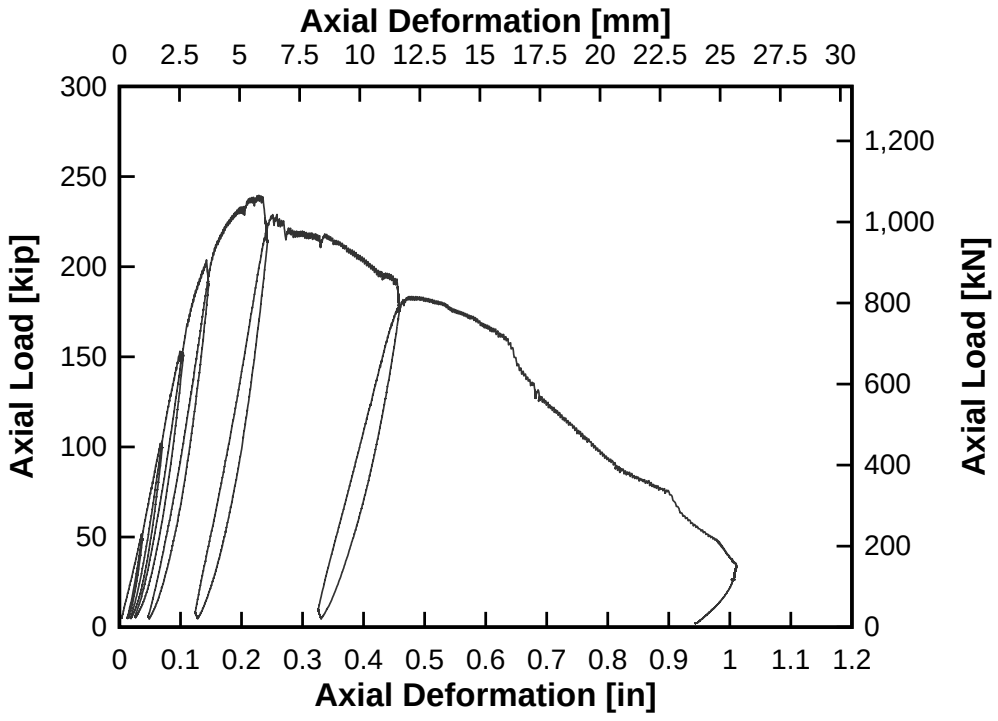

Figure 4-46. RC-1Hr Axial Load-Deformation Response

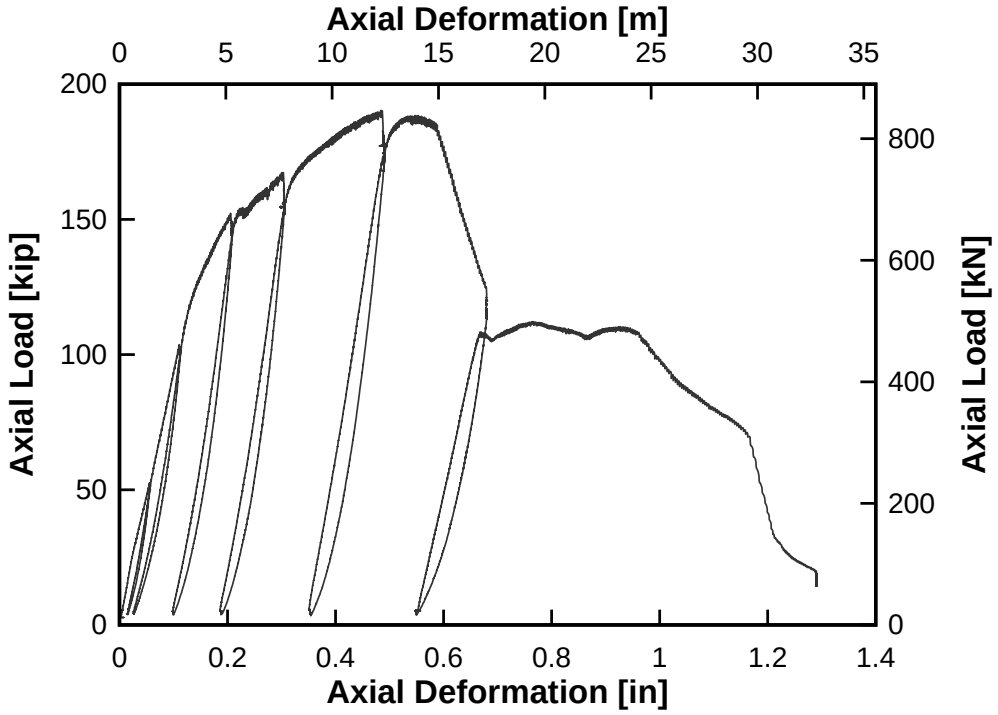

Figure 4-47. RC-2Hr Axial Load-Deformation Response

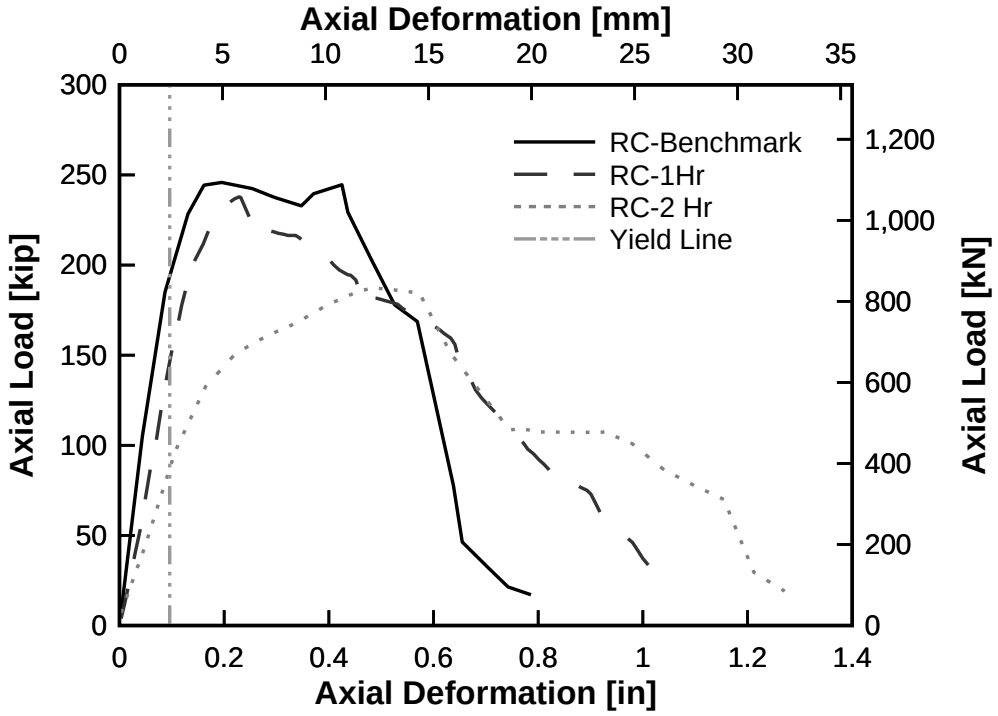

Figure 4-48. RC-Fire Axial Load-Deformation Comparison

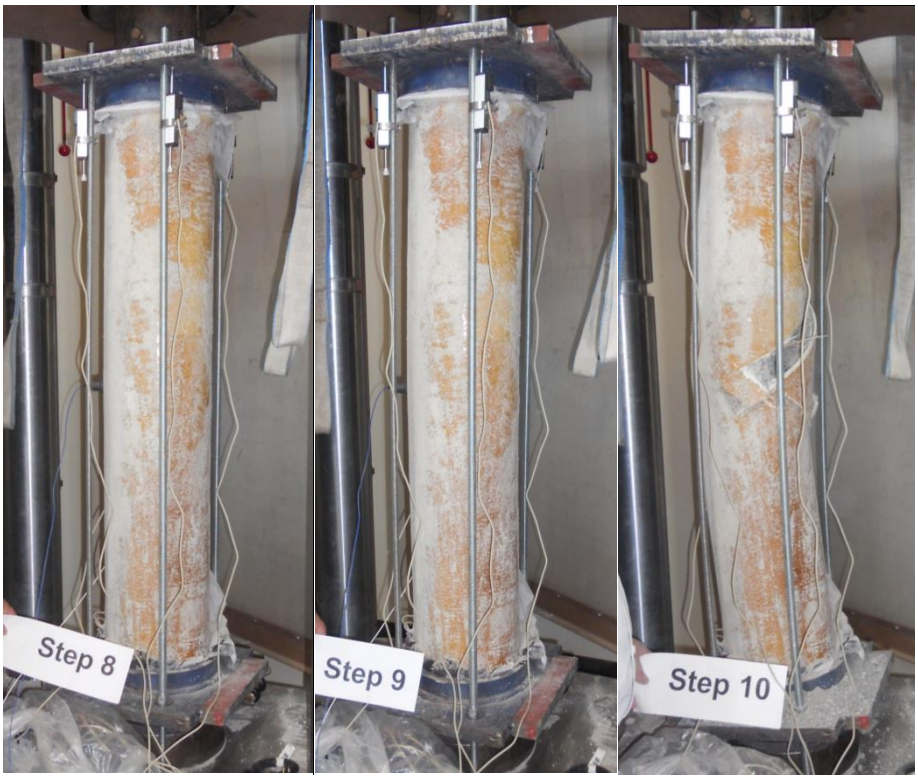

Figure 4-49. Failure Progression of CFFT-1Hr Column

Figure 4-50. Failure Progression of CFFT-2Hr Column

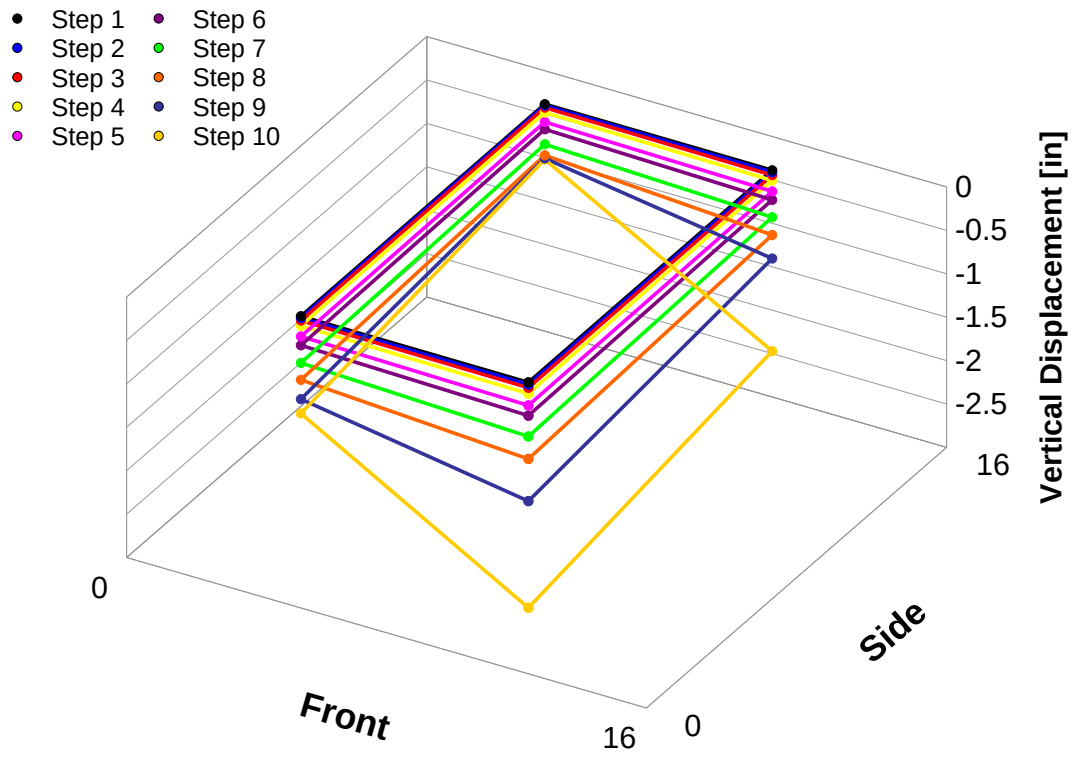

Figure 4-51. CFFT-1Hr 3-D Cap Displacement

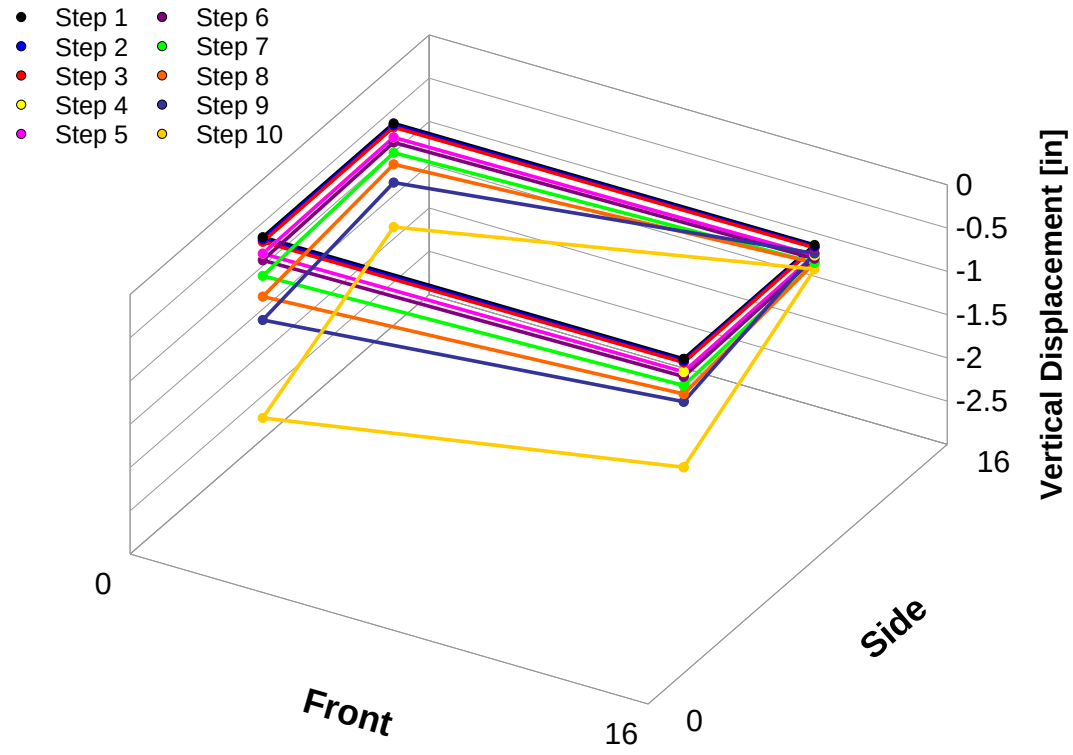

Figure 4-52. CFFT-2Hr 3-D Cap Displacement

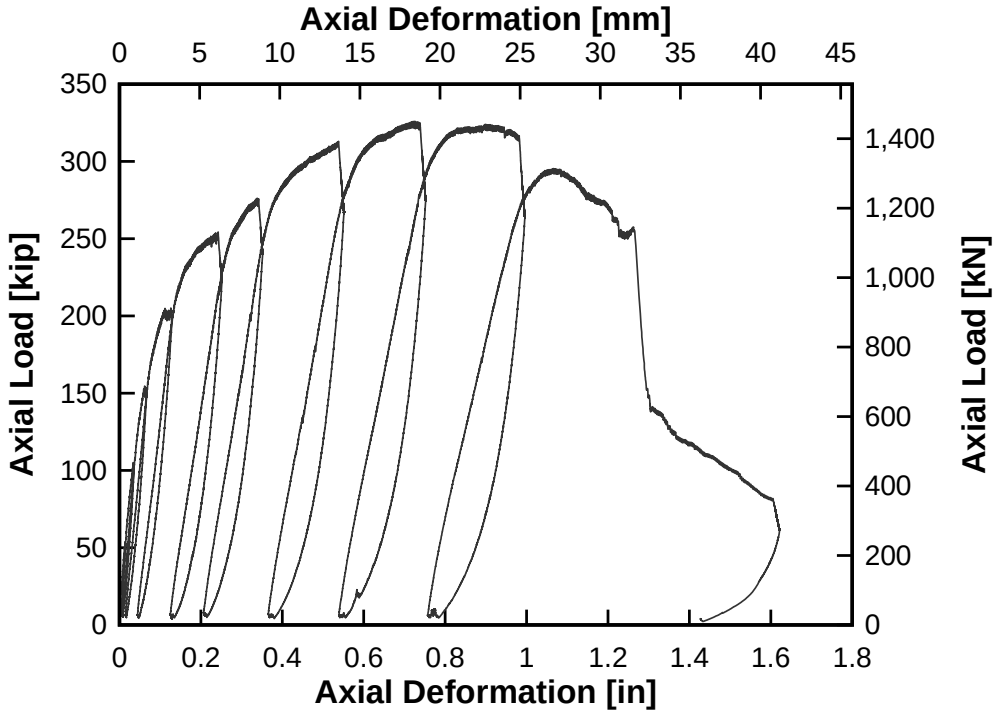

Figure 4-53. CFFT-1Hr Axial Load-Deformation Response

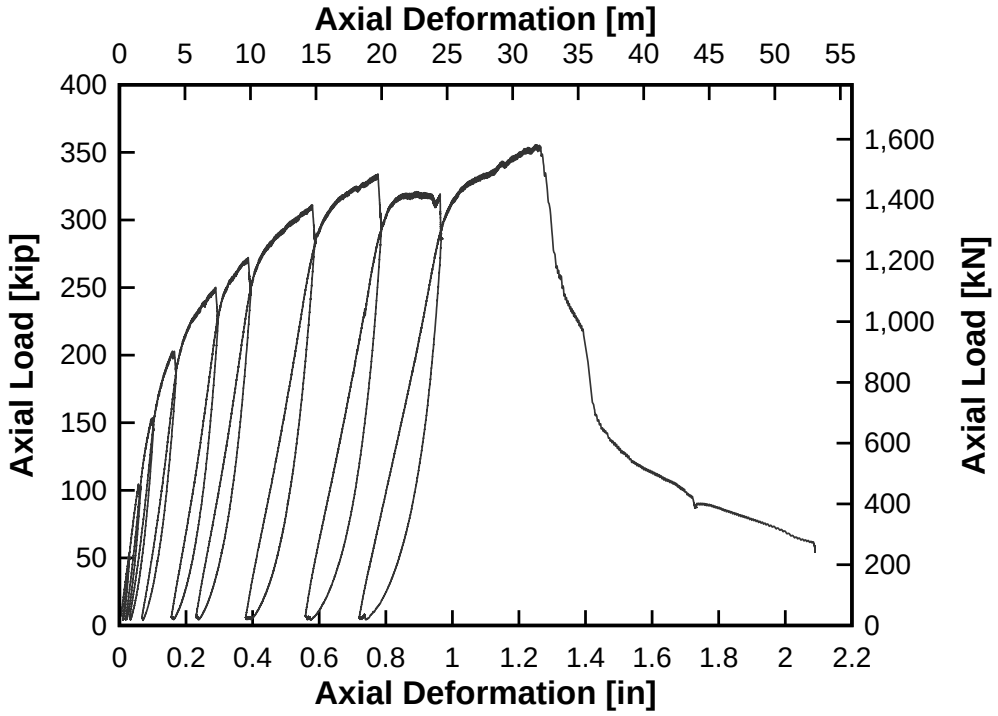

Figure 4-54. CFFT-1Hr Axial Load-Deformation Response

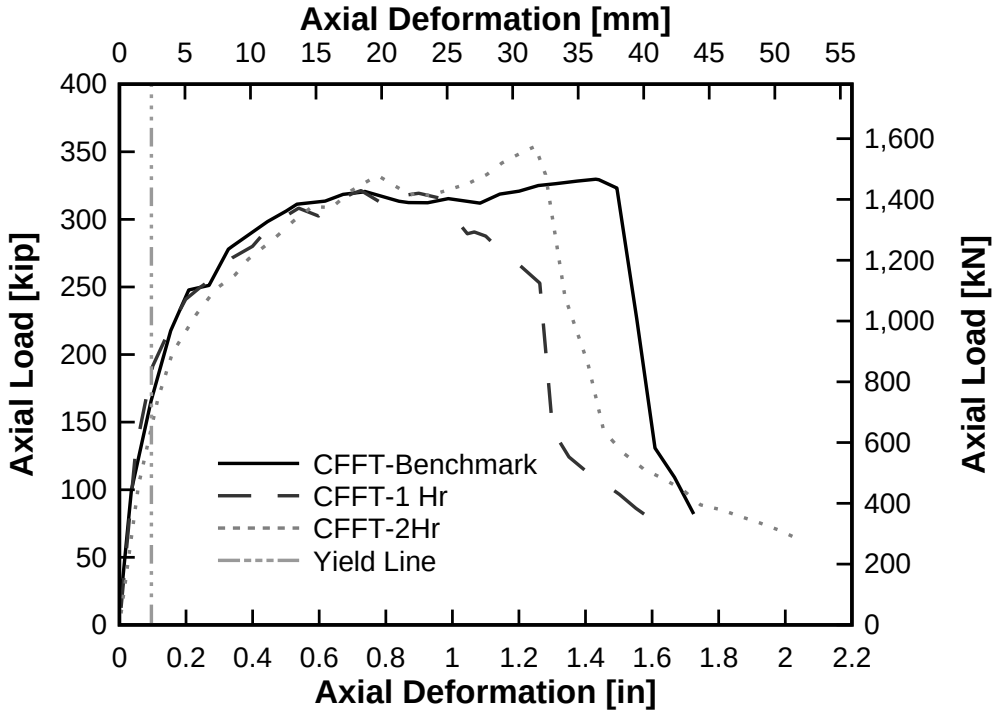

Figure 4-55. CFFT-Fire Axial Load-Deformation Comparison

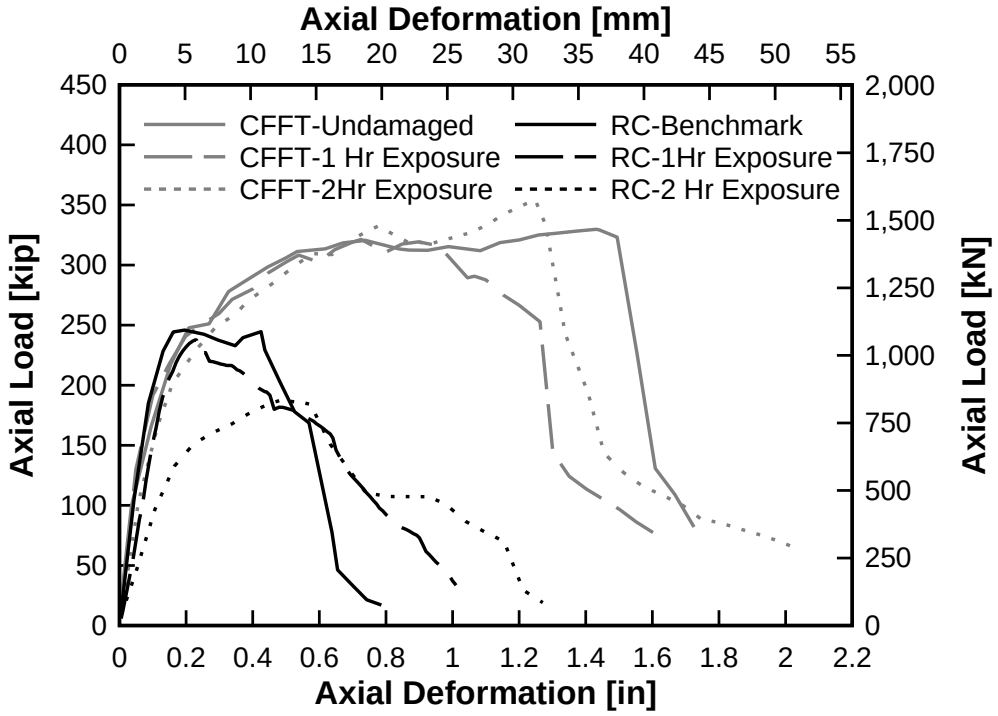

Figure 4-56. RC- and CFFT-Fire Axial Load-Deformation Comparison

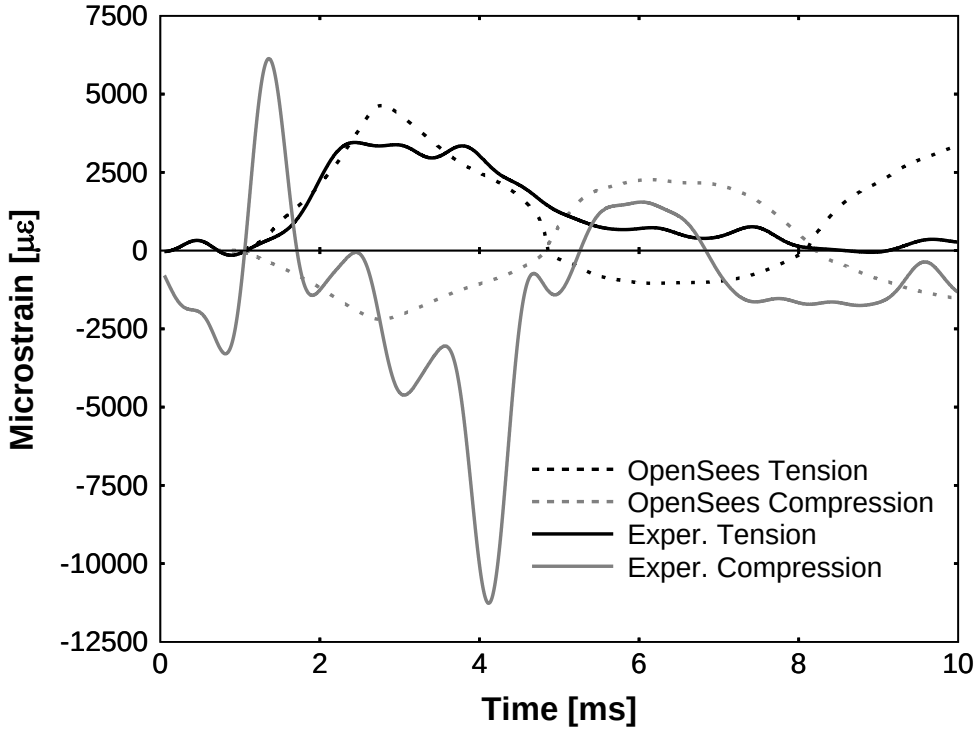

Figure 5-1. RC-Moderate Experimental and Analytical Strain History Comparison

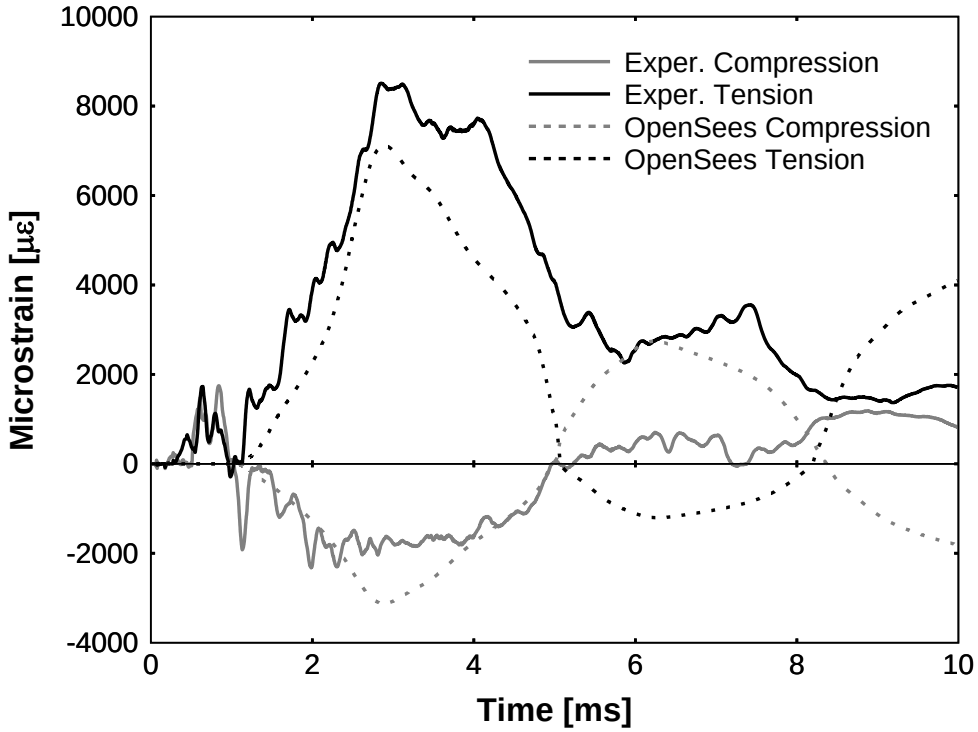

Figure 5-2. RC-Severe Experimental and Analytical Strain History Comparison

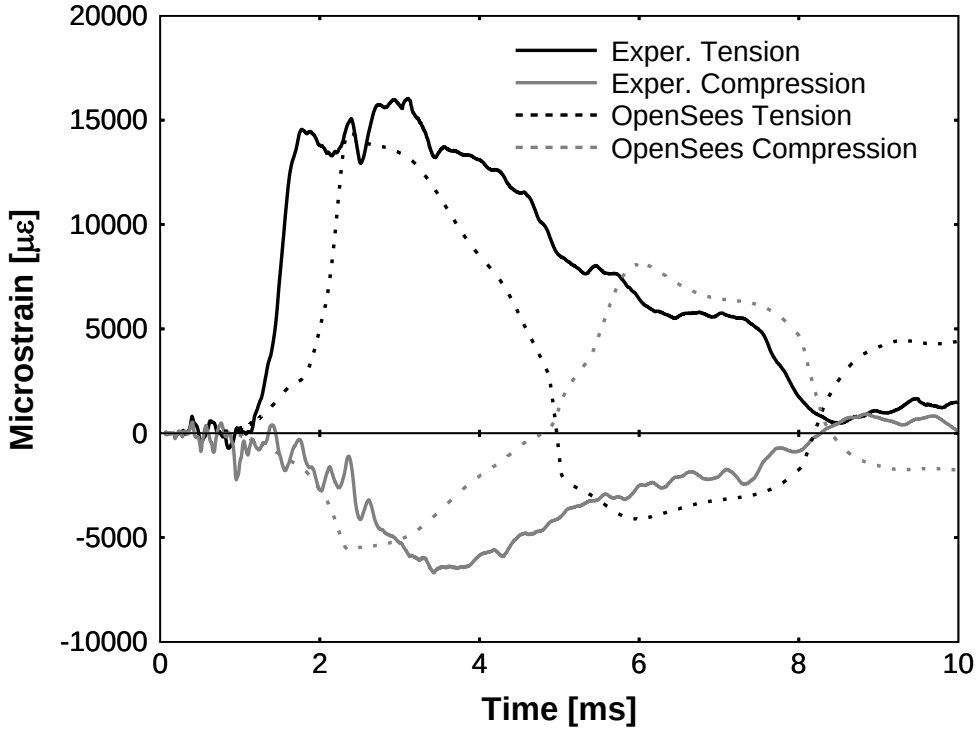

Figure 5-3. RC-Severe-2 Experimental and Analytical Strain History Comparison

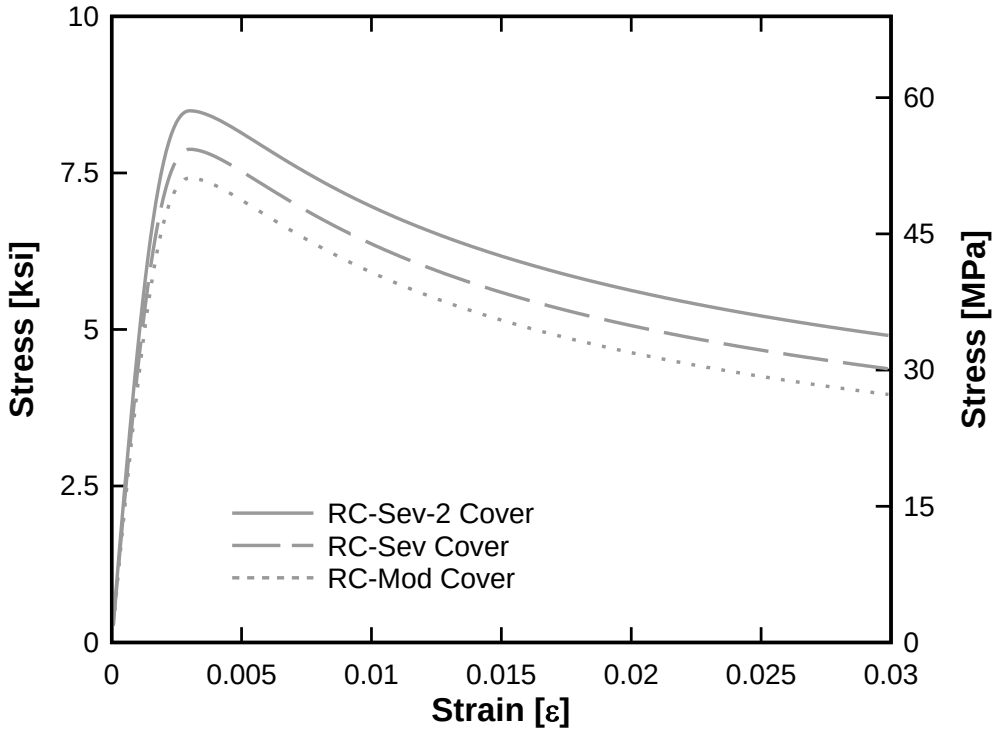

Figure 5-4. Stress Strain Curves for Cover Material Models Including Dynamic Effects

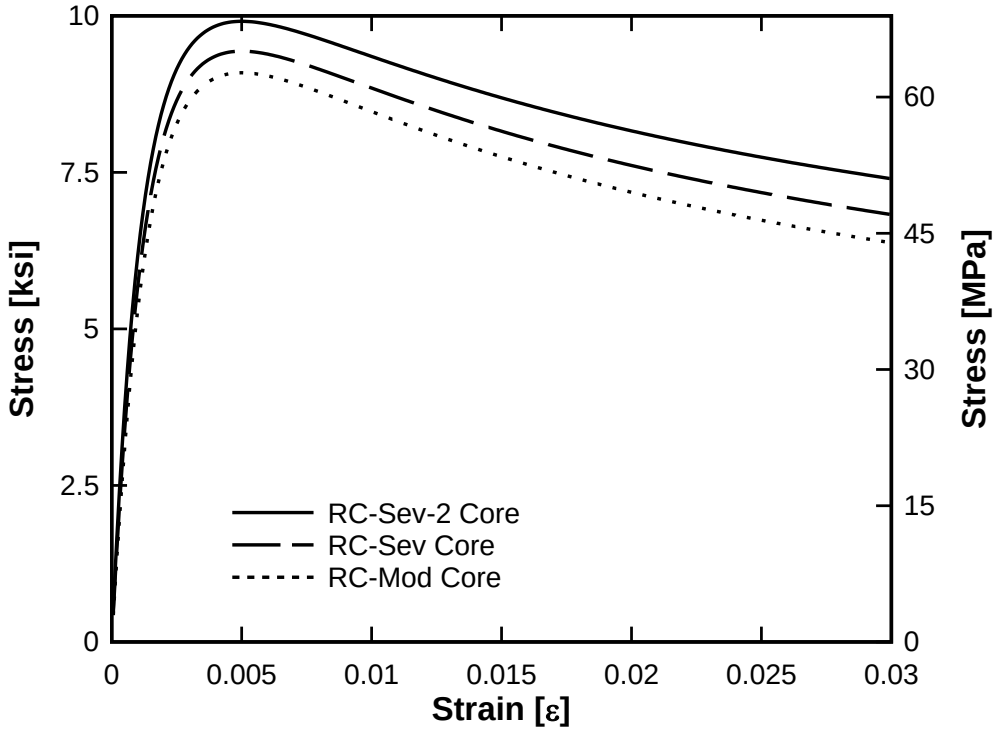

Figure 5-5. Stress Strain Curves for Core Material Models Including Dynamic Effects

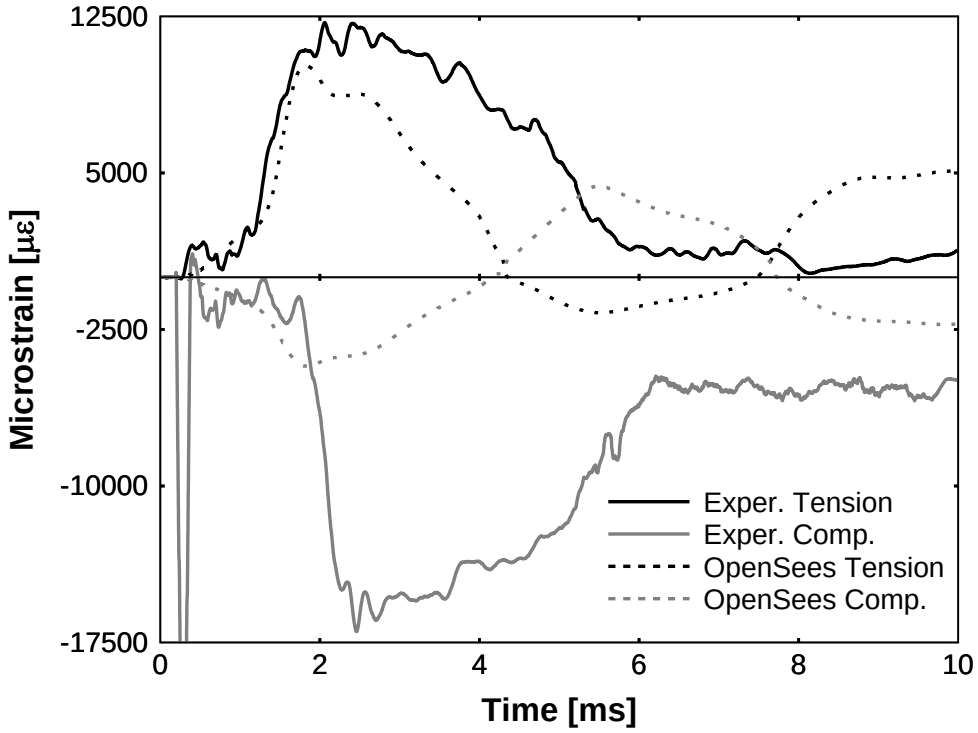

Figure 5-6. CFFT-Moderate Experimental and Analytical Strain History Comparison

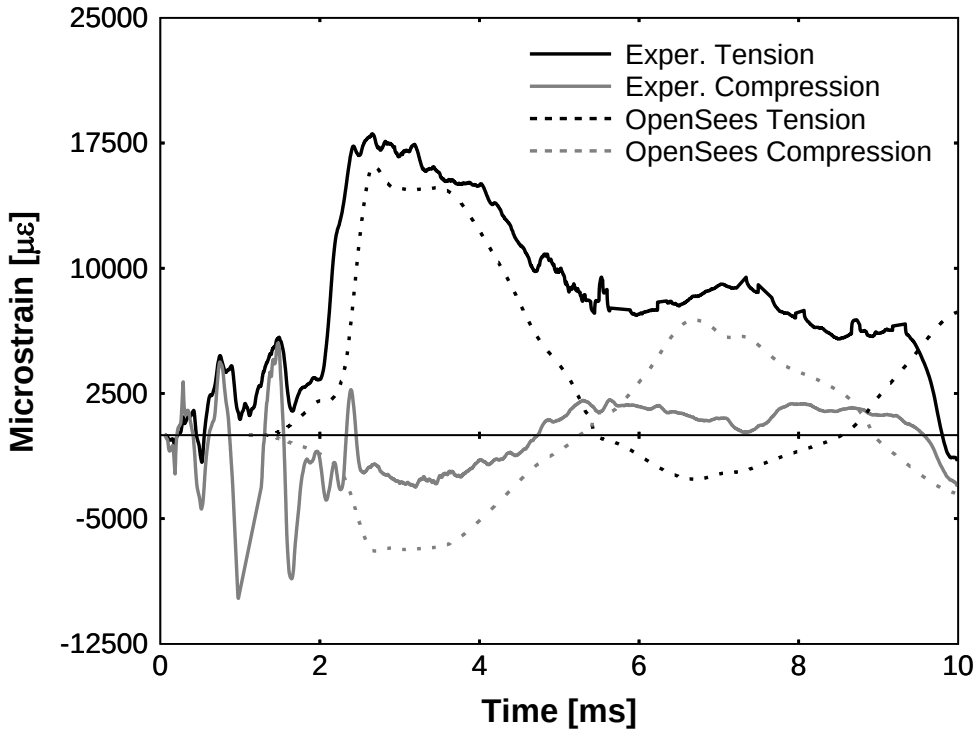

Figure 5-7. CFFT-Severe Experimental and Analytical Strain History Comparison

Figure 5-8. UNR Two Column Bent During Construction Phase

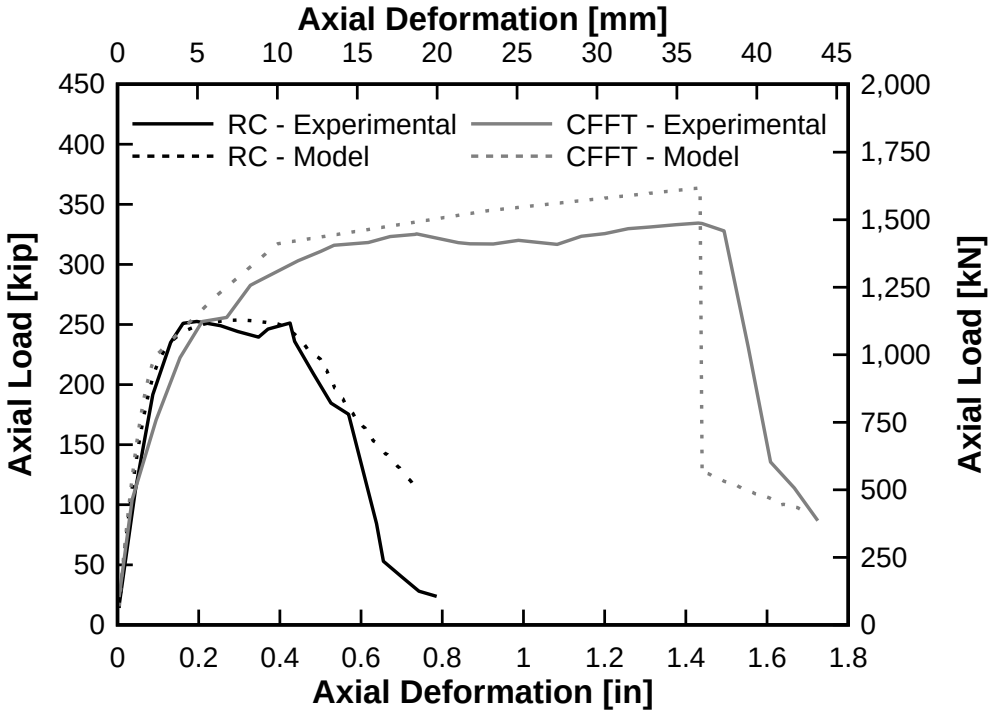

Figure 5-9. Axial Capacity Comparison of RC and CFFT Experiments and OpenSees Models

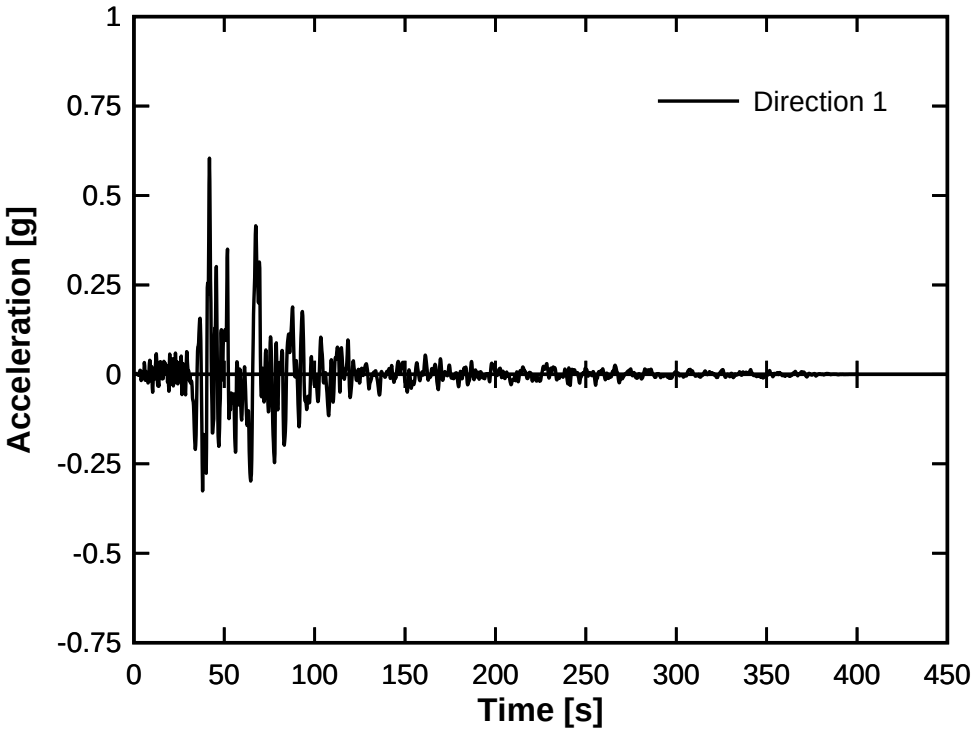

Figure 5-10. Sylmar Olive View Medical Center Horizontal Ground Motion Direction 1

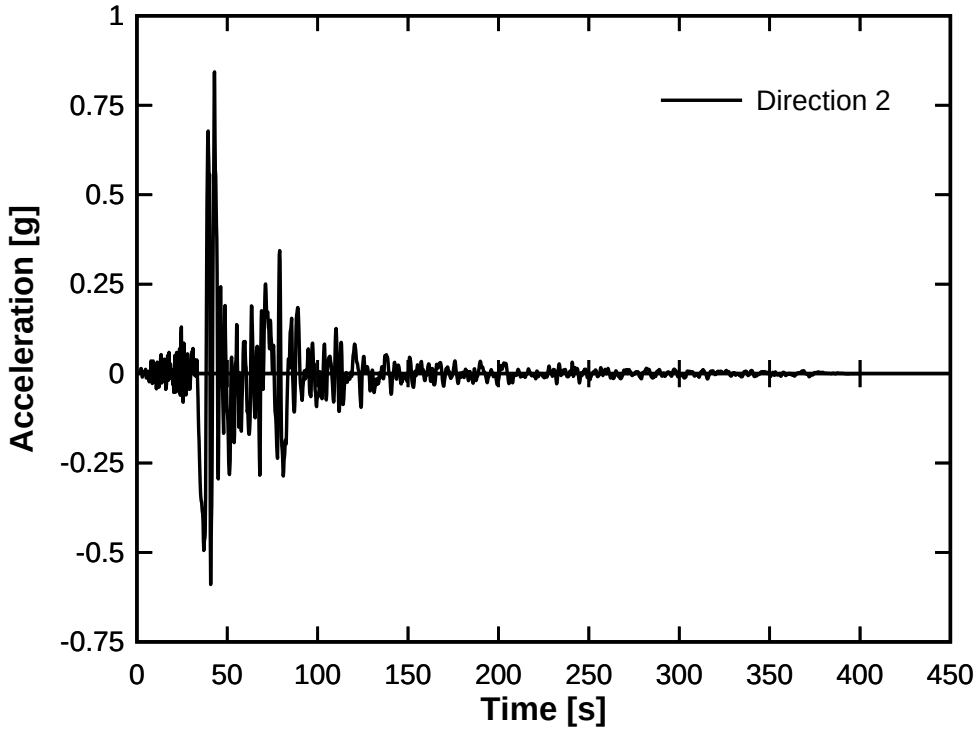

Figure 5-11. Sylmar Olive View Medical Center Horizontal Ground Motion Direction 2

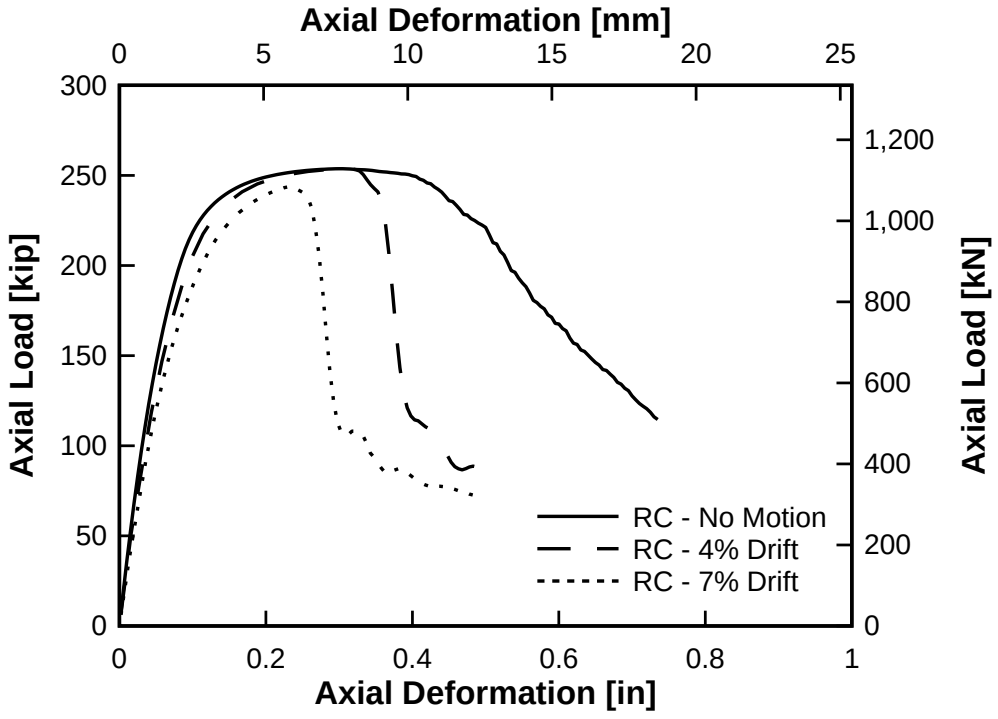

Figure 5-12. Axial Capacity Comparison of RC Columns under No Motion, 4% Drift, and 7% Drift

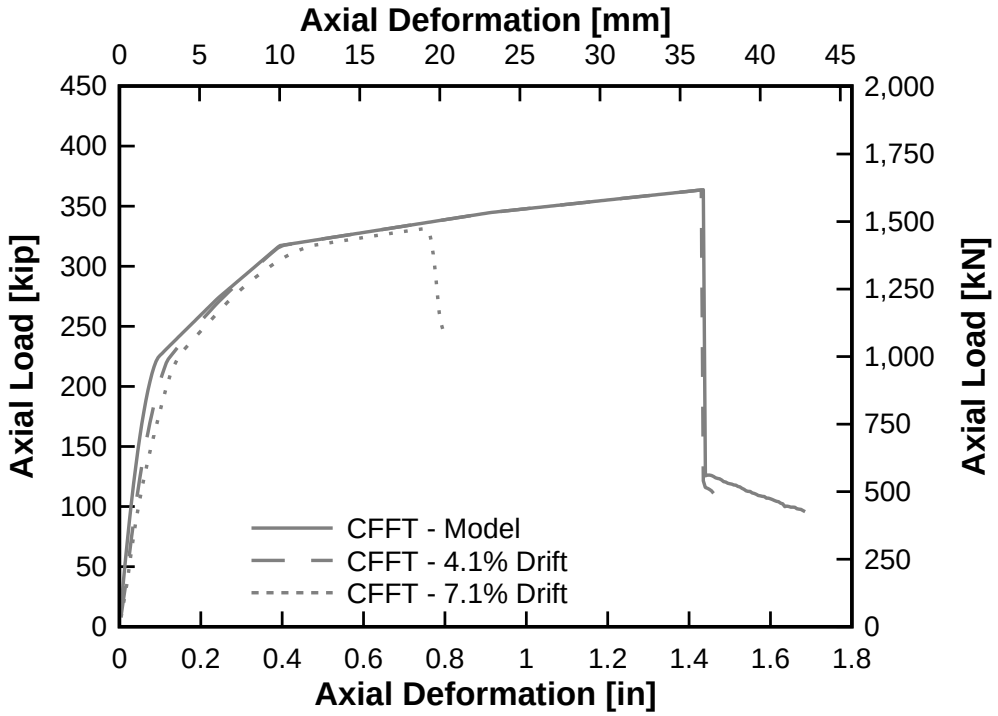

Figure 5-13. Axial Capacity Comparison of CFFT Columns under No Motion, 4% Drift, and 7% Drift

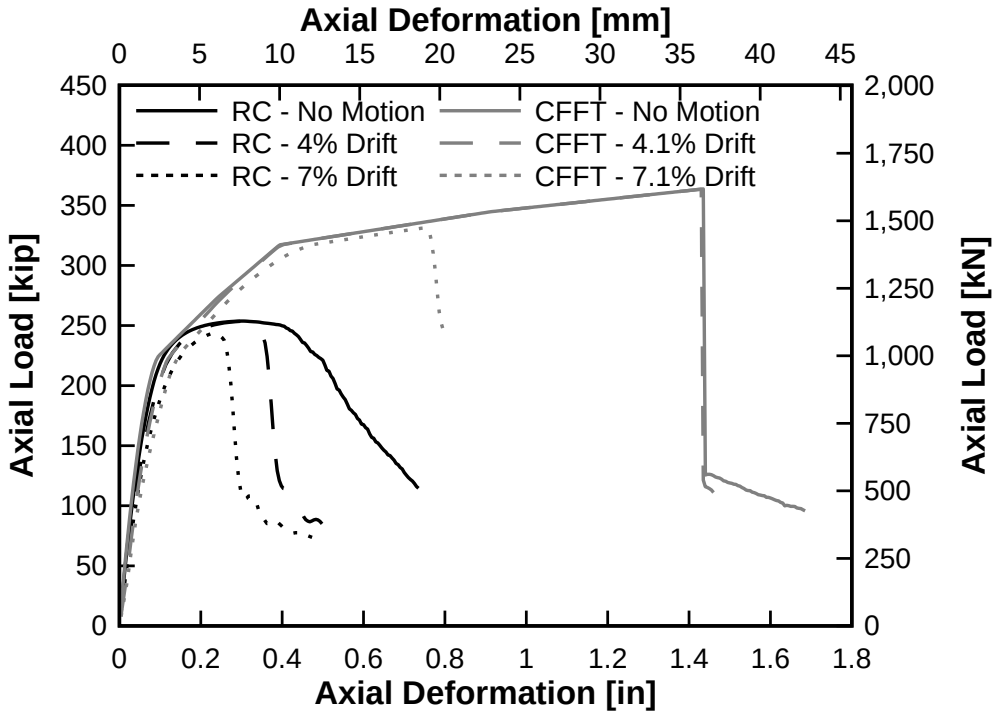

Figure 5-14. Axial Capacity Comparison of RC and CFFT Columns under No Motion, 4% Drift, and 7% Drift

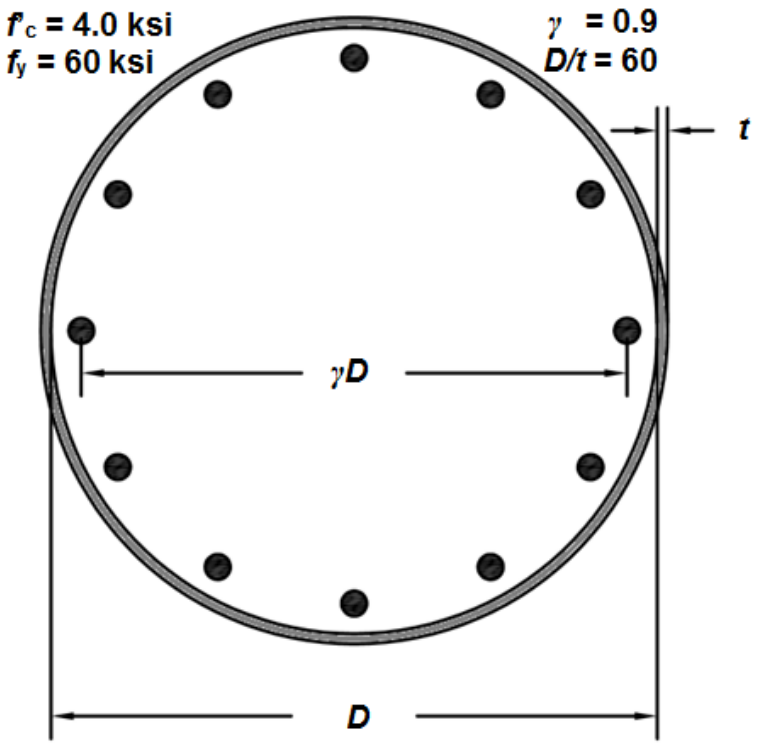

Figure 7-1. Generic CFFT Cross Section

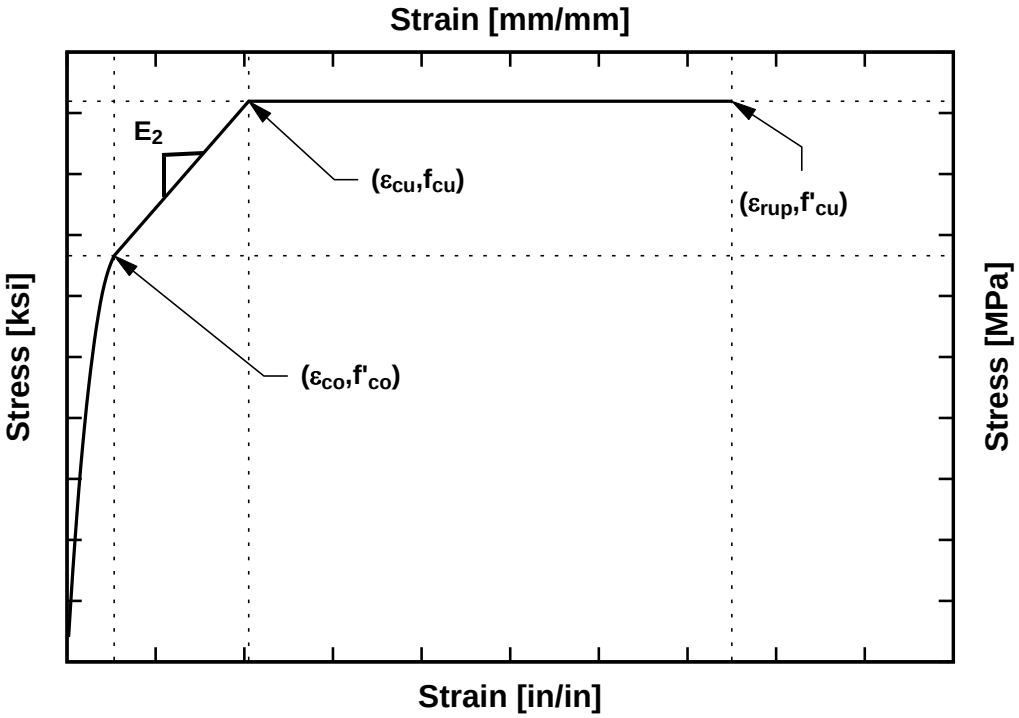

Figure 7-2. Stress-Strain Relationship of FRP Tube Confined Concrete

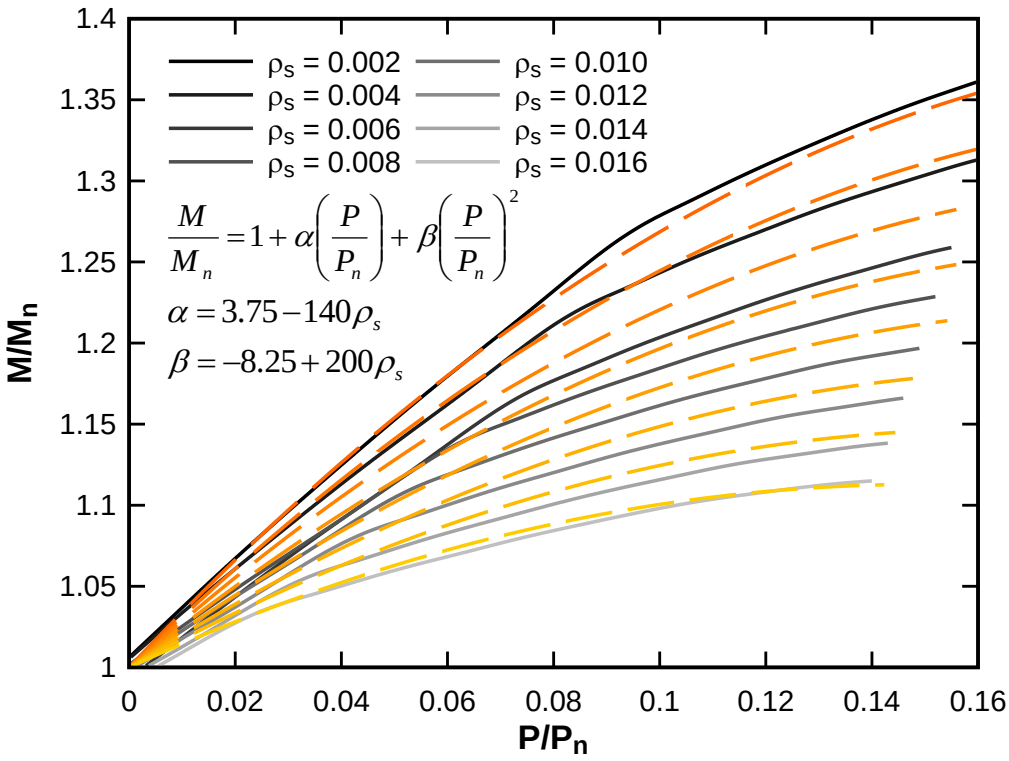

Figure 7-3. P-M Interaction Curve Validation

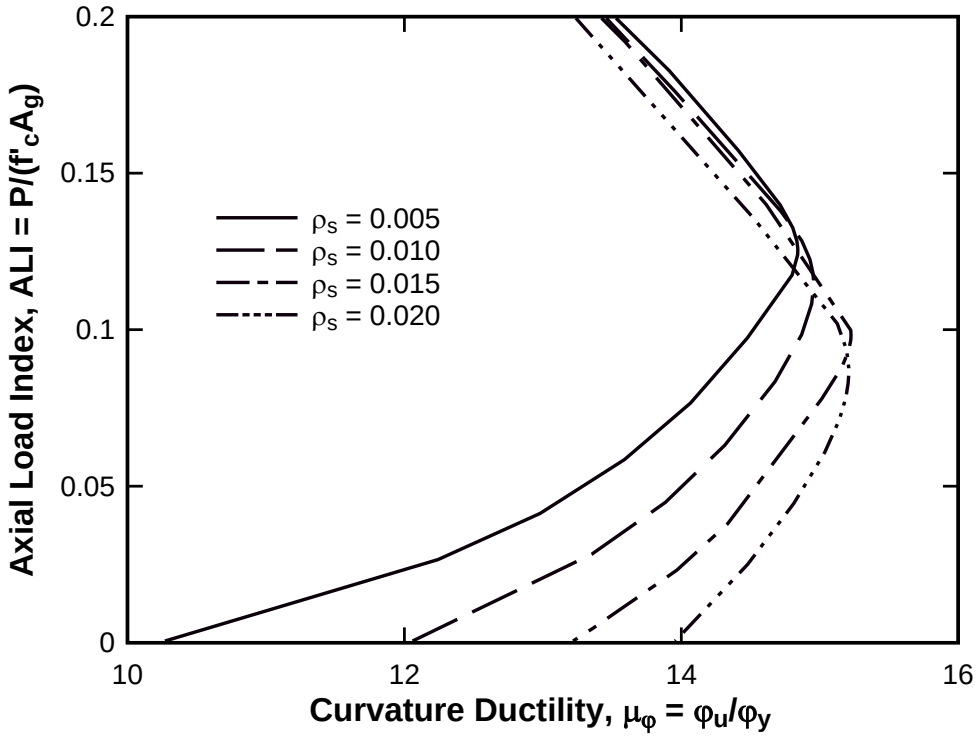

Figure 7-4. Curvature Ductility Curves for Common Design Values of ρ_s

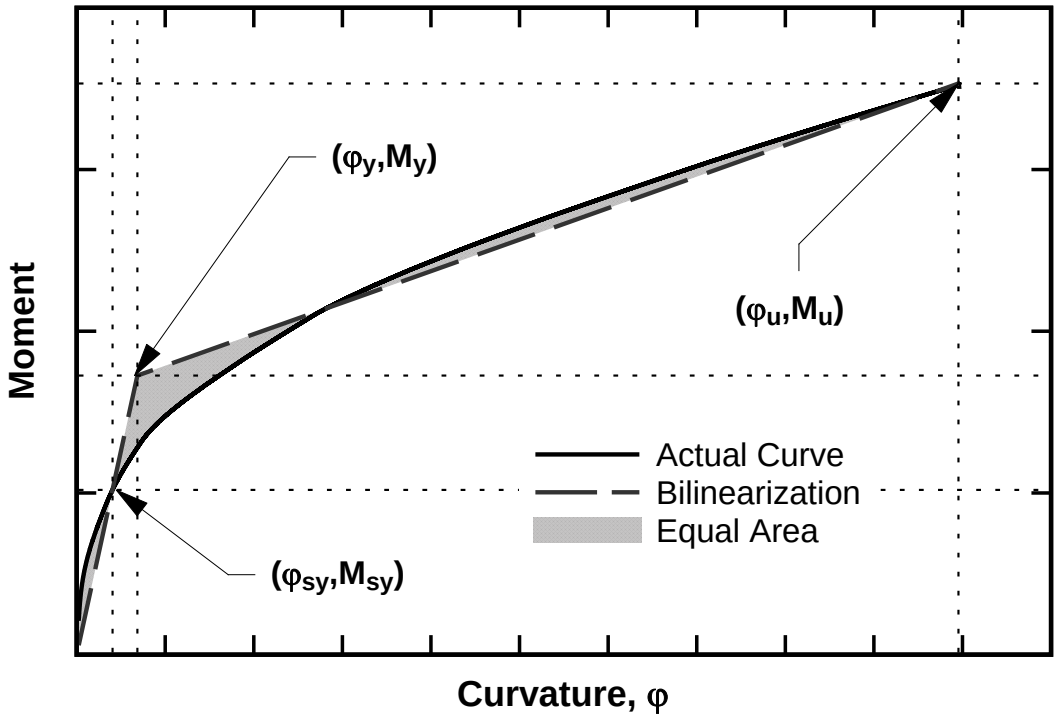

Figure 7-5. Bilinearization Method for CFFT Columns